

Advances in Sustainability Science and Technology

V. Bindhu

João Manuel R. S. Tavares

Stefan Talu *Editors*

Proceedings of Sixth International Conference on Inventive Material Science Applications

ICIMA 2023



 Springer

Advances in Sustainability Science and Technology

Series Editors

Robert J. Howlett Bournemouth University and KES International,
Shoreham-by-Sea, UK

John Littlewood, School of Art & Design, Cardiff Metropolitan University, Cardiff,
UK

Lakhmi C. Jain KES International, Shoreham-by-Sea, UK

The book series aims at bringing together valuable and novel scientific contributions that address the critical issues of renewable energy, sustainable building, sustainable manufacturing, and other sustainability science and technology topics that have an impact in this diverse and fast-changing research community in academia and industry.

The areas to be covered are

- Climate change and mitigation, atmospheric carbon reduction, global warming
- Sustainability science, sustainability technologies
- Sustainable building technologies
- Intelligent buildings
- Sustainable energy generation
- Combined heat and power and district heating systems
- Control and optimization of renewable energy systems
- Smart grids and micro grids, local energy markets
- Smart cities, smart buildings, smart districts, smart countryside
- Energy and environmental assessment in buildings and cities
- Sustainable design, innovation and services
- Sustainable manufacturing processes and technology
- Sustainable manufacturing systems and enterprises
- Decision support for sustainability
- Micro/nanomachining, microelectromechanical machines (MEMS)
- Sustainable transport, smart vehicles and smart roads
- Information technology and artificial intelligence applied to sustainability
- Big data and data analytics applied to sustainability
- Sustainable food production, sustainable horticulture and agriculture
- Sustainability of air, water and other natural resources
- Sustainability policy, shaping the future, the triple bottom line, the circular economy

High quality content is an essential feature for all book proposals accepted for the series. It is expected that editors of all accepted volumes will ensure that contributions are subjected to an appropriate level of reviewing process and adhere to KES quality principles.

The series will include monographs, edited volumes, and selected proceedings.

V. Bindhu · João Manuel R. S. Tavares · Stefan Talu
Editors


Proceedings of Sixth International Conference on Inventive Material Science Applications

ICIMA 2023

 Springer

Editors

V. Bindhu
PPG Institute of Technology
Coimbatore, Tamil Nadu, India

João Manuel R. S. Tavares 
Departamento de Engenharia Mecânica
Universidade do Porto
Porto, Portugal

Stefan Talu
The Technical University of Cluj-Napoca
Cluj-Napoca, Romania

ISSN 2662-6829 ISSN 2662-6837 (electronic)
Advances in Sustainability Science and Technology
ISBN 978-981-99-4188-9 ISBN 978-981-99-4189-6 (eBook)
<https://doi.org/10.1007/978-981-99-4189-6>

© The Editor(s) (if applicable) and The Author(s), under exclusive license to Springer Nature Singapore Pte Ltd. 2023

This work is subject to copyright. All rights are solely and exclusively licensed by the Publisher, whether the whole or part of the material is concerned, specifically the rights of translation, reprinting, reuse of illustrations, recitation, broadcasting, reproduction on microfilms or in any other physical way, and transmission or information storage and retrieval, electronic adaptation, computer software, or by similar or dissimilar methodology now known or hereafter developed.

The use of general descriptive names, registered names, trademarks, service marks, etc. in this publication does not imply, even in the absence of a specific statement, that such names are exempt from the relevant protective laws and regulations and therefore free for general use.

The publisher, the authors, and the editors are safe to assume that the advice and information in this book are believed to be true and accurate at the date of publication. Neither the publisher nor the authors or the editors give a warranty, expressed or implied, with respect to the material contained herein or for any errors or omissions that may have been made. The publisher remains neutral with regard to jurisdictional claims in published maps and institutional affiliations.

This Springer imprint is published by the registered company Springer Nature Singapore Pte Ltd. The registered company address is: 152 Beach Road, #21-01/04 Gateway East, Singapore 189721, Singapore

The conference is dedicated to the outstanding reviewers, authors, editors, and organizers of the conference to commemorate their inevitable contributions to advanced materials science and related fields. Without their participation, it would have been impossible to hold the 6th ICIMA 2023 successfully and ensure high quality papers were published in the conference proceedings.

Preface

We are very pleased to introduce the Proceedings of the 6th International Conference on Inventive Material Science Applications (ICIMA 2023). The 6th ICIMA event was held at PPG Institute of Technology, from 11th to 12th May 2023.

One of the significant and valuable dimensions of this 6th conference edition is the way to researchers, academicians, and engineers in the field from different countries come to one place and initiate discussion on the relevant issues, challenges, opportunities, and research findings. The primary focus of ICIMA 2023 is to provide an excellent platform for the conference participants to share and exchange novel and innovative ideas of original research, and to build international association. The main intent of this conference is to create a smart and advanced research landscape for the areas of inventive material science.

Out of 46 submissions received from different parts of the world, only 13 submissions were accepted as full papers for publication and presentation in ICIMA 2023. These papers provide a brief illustration of current research on relevant topics, covering sustainable strategy, micro/nanomaterials, biomaterials, hybrid electronic materials, innovative electronic materials processing, computational material science, material characterization, fabrication, and synthesis technologies.

The success of the conference is due to the collective efforts of all the reviewers and advisory/review board members. We would like to express and record our gratitude and appreciation to the authors for their contributions. Many thanks to the reviewers, who helped us to maintain high-quality manuscripts included in the proceedings. We also express our sincere thanks to the keynote member 'Dr. M. V. Reddy, Institute of Research Hydro Quebec, Canada', members of the conference committees and

organizing team for their hard work. We wish that all the authors and delegates find ICIMA 2023 proceedings interesting, exciting, and inspiring.

Dr. V. Bindhu
Professor and Head, ECE
PPG Institute of Technology
Coimbatore, India

Dr. João Manuel R. S. Tavares
Professor
Universidade do Porto (FEUP)
Porto, Portugal

Dr. Stefan Talu
The Technical University
of Cluj-Napoca
Cluj-Napoca, Romania

Contents

1	Experimental Investigation of Tribological Characterization of Bio-Nanolubricants	1
	Ravikiran, S. L. Aravind, B. G. Chetan, Afnaan Ali Khan, Prashanth, H. Poornananda, K. S. Sathvik, and K. Shriharsha	
2	Effect of Eu^{3+} on the Luminescence and Photocatalytic Properties of ZnS Nanoparticles	13
	Lallianmawii and N. Mohondas Singh	
3	Buckling of Stiffened Carbon Nanotube-Reinforced Composite (CNTRC) Plates	29
	S. M. Shiyekar and Ranjit Wadkar	
4	Experimental Investigation of Machining Parameters of Monel 400 in Powder Mixed EDM Process	43
	Abhishek Kumar and T. Jagadeesha	
5	Synthesis of Estolides from Coconut, Sunflower and Karanja Oils	53
	P. V. Maneesh Kumar and T. Jagadeesha	
6	Innovative Methods for Increasing the Tool Life of Cutting Tools in Complex Surface Treatment	63
	J. O. Sharipov	
7	Nano-Severe Plastic Deformation Process on Aluminum Alloy and Composites: An Overview	79
	K. G. Sagar	
8	Review of Mechanized Garbage-Picking Machines: Challenges and Advancements in Sweeping and Handling of Trash	89
	Nihal Wargantiwar, V. N. Bhaiswar, and V. W. Khond	

9	Study of Leakage Currents in FinFET SRAM Cells.....	101
	David Gavini, E. Pallavi, B. Kiran Kumar, and Pavankumar Bikki	
10	Advanced Characterization of Estolides from Coconut, Sunflower and Karanja Oils.....	113
	P. V. Maneesh Kumar and T. Jagadeesha	
11	Manufacturing of $AlSi_0Cu_2$ Foam Using Centrifugal Casting Route and $LiAlH_4$ Foaming Agent	127
	Anandarao S. Kashid and Abhijit A. Patil	
12	Synthesis and Characterization of Nano-CuO Complexed HPMC:PVA Polymer Blend Electrolytes.....	135
	N. Sandhya Rani, Sunil Kumar, B. Vinod, C. S. Dileep, C. Manasa, and N. Srikantamurthy	
13	Study on Effect of Pista Shell as Filler Material on Mechanical Performance of Banana Fiber Reinforced Polymer Composite... ..	145
	B. Vinod, L. J. Sudev, B. B. Ganesha, K. N. Arunkumar, and C. S. Thammegowda	
	Author Index.....	155

About the Editors

V. Bindhu received B.E. degree in Electronics and Communication Engineering from Bharathiar University, Coimbatore, in 2002, M.E. degree in Applied Electronics from Anna University, Chennai, in 2007, and Ph.D. degree from Anna University, Chennai, in 2014. She has 10 years of teaching experience and 5 years of research experience. Currently, she is a professor at PPG Institute of Technology, Coimbatore. Her areas of interest include signal processing and VLSI design.

João Manuel R. S. Tavares has a B.Sc. degree in Mechanical Engineering, M.Sc. and Ph.D. degrees in Electrical and Computer Engineering, and Habilitation in Mechanical Engineering. He is the Editor-in-Chief of the Computer Methods in Biomechanics and Biomedical Engineering: Imaging & Visualization and Computer Methods in Biomechanics and Biomedical Engineering journals and the editor of the book series Lecture Notes in Computational Vision and Biomechanics.

Stefan Talu the holder of Ph.D. degree in Engineering, is currently teaching Descriptive Geometry and Engineering Graphics at the Technical University of Cluj-Napoca, Cluj-Napoca, Romania. He obtained his Ph.D. degree in Technical Sciences, in 1998, from the Technical University of Cluj-Napoca, Romania. He has published 19 books and 380 scientific papers (200 papers as a single author or first author), in journals, at symposia, and scientific national and international conferences, in country or abroad, among them 99 papers in Clarivate Analytics indexed journals, with impact factor and relative influence score, 146 papers in international databases, 40 papers at national conferences and 95 papers at international conferences, in collaboration with 210 researchers from 27 foreign countries. He is an expert in the following fields: mechanical and tribological characterizations of macro-micro-nanostructures; topographical and morphological characterizations of three-dimensional surfaces; computer-aided engineering and designing industrial processes, and fractal and multifractal geometry applied in technique.

Chapter 1

Experimental Investigation of Tribological Characterization of Bio-Nanolubricants



Ravikiran, S. L. Aravind, B. G. Chetan, Afnaan Ali Khan, Prashanth, H. Poornananda, K. S. Sathvik, and K. Shriharsha

Abstract The growing environmental concerns in recent years have led to the acceptance of vegetable oil bio-based lubricants as an acceptable replacement for petroleum-based lubricants. In this article, we analyze the tribological properties of three different bio-nano-lubricants with ZrO₂, TiO₂, and ZnO as additives, and explain how the nanoparticles diffuse into mixed vegetable oils. Lubricant samples are prepared by mixing two different vegetable oils, such as castor oil and sunflower oil, in different ratios, then dispersing the nanoparticles in the mixed oil and sonicating to ensure homogeneity of the mixture using a magnetic stirrer. The viscosity is determined using a Redwood viscometer. Measurement of the flash point and ignition point is done with the Pensky–Martin Closed Cup Tester. All friction and anti-wear properties of lubricating fluids are measured using a four-ball tester according to ASTM D 4172–92. Results are compared with several mineral oils. The use of nanoparticles significantly improves friction and wear properties compared to other types of mineral oils. The results of this study also showed superior levels of other attributes, including viscosity, when compared to mineral oil-based lubricants.

Keywords Nanolubricants · Nanoparticles · Viscosity · Flash point and Fire point · Four-ball tester · Friction wear

Ravikiran (✉) · S. L. Aravind · B. G. Chetan · A. Ali Khan · Prashanth · H. Poornananda · K. S. Sathvik · K. Shriharsha
Department of Mechanical Engineering, The National Institute of Engineering, Mysore, Karnataka, India
e-mail: nayak.ravikiran@gmail.com

S. L. Aravind
e-mail: aravindsl@nie.ac.in

1 Introduction

Lubricants are essential products that are made from mineral oils. These oils are utilized for a variety of things, including the efficient operation of all machinery and their tools [1]. Since long before the emergence of modern technology, humans have sought a substance to minimize friction between surfaces that come into contact. For a machine to operate effectively and for a prolonged period, and friction should be minimized as it contributes to heat generation, component wear, and other problems. Lubricants are available in a variety of forms, including solid, liquid, dry film, and coating [2, 3].

Often these lubricants used worldwide end up harming the environment because they're poisonous and hazardous to soil and aquatic species. Global climate change is caused by a rise in greenhouse gas concentrations in the atmosphere as a result of the increasing use of mineral oil-based lubricants. The usage of bio-lubricants is becoming more popular in the lubricating industry around the world in an attempt to reduce all current environmental concerns [4, 5].

Vegetable oils possess a great degradation rate, low temperature stability, high viscosity index, and reduced toxicity compared to mineral resources. There are two possible ways to use vegetable oils: one is to simply use the best vegetable oils alone, without mixing; the other is to blend the vegetable oils in a certain proportion with the industrial lubricants [6, 7]. In comparison to other mineral-based oils, vegetable oils have a greater lubricating performance and have the lowest frictional coefficient [8].

Various studies have been focusing on improving the machining capabilities of vegetable oil by including nanoparticles [9, 10]. Vegetable oils perform better when nanoparticles are added, because nanoparticles minimize friction coefficient and cutting temperature, in addition, results showed that the viscosity, friction coefficient, and wear rate were all improved by the inclusion of nanoparticles [11]. The effect of incorporating ZnO, CuO, and ZrO₂ nanoparticles into oils was discovered to reduce friction and wear due to the nanoparticles serving as load-bearings.

This paper aims to study the various enhancing lubricating properties by blending vegetable oils with mineral oxide nanoparticles [12, 13]. It is important to mention here that the investigated present work focuses on an enhanced high-grade lubricating oil such as SAE 15W40 engine oil [14, 15]. Therefore, the main aim present work is to study the effect of adding 0.2–1% percentage variation of TiO₂ into castor oil (70–75%) and sunflower oil (24–30%) in comparison with the results of 0.25–1% percentage variation of ZrO₂ nanoparticles into the blend of castor oil (70–90%) and sunflower oil (10–30%) on the properties such as viscosity, coefficient of viscosity, flash point, fire point of nanolubricants [16].

2 Methodology

2.1 Sample Preparation

Castor oil and sunflower oil are used as basic oils, and TiO_2 and ZrO_2 are added as nanoparticles in various combinations to create nanolubricants. The mixture was heated to 60°C and agitated constantly for 40 min at 450–500 rpm using a magnetic stirrer, as shown in Fig. 1. The concoction was then agitated constantly, and air quenched to bring it to room temperature. The different combinations of basic oil and nanoadditives are illustrated in Tables 1 and 2.

Fig. 1 Magnetic stirrer



Table 1 Castor oil + Sunflower oil + $\text{TiO}_2 \rightarrow (100 \text{ gm})$

Sl. no	Castor oil (gm)	Sunflower oil (gm)	TiO_2 (gm)
1	70	30	0.25
2	70	30	0.5
3	75	30	1

Table 2 Castor oil + Sunflower oil + $\text{ZrO}_2 \rightarrow (100 \text{ gm})$

Sl no	Castor oil (gm)	Sunflower oil (gm)	ZrO_2 (gm)
1	70	30	0.25
2	70	30	0.5
3	75	30	1

Fig. 2 Redwood viscometer



2.2 Absolute Viscosity Measurement

A viscometer, as shown in Fig. 2, is the Redwood Viscometer, which measures how long it takes an oil sample to flow through a standard opening called an orifice and is then collected in a 50 ml beaker, giving a numerical value for the oil's viscosity in Redwood seconds. The kinematic viscosity of the prepared oil is calculated using the formula [17]

$$\nu = (0.00247t - (0.65/t))$$

The absolute viscosity is calculated using the formula $\mu = \text{kinematic viscosity} * \text{mass density of the oil at corresponding temperature}$.

2.3 Flash and Fire Points

The Pensky–Martens closed-cup flash point is an instrument for determining the flash point of flammable liquids, as shown in Fig. 3. In this oil, sample is poured into a cup. The meter is placed in oil, and the oil is heated. The test flame is passed over the cup at every 2 °C increase in sample temperature. When the sample vapors ignite momentarily in air [18], the flash point temperature is reached. When the sample vapors sustain combustion for at least five seconds, the fire point temperature is reached.

Fig. 3 Pensky–Martin’s closed-cup tester



Table 3 Test parameters

Parameters	Condition
Load	40 kg
Temperature	75 °C
Speed	1200 rpm
Time	60 min

2.4 Four-Ball Test

The test was performed on the following samples according to ASTM D4172–92. The balls used comprised a diameter of 12.7 mm, a mirror finish, and an HRC of 64–66. These balls were composed of chromium steel manufactured by SKF. With the aid of an optical microscope and a four-ball tester, the value of the coefficient of friction and wear scar diameter were measured. Test parameters are listed in Table 3.

3 Results and Discussions

The outcomes of testing samples under various circumstances are compared to those of mineral oils and bio-lubricants.

3.1 Viscosity Measurement

From the tables and figures (Figs. 5 and 6), it can be observed that the viscosity decreases with the rise in temperature as usual; therefore, the viscosity of lubricating

Fig. 4 Four-ball test apparatus

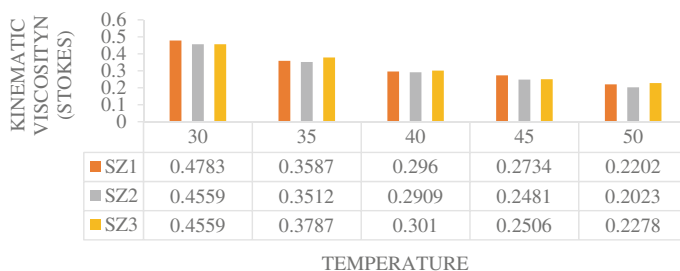


Fig. 5 Kinematic viscosity versus temperature graph for Sunflower oil + ZnO NP

oil also varies. Tables 4 and 5 show that the viscosity of ZnO NP dispersed sunflower oil was found to be higher than the TiO₂ NP dispersed castor and sunflower blended oil and an increase in temperature enhances the movements of the molecules and reduces intermolecular forces so the layers of liquid easily pass over one on another and thus contribute to the reduction of viscosity.

3.2 Flash and Fire Points

Tables 6 and 7 show the flash point and fire point parameters.

From Fig. 7, it is found that SZ3 shows the high flash and fire point followed by SZ2 and SZ1. From Fig. 8, it is found that CST1 shows high flash and fire points followed by CST3 and CST2. Combining both results, TiO₂ NP dispersed castor

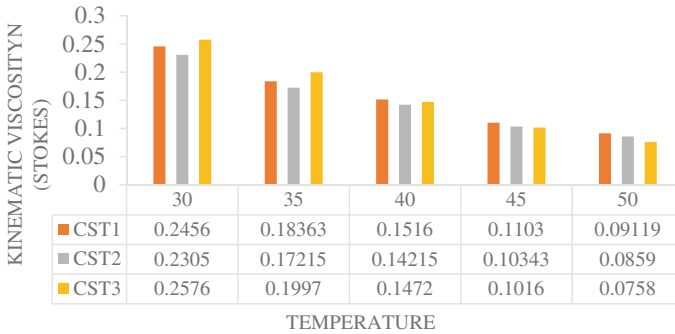


Fig. 6 Kinematic viscosity versus temperature graph for Castor oil+ Sunflower oil + TiO2 NP

Table 4 Sunflower oil + ZnO nanoparticles

Temperature (°C)	SZ1		SZ2		SZ3	
	Kinematic viscosity	Absolute viscosity	Kinematic viscosity	Absolute viscosity	Kinematic viscosity	Absolute viscosity
	ν (stokes)	μ (poise)	ν (stokes)	μ (poise)	ν (stokes)	μ (poise)
30	0.4783	0.4194	0.4559	0.4359	0.4559	0.4559
35	0.3587	0.3145	0.3512	0.3358	0.3787	0.3512
40	0.296	0.2595	0.2909	0.2782	0.301	0.2909
45	0.2734	0.2397	0.2481	0.2372	0.2506	0.2481
50	0.2202	0.1931	0.2023	0.1934	0.2278	0.2023

Table 5 Castor oil + sunflower oil + TiO2 NP

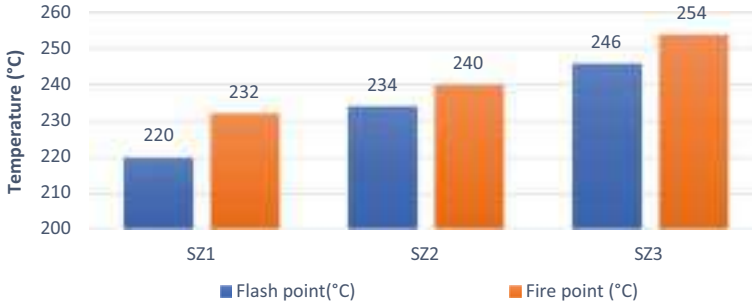
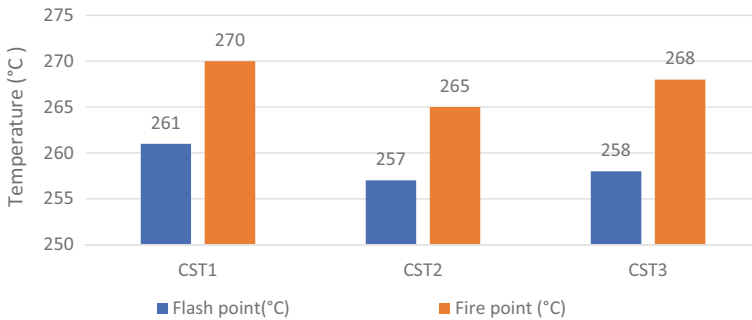
Temperature (°C)	CST1		CST2		CST3	
	Kinematic viscosity	Absolute viscosity	Kinematic viscosity	Absolute viscosity	Kinematic viscosity	Absolute viscosity
	ν (stokes)	μ (poise)	ν (stokes)	μ (poise)	ν (stokes)	μ (poise)
30	0.2456	0.2305	0.27151	0.2576	0.2365	0.2206
35	0.18363	0.17215	0.20982	0.1997	0.1909	0.1779
40	0.1516	0.14215	0.15512	0.1472	0.1466	0.1366
45	0.1103	0.10343	0.10708	0.1016	0.0995	0.0927
50	0.09119	0.0859	0.07895	0.0758	0.07396	0.0689

Table 6 Sunflower oil + ZnO NP

Parameter	CST1	CST2	CST3
Flash point	220	230	246
Fire point	232	240	254

Table 7 Castor oil + Sunflower oil + TiO₂ NP

Parameter	SZ1	SZ2	SZ3
Flash point	220	230	246
Fire point	232	240	254

**Fig. 7** Flash and fire points of sunflower oil samples**Fig. 8** Flash and fire points of castor oil samples

sunflower blend (CST) shows a higher value of flash and fire points compared to ZnO NP dispersed sunflower oil (SZ).

3.3 Tribological Properties

One of the important factors to consider when examining the tribological properties of the tested nanolubricants is the coefficient of friction (COF). For all of the examined lubricants with the nanoparticles, decreased friction coefficients were observed as well in this investigation. For the first 10 min of the wear process, the friction coefficients increased; following which friction reduced. The data on the friction coefficient shown in Fig. 9 has been collected during the four-ball test. However, the

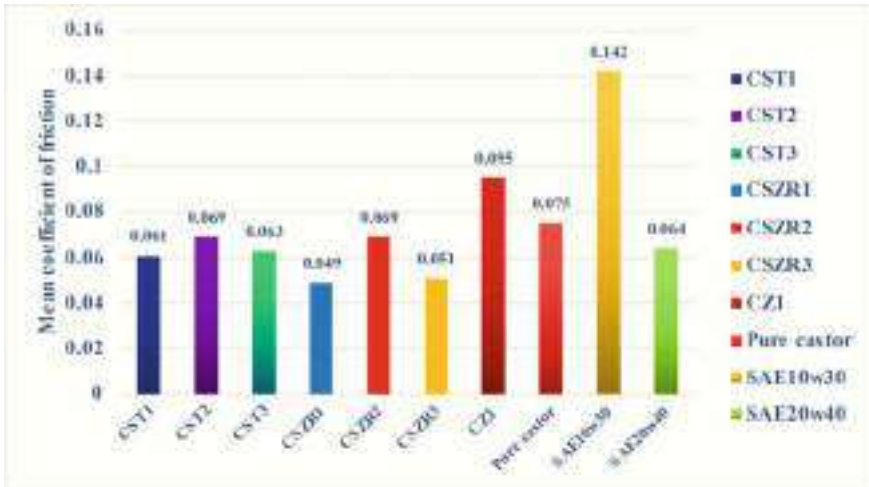


Fig. 9 Mean coefficient of friction of sunflower, castor oil, and SAE grade lubricants

peak values of the friction coefficient in the tests with ZnO were lower than those in the tests with other nanoparticles during the first 10 min of testing. The presence of the nanoparticles could reduce the immediate contact between the ball and disc and make up for any nanodefects on the first contact surfaces.

From the mean friction coefficient values shown in Fig. 9, CSZR1 and CSZR3 exhibit the lowest friction coefficient value of 0.049 and 0.051. When less %wt. ZrO₂ dispersed castor sunflower blended nanolubricant is compared to pure castor oil, the coefficient of friction is reduced approximately by 40%, but CSZR₂ exhibits a little high coefficient of friction compared to CSZR1 and CSZR3. In the case of TiO₂ nanoparticles dispersed castor and sunflower blend, all three CST1, CST2, and CST3 samples exhibit a similar coefficient of friction 0.061, 0.069, and 0.063, respectively. When the mean COF of CSZR1 and CSZR3 is compared with the mean coefficient of friction of synthetic lubricants like SAE10W30 and SAE20W40, even TiO₂ dispersed castor sunflower oil blended lubricants show a similar friction coefficient with SAE10W30 and SAE20W40 but little high friction coefficient than ZrO₂ nanoparticles dispersed castor sunflower oil blended lubricants. The ZnO nanoparticles are dispersed ssn flower oil alone shows a high coefficient of friction compared to all other sample tests. The variation of friction coefficient in Fig. 9 is considered to be independent of the working conditions and temperature.

4 Conclusion

In the lubricating market, most lubricants are made of mineral oil. Lubricants made from mineral oil have many disadvantages after use. It causes environmental pollution like soil pollution, air pollution, water pollution, etc. The quality and properties of vegetable oil blends by adding nanoparticles as additives were evaluated through this study using different parameters. This study shows that when the mean coefficient of friction of $CSZr_1$ and $CSZr_3$ is compared with the mean coefficient of friction of synthetic lubricants like SAE10W30 and SAE20W40, ZrO_2 nanoparticles dispersed castor sunflower oil blended lubricants shows less coefficient of friction. Lubricants containing ZrO_2 nanoparticles dispersed in castor and sunflower oils perform better than SAE10W30 and SAE20W40 due to reduced coefficient of friction and lower value of wear scar diameter. Followed by TiO_2 nanoparticles dispersed castor sunflower blended lubricants which show a similar coefficient of friction with SAE10W30 and SAE20W40 and a better coefficient of friction than pure castor oil. Also, wear scar diameter for the 1% wt. ZrO_2 nanoparticles dispersed castor sunflower blended oil has a lower value at 70:30 ratio. As a result, it is possible that a mixture of castor oil, sunflower oil, and ZrO_2 nanoparticles will work as an anti-wear lubricant. According to analysis, castor oil blends with nanoparticles scattered in them may one day serve as a partial replacement for bio-lubricants. This is due to the fact that blends have no adverse impacts on wear phenomena or lubrication functioning.

References

1. Chandrakar JK, Suhane A (2014) The prospects of vegetable based oils as metal working fluids in manufacturing application—a review. *Int J Eng Res Technol (IJERT)* 03(05)
2. Karmakar G, Ghosh P, Sharma BK (2017) Chemically modifying vegetable oils to prepare green lubricants. *Lubricants* 5(4):44. <https://doi.org/10.3390/lubricants5040044>
3. Chinchkar DS, Satpute ST, Kumbhar NR (2012) Castor oil as green lubricant: a review. *Int J Eng Res Technol (IJERT)* 01(05)
4. Talkit KM, Mahajan DT, VH Masand (2015) Analytical studies on lubrication properties of different vegetable oils blends at different temperatures
5. Kannan I, Karthikeyan S, Ravikumar K (2020) Lubrication performance of castor oil blended with other vegetable oils in grinding of inconel 625. *IOP Conf Ser Mater Sci Eng* 923:012027. <https://doi.org/10.1088/1757-899X/923/1/012027>
6. Husain A, Mehdi M, Ali A, Adeel M, Hassan M, Ani F (2018) Investigation the tribological characteristics of castor oil with mineral oil blends. *J Eng Appl Sci* 37:1–6
7. Jhodkar D, Gupta K Effect of CuO nanoparticles-based vegetable oil on the machining performance of WC tool insert while turning EN 8 steel
8. Cortes V, Sanchez K, Gonzalez R, Alcoutlabi M, Ortega JA (2020) The performance of SiO_2 and TiO_2 nanoparticles as lubricant additives in sunflower oil. *Lubricants* 8(1):10. <https://doi.org/10.3390/lubricants8010010>
9. Ta T-N, Chern S-Y, Horng J-H (2021) Tribological behavior of ionic liquid with nanoparticles. *Materials* 14:6318. <https://doi.org/10.3390/ma14216318>

10. Mallick P, Sahu S (2012) Structure, microstructure and optical absorption analysis of CuO nanoparticles synthesized by sol-gel route. *Nanosci Nanotechnol* 2:71–74. <https://doi.org/10.5923/j.nn.20120203.05>
11. Bekru A, Zelekew OA, Andoshe DM, Sabir FK, Eswaramoorthy R (2021) Microwave-assisted synthesis of CuO nanoparticles using cordia africana Lam. Leaf extract for 4-nitrophenol reduction. *J Nanotechnol* 1–12. <https://doi.org/10.1155/2021/5581621>
12. Silva N, Ramírez S, Díaz I, García A, Hassan N (2019) Easy, quick, and reproducible sonochemical synthesis of CuO nanoparticles
13. Hasnidawani JN, Azlina HN, Norita H, Bonnia NN, Ratim S, Ali SE (2016) Synthesis of ZnO nanostructures
14. Al Abdullaha K, Awada S, Zaraketb J, Salameb C (2017) Synthesis of ZnO nano powders by using sol-gel and studying their structural and electrical properties at different temperature
15. Savi BM, Rodrigues L, Bernardin AM (2011) Synthesis of ZnO nanoparticles by sol-gel processing
16. Shahabuddin M, Masjuki HH, Kalam MA (2013) Experimental investigation into tribological characteristics of bio-lubricant formulated from jatropha oil. *Proc Eng* 56:597–606. <https://doi.org/10.1016/j.proeng.2013.03.165>
17. Li X, Murashima M, Umehara N (2018) Effect of nanoparticles as lubricant additives on friction and wear behavior of tetrahedral amorphous carbon (ta-C) coating. *J Tribologi* 16:15–29
18. Syahrullail S, et al (2013) Performance of vegetable oil using sol-gel method. *Proc Chem* 19:211–216. <https://doi.org/10.1016/j.proche.2016.03.095> as Lubricant in extreme pressure condition. *Proc Eng* 68(2013):172–177

Chapter 2

Effect of Eu^{3+} on the Luminescence and Photocatalytic Properties of ZnS Nanoparticles



Lallianmawii and N. Mohondas Singh

Abstract Eu^{3+} doped ZnS was prepared using a reflux method. Using different techniques such as XRD, SEM, TEM, FTIR, PL, and UV, the structural, morphological, and optical properties were examined. Photoluminescence studies show the most intense electric dipole transition ${}^5\text{D}_0 \rightarrow {}^7\text{F}_2$, which is particularly sensitive to the chemical bond in the vicinity of an ion of europium (III) when excited at 350 nm. The CIE studies show all the prepared samples fall in the white regions, which have potential applications in optical devices, lightning outdoors, etc. The degradation percentage of methyl red was found to be 90% and follows first-order kinetics. Additionally, the Eu^{3+} plays a crucial role in the production of free radicals. As a result, the catalyst has enhanced degradation activity, high stability, and can be utilized for the degradation of toxic dyes present in the environment.

Keywords Photoluminescence · Degradation · Methyl red · Catalyst · Dyes · Environment

1 Introduction

Environmental contaminants are often regarded as one of the main problems that have a negative impact on human health. Water evaporation, surface water contamination, and drinking water shortages have been identified as major global issues in recent years [1]. The pharmaceutical, chemical, and textile industries, which carelessly dump their waste into the environment and water bodies, are the primary sources of various organic pollutants that contaminate water. The ecosystem and aquatic life are severely harmed by these hazardous organic effluents [2]. The integrity of the world's water supply has gotten worse due to the numerous colours and toxic organic pollutants in aquatic environments [3]. The fast growth of the textile industry has also

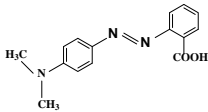
Lallianmawii · N. M. Singh (✉)
Department of Chemistry, Mizoram University, Tanhril, Mizoram, India
e-mail: nmdas08@rediffmail.com

raised concerns about water contamination due to the durability and toxicity of these dyes to both aquatic and terrestrial organisms [4]. When compared to primary effluent treatment methods, which are less successful and also create secondary pollutants, semiconductor photocatalysis is exceptionally effective at completely breaking down organic contaminants [5].

Dyes are frequently employed as colouring agents in a variety of sectors, including cloth, fleece, food, plastics, and cosmetics [6]. The dyes are intricate, water-soluble chemical compounds with low biodegradability that are also potentially carcinogenic and mutagenic. Natural dyes and synthetic/artificial dyes are the two main categories of dyes [7]. Natural dyes are derived from plant materials, including bark, leaves, wood, roots, etc., whereas synthetic dyes are created from substances like chemicals, minerals, and petroleum derivatives and are used in the paper, textile, and cosmetic industries as colouring agents and printing processes [8]. Synthetic dyes are organic molecules that are identified by chromophores in their molecular structures. They are frequently divided into a number of classes based on the chromophore groups they contain, such as azo, anthraquinone, indigoide, phthalocyanine, sulphur, and triphenylmethane derivatives [9, 10]. Organic colours that are highly cytotoxic to mammalian tissues, including azo and fluorescein dyes, are difficult to break down naturally. Based on the sort of change they have, dyes are also divided into two major categories: non-ionic dyes and ionic dyes [11]. The two types of ionic dyes are cationic and anionic, which have positive and negative charges, respectively. Due to their limited biodegradability, organic dyes have produced significant environmental contamination issues. So, it is crucial for environmental protection that dye molecules are removed from industrial effluent. Diverse technologies, such as carbon adsorption, flocculation, ozonization, and activated sludge procedures, are currently available to treat industrial effluent dyes. Nevertheless, these processes are expensive, and it has been discovered that the degradation kinetics are slow and ineffective [12]. Advanced oxidation processes (AOPs), which use photocatalytic reactions to produce superoxide (O_2^-), reactive oxygen species (ROS), and hydroxyl (OH) radicals, are promising techniques for eliminating dye contaminants [13]. With its efficiency and wide applicability, photocatalysis is an environmentally friendly and green process that has the potential to completely remove toxic pollutants from the environment. It also has a number of advantages, such as the capacity to mineralize hazardous organic pollutants into non-toxic inorganics like carbon dioxide and water and to break down toxins without the use of secondary chemicals [14].

Due to its superiority, environmental friendliness, efficacy, and good stability, photocatalytic degradation of semiconductors serving as photocatalysts is acknowledged as a highly successful method of treating antibiotic residues [15]. ZnS is an n-type semiconductor photocatalyst with a suitable negative redox potential in the conduction band and valence band and a large bandgap of 3.68 eV. It has remarkable chemical stability against oxidation and hydrolysis [16]. Due to their lack of toxicity, ZnS nanoparticles are the preferred material for use in biological and photocatalytic processes. ZnS has recently been thoroughly investigated as an innovative semiconductor in the fields of photocatalysis, sensing, and imaging due to its significant qualities, such as visible-light responsiveness, acceptable band locations, greater

Table 1 Physiochemical properties of methyl red

Sample	Molecular formula	Molecular structure	Density	M_w (g/mol)
Methyl red	$\text{C}_{15}\text{H}_{15}\text{N}_3\text{O}_2$		0.839 g/mL–25 °C	269.3 g/mol

chemical and thermal stability, and non-toxic and affordable manufacture [17]. The lower hazardous content, higher surface area, commercial viability, biocompatibility, and chemical inertness of the nanoparticles make the modification with transition metal ion doping significant [18]. Doping is a common and efficient method for changing the energy levels, surface states, and structural, optical, magnetic, and spintronic properties of semiconductors [19]. Owing to the critical role that dopants play in semiconductor devices, researchers have been looking into the properties and prospective applications of these semiconductor nanoparticles that have been purposefully doped. In this study, a reflux approach was used to synthesize Eu^{3+} doped ZnS nanoparticles. The characteristics of ZnS nanoparticles are altered by the addition of Eu^{3+} dopants. Physiochemical properties of Methyl red is shown in Table 1.

2 Experimental Section

2.1 Chemical Used

Europium (III) nitrate hexahydrate ($\text{EuH}_{12}\text{N}_3\text{O}_{15}$), Alfa Aesar purity 99.9%, Zinc acetate dehydrate $(\text{CH}_3\text{COO})_2\text{Zn} + 2\text{H}_2\text{O}$ Alfa Aesar, purity 98.0%, and Sodium Sulfide $\text{H}_2\text{Na}_2\text{OS}$ purity 98.0% Alfa Aesar was used to synthesize Eu^{3+} doped ZnS.

2.2 Synthesis

Eu^{3+} doped ZnS (2, 4, 6 at.%) was synthesized using the reflux method. Zinc acetate dehydrate and europium (III) nitrate hexahydrate were dissolved in 50 ml of distilled water and stirred for 1 h at room temperature. After stirring at room temperature, sodium sulfide was added drop by drop, and the solution was refluxed at 150 °C for 3 h. The obtained precipitate was ultrasonically treated for 30 min. Finally, the solution was centrifuged at 7000 rpm. After drying, the samples were used for characterization.

2.3 Characterization

Rigaku Cu K ν Smart Lab was used to obtain XRD data. Image from TEM was taken by FEI Tecnai (G2 F20 X-TWIN). Supra 55 FESEM model with a high resolution was used to capture the FESEM image. Shimadzu IR affinity-1S FT-IR data were collected. Photoluminescence studies were done using a Hitachi F-7000 fluorescence spectrometer. Thermo-Scientific evolution of 220 was used to study UV visible spectrophotometer.

3 Results and Discussions

3.1 XRD

Figure 1 displays the XRD patterns of Eu^{3+} doped ZnS nanoparticles. The planes (111), (220), and (311) of the face-centred cubic (FCC) of ZnS were observed as three large peaks corresponding to (JCPDS No.05–0566). The Debye–Scherrer equation is used to determine the particle size [16]:

$$D = K\lambda/\beta\cos\theta$$

Fig. 1 X-ray diffraction of Eu^{3+} doped ZnS 2, 4, 6 at.%

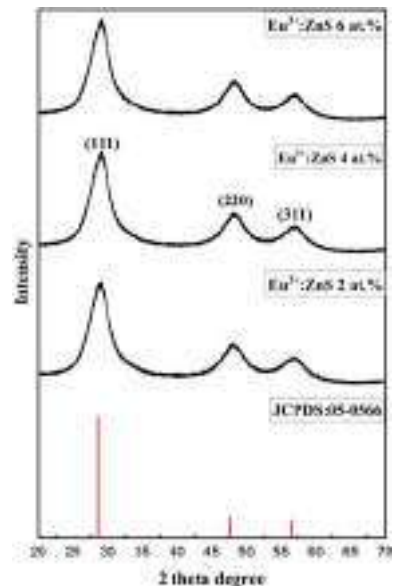


Table 2 Calculation of crystal size, cell volume, and lattice parameters from XRD

Sample	Lattice parameters	Cell volume	Crystal size (nm)
Eu^{3+} 2 at.%	5.344	157.76	9.45
Eu^{3+} 4 at.%	5.835	157.79	11.21
Eu^{3+} 6 at.%	5.423	157.81	13.54

where the crystal size is denoted by D , ρ is the X-ray wavelength, maximum diffraction angle is θ , and K is a constant (0.9). No similar diffraction peaks were observed for samples that contained Eu , indicating that the Eu ions are properly integrated into the ZnS lattice. The full-width half maximum (FWHM) of the diffraction peaks broadens as the doping concentration increases due to the quantum size effect. Dopants frequently serve as nucleation sites during the synthesis of nanoparticles, lowering the energy needed for the formation of the first particle and promoting the growth of a higher number of smaller ones [20]. The dopant atoms' drag force against the increase in crystallite size is the main cause of it. It ultimately results in a smaller crystallite size. The particle size was found to be 9–13 nm. Calculation of crystal size, cell volume, and lattice parameters from XRD are shown in Table 2.

3.2 Morphological Analysis of SEM

Many optoelectronic applications heavily depend on microstructure and surface shape. Figure 2a shows the morphology of the as-prepared Eu -doped ZnS nanoparticles as determined by SEM. Small, uniformly sized grains with a uniform shape can be found in the SEM image of Eu -doped ZnS . Due to the Eu -doped ZnS 's reduced size and increased surface energy, the sample seems to be more aggregated. From Fig. 2b, the EDX spectra, we can confirm the presence of Eu , Zn , and S . The average particle size calculated from Eu^{3+} doped ZnS 4 at.% was found to be 22 nm Fig. 2c.

3.3 TEM

Figure 3a shows a TEM image of Eu^{3+} doped ZnS 4 at.%. The particle size was found to be 13 nm. It agrees exactly with the results of the XRD's Scherer equation based calculation of crystallite size. The catalyst's photocatalytic activity is greatly influenced by the size of its particle. A thin layer of ZnS was laid over the surface of the Eu^{3+} doped ZnS nanocrystals. Figure 3a depicts the formation of a thin ZnS shell layer on top of the nanocrystals [21]. Reduced particle size produces a wide surface area that is ideal for high photocatalytic activity. The SAED pattern enables the exact indexing of various rings (311, 220, and 111) in the same positions.

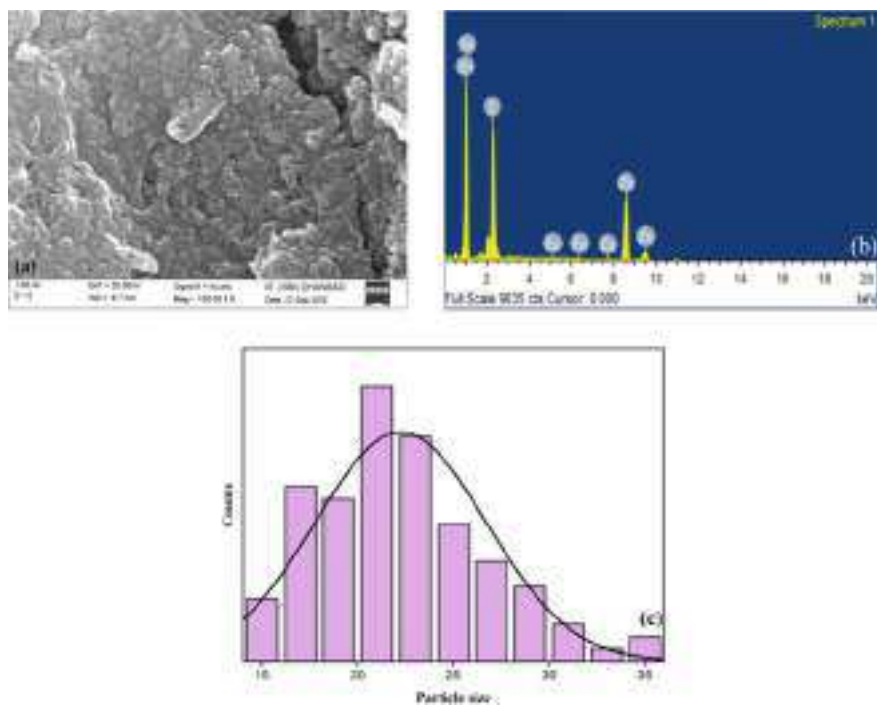


Fig. 2 a SEM image of Eu³⁺ doped ZnS 4 at.% b EDX spectra of Eu³⁺ doped ZnS c Average size particle size of Eu³⁺ doped ZnS 4 at.%

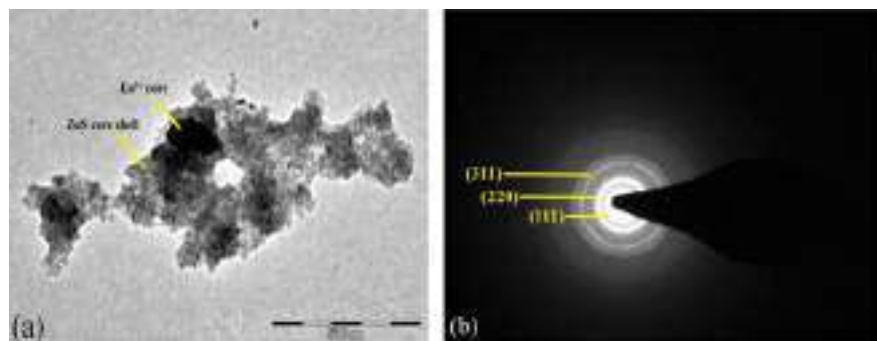
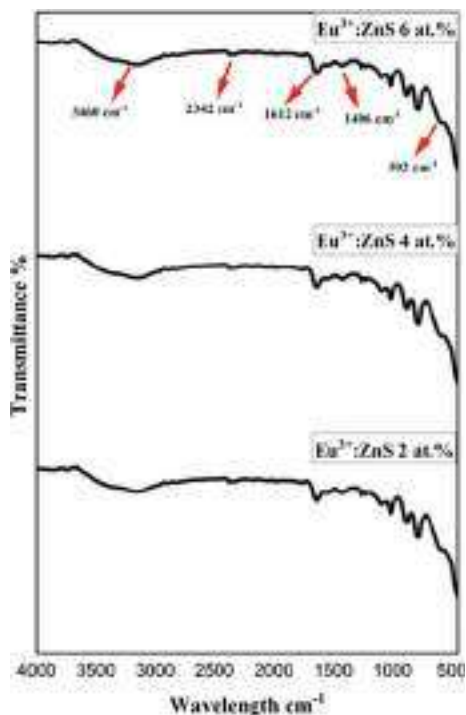


Fig. 3 a TEM image of Eu³⁺ doped ZnS 4 at.% b SAED spectra of Eu³⁺ doped ZnS

3.4 FTIR

Figure 4 shows a large absorption band at 3460 cm^{-1} , which is associated with the stretching vibration of N–H. The distinctive stretching vibration of C–H is what

Fig. 4 FTIR spectra of Eu^{3+} 2 at%, 4 at.% and 6 at.%



causes the peak to appear at 2342 cm^{-1} . The N–H and C–H bending peaks are visible at 1612 cm^{-1} and 1406 cm^{-1} , respectively. In addition, the peak at 592 cm^{-1} belongs to the stretching vibration of Zn–S, which is also similarly reported in the literature [22].

3.5 Photoluminescence Studies

At room temperature, the excitation and emission properties of solid-state photoluminescence were studied. When excited at 350 nm, the major emission peaks observed are given in Fig. 5a. Different transitions of 528 nm (${}^5\text{D}_0 \rightarrow {}^7\text{F}_1$), 543 nm (${}^5\text{D}_0 \rightarrow {}^7\text{F}_2$), 565 nm (${}^5\text{D}_0 \rightarrow {}^7\text{F}_3$), 572 nm (${}^5\text{D}_0 \rightarrow {}^7\text{F}_4$), 603 nm (${}^5\text{D}_0 \rightarrow {}^7\text{F}_5$), and 636 nm (${}^5\text{D}_0 \rightarrow {}^7\text{F}_6$) were obtained. The strongest was the induced electric dipole transition ${}^5\text{D}_0 \rightarrow {}^7\text{F}_2$, which is especially susceptible to the chemical bond in close proximity to an ion of europium (III) and emits red when exposed to UV light [23, 24]. Whereas the electric dipole transition (${}^5\text{D}_0 \rightarrow {}^7\text{F}_2$) is relatively strong, the magnetic dipole transition (${}^5\text{D}_0 \rightarrow {}^7\text{F}_1$) is less susceptible to the coordinated environment. When emitted at 510 nm, the excitation peaks of europium are observed at 362 nm

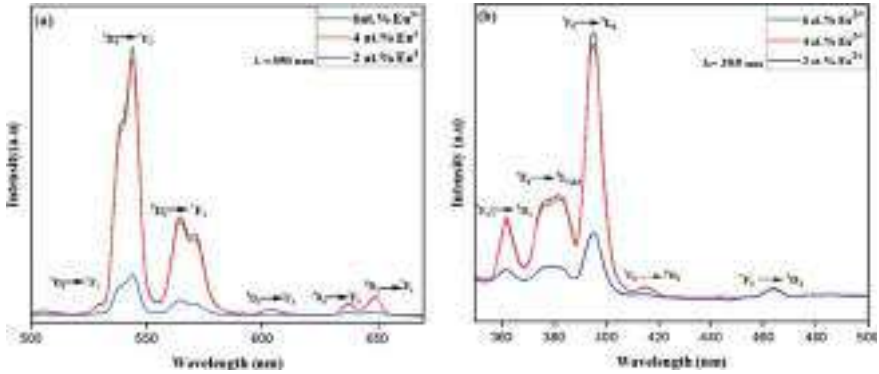


Fig. 5 a Emission spectra of Eu^{3+} doped ZnS b Excitation spectra of Eu^{3+} doped ZnS

(${}^7\text{F}_0 \rightarrow {}^5\text{D}_4$), 377, 380, 382 nm (${}^7\text{F}_0 \rightarrow {}^5\text{L}_{7, 8, 9}$), 395 nm (${}^7\text{F}_0 \rightarrow {}^5\text{L}_6$), 415 nm (${}^7\text{F}_0 \rightarrow {}^5\text{D}_3$), 463 nm (${}^7\text{F}_0 \rightarrow {}^5\text{D}_2$).

3.6 CIE Analysis

The chromaticity diagram from the Commission International de L’Eclairage (CIE) shows that the coordinates are highly helpful in defining the perceived colour of a phosphor’s emission. The emission spectra-derived colour coordinates and their accompanying co-related colour temperatures are provided in Table 3. McCamy’s equation was used to determine the co-related colour temperatures (CCT) [25] for Eu^{3+} doped ZnS.

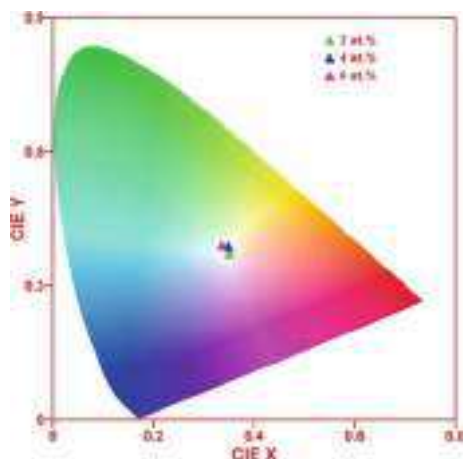
$$CCT = -437n^3 + 3601n^2 - 6861n + 5514.31 \text{ and } n = (x - xe)/(y - ye)$$

The determined colour coordinates are represented by x and y in this case. Figure 6 depicts the CIE chromaticity diagram for the obtained Eu^{3+} doped ZnS doped with various concentrations.

Table 3 CCT colour coordinates

Sample	Calculated colour coordinates		CCT
	x	y	
2 at.% Eu^{3+}	0.351	0.372	4854
4 at.% Eu^{3+}	0.349	0.388	4965
6 at.% Eu^{3+}	0.335	0.390	5417

Fig. 6 CIE chromaticity diagrams of the Eu^{3+} doped ZnS (2, 4, 6 at.%)

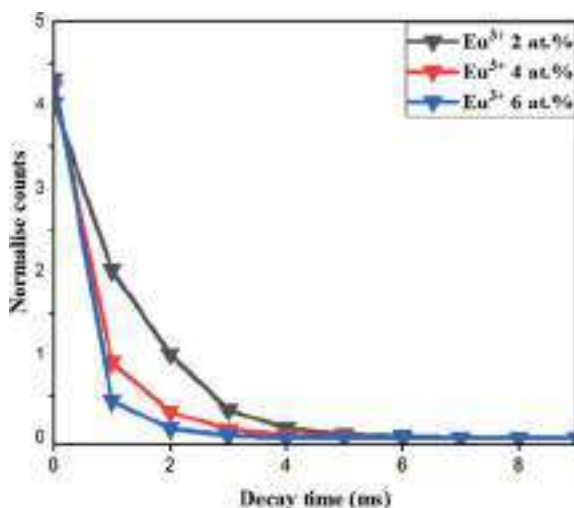


3.7 Lifetime Study

Eu^{3+} doped ZnS nanoparticles have been assessed based on their luminescence decay curves. The excitation and emission wavelengths were fixed at 350 and 510 nm for each concentration, respectively, to measure the decay curves. Figure 7 displays the calculated decay curves. With the use of the bi-exponential equation, all observed decay curves are successfully fit [26].

$$I = I_1 \exp(-t/\tau_1) + I_2 \exp(-t/\tau_2)$$

Fig. 7 Bi-exponential fitting of the photoluminescence decay curve of Eu^{3+} doped ZnS



In this case, I_1 and I_2 stand for the intensities at two distinct time points, whereas β_1 and β_2 stand for the respective decay times. The following equation can be used to calculate the average decay time. Average lifetimes of 1.41, 1.69, and 1.79 ms were determined for Eu^{3+} doped ZnS concentrations of 2 at.%, 4 at.%, and 6 at.%, respectively. Their goodness of fitting (R^2) for the aforementioned concentrations is 0.958, 0.968, and 0.983, respectively.

4 UV–Visible Spectroscopy

4.1 Effect of Initial Dye Concentration

At various concentrations between 5 and 30 ppm, the impact of the initial dye concentration on the photodegradation of methyl red was studied. The degradation at varied initial dye concentrations is shown in Fig. 8. When the initial dye concentration was raised, it was noticed that the percent degradation gradually dropped. This could be a result of the reaction mixture's colour getting darker and darker as the dye's initial concentration rises. This limits the ability of light to reach the catalyst's surface. Due to the constant light intensity and irradiation time, the relative amount of ($\text{OH}\cdot$ and $\text{O}_2\cdot^-$) production on the catalyst surface does not increase. Since the light photons are largely absorbed by the dye molecules and are not able to reach the catalyst surface, their concentrations will decrease as the dye concentration increases [27]. As a result, the dye's ability to degrade becomes less effective as dye concentration rises. We found that 15 ppm was the optimum dye concentration.

Fig. 8 Effect of initial concentration of dye (in ppm)

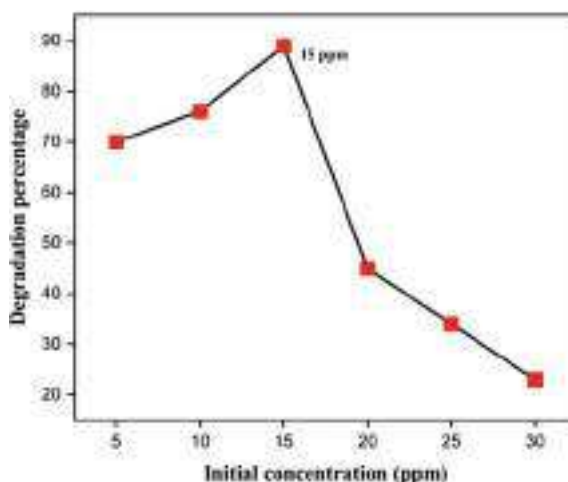
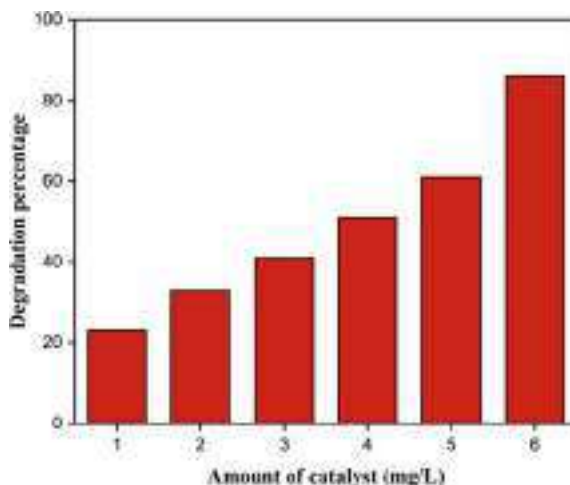


Fig. 9 Effect of amount of catalyst (mg/L)



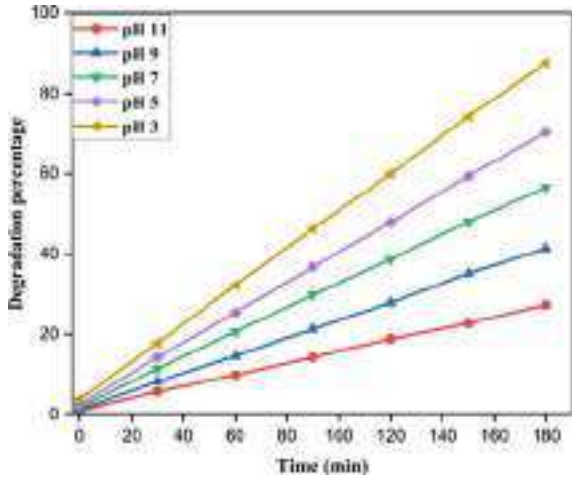
4.2 Effect of Amount of Catalyst

By irradiating dye solution (15 ppm), various catalytic doses ranging from 1 to 6 mg/L, the impact of photocatalyst concentration on dye degradation was examined. Figure 9 displays a plot of dye degradation percentage versus catalytic dosage. With an increase in catalytic dosage, the percentage of degradation rises. The dye was shown to decolorize most when exposed to radiation for 180 min at a catalytic dose of 6 mg/L. Hence, a 6 mg/L optimal catalytic dose was chosen (Fig. 9).

4.3 Effect of pH

Figure 10 displays the rate of methyl red degradation as a function of time and pH. This anionic dye degraded more quickly under photochemical conditions at pH 3 as shown in the figure. The electrostatic interactions between a semiconductor surface, substrate, and charged radicals during a photocatalytic oxidation are highly dependent on the pH of the solution. The surface of the catalyst has a higher positive charge in an acidic environment, which facilitates dye molecule adsorption. Acidic media also reduces the amount of e^-/h^+ recombination [28]. The catalyst surface becomes negatively charged when the pH rises, and dye molecules may repel one another, resulting in low molecule adsorption and a reduction in the efficiency of degradation. Hence, raising pH maximizes photocatalytic performance.

Fig. 10 Effect of pH



Methyl red was degraded following the optical parameters such as the effect of catalytic dosage, initial concentration, and amount of catalyst. Using 15 ppm of initial concentration, 6 mg/L of catalytic dosage, and pH 3, methyl red was degraded within 180 min. The percentage degradation of dye was calculated from the following equation:

$$\text{Percentage of Degradation} = \frac{A_0 - A_t}{A_0} \times 100$$

A_0 is the initial dye absorption before degradation and the absorbance of dye is A_t . The degradation percentage of methyl red was found to be 90% Figs. 11.

Fig. 11 Degradation of methyl red within 180 min

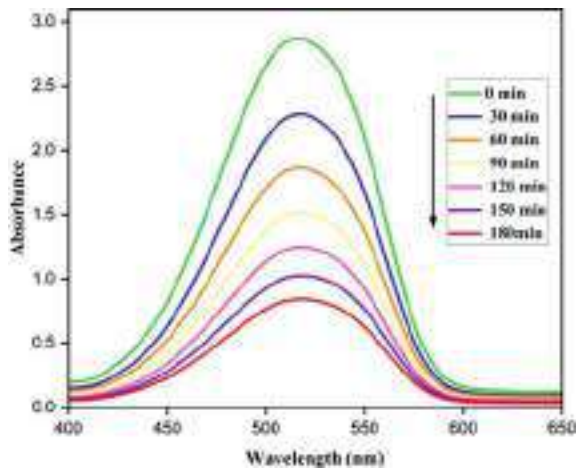


Fig. 12 Kinetic study of Eu^{3+} doped ZnS 2, 4, 6 at. %

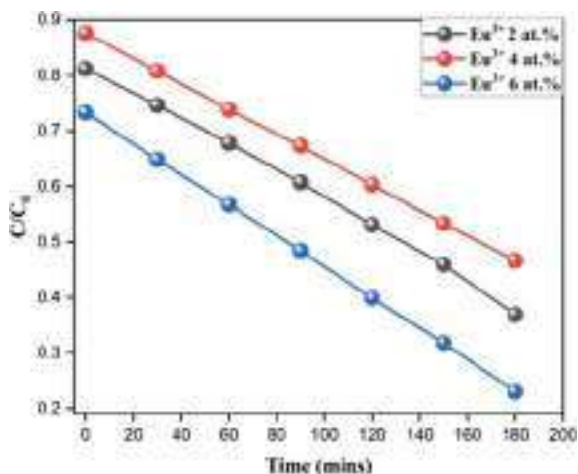


Table 4 Kinetic study of Eu^{3+} doped ZnS

Sample	Rate constant $k(\text{min}^{-1})$	R^2	DE%
Eu^{3+} 2 at. %	4.04×10^{-3}	0.958	62
Eu^{3+} 4 at. %	3.12×10^{-2}	0.968	87
Eu^{3+} 6 at. %	3.89×10^{-2}	0.983	90

4.4 Kinetic Study

Kinetic studies can be used to clarify the process and efficacy of the photodegradation. A linear fitting of $\ln C_0/C_t$ versus t was used to apply the first-order kinetic model [29]:

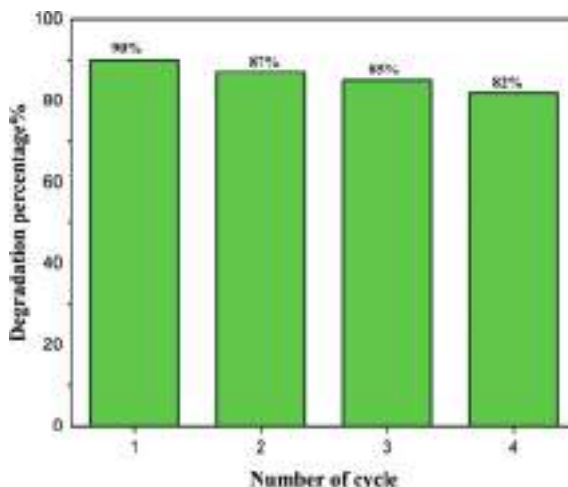
$$\ln C_0/C_t = kt$$

where (k) is the response rate constant and (t) is the time. As a result, it is evident that under UV light illumination, catalysts that are 6 at. % doped have better photodegradation efficiencies than catalysts that are 2 at. % or 4 at. %. Kinetic study of Eu^{3+} doped ZnS 2, 4, 6 at. % is shown in Fig. 12. Kinetic study of Eu^{3+} doped ZnS is tabulated in Table 4.

4.5 Stability Analysis

After the first cycle was finished, the catalyst was carefully removed by centrifugation, washed with ethanol/water, and dried at 120°C in order to conduct the stability

Fig. 13 Number of cycles performed



study. By utilizing a 180-min dye solution degradation process, the catalyst regenerated was used to assess its stability and reusability. The same amount of catalyst and dye was used for each cycle. The degradation of methyl red was 82% after the fourth cycle. The number of cycles performed is shown in Fig. 13.

5 Conclusion

We can conclude that Eu^{3+} doped ZnS nanoparticles of 2at.%, 4 at.%, and 6 at.% were synthesized by using a reflux method. The XRD studies show the particles are nanosized. Different transitions of 528 nm ($^5\text{D}_0 \rightarrow ^7\text{F}_1$), 543 nm ($^5\text{D}_0 \rightarrow ^7\text{F}_2$), 565 nm ($^5\text{D}_0 \rightarrow ^7\text{F}_3$), 572 nm ($^5\text{D}_0 \rightarrow ^7\text{F}_4$), 603 nm ($^5\text{D}_0 \rightarrow ^7\text{F}_5$), and 636 nm ($^5\text{D}_0 \rightarrow ^7\text{F}_6$) were obtained from the photoluminescence studies. According to the CIE diagram, all of the prepared samples gave out a nearly white colour that may be employed in optical devices. Methyl red can be degraded successfully by employing 6 mg/L of the catalyst, initial concentration of 15 ppm, and at pH 3. The degradation percentage was found to be 90%, and it also follows the first-order kinetics. Therefore, the synthesized Eu^{3+} doped ZnS nanoparticles can be used for removing toxic chemicals present in the environment.

Acknowledgements Not applicable.

Conflict of Interest No potential conflict of interest was declared by the author.

References

1. Elango G, Roopan SM (2016) Efficiency of SnO_2 Nanoparticles toward Photocatalytic Degradation of Methylene Blue Dye. *J Photochem Photobiol B Biol* 155:34–38
2. Shabani M, Haghghi M, Kahforoushan D, Haghghi A (2018) Mesoporous-mixed-phase of hierarchical bismuth oxychlorides nanophotocatalyst with enhanced photocatalytic application in treatment of antibiotic effluents. *J Clean Prod*
3. Amini M, Ashrafi M (2016) Photocatalytic degradation of some organic dyes under solar light irradiation using TiO_2 and ZnO nanoparticles. *1*(1):79–86
4. Hasanpour M, Hatami M (2020) Photocatalytic performance of aerogels for organic dyes removal from wastewaters: review study. *J Mol Liq* 309:113094
5. Pavithra KG, Kumar PS, Jaikumar V, Rajan PS (2019) Removal of colorants from wastewater : a review on sources and treatment. *J Ind Eng Chem*
6. Lai X, Guo R, Xiao H, Lan J, Jiang S, Cui C, Ren E (2019) Rapid microwave-assisted bio-synthesized silver/dandelion catalyst with superior catalytic performance for dyes degradation. *J Hazard Mater* 371:506–512
7. Hussain W, Badshah A, Hussain RA (2017) Graphical abstract SC. *Mater Chem Phys*
8. Hussain W, Malik H, Bahadur A, Hussain RA, Shoaib M, Iqbal S, Hussain H (2018) Synthesis and characterization of cds photocatalyst with different morphologies: visible light activated dyes degradation study. *Kinet Catal* 59(6):710–719
9. Anwer H, Mahmood A, Lee J, Kim K, Park J, Yip ACK (2019) Photocatalysts for degradation of dyes in industrial effluents : opportunities and challenges. *Nano Res* 12(1)
10. Das TK, Remanan S, Ghosh S, Ghosh SK, Das NC (2021) Efficient synthesis of catalytic active silver nanoparticles illuminated cerium oxide nanotube : A mussel inspired approach. *Environ Nanotechnol Monit Manag* 15:100411
11. Hitam CNC, Jalil AA (2019) A review on exploration of Fe_2O_3 photocatalyst towards degradation of dyes and organic contaminants. *J Environ Manage* 258:110050
12. Preet K, Gupta G, Kotal M, Kansal SK, Salunke DB (2019) Mechanochemical synthesis of a new triptycene-based imine-linked covalent organic polymer for degradation of organic dye. *Cryst Growth Des* 19:2525–2530
13. Tanveer M, Cao C, Aslam I, Ali Z, Idrees F, Tahir M, Khan WS, Butt FK, Mahmood A (2014) Effect of the morphology of CuS upon the photocatalytic degradation of organic dyes. *RSC Adv* 4(108):63447–63456
14. Yan X, Wu Z, Huang C, Liu K, Shi W (2016) Author's accepted manuscript. *Ceram Int*
15. Jrad A, Naouai M, Abdallah A, Ammar S, Turki-Kamoun N (2021) Doping ZnS films with cobalt: structural, compositional, morphological, optical, electrical, magnetic and photocatalytic properties. *Phys B Condens Matter* 603:412776
16. Annalakshmi M, Kumaravel S, Chen SM, Balasubramanian P, Balamurugan TST (2020) A straightforward ultrasonic-assisted synthesis of zinc sulfide for supersensitive detection of carcinogenic nitrite ions in water samples. *Sens Actuat B Chem* 305:127387
17. Sharma K, Raizada P, Hasija V, Singh P, Bajpai A, Nguyen VH, Rangabhashiyam S, Kumar P, Nadda AK, Kim SY, Varma RS, Le TTN, Van Le Q (2021) ZnS -based quantum dots as photocatalysts for water purification. *J Water Process Eng* 43:102217
18. Lin Y-F, Chang Y-H, Chang Y-S, Tsai B-S, Li Y-C (2006) Luminescent properties of trivalent praseodymium-doped barium zinc sulfide. *J Electrochem Soc* 153(6):G543
19. Kaur J, Sharma M, Pandey OP (2015) Structural and optical studies of undoped and copper doped zinc sulphide nanoparticles for photocatalytic application. *Superlattices Microstruct* 77:35–53
20. Murugadoss G, Prakash J, Kumar MR, Alothman AA, Habila MA, Peera SG (2022) Controlled synthesis of europium-doped SnS quantum dots for ultra-fast degradation of selective industrial dyes. *Catalysts*
21. Zhang Y, Das GK, Xu R, Thatt T, Tan Y (2009) Tb-doped iron oxide : bifunctional fluorescent and magnetic nanocrystals. 3696–3703

22. Online VA, Gong X, Liu Z, Yan D, Zhao H, Li N, Zhang X, Du Y (2015) Nanocrystals constructed by co-thermal solution phase. *3(Cd)*:3902–3907
23. Monteiro JHKS, De Bettencourt-Dias A, Mazali IO, Sigoli FA (2015) The effect of 4-halogenobenzoate ligands on luminescent and structural properties of lanthanide complexes: experimental and theoretical approaches. *New J Chem* 39(3):1883–1891
24. Hussain S, Chen X, Harrison WTA, Elsegood MRJ, Ahmad S, Li S, Muhammad S, Awoyelu D (2019) Synthesis, crystal structures and photoluminescent properties of one-dimensional Europium(III)- and Terbium(III)-Glutarate coordination polymers, and their applications for the sensing of Fe³⁺ and nitroaromatics. *Front Chem* 7:1–14
25. Naorem RS, Singh NP, Singh NM (2022) Photoluminescence properties of Tb³⁺ doped BiPO₄ nanophosphor synthesised by co-precipitation method using ethylene glycol. *Mater Technol* 37(8):610–617
26. Premjit Singh N, Rangeela Devi Y, Rajmuhon Singh N, Mohondas Singh N (2019) Synthesis of Tb³⁺ ion doped ZnWO₄ phosphors and investigation of their photoluminescence properties: concentration effect. *Bull Mater Sci* 42(3):17–20
27. Sahoo C (2005) Photocatalytic degradation of methyl red dye in aqueous solutions under UV irradiation using Ag+doped TiO₂. 181:91–100
28. Thota S, Tirukkavalluri SR, Bojja S (2014) Visible light induced photocatalytic degradation of methyl red with codoped Titania. 2014
29. Naorem RS, Singh NP, Singh NM (2022) Synthesis of SnS₂ photocatalysts and investigation of their photocatalytic activities under sun light irradiation. *Adv Mater Process Technol* 8(4):4720–4730

Chapter 3

Buckling of Stiffened Carbon Nanotube-Reinforced Composite (CNTRC) Plates



S. M. Shiyekar and Ranjit Wadkar

Abstract This article explores the buckling phenomenon in UG-CNTRC plates exposed to in-plane loading. The analytical modelling approach employed a Reissner–Mindlin (FOST), and a numerical computational coding, ABAQUS, was utilized to examine the performance of the (UD-CNTRC) plate-subjected buckling. Effective material properties of SWCNT were obtained by applying RM. The validity of the results from the computational tool was validated by comparison with existing literature and analytical FOST. An analysis was conducted on different variables, including the side-to-thickness ratio, CNT volume fraction, loading as well as boundary specification, to investigate their impacts on the stability performance of plates. The research further examined stiffened CNTRC plates, and the findings were presented.

Keywords Analytical solution · Uni-directional · Carbon nanotube reinforced composite · Plate · First-order shear deformation theory · ABAQUS

1 Introduction

Composites are manufactured by blending two or more disparate materials to create a unique material with enhanced properties when compared to the separate components. Nanocomposites refer to materials in which nanoparticles are added to enhance a specific property. The incorporation of nanoparticles can enhance material attributes such as endurance and conductivity. The use of nanoparticles in structural material components results in a high strength-to-weight ratio.

S. M. Shiyekar (✉)

Department of Civil Engineering, D Y Patil College of Engineering, Akurdi, Pune, India
e-mail: smshiyekar@dypcoeakurdi.ac.in

R. Wadkar

Department of Civil Engineering, Rajarambapu Institute of Technology, Rajaramnagar, Maharashtra, India

Innovation by Iijima [1] in 1991, attracted researchers and they referred to it as the “material for the twenty-first century” [2]. CNTs have nanodimensions comprised of rolled layers of graphite and can be arrived in different shapes such as “zigzag,” “chiral,” and “armchair”. SWCNT (“Single-wall carbon nanotube reinforced composite plates”) or MWCNT (multi-wall) tubes may be formed considering the layer of graphite is rolled along. Previous research [3–5] has demonstrated that CNTs exhibit excellent properties, such as exceptional stiffness and strength. Researchers [6, 7] have conducted experiments and simulations [8] to demonstrate the load-taking abilities of CNTs in composites. Despite the great potential of CNT-based composites, there are also significant challenges in their development. Researchers have used various methods, such as RVE, FEM, and MD simulations, to evaluate actual material attributes related to CNT-based composites and also to examine their thermo-mechanical properties. Studies have also explored the stress–strain performance of CNT composites [9–13].

The studies mentioned above provide useful insights into the performance of CNTRCs in different structures. Wuite and Adali [14] examined CNTRC beams. Vodenitcharova and Zhang [15] explored the flexure local buckling and pure bending of nanobeams strengthened by an SWNT. Lei et al. [16] presented a report on the stability of functionally graded and uniformly distributed (FG and UD) CNTRC plates. Similarly, Malekzadeh and Shojaee [17] researched the buckling of CNTRC thick plates. A stability investigation of FG nanocomposite bi-directional plates reinforced by SWCNTs was carried out by Jafari et al. [18]. To ascertain the SWCNT’s material characteristics, they used the “extended rule of mixture” (ERM). Formica et al. [19] used the “classical laminated plate theory” (CLPT) and “third-order theory” (TOT) to study the dynamics of CNTRC plates. The CLPT was used by Arani et al. [20] to illustrate the buckling of CNTRC bi-directional plates. This plate is subject to a variety of boundary constraints. The MT (Mori–Tanaka) approach is used to assess the efficient elastic modulus of composites containing straight nanotubes using the “finite element method” (FEM) tool. Shen [21–23] examined the post-buckling properties of cylindrical FG CNTRC shells exposed to axial compression at temperature. Christian Mittelstedt [24] presented the buckling of orthotropic and isotropic plates with stiffeners. Kant and Swaminathan [25] investigated the stability of laminated composite and sandwiches. Timoshenko and Gere [26] conducted a buckling analysis of an isotropic plate. Kurkute and Shiyekar [27] presented the buckling of laminates using higher-order theory. Mayandi and Jeyaraj [28] discussed flexure, buckling and free vibrations of FG CNT beams under thermal loads. Shiyekar and Lavate [29] analyzed FG plates using ABAQUS UMAT.

The present study focuses on UD-CNTRC plate buckling under in-plane forces with various boundary parameters. The FEM and the Mindlin [30] (FOST) are used. The commercial program ABAQUS [31] is employed as the computational tool. The study includes three categories of plates: isotropic plate, UD-CNTRC plates, and CNTRC plates with stiffeners along the longitudinal direction. The influences of several factors, including plate aspect ratio, CNT volume fraction, as well as boundary limits on the CNTRC plate buckling strength, are studied.

2 Modeling of CNTRC Material

2.1 Extended Rule of Mixture (ERM)

The CNTRC plates are produced through a fusion of SWCNTs and polymer matrix, where the attributes of SWCNTs vary depending on their handedness size and thermal conditions. The present study considers UD-CNTRC: “Carbon nanotube-reinforced composite” plates with ‘*h*’ thickness, ‘*a*’ length, and ‘*b*’ width (Fig. 1), and the MT methodology or the RM (Rule of Mixture) will be used to identify the real material characteristics of these composites. The RM involves introducing CNT efficiency parameters, and assuming that CNTs are distributed uniformly across the UD-CNTRC plate thickness, as shown in (Fig. 1). Volume fraction of CNT is given as

$$V_{CNT} = V_{CNT}^*(UD \cdot CNTRC) \tag{1}$$

where

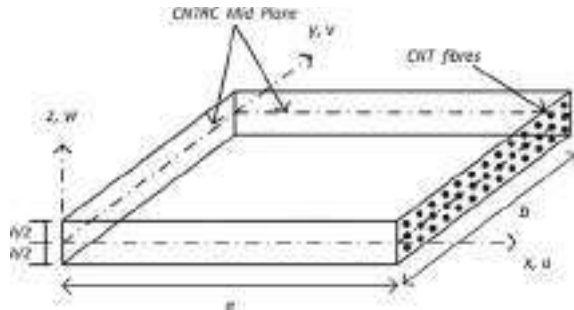
$$V_{CNT}^* = \frac{w_{CNT}}{w_{CNT} + \left(\frac{\rho_{CNT}}{\rho_m}\right) - \left(\frac{\rho_{CNT}}{\rho_m}\right)w_{CNT}} \tag{2}$$

where the CNT mass fraction in the composite plate is given by w_{CNT} . The CNT and matrix density is denoted by ρ_{CNT} and ρ_m . The ρ density and ν_{12} Poisson’s ratio of the nanocomposite plates are computed as

$$\nu_{12} = V_{CNT}\nu_{12}^{CNT} + V_m\nu_m \tag{3}$$

$$\rho = V_{CNT}\rho_{CNT} + V_m\rho_m \tag{4}$$

Fig. 1 Configuration of the uniformly distributed carbon nanotube reinforced composite plates (UD CNTRC)



where Poisson's ratio ν_m and ν_{CNT} of matrix and CNT correspondingly. ERM can be utilized to find the actual material characteristics of plates. By incorporating the CNT efficiency factor, the real material characteristics of the composites will be computed using this approach.

$$E_{11} = \eta_1 V_{CNT} E_{11}^{CNT} + V_m E^m \quad (5)$$

$$\frac{\eta_2}{E_{22}} = \frac{V_{CNT}}{E_{22}^{CNT}} + \frac{V_m}{E^m} \quad (6)$$

$$\frac{\eta_3}{G_{12}} = \frac{V_{CNT}}{G_{12}^{CNT}} + \frac{V_m}{G^m} \quad (7)$$

where E_{11}^{CNT} , E_{22}^{CNT} are the Modulus of Elasticity of along the length and normal directions, respectively, and G_{12}^{CNT} are shear modulus of CNTs. CNT efficiency factor (η_i) was presented to find out scale-dependent material attributes. It may be used to match the effective CNTRC characteristics discovered by the Mori–Tanaka simulation. The matrix, as well as CNT, volume is denoted by V_m and V_{CNT} correspondingly. The addition of these fractions of phases equals unity

$$V_{CNT} + V_m = 1 \quad (8)$$

3 Theoretical Formulations

FOST is used to analyse buckling in the CNTRC plate. A complete analytical solution and formulation are revealed for a simply supported CNTRC plate. The plate geometry is side 'a' is on the x-axis, 'b' is on the y-axis, and the plate thickness is represented by 'h' and matches with the 'z' direction. Figure 1 depicts that the mid-plane is situated at a distance of $+h/2$ from the top and $-h/2$ from CNTRC plate bottom. The mid-plane positive displacement set with the (x-y-z) axes is utilized with the reference cartesian axis system. The CNTRC plate stability is examined using the given below displacement domain.

$$\begin{aligned} u(x, y, z) &= u_0(x, y) + z\theta_x(x, y) \\ v(x, y, z) &= v_0(x, y) + z\theta_y(x, y) \\ w(x, y) &= w_0(x, y) \end{aligned} \quad (9)$$

This strain–displacement connections for small displacements generally may be expressed as follows according to the linear theory of solid mechanics.

$$\begin{Bmatrix} \varepsilon_x \\ \varepsilon_y \\ \varepsilon_z \\ \gamma_{xy} \\ \gamma_{xz} \\ \gamma_{yz} \end{Bmatrix} = \left\{ \frac{\partial u}{\partial x} \frac{\partial v}{\partial y} \frac{\partial w}{\partial z} \frac{\partial u}{\partial y} + \frac{\partial v}{\partial x} \frac{\partial u}{\partial z} + \frac{\partial w}{\partial x} \frac{\partial v}{\partial z} + \frac{\partial w}{\partial y} \right\}^T \quad (10)$$

Strains are obtained according to the displacement field

$$\begin{aligned} \varepsilon_x &= \frac{\partial u_0}{\partial x} + z \frac{\partial \theta_x}{\partial x}, \quad \varepsilon_y = \frac{\partial v_0}{\partial y} + z \frac{\partial \theta_y}{\partial y}, \quad \varepsilon_z = 0 \\ \gamma_{xy} &= \frac{\partial u_0}{\partial y} + \frac{\partial v_0}{\partial x} + z \left(\frac{\partial \theta_x}{\partial y} + \frac{\partial \theta_y}{\partial x} \right), \quad \gamma_{xz} = \theta_x + z \frac{\partial w_0}{\partial x} \\ \gamma_{yz} &= \theta_y + z \frac{\partial w_0}{\partial y} \end{aligned} \quad (11)$$

The material constitutional association is written for composite material as.

$$\begin{Bmatrix} \sigma_x \\ \sigma_y \\ \tau_{xy} \\ \tau_{xz} \\ \tau_{yz} \end{Bmatrix} = \begin{bmatrix} C_{11} & C_{12} & 0 & 0 & 0 \\ C_{12} & C_{22} & 0 & 0 & 0 \\ 0 & 0 & C_{44} & 0 & 0 \\ 0 & 0 & 0 & C_{55} & 0 \\ 0 & 0 & 0 & 0 & C_{66} \end{bmatrix} \begin{Bmatrix} \varepsilon_x \\ \varepsilon_y \\ \gamma_{xy} \\ \gamma_{xz} \\ \gamma_{yz} \end{Bmatrix} \quad (12)$$

$$\text{where } C_{11} = \frac{E_{11}}{1 - \nu_{12}\nu_{21}}, \quad C_{12} = \frac{\nu_{21}E_{11}}{1 - \nu_{12}\nu_{21}}, \quad C_{22} = \frac{E_{22}}{1 - \nu_{12}\nu_{21}},$$

$$C_{44} = G_{12}, \quad C_{55} = G_{13}, \quad C_{66} = G_{23}$$

For stress analysis, the governing differential equilibrium forms have resulted from the “principle of minimum potential energy”. The mathematical equation is expressed as follows:

$$\int (\delta U - \delta W) dV + \int (\sigma' \delta \varepsilon'_x + \sigma' \delta \varepsilon'_y + \tau'_{xy} \delta \gamma'_{xy}) dV = 0 \quad (13)$$

where the strain energy due to deformations is denoted by U , the work performed by outside loads W , the second term in the above equation is potential energy because of given in-plane compressive and shear load (i.e., σ'_x , σ'_y , τ'_{xy}). The midplane strains caused by transverse displacement are ε'_x , ε'_y , γ'_{xy} and the variational symbol is given by δ . The final expression will be after the necessary quantities of energy have been entered into the equation.

$$\left[\int_{-\frac{h}{2}}^{\frac{h}{2}} \int_A (\sigma_x \delta \varepsilon_x + \sigma_y \delta \varepsilon_y + \tau_{xy} \delta \gamma_{xy} + \tau_{yz} \delta \gamma_{yz} + \tau_{xz} \delta \gamma_{xz}) dAdz - \int_A p_z^+ \delta w^+ dA \right] + \int_{-\frac{h}{2}}^{\frac{h}{2}} \int_A (\sigma' \delta \varepsilon'_x + \sigma' \delta \varepsilon'_y + \tau'_{xy} \delta \gamma'_{xy}) dAdz = 0 \quad (14)$$

where the through-thickness displacement of any point is denoted by $w^+ = w_0$ and the transverse load given to the CNTRC plate top is represented by p_z^+ . By applying the above Eqs. (9) to (13) in (14) and integrating the equations by parts, the following relationships of equilibrium are obtained.

$$\begin{aligned} \delta u_0 : \frac{\partial N_x}{\partial x} + \frac{\partial N_{xy}}{\partial y} &= 0, \quad \delta v_0 : \frac{\partial N_y}{\partial y} + \frac{\partial N_{xy}}{\partial x} = 0, \\ \delta w_0 : \frac{\partial Q_x}{\partial x} + \frac{\partial Q_y}{\partial y} + \left(\frac{\partial w_0}{\partial x} \frac{\partial \bar{N}_y}{\partial x} \right) + \left(\frac{\partial w_0}{\partial y} \frac{\partial \bar{N}_x}{\partial y} \right) \\ + \bar{N}_x \frac{\partial^2 w_0}{\partial x^2} + \bar{N}_y \frac{\partial^2 w_0}{\partial y^2} - \left(\frac{\partial^2 \bar{N}_{xy}}{\partial x \partial y} \right) &= 0, \\ \delta \theta_x : \frac{\partial M_x}{\partial x} + \frac{\partial M_{xy}}{\partial y} - Q_x &= 0, \quad \delta \theta_y : \frac{\partial M_y}{\partial y} + \frac{\partial M_{xy}}{\partial x} - Q_y = 0 \end{aligned} \quad (15)$$

where the stress resultants are presented by

$$\begin{bmatrix} M_x \\ M_y \\ M_{xy} \end{bmatrix} = \int_{-\frac{h}{2}}^{+\frac{h}{2}} \begin{Bmatrix} \sigma_x \\ \sigma_y \\ \tau_{xy} \end{Bmatrix} [z] dz, \quad \begin{bmatrix} Q_x \\ Q_y \end{bmatrix} = \int_{-\frac{h}{2}}^{+\frac{h}{2}} \begin{Bmatrix} \tau_{xz} \\ \tau_{yz} \end{Bmatrix} dz, \quad \begin{bmatrix} N_x \\ N_y \\ N_{xy} \end{bmatrix} = \int_{-\frac{h}{2}}^{+\frac{h}{2}} \begin{Bmatrix} \sigma_x \\ \sigma_y \\ \tau_{xy} \end{Bmatrix} dz,$$

and

$$[\bar{N}_x \quad \bar{N}_y \quad \bar{N}_{xy}] = \int_{-\frac{h}{2}}^{+\frac{h}{2}} [\sigma'_x \quad \sigma'_y \quad \tau'_{xy}] dz \quad (16)$$

The resultants are related to the displacement and strain relationship and may be further written in the given equation as displacements

$$\begin{aligned}
N_x &= h \left(Q_{12} \frac{\partial v_0}{\partial y} + Q_{11} \frac{\partial u_0}{\partial x} \right), N_y = h \left(Q_{22} \frac{\partial v_0}{\partial y} + Q_{12} \frac{\partial u_0}{\partial x} \right), \\
N_{xy} &= h Q_{44} \left(\frac{\partial u_0}{\partial y} + \frac{\partial v_0}{\partial x} \right), M_x = \frac{h^3}{12} \left(Q_{12} \frac{\partial \theta_y}{\partial y} + Q_{11} \frac{\partial \theta_x}{\partial x} \right), \\
M_y &= \frac{h^3}{12} \left(Q_{22} \frac{\partial \theta_y}{\partial y} + Q_{12} \frac{\partial \theta_x}{\partial x} \right), M_{xy} = \frac{h^3}{12} Q_{44} \left(\frac{\partial \theta_x}{\partial y} + \frac{\partial \theta_y}{\partial x} \right), \\
Q_x &= h Q_{66} \left(\frac{\partial w_0}{\partial x} + \theta_x \right), Q_y = h Q_{55} \left(\frac{\partial w_0}{\partial y} + \theta_y \right).
\end{aligned} \tag{17}$$

Substituting the above stress resultants in the equilibrium Eq. (15), the new set of governing mathematical forms are deduced as displacements as follows:

$$\begin{aligned}
h Q_{44} \frac{\partial^2 u_0}{\partial y^2} + h Q_{12} \frac{\partial^2 v_0}{\partial x \partial y} + h Q_{44} \frac{\partial^2 v_0}{\partial x \partial y} + h Q_{11} \frac{\partial^2 u_0}{\partial x^2} &= 0 \\
h Q_{22} \frac{\partial^2 v_0}{\partial y^2} + h Q_{12} \frac{\partial^2 u_0}{\partial x \partial y} + h Q_{44} \frac{\partial^2 u_0}{\partial x \partial y} + h Q_{44} \frac{\partial^2 v_0}{\partial x^2} &= 0 \\
h Q_{55} \frac{\partial \theta_y}{\partial y} + h Q_{55} \frac{\partial^2 w_0}{\partial y^2} + h Q_{66} \frac{\partial \theta_x}{\partial x} + h Q_{66} \frac{\partial^2 w_0}{\partial x^2} + q &= 0 \\
\frac{h^3}{12} Q_{44} \frac{\partial^2 \theta_x}{\partial y^2} - h Q_{66} \frac{\partial w_0}{\partial x} + \frac{h^3}{12} Q_{12} \frac{\partial^2 \theta_y}{\partial x \partial y} + \frac{h^3}{12} Q_{44} \frac{\partial^2 \theta_y}{\partial x \partial y} + \frac{h^3}{12} Q_{11} \frac{\partial^2 \theta_x}{\partial x^2} - h Q_{66} \theta_x &= 0 \\
\frac{h^3}{12} Q_{22} \frac{\partial^2 \theta_y}{\partial y^2} - h Q_{55} \frac{\partial w_0}{\partial y} + \frac{h^3}{12} Q_{12} \frac{\partial^2 \theta_x}{\partial x \partial y} + \frac{h^3}{12} Q_{44} \frac{\partial^2 \theta_x}{\partial x \partial y} + \frac{h^3}{12} Q_{44} \frac{\partial^2 \theta_y}{\partial y^2} - h Q_{55} \theta_y &= 0
\end{aligned} \tag{18}$$

The displacement solution is determined by applying Navier's solution. Basic supported boundary limits are applied to all sides.

$$\text{At edges } x = a, \text{ and } x = 0 : v_0 = 0, w_0 = 0, \theta_y = 0, \theta_z = 0, M_x = 0, N_x = 0. \tag{19}$$

$$\text{At edges } y = 0, \text{ and } y = b : u_0 = 0, w_0 = 0, \theta_x = 0, \theta_z = 0, M_y = 0, N_y = 0. \tag{20}$$

The following system may be used to express the result of the displacement quantities supporting the aforementioned boundary situations:

$$\begin{aligned}
u_0 &= \sum_{m=1}^{\infty} \sum_{n=1}^{\infty} u_{0mn} \cos(\alpha x) \sin(\beta y), v_0 = \sum_{m=1}^{\infty} \sum_{n=1}^{\infty} v_{0mn} \sin(\alpha x) \cos(\beta y), \\
w_0 &= \sum_{m=1}^{\infty} \sum_{n=1}^{\infty} w_{0mn} \sin(\alpha x) \sin(\beta y), \theta_x = \sum_{m=1}^{\infty} \sum_{n=1}^{\infty} \theta_{xmn} \cos(\alpha x) \sin(\beta y), \\
\theta_y &= \sum_{m=1}^{\infty} \sum_{n=1}^{\infty} \theta_{ymn} \sin(\alpha x) \cos(\beta y)
\end{aligned} \tag{21}$$

where $\alpha = m\pi/a$, and $\beta = n\pi/b$. Substituting Eqs. (21) in (18), and the components of the coefficient matrix $[X]$ will be generated by obtaining the coefficients for the displacements.

$$([X]_{5 \times 5} - \lambda[G]_{5 \times 5}) \begin{Bmatrix} u_0 \\ v_0 \\ w_0 \\ \theta_x \\ \theta_y \end{Bmatrix}_{5 \times 1} = \{0\} \quad (22)$$

where $\lambda =$ buckling load factor. For given m and n values, the geometric stiffness matrix $[G]$ refers to the stiffness matrix because of in-plane forces. The components of matrices $[G]$ & $[X]$ are provided in Appendix 1. The aforementioned equation may be obtained, and the essential buckling load factor is the lowest eigenvalue and the essential uniaxial load is given by the relation.

$$[\bar{N}_x]_{cr} = \lambda_{cr}[\bar{N}_x] \quad (23)$$

4 Results and Discussions

Validation of the present FOST and ABQUS is studied through the following examples. Poly Vinylene, denoted as PmPV is deemed to be the polymer matrix in this problem. The elastic properties are supposed to be $\nu_m = 0.34$, $E_m = 2.1$ Gpa, and $\rho_m = 1.15$ g/cm³ at 300 K temperature. In this paper, the armchair (10, 10) SWCNTs are considered as reinforcement. The SWCNT characteristics are calculated by the MD simulation process and are presented in Table 1.

ERM is used to forecast actual material attributes of CNTRCs. Carbon nanotube efficiency variables η_j included in Eqs. (5) using (7). We consider for $V_{CNT} = 0.11$, η_1 and η_2 values are 0.149 and 0.934 and for $V_{CNT} = 0.14$, values are 0.150 and 0.941 and for $V_{CNT} = 0.17$, values are 0.149 and 1.381, correspondingly. Additionally, we suppose that $\eta_3 = \eta_2$ and $G_{23} = G_{13} = G_{12}$ are considered in the subsequent numerical examples.

Table 1 Temperature-dependent material properties of (10, 10) SWCNT (L = 9.26 nm, R = 0.68 nm, h = 0.067 nm, $\nu_{12}^{CNT} = 0.175$)

Temperature (K)	E_{11}^{CNT} (TPa)	E_{22}^{CNT} (TPa)	G_{12}^{CNT} (TPa)	α_{11}^{CNT} ($10^{-6}/K$)	α_{12}^{CNT} ($10^{-6}/K$)
300	5.6466	7.0800	1.9645	3.4584	5.1682
500	5.5308	6.9348	1.9643	4.5361	5.0189
700	5.4744	6.8641	1.9644	4.6677	4.8943

Table 2 Buckling load for all edges simply supported square isotropic plates under uniaxial compression

Mode	SSSS isotropic plate ($b/h = 10$)		
	Analytical [26]	Present (ABAQUS)	% Error
1	39.4761	39.1063	0.93
2	61.6814	61.6116	0.11
3	109.656	111.3795	-1.57
4	157.9040	157.3482	0.35

4.1 Example 1: Buckling of an Isotropic Plate Under Compressive Force

To validate the present method of analytical FOST and numerical ABAQUS, comparisons are shown for isotropic plates that are simply supported on both sides and compressed by uniaxial force. Dimensions and elastic of the plate are , $a = b = 0.254$ m, $E = 10.3 \times 10^3$ MPa (3×10^6 psi), $h = 0.0508$ m, and Poisson ratio $\nu = 0.3$. The buckling load is normalized as $\bar{N}_{cr} = (N_{cr}a^2/D_0)$, $D_0 = Eh^3/12(1 - \nu^2)$. The aspect ratio is taken as 10. The critical buckling load at fundamental 4 modes from the ABAQUS gives good agreement with analytical solutions given by Timoshenko and Gere [26] and presented in Table 2 with a maximum % error of 1.57.

4.2 Example 2: Buckling of CNTRC Plate Under (SSSS) Uniaxial Compressive Force

CNTRC plate under uniaxial condition for all sides simply supported is analyzed for $b/h = 20$ and $V_{CNT} = 0.11$. Results are compared with EF Ritz [17], DQM [18], and Exact [18] and present FOST and ABAQUS in Table 3. The first four modes are observed and the buckling load is normalized as $\bar{N}_{cr} = N_{cr}b^2/Eh^3$. Uniaxial and biaxial compression on CNTRC plates is done using a side-to-thickness ratio of 10 and $V_{CNT} = 0.11$ are presented in Table 4. In the table, the literature and the present ABAQUS buckling load values are compared. The following boundary conditions are used: (1) SSSS–Fully supported four sides, (2) CCCC–Fully clamped four sides (fixed), (3) SCSC–Two opposite supported sides and rest two are clamped sides, (4) SFSF–Two opposite supported sides and rest two are free sides, (5) CCCF–Three clamped sides and one side free, (6) SSSF–Three simply supported sides and one free side.

Table 3 Comparison of different methods of the critical buckling load for simply supported plate with single CNTRC layer under uniaxial compression, $V_{CNT} = 0.11$, $b/h = 20$

Methods	Buckling load
Exact [18]	31.5258
DQM [18]	31.5258 [0]
EF-Ritz [17]	30.9076 [1.96]
Present analytical (FOST)	29.4578 [6.55]
Present (ABAQUS)	32.3200 [-2.51]

[]-% error with respect to Exact [18]

Table 4 Buckling load for all edges simply supported and all edge clamped (fixed) square CNTRC plates under uniaxial and biaxial compression with $b/h = 10$, $V_{CNT} = 0.11$. (M = Modes)

M	SSSS uniaxial			CCCC uniaxial		
	Ref. [16]	Present (ABAQUS)	% Error	Ref. [16]	Present (ABAQUS)	% Error
1	14.1073	14.2519	-1.02	25.7329	24.5720	4.51
2	23.3149	22.3948	3.94	26.2788	25.8263	1.72
3	25.6506	24.4761	4.57	29.6661	28.2214	4.86
4	27.0498	26.1428	3.35	29.7356	28.0410	5.69
M	SCSC uniaxial			SFSF uniaxial		
1	17.2424	18.0661	-4.77	12.0697	12.71	-5.30
2	24.0481	23.1510	3.73	13.0216	13.44	-3.21
3	26.3993	24.3514	7.75	20.3912	20.61	-1.07
4	27.4953	26.7247	2.80	22.4198	20.96	6.51
M	CCCF uniaxial			SSSF uniaxial		
1	22.6023	21.3624	5.48	12.3145	12.85	-4.34
2	24.8135	23.7648	4.22	16.6801	16.15	3.17
3	26.4696	25.0480	5.37	22.5393	21.68	3.81
4	26.9602	25.4476	5.61	24.1999	23.26	3.88
M	SCSC biaxial			SFSF biaxial		
1	5.8831	5.5501	5.66	9.2830	9.6385	-3.82
2	6.9772	6.7253	3.61	9.8992	10.3062	-4.11
3	7.8892	7.6581	2.92	13.1796	13.2719	-0.70
4	10.6318	10.189	4.16	13.5820	13.3671	1.58
M	CCCF biaxial			SSSF biaxial		
1	8.1646	8.2351	-0.86	3.4105	3.5380	-3.73
2	9.1246	8.9658	1.74	6.0446	5.7142	5.46
3	9.8991	9.5323	3.70	7.8034	7.6432	2.05
4	11.2443	10.8740	3.29	7.9533	8.0550	-1.27

Table 4 shows that among the six diverse boundary situations, plates that have all four edges clamped (CCCC) exhibit the highest load, while two supported edges and rest two free edges (SFSF) plates exhibit the lower load.

The results show that raising the V_{CNT} causes CNTRC plates to be stiffer, which raises the plates' buckling load parameter. The data demonstrates that when the ratio of width-to-thickness of UD-CNTRC plates rises, so do the non-dimensional buckling load characteristics.

4.3 Example 3: Buckling of Stiffened CNTRC Plates Under Compressive Pressure

The stiffening impact on the buckling behaviour of rectangular CNTRC plates (SSSS) in uniaxial compression is presented in this section. Table 1 displays that the ERM is utilized to find the actual material characteristics of CNTRCs. The geometric characteristics of the CNTRC plate and stiffener are adopted from Christian Mittelstedt [24], where the plate dimensions are $a = 300$ mm and $b = 100$ mm, and the height and thickness of both the plate and stiffener are 13.5 and 1 mm, respectively. The different stiffening systems used for CNTRC plates, include: (a) One-side stiffeners running parallel to the CNTRC plate length. (b) Middle stiffeners running parallel to the length of the CNTRC plate. (c) Two-side stiffeners running parallel to the CNTRC plate length. Table 5 illustrates the buckling load of these different stiffener positions for CNTRC plates (SSSS). The results indicate that the two-side stiffener system produces the highest buckling load, which suggests that the plate becomes stiffer in the following order: side stiffeners to the CNTRC plate length, middle stiffeners to the CNTRC plate length, and two-side stiffeners to the length of CNTRC plate. The buckling loads were also can be seen to rise as the volume percent of CNTs increased. Figure 2 displays the buckling modes of plates featuring different stiffener systems.

Table 5 Buckling load for all edges simply supported rectangle CNTRC plates under uniaxial compression

M	V_{CNT}	Without stiffeners of the CNTRC plate (ABAQUS)	One side stiffeners of the CNTRC plate (ABAQUS) (a)	Middle stiffeners of the CNTRC plate (ABAQUS) (b)	Two side stiffeners of the CNTRC plate (ABAQUS) (c)
1	0.11	12.9266	32.4392	54.3448	85.9762
2		13.0781	32.8169	54.3867	85.8039
3		13.9681	35.0879	56.3190	85.9905
4		14.1024	35.8324	28.1905	94.3638

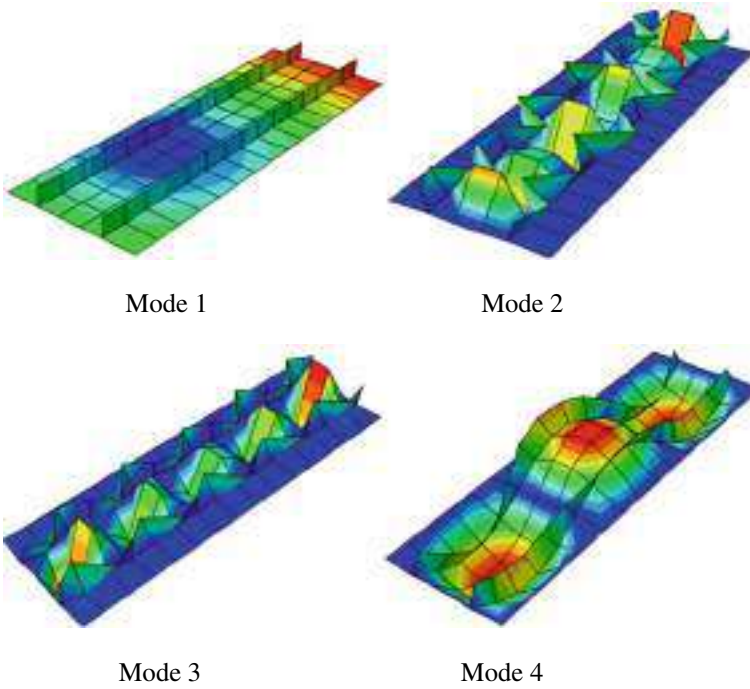


Fig. 2 Buckling modes of stiffened CNTRC plates for $V_{CNT} = 0.14$ and $b/h = 10$ under uniaxial compression

5 Conclusion

This article aims to estimate the buckling performance of isotropic and CNTRC plates using two methods: FOST, the analytical method and the ABAQUS computational tool. When the findings from the current approaches are compared to those from the literature, there is a high level of agreement. The ERM is applied to find the real material characteristics of the SWCNT-reinforced plates. Comprehensive case studies are performed, and CCCC, i.e., fully clamped four edges plate displays the most buckling stress, whereas SFSF, i.e., two supported edges and the rest two free edges plate exhibits the least amount of buckling load among the six alternative boundary conditions. As V_{CNT} rises, the load also increases. The buckling performance of CNTRC plates with stiffeners along the length is also investigated, and it is concluded that the plate with two stiffeners exhibits the maximum buckling load. It is important to note that various CNTRC plate configurations' buckling strength may be significantly affected by altering V_{CNT} , ratio of width-to-thickness, and aspect ratio, and the boundary and loading limits.

Appendix 1

Coefficient of Matrix [X]

$$\begin{aligned}
 X[1, 1] &= Q_{11}h\alpha^2 + Q_{44}h\beta^2, X[1, 2] = Q_{12}h\alpha\beta + Q_{44}h\alpha\beta, X[1, 3] = 0, \\
 X[1, 4] &= 0, X[1, 5] = 0, X[2, 1] = A[1, 1]\alpha^2 + B[1, 1]\beta^2, \\
 X[1, 2] &= A[1, 2]\alpha\beta + A[1, 2]\alpha\beta, X[1, 3] = 0, X[1, 4] = 0, X[1, 5] = 0 \\
 X[2, 1] &= Q_{12}h\alpha\beta + Q_{44}h\alpha\beta, X[2, 2] = Q_{44}h\alpha^2 + Q_{22}h\beta^2, \\
 X[2, 3] &= 0, X[2, 4] = 0, X[2, 5] = 0, X[3, 1] = 0, X[3, 2] = 0, \\
 X[3, 3] &= Q_{66}h\alpha^2 + Q_{55}h\beta^2, X[3, 4] = Q_{66}h\alpha, X[3, 5] = Q_{55}h\beta, X[4, 1] = 0, \\
 X[4, 2] &= 0, X[4, 3] = Q_{66}h\alpha, X[4, 4] = \frac{h^3}{12}(Q_{11}\alpha^2 + Q_{44}\beta^2) + Q_{66}h, \\
 X[4, 5] &= \frac{h^3}{12}(Q_{12}\alpha\beta + Q_{44}\alpha\beta), X[5, 1] = 0, X[5, 2] = 0, X[5, 3] = Q_{55}h\beta, \\
 X[5, 4] &= \frac{h^3}{12}(Q_{12}\alpha\beta + Q_{44}\alpha\beta), X[5, 5] = \frac{h^3}{12}(Q_{44}\alpha^2 + Q_{22}\beta^2) + Q_{55}h.
 \end{aligned}$$

Coefficient of Geometric Matrix [G]

$$G_{3,3} = \alpha^2 \text{ and } G_{i,j} = 0 \text{ for all } i, j = 1, 2, \dots, 5 (i \neq j \neq 3).$$

References

1. Ijima S (1991) Helical microtubes of graphite carbon. *Nature* 354:56–58
2. Harris PJF (2001) Carbon nanotubes and related structures: a new material for the twenty-first century. Cambridge University Press
3. Esawi AMK, Farag MM (2007) Carbon nanotube reinforced composites: potential and current challenges. *Mater Des* 28:2394–2401
4. Lau AKT, Hui D (2002) The revolutionary creation of new advanced materials carbon nanotube composites. *Compos Part B* 33:263–277
5. Thostenson ET, Ren Z, Chou TW (2001) Advances in the science and technology of carbon nanotubes and their composites: a review. *Comp Sci Technol* 61:1899–1912
6. Qian D, Liu WK, Ruoff RS (2001) Mechanics of C60 in nanotubes. *J Phys Chem B* 105:10753–10758
7. Bower C, Rosen R et al (1999) Deformation of carbon nanotubes in nanotube-polymer composites. *Appl Phys Lett* 74:3317–3319
8. Chen XL, Liu YJ (2003) Square representative volume elements for evaluating the effective material properties of carbon nanotube-based composites. *Comput Mater Sci* 28:2394–2401

9. Joshi UA, Joshi P, Harsha SP, Sharma SC (2010) Evaluation of the mechanical properties of carbon nanotube based composites by finite element analysis. *Int J Eng Sci Technol* 2(5):1098–1107
10. Iijima AS, Ichihashi T (1993) Single-shell carbon nanotubes of 1-nm diameter. *Nature (London)* 363:603
11. Fidelus JD, Wiesel E, Gojny FH, Schulte K, Wagner HD (2005) Thermo-mechanical properties of randomly oriented carbon/epoxy nanocomposites. *Compos Part A* 36:1555–1561
12. Han Y, Elliott J (2007) Molecular dynamics simulations of the elastic properties of polymer/carbon nanotube composites. *Comput Mater Sci* 39:315–323
13. Zhu R, Pan E, Roy AK (2007) Molecular dynamics study of the stress–strain behaviour of carbon-nanotube reinforced Epon 862 composites. *Mater Sci Eng A* 447:51–57
14. Wuite J, Adali S (2005) Deflection and stress behaviour of nanocomposite reinforced beams using a multiscale analysis. *Compos Struct* 71:388–396
15. Vodenitcharova T, Zhang LC (2006) Bending and local buckling of a nanocomposite beam reinforced by a single-walled carbon nanotube. *Int J Solids Struct* 43:3006–3024
16. Lei ZX, Liew KM, Yu JL (2003) Buckling analysis of functionally graded carbon nanotube-reinforced composite plates using the element-free kp-Ritz method. *Compos Struct* 98:160–168
17. Malekzadeh P, Shojaee M (2013) Buckling analysis of quadrilateral laminated plates with carbon nanotubes reinforced composite layers. *Thin-Walled Struct* 71:108–118
18. Mehrabadi Jafari S, Sobhani A, Khoshkharesh V, Taherpour A (2013) Mechanical buckling of nanocomposite rectangular plate reinforced by aligned and straight single-walled carbon nanotubes. *Compos Part B* 43:160–168
19. Formica G, Lacarbonara W, Alessi R (2010) Vibrations of carbon nanotube-reinforced composites. *J Sound Vib* 329:1875–1889
20. Arani A, Maghamikia S, Mohammadimehr M, Arefmanesh A (2011) Buckling analysis of laminated composite rectangular plates reinforced by SWCNTs using analytical and finite element methods. *J Mech Sci Technol* 25:809–820
21. Shen HS (2011) Postbuckling of nanotube-reinforced composite cylindrical shells in thermal environment. Part I: axially-loaded shells. *Compos Struct* 93:2096–2108
22. Shen HS (2011) Postbuckling of nanotube-reinforced composite cylindrical shells in thermal environments. Part II: pressure-loaded shells. *Compos Struct* 93:2496–2503
23. Shen HS (2013) Thermal buckling and post-buckling behaviour of functionally graded carbon nanotube-reinforced composite cylindrical shells. *Compos B Eng* 50:239–247
24. Mittelstedt C (2008) Explicit analysis and design equations for buckling loads and minimum stiffener requirements of orthotropic and isotropic plates under compressive load braced by longitudinal stiffeners. *Thin-Walled Struct* 46:1409–1429
25. Kant T, Swaminathan K (2000) Analytical solutions using a higher order refined theory for the stability analysis of laminated composites and sandwich plates. *Struct Eng Mech* 10:337–357
26. Timoshenko S, Gere J (1961) *Theory of elastic stability*, 2nd edn. McGraw-Hill, New York
27. Kurkute JV, Shiyekar SM (2018) Buckling of a composite laminated plate subjected to the thermal environment using higher order shear and normal deformation theory. *Int J Adv Res Eng Technol (IJARET)* 9(5):220–228
28. Mayandi K, Jeyaraj P (2015) Bending, buckling and free vibration characteristics of FG-CNT-reinforced polymer composite beam under non-uniform thermal load. *Proc Inst Mech Eng Part L J Mater Design Appl* 229(1):1–9
29. Shiyekar SM, Lavate P (2015) Flexure of power law governed functionally graded plates using ABAQUS UMAT. *Aerosp Sci Technol* 46:51–59
30. Mindlin RD (1951) Influence of rotary inertia and shear on flexural motions of isotropic elastic plates. *J Appl Mech* 18:31–38
31. ABAQUS User's Manual (2003) ABAQUS Version.6.10

Chapter 4

Experimental Investigation of Machining Parameters of Monel 400 in Powder Mixed EDM Process



Abhishek Kumar and T. Jagadeesha

Abstract Electric Discharge Machining (EDM) is basically a die-sinking process. First, material is removed where the current density is high, and a replica of the tool is reproduced on the work. The productivity of EDM can be increased by increasing the spark frequency. This is done by introducing conductive metal powder. Process performance of EDM depends both on the tool as well as the work material. In this current research work, the effect of graphite powder of size 30–40 μ is used with a combination of Monel 400 as a workpiece material and copper as a cathode. Monel 400 is a nickel-based superalloy material and is widely used in the chemical processing industry, automotive, marine industry, oil and gas extraction, pollution control, and waste processing industry, and high-temperature applications. Processes parameters chosen for the experiments include powder concentration, peak current and pulse-on time. The effect of these parameters on Tool Wear Rate (TWR) and Material Removal Rate (MRR) is investigated. The Taguchi orthogonal array was used as the basis for the studies. Peak current and tool material were shown to have a significantly higher impact on MRR and TWR using ANOVA. A hybrid method of dimensional and regression analysis was used using MINITAB to build semi-empirical models for material removal rate based on machining parameters and significant thermo-physical characteristics.

Keywords Powder mixed Electrical discharge machining · Monel 400 · Dimensional analysis · Regression analysis

A. Kumar · T. Jagadeesha (✉)

Department of Mechanical Engineering, National Institute of Technology, Calicut,
Kerala 673 601, India

e-mail: jagdishg@nitc.ac.in

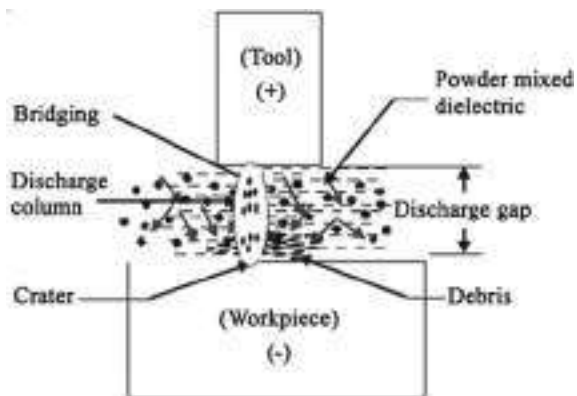
1 Introduction

Powder-mixed Electrical Discharge Machining (EDM) is a modern machining technique that involves the use of a conductive powder mixed with a dielectric fluid to enhance the machining performance and surface quality. The use of powder in EDM can improve machining efficiency, reduce tool wear, and enhance the surface finish of the machined parts. Figure 1 shows the typical schematic diagram of the powder-mixed EDM process.

Superalloys are a class of high-performance alloys that exhibit excellent mechanical strength, corrosion resistance, and high-temperature stability. Monel 400 is a popular nickel-copper superalloy. In recent years, the application of Monel 400 in powder-mixed EDM has gained significant attention due to its superior mechanical and chemical properties. The addition of Monel 400 powder in EDM can enhance the machining performance by reducing the Tool Wear Rate (TWR), improving the surface finish, and reducing the machining time. Moreover, using Monel 400 powder can also improve the electrical and thermal conductivity of the dielectric fluid, which can further enhance the machining performance. Buckingham Pi theorem was used to develop a model for the Material Removal Rate (MRR) with the help of multiple linear regression equations.

Investigation of electrical discharge machining with powder is of special significance. Understanding the Powder Mixed EDM (PMEDM) idea thoroughly and studying the process parameters in greater detail, especially to get improved performance and the powder used in PMEDM, plays a vital role in enhancing MRR and decreasing TWR compared to the traditional EDM process [1]. Examination of Nickel-Based Superalloy Powder Mixed EDM utilizing powdered cobalt, zinc, and molybdenum Better MRR was created by cobalt and zinc, and reduced tool wear rate was obtained by molybdenum powder [2]. The potential of graphite powder is realized in increasing the machining rate in AEDM of nickel-based Super Alloy 718. The overall machining rate increases by 26.85 if fine graphite powder contributes 2.4% to the process [3].

Fig. 1 Schematic diagram of the PMEDM process



Semi-empirical models have been created for the responses, using a hybrid method, for the PMEDM process of aluminum/alumina composites with metal matrix, and the PCA technique has been used to determine the weights for responses while GRA has been used to combine the multiple objectives into single [4]. The frequency of sparking and energy per spark are important parameters that affect the MRR [5]. Arching in powder EDM gives a rough surface and has to be avoided under all circumstances. It is found that silicon powder gives more arching during PMEDM and thus, surface roughness is greatly affected [6]. EDM performance has been identified as particle size, particle concentration, particle density, electrical resistivity, and thermal conductivity [7, 8].

2 Materials and Experimental Conditions

In this experiment, the graphite powder of size 30–40 μm is used with cathode as a copper rod of diameter 11 mm and height 50 mm, with 99% purity. Work material is nickel-based superalloy, Monel 400 rod of diameter 10 mm and height 30 mm. Physical properties of Monel 400 are given in Table 1. The various process parameters such as sparking voltage, pulse on–off time, and current are given in Table 2. A complete experimental setup to carry out powder based EDM is shown in Figs. 2 and 3.

Table 1 Physical properties of Monel

Parameter	Value
Density (kg/m^3)	8800
Melting temp. ($^{\circ}\text{C}$)	1325
Thermal conductivity (W/mk)	21.8
Specific heat capacity (J/kgK)	427
Tensile strength (MPa)	550

Table 2 Process parameters for the experiment

Conditions	Value
Sparking voltage (V)	40
Peak current (I)	12, 15, 28
Pulse on time (μs)	20, 40, 75
Pulse off time (μs)	10
Powder concentration (g/l)	0, 2.5, 5
Tool polarity	Negative
Dielectric used	DI water
Tool materials	Copper
Work materials	Monel 400

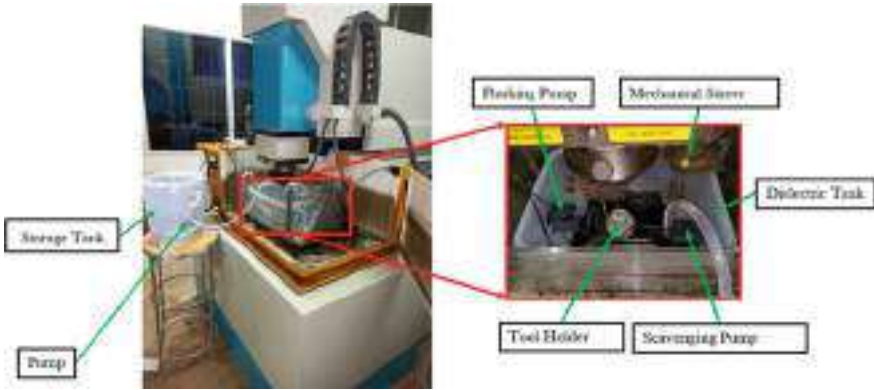
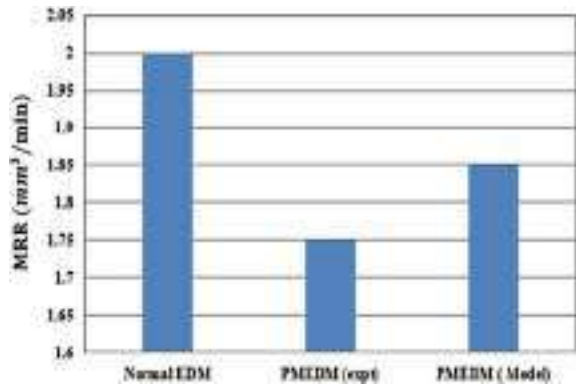


Fig. 2 Experimental setup of PMEDM

Fig. 3 Comparison of Avg. MRR



The precise weighing scale is used to calculate the weight of the tool/work before and after machining, and weight loss is calculated based on the loss of tool/work material. TWR or MRR is calculated using the theoretical formula

$$MRR \text{ or } TWR = \frac{(W_b - W_a) \times 1000}{\rho t} \text{mm}^3/\text{min}$$

where

- W_b = weight of the anode or cathode prior to machining (g);
- W_a = weight of the anode or cathode after post-machining (g);
- t = machining time for each trial (s);
- ρ = density of material (g/cm³).

3 Mathematical Modeling of MRR Using Dimensional Analysis

The mathematical relationship between MRR and process parameters is expressed using the principle of dimensional analysis and the Buckingham π theorem. The various process factors, their units, and dimensions are given in Table 3. Multiple linear regression analysis is used to calculate the MRR.

Mathematically, Buckingham ν theorem is expressed as

$$MRR(Q) = f(S, \rho, I_p, V_g, T_{on}, K, P_c, C)$$

$$n = 9, m = 5, n - m, = 4$$

n = number of variables, m = no.of fundamental dimensions,

$$n - m = \text{no.of } \pi \text{ terms}$$

Each ν term is expressed as a function given by Eq. (1).

$$f(\nu_1, \nu_2, \nu_3, \nu_4) = 0 \tag{1}$$

$$\pi_1 = S^{a1} \rho^{b1} I_p^{c1} K^{d1} V_g^{e1} Q$$

$$\pi_2 = S^{a2} \rho^{b2} I_p^{c2} K^{d2} V_g^{e2} T_{on}$$

$$\pi_3 = S^{a3} \rho^{b3} I_p^{c3} K^{d3} V_g^{e3} P_c$$

$$\pi_4 = S^{a4} \rho^{b4} I_p^{c4} K^{d4} V_g^{e4} C$$

Table 3 Response and variables dimension

Factor	Unit	Dimension
MRR (Q)	mm ³ /min	L ³ T ⁻¹
Powder size (S)	μm	L
Density (ρ)	g/cm ³	ML ⁻³
Peak current (I _p)	A	I
Gap voltage (V _g)	V	ML ² T ⁻³ I ⁻¹
Pulse on time (T _{on})	μs	T
Thermal conductivity (K)	W/mK	MLT ⁻³ θ ⁻¹
Powder concentration (P _c)	g/l	ML ⁻³
Specific heat (C)	J/KgK	L ² T ⁻² θ ⁻¹

By solving the above set of equations, π_1 , π_2 , π_3 and v_4 are expressed as

$$v_1 = \left(\frac{\rho}{I_p V_g} \right)^{0.33} \frac{Q}{S^{1.33}}$$

$$v_2 = \left(\frac{I_p V_g}{\rho} \right)^{0.33} \left(\frac{T_{on}}{S^{1.66}} \right)$$

$$v_3 = \left(\frac{P_c}{\rho} \right)$$

$$v_4 = \frac{(SI_p V_g \rho^2)^{0.33} C}{K}$$

By expressing v_1 in terms π_2 , π_3 and v_4 , Eq. 2 is obtained.

$$v_1 = f(v_2, v_3, v_4) \quad (2)$$

Using the principle of Buckingham ν theorem, v_1 in exponential form is

$$v_1 = M(v_2^{\beta_1})(v_3^{\beta_2})(v_4^{\beta_3})$$

The final form of the equation is given in Eq. 3.

$$\left(\frac{\rho}{I_p V_g} \right)^{0.33} \left(\frac{Q}{S^{1.33}} \right) = M \left[\left(\frac{I_p V_g}{\rho} \right)^{0.33} \left(\frac{T_{on}}{S^{1.66}} \right) \right]^{\beta_1} \left(\frac{P_c}{\rho} \right)^{\beta_2} \left(\frac{(SI_p V_g \rho^2)^{0.33} C}{K} \right)^{\beta_3} \quad (3)$$

Taking logarithms on both sides of Eq. 3

$$\log \pi_1 = \log M + \beta_1 \log(\pi_2) + \beta_2 \log(\pi_3) + \beta_3 \log(\pi_4)$$

Multiple linear regression equation thus becomes where

$$Y = \beta_0 + \beta_1 X_1 + \beta_2 X_2 + \beta_3 X_3 \quad (4)$$

Y = response variable

β = regression coefficient

X = set of 'n' dependent variables.

Regression coefficient obtained after solving Eq. 4 is given as

$$\beta_0 = \log M = -31 \quad \beta_1 = 1.9$$

$$\beta_2 = 1.4 \quad \beta_3 = 10.12$$

Inserting all the regression coefficients, the MRR equation is obtained as

$$\text{MRR}(Q) = \left(\frac{S^{1.33}}{\left(\frac{\rho}{I_p V_g}\right)^{0.33}} \right) M \left[\left(\frac{I_p V_g}{\rho} \right)^{0.33} \left(\frac{T_{on}}{S^{1.66}} \right) \right]^{1.9} \left(\frac{P_c}{\rho} \right)^{1.4} \left(\frac{(S I_p V_g \rho^2)^{0.33} c}{K} \right)^{10.12} \quad (5)$$

Rearranging the terms in Eq. (5)

$$\text{MRR}(Q) = \frac{(S)^{1.8} (P_c)^{1.4} (\rho)^{4.5} (I_p V_g)^{4.3} (T_{on})^{1.9} (C)^{10.12}}{(K)^{10.12} \times (10)^{36}}$$

4 Results and Discussion

Twenty seven experiments with three factors and three variables are conducted experimentally. MRR of the workpiece material and tool wear of the cathode is calculated by the weight difference. The results are compared with the mathematical model developed. The experimental and mathematical modeling results are given in Table 4.

Material removal rate in normal EDM and power mixed EDM are calculated experimentally and compared with a mathematical model developed through dimensional analysis. Figure 3 shows the average values of MRR for each configuration. Tool wear rates in normal EDM and powder mixed EDM are evaluated experimentally, and the results are shown in Fig. 4.

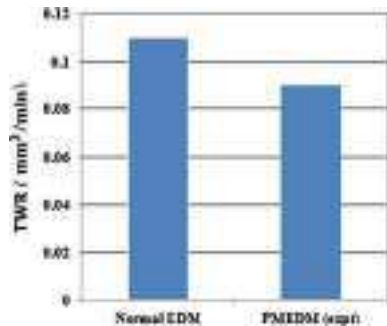
5 Conclusion

In this research work, various experiments are carried out to find out the Material Removal Rate (MRR) and tool wear rate with graphite powder in Electrical Discharge Machining (EDM) process. The detailed mathematical model has been developed using dimensional analysis principles. It is observed that MRR in normal EDM is slightly higher than Powder mixed EDM (PMEDM) with graphite powder in the concentration range of 2.5 to 5 g/l. This lower MRR is due to the concentration range. MRR is also evaluated using a mathematical model developed using Buckingham ν theorem, and it is found that mathematical model results are close to experimental value. The deviation between mathematical modeling and experimental method is approx. 6.18%. Therefore, it can be concluded that a developed mathematical model can be used to predict the MRR in PMEDM effectively with an acceptable error ranging between 6 and 10%. PMEDM graphite powder is found to give less tool

Table 4 Experimental and Predicted value of MRR and TWR

Sl no	T _{on}	I _p	P _c	MRR (Expt)	MRR (Model) PMEDM	TWR
1	20	12	0	1.138	0	0.132
2	40	12	0	2.069	0	0.066
3	75	12	0	2.425	0	0.276
4	20	15	0	1.217	0	0.125
5	40	15	0	2.191	0	0.161
6	75	15	0	2.591	0	0.020
7	20	18	0	0.898	0	0.032
8	40	18	0	2.225	0	0.116
9	75	18	0	3.419	0	0.118
10	20	12	2.5	1.633	0.058	0.097
11	40	12	2.5	1.643	0.218	0.062
12	75	12	2.5	1.694	0.72	0.053
13	20	15	2.5	0.621	0.152	0.102
14	40	15	2.5	1.802	0.569	0.055
15	75	15	2.5	2.036	1.881	0.036
16	20	18	2.5	1.465	0.334	0.095
17	40	18	2.5	2.047	1.247	0.079
18	75	18	2.5	2.584	4.119	0.034
19	20	12	5	0.353	0.154	0.146
20	40	12	5	0.910	0.576	0.115
21	75	12	5	1.334	1.901	0.107
22	20	15	5	0.482	0.402	0.137
23	40	15	5	1.532	1.503	0.119
24	75	15	5	3.403	4.964	0.131
25	20	18	5	2.418	0.882	0.14
26	40	18	5	2.915	3.293	0.105
27	75	18	5	3.005	10.872	0.045

Fig. 4 Comparison of Avg. TWR



wear rate compared to normal EDM, and therefore, PMEDM is very effective in increasing the productivity by increasing the tool life. Reduction of tool wear up to 21.85% is obtained in experimental PMEDM.

References

1. Ayanesh Joshi Y, Anand Joshi Y (2019) A systematic review on powder mixed electrical discharge machining. *Heliyon* 5(12):1–12
2. Ramesh S, Jenarathanan MP (2021) Investigation of powder mixed EDM of nickel-based superalloy using cobalt, zinc and molybdenum powders. *Int J Adv Manuf Technol* 74:923–936
3. Kumar A, Maheshwari S, Sharma C, Beri N (2010) Realizing potential of graphite powder in enhancing machining rate in AEDM of nickel based super alloy 718. *Proc Int Conf Adv Mech Eng* 1:1–4
4. Talla G, Gangopadhyay S, Sahoo DK, Biswas CK (2015) Modeling and multi-objective optimization of powder mixed electric discharge machining process of aluminum/alumina metal matrix composite. *Eng Sci Technol Int J* 18:369–373
5. Bhattacharya A, Batish A, Singh G (2012) Optimal parameter settings for rough and finish machining of die steels in powder-mixed EDM. *Int J adv Manuf Technol* 61:537–548
6. Pecas P, Henriques E (2003) Influence of silicon powder-mixed dielectric on conventional electrical discharge machining. *Int J Mach Tools Manuf* 43:1465–1471
7. Tzeng Y-F, Lee C-Y (2001) Effects of powder characteristics on electrodischarge machining efficiency. *Int J Adv Manuf Technol* 17:586–592
8. Chakraborty S, Dey V, Ghosh SK (2015) A review on the use of dielectric fluids and their effects in electrical discharge machining characteristics. *Precis Eng* 40:1–6

Chapter 5

Synthesis of Estolides from Coconut, Sunflower and Karanja Oils



P. V. Maneesh Kumar and T. Jagadeesha

Abstract Lubricating machines with mineral-based lubricants have become a major cause of pollution now. To use natural oils for making lubricants instead of petroleum is something mainstream researchers have been looking at for a few decades. Though vegetable oils show excellent biodegradability, their cold flow properties are poor compared to functional lubricants. Biodegradable lubricant oils must have excellent cold flow properties as well as competitive costs in order to be accepted widely as usable base stock to industrially usable lubricants. Cold flow characteristics of natural oils are generally subpar to industrial lubricants. This is one major drawback that limits the usage of otherwise abundant vegetable oil. Though vegetable oils show excellent biodegradability, their cold flow properties are poor compared to functional lubricants. In this present study, three vegetable oils have been synthesized to obtain their estolides, they are coconut, sunflower and karanja oils, to analyze the variations. SPARTAN molecular dynamics software is utilized in parallel to understand the molecular structure of products.

Keywords Estolides · SPARTAN · Saturated fatty acids · Pour point

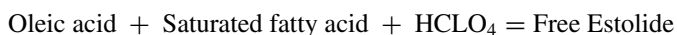
1 Introduction

Lubrication is one essential aspect of our industrial civilization. It has been practiced for thousands of years. Majority of lubricants consumed today are derived from mineral oils and it has become one major environmental concern. Estolides belong to the family of esters synthesis from natural oils as the carboxylic acid functional group of the fatty acid forms an ester linkage with the unsaturated site of another fatty acid [1]. Estolide number represents the mean number of additional fatty acids attached to base fatty acids. This value changes with respect to temperature, type of

P. V. Maneesh Kumar (✉) · T. Jagadeesha
Department of Mechanical Engineering, National Institute of Technology, Calicut,
Kerala 673 601, India
e-mail: maneesh_p210081me@nitc.ac.in

saturated fatty acid being supplied and other various parameters. Lubricants of today are 90% base stock with 10% additives [2]. Continuous use of these mineral-based lubricants leads to environmental issues as well as health problems for its operators. Thus, alternative lubricants synthesized from vegetable oils are Generally Regarded as Safe products. Vegetable oils are an eco-friendly alternative for the base stock of industrial lubricants as they are more biodegradable and less toxic. Vegetable oils have many positive properties of lubricants, such as high viscosity index, improved contact lubrication, good flash points and very low volatility. Vegetable oils show a wide range of viscosities, whereas mineral oils have an average viscosity range of 441 mPa.S at 60 °C [3]. However, vegetable oils possess some weaknesses. One major weakness of vegetable oils is their subpar cold-flow properties. At lower temperatures, vegetable oils lose their fluidity due to clouding, thus, bad cold-flow properties of natural oils are one important challenge for using them as lubricants or as base stock of lubricants.

Estolides are esters derived by modifying fatty acids. They have found application in many cosmetics, bio-lubricants, and coatings. Estolide synthesis occurs when the fatty acids stack on the unsaturated sites of other fatty acids. Estolide number is the mean number of additional fatty acids branched on the base. These ester linkages are strong against hydrolysis, giving them improved properties against pure natural oils [4]. Estolides are naturally occurring and are also manufactured in labs [5]. We have synthesized oleic estolides further reacted to 2-ethylhexanol.



SPARTAN is a molecular dynamics software working on quantum chemical calculations to formulate the structure of molecules. The structure alone will be providing valuable insights into the properties and the variations caused by the molecular structure. The objective of the present study is to synthesize estolides from these three natural oils and to compare their properties over their base oil to analyze the improvements along with molecular dynamics analysis.

2 Experimental Procedure

2.1 Materials

Coconut, Sunflower, Karanja and Castor oils were procured locally as they are readily available for cooking purposes. Oleic acid, Perchloric acid, 2-ethyl hexanol, KOH, Ethanol and Silica gel was obtained from SIGMA ALDRICH Chemical Company, supplied by Alpha Chemicals, Ernakulam.

2.2 Preparation of Estolides

Estolides were synthesized from Coconut, Sunflower and Karanja oils through condensation reactions catalyzed with acids. The reactions took place in a 750 ml 3-necked flask. The reaction was conducted at standard atmospheric conditions. The reactant mixture for estolide contains 90 g base oil, 10 g of castor oil and 20.3 g of oleic acid. The mixture was heated in a Rota mantle to a temperature of 60 ± 0.1 °C. A magnetic stirrer was used for mixing. Once the temperature reached 60 °C 3 g of Perchloric acid (HClO_4) was incorporated drop by drop. Then the reactants were heated for 24 h. After 24 h, 56.5 g of 2-ethyl hexyl alcohol was added to the reactant flask and the reactants were further heated for 2 h. For quenching, 2 g potassium hydroxide (KOH) mixed through ultrasonic stirring for 180 s in a 90% ethanol–water mixture was added. The synthesis of estolide ester in Rota Mantle is shown in Fig. 1. Water washing in the separating funnel is shown in Fig. 2.

The completed reactions were cooled for 30 min. The reactant mixture was moved to a separating funnel, and 100 g hexane was added for extracting the organic layer. The estolide synthesized was then further water-washed with warm water at 60 °C till the pH of washed water obtained equals the pH of normal water. For further water removal, the estolides were kept in an open beaker surrounded by silica gel in a closed vessel for 24 h. Commercially available coconut, sunflower and karanja oils were used for experiments. Estolide ester placed between silica gel for water absorption is shown in Fig. 3. Coconut, sunflower and karanja oils and estolide are shown in Figs. 4 and 5.

Fig. 1 Synthesis of estolide ester in Rota Mantle



Fig. 2 Water washing in separating funnel



Fig. 3 Estolide ester placed between silica gel for water absorption





Fig. 4 Coconut, sunflower and Karanja oils



Fig. 5 Coconut, sunflower and Karanja estolides

2.3 Pour-Point Analysis

Pour point of the oils and synthesized estolides were evaluated in a pour-point testing apparatus with iso-propyl alcohol coolant as per ASTM D 97 standards. The oils were placed in apparatus in a test tube with a thermometer stoppered on it at room temperature and were kept for cooling. At every 3 °C reduction in temperature, the test tube was taken out to check fluidity by tilting. Cloud point, which is the temperature at which clouds start to form, is analyzed visually and is noted. Pour points are also evaluated visually and are noted.

2.4 Quantum Chemical Analysis

SPARTAN is a molecular dynamics software that works on the basis of quantum chemical applications that can give the appropriate molecular structures of complex chemicals. The estolide esters synthesized were given to SPARTAN for understanding their chemical structure and to estimate their electrostatic potential.

3 Results and Discussion

3.1 Quantum Chemical Analysis

Initially, base fatty acids were imagined to analyze and predict the tribological properties. Since estolide formation is prone to fatty acids with double bonds in them, saturated fatty acids were analyzed along with their estolides to compare. We can observe estolides as branched structures with loosely distributed Electrostatic potentials. This variation with the regular base oil configuration will surely cause variations in the properties as crystallization is attained by the uniform stacking of molecules over one another and the variation in the structures, especially from linear-easily stackable structures to branched—not so easily stackable structures will show the variations.

From the structure of these molecules (Figs. 6, 7, 8, 9 and 10), it is evident that the added molecular mass will improve the viscosity of the liquid. The complex structure of the molecules will make the crystallization a slow process delaying the pour points.

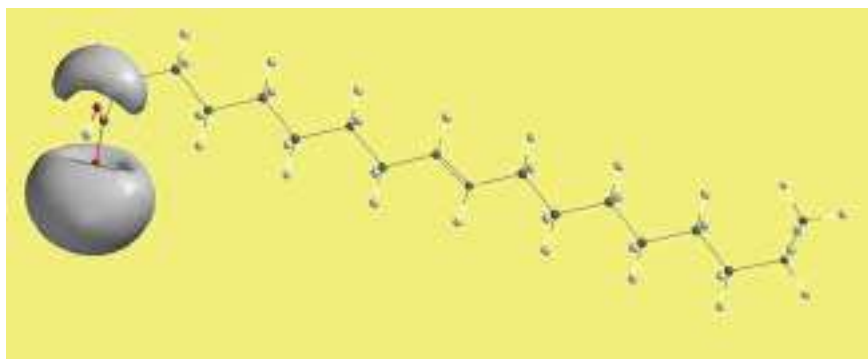


Fig. 6 Molecular structure of oleic acid shown with electrostatic potential (grey cloud)

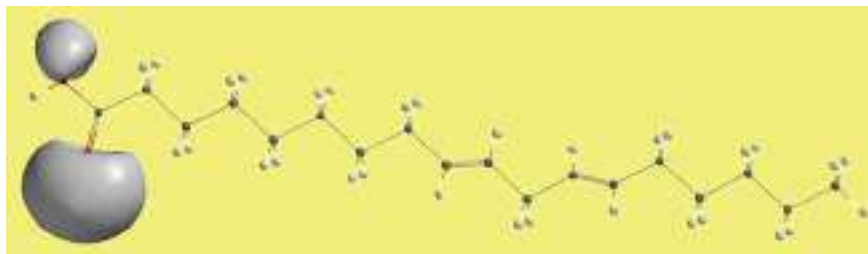


Fig. 7 Molecular structure of linoleic acid shown with electrostatic potential

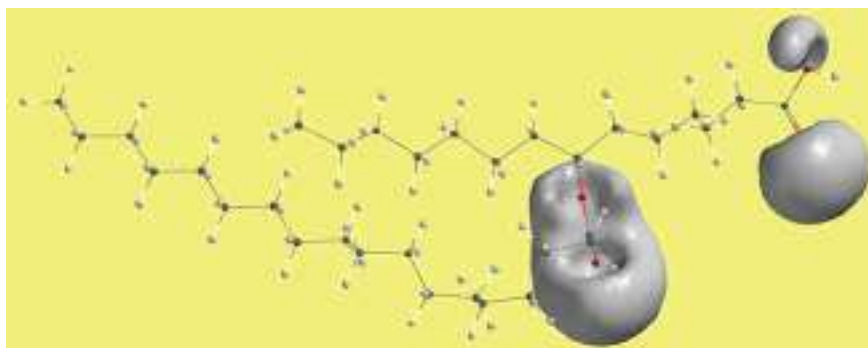


Fig. 8 Estolide of 2 oleic acid molecules ($N = 1$)

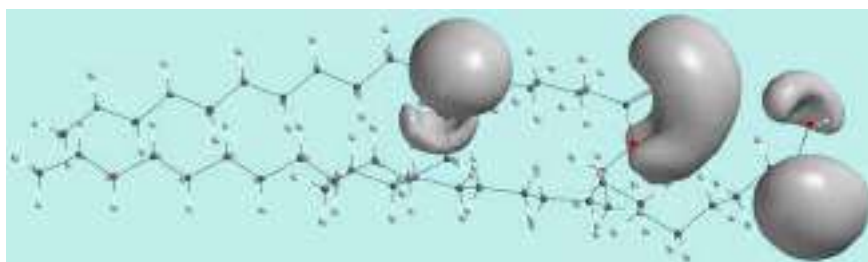


Fig. 9 Estolide of 2 oleic acid with a linoleic acid ($N = 2$)

3.2 *Pour-Point Analysis*

Pour point is one major aspect of lubricants and is one area where natural oils show poor properties. Cloud points of base oils and estolides were evaluated using ASTM D 97 standards. Variation in cold flow properties of base oils and estolides SAE20W40 is shown in Table 1.

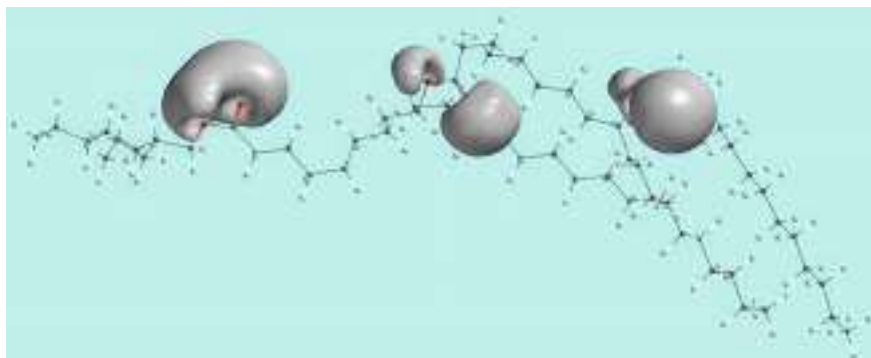


Fig. 10 Estolide ester of 2 oleic acid with a linoleic acid molecule

Table 1 Variation in cold flow properties of base oils and estolides SAE20W40

Sl no	Sample	Cloud point °C	Pour point °C	ΔT
1	Coconut oil	25	22	-24
2	Coconut estolide	0	-2	
3	Sunflower oil	-16	-18	-3
4	Sunflower estolide	-18	-21	
5	Karanja oil	6	9	-21
6	Karanja estolide	-6	-12	
7	SAE20W40	-18	-21	

The samples were kept in a test tube with a $-50\text{ }^{\circ}\text{C}$ thermometer. The test tube was placed in a cooling apparatus with isopropyl alcohol for cooling. The temperature at the beginning of the experiment was at room temperature and the reduction in temperature was noted at every $3\text{ }^{\circ}\text{C}$ to check if clouding had occurred. Once clouding begins clotting of oils is to follow, which shows the pour point of the sample.

4 Conclusion

Vegetables stack on each other as temperature reduces on the path to crystallization, as branches form on these structures, stacking is delayed leading to a reduced pour point [6]. Pour points, which are the major demerits of vegetable oils, can be improved by attaching other fatty acid chains of similar or other oil molecules with appropriate chemical processes. This hinders the close packing of these molecules while solidification occurs. Their cold-flow properties show significant improvements. Unsaturation/Double bond sites present in mono- and polyunsaturated fatty acids can be

suitable locations for attaching branches. The reduction of internal symmetry associated with branching also slows down the stacking, reducing the pour-point further in the temperature scale [7]. Further addition of 2-ethylhexanol for capping increases the molecular weight and forms an additional branch [8]. As estolides are obtained from vegetable oils, it is normal to expect them to have poor cold-flow properties, but the results are showing very good improvement in this area to a point that is even comparable with commercial lubricants. We can source raw materials required for most of our applications from the plants itself [9]. Recent developments in this area are reassuring the benefits of plant-based industrial fluids [10]. Polyols obtained from natural oils are another well-behaved bio-based lubricant capable of huge improvements [11]. Another positive information is that the characteristics can be further improved by varying the molecular weight of components [12]. The capability of estolide esters to become biofuel is another strength of this bio-based molecule [13]. The biofuel thus created is also showing very good cold flow characteristics [14], and there are many novel methods for further advancing the cold flow capabilities of these liquids [15]. Industrial fluids are being replaced by natural oil based fluids and are visible in many industries [16]. Additionally, nanomaterials can be used for improving these fluids, and this area is to be further investigated.

References

1. Cermak SC, Bredsguard JW, Dunn RO, Thompson T, Feken KA, Roth KL, Kenar JA, Isbell TA, Murray RE (2014) Comparative Assay of Antioxidant Packages for Dimer of Estolide Esters. *J Am Oil Chem Soc*
2. Ho CK, McAuley KB, Peppley BA (2019) Biolubricants through renewable hydrocarbons: a perspective for new opportunities. *Renew Sustain Energy Rev*
3. Bin X, Ding R, Yang Z, Sun Y, Zhang J, Kaiji L, Cao D, Gao A (2023) Investigation on performance of mineral-oil-based rejuvenating agent for aged high viscosity modified asphalt of porous asphalt pavement. *J Clean Prod* 395:136285
4. Garcia-Zapateiro LA, Franco JM, Valencia C, Delgado MA, Gallegos C (2013) Viscous, thermal and tribological characterization of oleic and ricinoleic acids-derived estolides and their blends with vegetable oils. *J Indus Eng Chem*
5. Cermak SC (2001) Synthesis of estolides from oleic and saturated fatty acids. *J Am Oil Chem Soc* 06
6. Ajithkumar G (2009) Analysis of the pour point of coconut oil as a lubricant base stock using differential scanning calorimetry. *Lubric Sci* 01
7. Greco-Duarte J, Collaço ACA, Costa AMM, Silva LO, Da Silva JAC, Torres AG, Fernandez-Lafuente R, Freire DMG (2019) Understanding the degree of estolide enzymatic polymerization and the effects on its lubricant properties. *Fuel*
8. Isbell TA, Edgcomb MR, Lowery BA (2001) Physical properties of estolides and their ester derivatives. *Indus Crops Prod*
9. Ray AK, Stark RE (1998) Isolation and molecular structure of an oligomer produced enzymatically from the cuticle of lime fruit. *Phytochemistry* 48(8):1313–1320
10. Perera M, Yan J, Xu L, Yang M, Yan Y (2022) Bioprocess development for biolubricant production using non-edible oils, agro-industrial byproducts and wastes. *J Clean Prod* 357:131956

11. Åkermana CO, Gaber Y, Abd Ghani N, Lämsä M, Hatti-Kaul R (2011) Clean synthesis of biolubricants for low temperature applications using heterogeneous catalysts. *J Mol Catal B Enzym* 72:263–269
12. Bantchev GB, Cermak SC (2022) Correlating viscosity of 2-ethylhexyl oleic estolide esters to their molecular weight. *Fuel* 309:122190
13. de Haro JC, del Prado Garrido M, Perez A, Carmona M, Rodríguez JF (2018) Full conversion of oleic acid to estolides esters, biodiesel and choline carboxylates in three easy steps. *J Clean Prod* 184:579–585
14. Smith PC, Ngothai Y, Nguyen QD, O'Neill BK (2010) Improving the low-temperature properties of biodiesel: methods and consequences. *Renew Energy* 35:1145–1151
15. Sierra-Cantora JF, Guerrero-Fajardo CA (2017) Methods for improving the cold flow properties of biodiesel with high saturated fatty acids content: a review. *Renew Sustain Energy Rev* 72:774–790
16. Zhang C, Garrison TF, Madbouly SA, Kessler MR (2017) Recent advances in vegetable oil-based polymers and their composites. *Prog Polym Sci* 71:91–143

Chapter 6

Innovative Methods for Increasing the Tool Life of Cutting Tools in Complex Surface Treatment



J. O. Sharipov

Abstract In this article, a high-speed cutting tool with complex surface treatment: ion nitriding, ion alloying and coating was used to cut difficult-to-cut chromium-nickel material. The effectiveness of chemical-thermal treatment before coating and its effect on the physicochemical properties has been studied. In the article, for the first time, the process of ion nitriding was carried out to harden the base casting, which contributes to surface hardening at a thickness of 80 microns. After the ion doping process, the surface is coated with (TiAl)N. The processed cutting tools were tested at the machine-building plant of the metallurgical plant. Complex processing of the cutting tool was carried out on a Fus-32 horizontal milling machine in the machine-building shop of the metallurgical plant. This article uses innovative methods of ion nitriding, ion alloying and coating in the complex processing of cutting tools. The main task of the research is to reduce the plastic deformation of the coating on the surface of the cutting tools working under high load.

Keywords High-speed tool · Nitriding · Alloying · Covering · Wear resistance · Hard alloy

1 Introduction

In spite of the year-after-year increasing application of tools made of hard alloys, cutting ceramics and extra-hard materials, the number of high-speed steels used in the manufacture of metal-working tools does not decrease at all. In our study of heat treatment and coating, we are dealing with work hardening caused by the passage of an elastic wave generated by a precisely pulsed electron beam. However, due to the short duration of the process and thermal inertia, the heating caused by compression and internal friction, most likely, should not be a physical factor that determines the

J. O. Sharipov (✉)
Bukhara Engineering-Technological Institute, Bukhara, Uzbekistan
e-mail: jamshid_sharipov_85@mail.ru

behavior of the material under such conditions. In this case, the key role should be played by the mechanical activation of high-speed physicochemical processes that inevitably occur in both liquid and solid phases. The appearance of a melt causes a sharp increase in the interfacial surface and an increase in the rate of the nitride formation reaction due to the additional release of energy during the exothermic reaction. At present, high-speed steel tools with various durable coverings based on nitrides of refractory metals obtained by the method of physical deposition are widely used [1].

Today, in order to create a high-speed cutting layer tool that slows down the rate of its erosion and has characteristics that meet many requirements, as well as to determine the conditions for the rational use of complex cutting tools research is being carried out and optimization of combined processing technologies remains relevant.

Covering contributes to a significant increase in the performance of tools made from these alloys at high cutting speeds. However, the efficiency of such tools decreases sharply as the increases the thickness of the shaving being cut. Under these conditions, carbide tools with a higher cobalt content work much better, as they have high bending strength and toughness, as well as a reduced tendency to brittle fracture.

A cutting tool intended for production is very important, and in some cases decisive, for the correct surface finish of the material. The reason for the low margin of stability of the cutting tool is its rapid wear or failure of the working surface. There are several ways to increase its stability, of which coating is the most common at present. These coatings are applied to the surface of the cutting tool and parts in two ways: physical and chemical.

In this research work, the difficult-to-machine heat-resistant chromium-nickel alloy 34XH1MA was processed on a Fus-32 horizontal milling machine with a cutting tool made of R6M5 high-speed tool steel [2].

High-speed steel tools have great advantages at low and medium cutting speeds in combination with medium and large shear sections, as they have relatively low heat resistance, medium hardness and the highest bending strength and toughness, as well as a high endurance limit. These same tools operate better in conditions that take advantage of the small radius of rounding that is characteristic of tools made of high-speed steels.

This is due to the fact that parts with certain requirements for the shape and quality of the surface in mechanical engineering are processed by metal cutting, since the implementation of such technical requirements for other processing methods is difficult. In machining, problems arise due to a number of production requirements on the part of designers and technologists: frequent failure or erosion of the cutting tool, improperly selected cutting mode, the use of a coating that is not intended for the material being processed, when using a cutting tool, the output.

The quality of manufactured parts, the level of accuracy, the productivity and efficiency of the machining process and the conditions of automated production and adaptive production systems mainly depend on the quality, reliability and performance of cutting tools used in mechanical engineering.

From the review of the literature, it was found that the main conditions for the use of cutting tools are based on the creation of a nitrogenized, i.e., reinforced layer, which develops one or another structural composition with a certain thickness and microhardness, which determines the performance of high-speed steel during the cutting process.

2 Materials and Methods

At present, the method of ion nitriding is rapidly developing and is widely used in the production of machine-building industry. Ion nitriding technology is considered to be simple and economical compared to carburizing and nitrocement technologies and is one of the last stages of parts manufacturing. Before placing the workpiece in the working chamber, it is degreased in gasoline until the conditional time of ion-nitriding.

Specially designed cutting disk mills with various options for combined surface ion-plasma processing were used as a cutting tool for milling (Fig. 1). The process of ion nitriding of a cutting tool made of R6M5 high-speed tool steel was carried out on an APP-2 unit. Thermal treatment was carried out at a temperature of 470 °C for 45 min, which makes it possible to create a thermochemically hardened layer up to 40 mm thick and with microhardness up to $HV_{50} = 140$ MPa on the surface. The ion nitriding process makes it possible to saturate cast iron, carbon, alloyed, tool, corrosion-resistant and heat-resistant steels, titanium and cermet hard alloys with nitrogen. The final wear-resistant covering (TiAl)N, (TiAl)N + ion-nitriding, (TiAl)N + ion-nitriding + ion-alloying (NbHf), with microhardness $HV_{50} = 350$ MPa was applied on a Platit $\pi 311$ unit. This covering is a combination of the adhesive layer of the composition and the gradient covering (TiAl)N. In the research work, after ion nitriding and ion alloying, disk cutters were applied to a Platit p311 device.

In addition, the layer formed under the coating has a high resistance to microplastic deformation, combining hardness with extreme heat resistance. This leads to significantly reducing the power of the main heat source for the cutting edge of the tool. Ion doping of materials, or, in other words, the introduction of ions and ion implantation, is currently becoming the main technological process used to modify the electro-physical, chemical, optical, mechanical, and other properties of the surface layers of materials.

Multiphase coating layer with a grain size of 50–150 nm elements (TiAl)N, (TiAl)N + ion-nitriding, (TiAl)N + ion-nitriding + ion-doping (NbHf) up to 5 nm, on the border of which there is an amorphous the Si₃N₄ phase suppresses the coagulation of the grains of the main phase both during the coating process and during the operation of the cutting tool. Interfacial boundaries, which are zones of intense energy dissipation, deflect emerging cracks from the direction of propagation, partially or completely slowing them down. Before applying the wear-resistant covering, some of the samples were subjected to near-surface alloying. Processing was carried out in the RITM-SP-M installation, which is a combination of a source of low-energy

Fig. 1 High-speed R6M5 disk mills



high-current electron beams (LHEB) “RHYTHM” and two systems of magnetron sputtering on one vacuum chamber [3]. The device allows covering films on the surface of the desired product, followed by liquid-phase mixing of the film and substrate materials using an intense pulsed electron beam.

Ion doping of a cutting tool, or, in other words, the introduction of ions into its surface and the transfer of ions, is currently one of the main technological processes used to change the electrophysical, chemical, optical, mechanical and other properties of the surface layers of materials [4, 6].

Today, for a more successful implementation of complex surface treatment of high-speed tool steel, the surface of a cutting tool due to insufficient quality of preparation (quality of chemical–thermal treatment, passivity in friction, surface roughness, the presence of chips, load mode, etc.), significant wear of cutting blades and an uncontrolled amount gases and metal ions accelerated on the working surface, thickness and phase of the nitrated layer.

A multiphase structure using ion-doping in an exothermic chemical reaction between the coating metal and the substrate was obtained by depositing a thin layer of nitride-forming elements ($\text{Nb}_{72}\text{Hf}_{28}$ alloy targets were used) on the surface of the tool before treating it with a precise electron beam. Unstable iron nitrides of nitrated high-speed steel were used as its donors. The outer layer is enriched with refractory nitride phases, which, due to the extremely high cooling rate, remain small and evenly distributed in the final product. The depth of the surface layer, in which the modified steel structure is obtained, is 2–10 mm, depending on the alloying composition.

Ion-doping is based on the controlled introduction of ionized atoms and molecules into a material (solid body) accelerated in an electrostatic field. The ion-doping method is especially promising for semiconductor electronics. This method has a number of advantages over others: diffusion, melting, fusion from solution, epitaxial formation. Complex processing significantly reduces the formation of eroded grooves on the front surface of the cutting tool.

Ion-nitriding, ion-alloying processes of cutting tools are chemical–thermal treatment. Chemical–thermal treatment leads to changes in the chemical composition, structure and properties of the surface. Increasing the strength of the coating applied to the surface of the cutting tool cannot achieve the expected result from the plastic deformation of the base during processing. The role of the ion-nitrided and ion-alloyed layer in the complex processing of high-speed tool steel cutting tools is extremely large, because they ensure the strong adhesion of the coating, the reduction of plastic deformation, which is the most important condition for the use of wear-resistant cutting tools.

The phase composition and structure of the ion-nitrided layer were studied using X-ray diffraction analysis, which was carried out on an automated Dron-4 diffractometer, which was controlled by software and recorded spectra. Symmetrical reflection recording of the samples was carried out using X-ray tubes with copper and cobalt radiation.

3 Results and Discussions

Figure 2 shows the microstructure of a disk cutter with surface ion-alloyed high-speed tool steel P6M5. After each subsequent treatment, the cutting tool was checked for changes under a microscope. After milling, the change of the geometry of the cutting part of the milling cutter was carried out by measuring the radius r of the rounding of the cutting edges and checking the stability of the edges with a metallographic microscope, and then compared with the size and appearance of the initial radius, which is one of the most important factors of the cutting process.

In the process of cutting, the forces of resistance to plastic deformation of this metal act on the blade of the cutting tool. The amount of total force applied to the cutting tool to perform the cutting process must be sufficient to overcome the total resistance force of this metal (Fig. 3).

In the cutting tool we developed, material samples were exposed to a series of pulses of a low-energy high-current electron beam with a wide aperture to initiate exothermic chemical reactions between the metal coating and nitrogen, carbon or aluminum in liquid and solid phases. This paper describes the processes of ion alloying on the surface of materials using the reaction of the formation of niobium-hafnium carbide in the form of a complex carbide on the surface of the carbide phase of a hard alloy [7, 9].

As a new method for increasing the productivity of a cutting tool, the principles of a complexly machined surface (CMS) were formulated, and a special technology for implementing the CMS method was developed. The anti-corrosion complex formed during the implementation of the developed CMS technology has multi-purpose functions (Figs. 3, 4). Such a complex treatment increases the strength of the base poured under the covering, increases its adhesive properties, resistance to erosion. The covering in this complex has the property of rapid heat release in the treatment zone [10, 12]. In the process of cutting, the cutting tool blade is affected by the



Fig. 2 The nitriding process of a disk cutter in the APP-2 ion-nitriding device of cutting tools

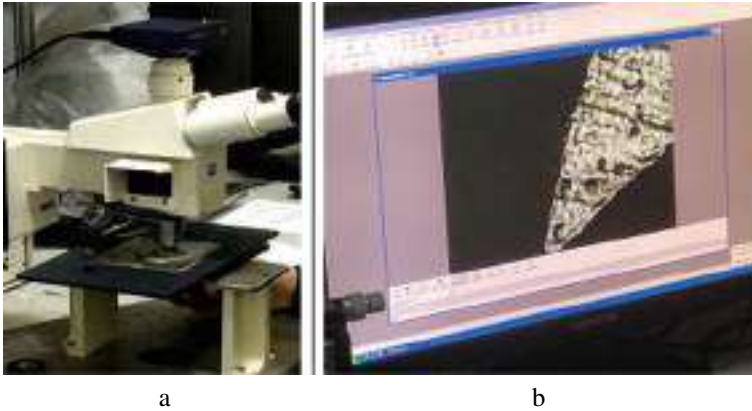


Fig. 3 Microscope SteREO Discovery V12 surface structure of the cutting tool. **a** The structure of the surface of nitrided R6M5 high-speed steel after exposure to LHEB, **b** The same after exactly electron-beam alloying with zirconium

forces of resistance to the plastic deformation of this metal. The magnitude of the total force applied to the cutting tool to perform the cutting process must be sufficient to overcome the total resisting force of that metal. Several scientists have conducted research on the calculation of shear strength. It is known that [58; 18-58-b] tangential

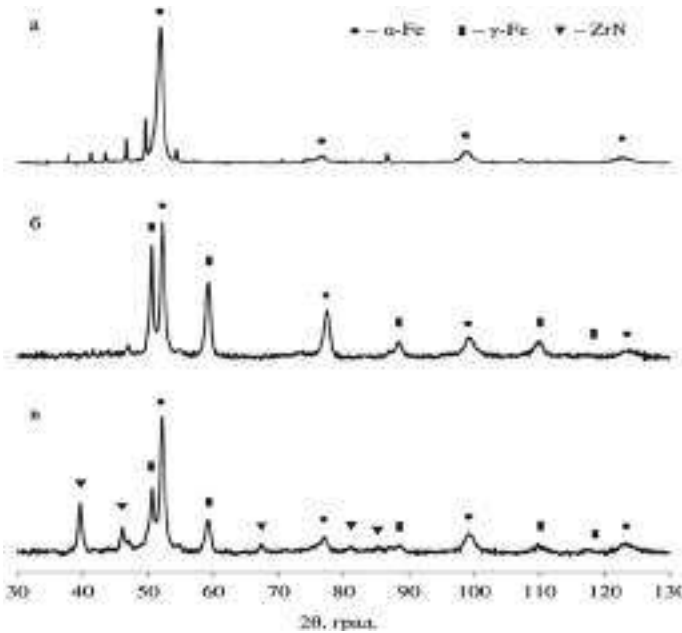


Fig. 4 Diffraction pattern of the sample surface. **a** Diffraction pattern (CoK α) from the surface of a sample of nitrided R6M5 steel, **b** after LHEB exposure, **c** after covering with NbHf film before irradiation

and radial components of shear force (P_z and P_y , respectively) were calculated for each of the indicated shear modes.

In order to determine the power spent on cutting, when calculating the strength and uniformity of the cutter, some details and parts of the machine, the cutting force R is placed on the three coordinate axes X , Y , Z and the elements P_z , P_y , P_x are formed. X is oriented along the vertical axis, and Y and Z axes are perpendicular and parallel to the detailed axis in the horizontal plane. P_z force is the main component of tangential, rotational force or shear force, P_x force is called radial force, P_y axial force or thrust force.

The magnitude of the equivalent shear force R can be determined from the following expression:

$$R = \sqrt{P_z + P_y + P_x}$$

The power consumed by the machine's prime mover electric motor is greater than the effective power consumed by the amount of losses occurring in the transmission from the electric motor to the spindle. These losses are determined by the efficiency of the transmission mechanisms.

Theoretically derived formulas are intended only for qualitative analysis of the dependence of shear force on mode forces, geometric and physical parameters, and

are not used in engineering practice. The relationship between the changes in the factors of the cutting process and the components of the cutting force is determined experimentally. Instruments that measure components of shear force are called dynamometers. According to the principles of operation, dynamometers are divided into 3: there are belt-mechanical, hydraulic and belt-electric types. Cutting forces are automatically controlled by all parameters in machines controlled by a new modern digital program.

The main factors affecting the cutting forces are the physical and mechanical properties of the processed material, the geometrical parameters of the cutting tool, the cutting mode and the lubrication-cooling technological environment. For a group of materials with the same chemical composition, the increase in shear stress with increasing reinforcement far outstrips the decrease in slag penetration coefficient. Therefore, when the tensile strength increases or the Vickers hardness increases, the shear strength components increase.

The change of cutting depth t and thrust S affects the change of all three constituents of cutting force P_z , P_y , P_x . The greater the depth and thrust, the greater the cross-sectional area of the cutting layer and the volume of metal being deformed, the cutting force and the resistance to the formation of slag. However, the effect of depth of cut and thrust on cutting forces is different. A large number of experiments show that the depth of cut has a stronger effect on the components of the cutting force than thrust

$$P_{zi \text{ чик}} = C_{pz} B^{X_{pz}} (S_z \sin \psi_i)^{Y_{pz}} S_z^{-Y_{pz}} V^{Z_{pz}} K_{pz} \quad (1)$$

$$P_{yi \text{ чик}} = C_{py} B^{X_{py}} (S_z \sin \psi_i)^{Y_{py}} S_z^{-Y_{py}} V^{Z_{py}} K_{py} \quad (2)$$

$$P_{xi \text{ чик}} = C_{px} B^{X_{px}} (S_z \sin \psi_i)^{Y_{px}} S_z^{-Y_{px}} V^{Z_{px}} K_{px} \quad (3)$$

The formation of chips at the beginning of the cutting process is determined by all deformation components in the field of friction and deformation of the contact surfaces when the tip of the blade cuts with less preparation (S_z) for the working stroke of the cutting tool.

When conducting research, it was found that the loads on the electric motor in the idle state and in the working state of the milling machine, when processing with milling cutters with different coatings and without coating, are different when compared. Compared to the uncoated cutters, it was found that the load on the electric motor is lower when the cutters with the complex treatment are measured in scissor ammeters.

Industrial surface modification technology is used to obtain specific properties of coatings applied in a vacuum arc discharge. Often, during coating, a negative potential is applied to the substrate, as a result of which the coating to be coated is bombarded with inert gas ions and spraying agents. In the process of cutting,

the forces of resistance to plastic deformation of this metal act on the blade of the cutting tool. The amount of total force applied to the cutting tool to perform the cutting process must be sufficient to overcome the total resistance force of this metal.

Izvestno, tak kak vykhod iz stroya rezhushchego instrumenta Usually, it is necessary to detail the technological equipment to understand that the technological system is full, and the instrument is not replaced. The graph of cutting tool wear versus cutting path is shown in Fig. 7.

Durability tests were carried out at IM “Navoi mechanization plant” of Navoi mining and smelting complex, when turning a forged, hard-to-cut alloy 34KhN1MA at cutting speed $V = 20$ m/min, feed $s = 0.150$ mm/rev, depth of cut $t = 4$ mm. The wear rate of the rear and front surfaces of 0.4 mm was chosen as the failure criterion for the cutting tool. The results obtained are presented in the Tables 1 and 2. A forged ingot of grade 34KhN1MA with a hardness of HB 375 was processed on a FUS-32 horizontal milling machine [13, 14].

The research work shows that the main factors affecting the cutting forces are the physical and mechanical properties of the material being processed, the geometric parameters of the cutting tool, the cutting mode and the lubricating and cooling technological environment [2]. When each pretty material is measured with an ambermeter, when measuring the load on the motor, a small load was found in the complex machined disc cutter (Fig. 5). The surface is strengthened during processing. The erosion of a tool is the main and important indicator of its working property. But the physical nature of deception comes from the extreme and repetitive processes of the cutting tool [15, 16] (Table 3).

When cutting with a raw tool, the characteristic point of wear was the tip of the disk mill. In the process of cutting hard-to-cut material with a complex cutting tool, it has been shown that the load on the electric motor is small, and the cutting force

Table 1 Chemical composition of the cutting tool tested preparation

Relevance of the brand according to the chemical composition				34XH1MA, chemical composition in %	
Element name	%	Element name	%	Element name	%
Carbon C	0.30	Sulfur S	0.015	Copper Cu	0.14
Silicon Si	0.34	Chrome Cr	1.40	Titan Ti	0.004
Manganese Mn	0.52	Molubden Mo	0.27	Hardness HB 375	
Phosphorus P	0.022	Nickel Ni	1.44		

Table 2 Physical composition of the cutting tool tested preparation

T	E 10^{-5}	α 10^6	Δ	P	C	R 10^9
Degree	Mpa	1/Deg	Vt/(M-deg)	Kg/M ³	Dj/(kg-deg)	OM-M
20	0,74			2850		
100		23,2				

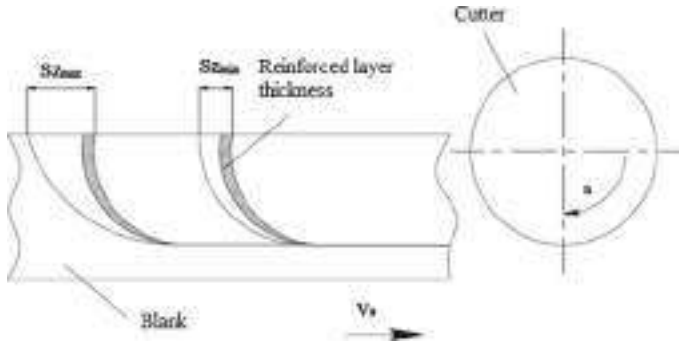


Fig. 5 Effect of shear rate Sz on components of shear forces at different thicknesses of the shear layer

is reduced. Adhesion of the processed material to the working surface of the milling cutter was evaluated by SteREO Discovery V12 stereomicroscopy. The radius r of the cutting edge rounding (undercut) was measured in MicroCAD lite Fig. 6. Change in the radius of penetration of the cutting blade ρ after 5 min of operation of the gasket is shown in Fig. 8 (Fig. 7).

It is known that when milling workpieces, wear of cutting tools occurs faster than when milling, since the cutting tool works under difficult conditions, and the teeth repeatedly hit the workpiece and enter and exit. The geometric parameters of a special cutting tool are characterized by the following geometric shapes: macro-geometry (drunk, compound, ovalrogomethy and microgegaometry (vegetable and pond). According to the general laws of erosion, sliding erosion of the cutting tool in the initial period of work is called initial erosion, and fast erosion occurs. In the initial period of wear, the cutting edge of the tool is machined, individual irregularities break up and migrate, and various lines, sharpening marks of the cutting edges are cleaned off and become smooth. This period of treated surfaces gadir is all slowly diminished [17–22].

Before applying a wear-resistant coating, the formation of rounding (lunch) in a disk electron-beam alloyed cutter is slower, and the cutting tool withstands high cutting forces, which slows down the onset of the rapid wear process. Cracks do not form on the cutting tool. If its partial rot is observed, it will quickly char and sharpen.

4 Conclusions

The results of the experiment indicate the possibility of obtaining modified surface layer, ion-nitriding, ion-alloying layers on the surface of a tool made of high-speed steel. These layers were obtained by initiating exothermic chemical reactions between the substrate and a $4 \mu\text{m}$ thin film deposited on it. In the reaction products,

Table 3 Wear of mills during machining

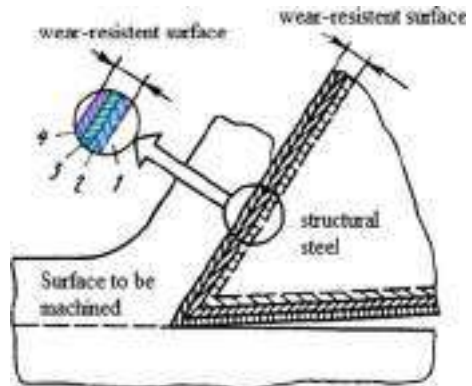
No	Name of the tool	Cutting modes			Tool durability T, min
		N, rpm	t, mm	S, mm/min	
1	Cut-off disk mill No. 1 ((TiCr)N-(TiAl)N-(CrAlSi)N + ion-nitriding covering)	350	4.0	150	1. Before machining the part, the outer diameter of the cutter was $\varnothing 99.5$ mm
					2. Depth of cut 4 mm for a length of 200 mm
					3. After processing, deterioration on the outer diameter was 0.3 mm
2	Cut-off disk mill No. 2 (diamond-like covering (DLC))	350	4.0	150	1. Before processing, the cutting tool and the outer diameter of the cutter were $\varnothing 99.3$ mm
					2. Depth of cut 4 mm for a length of 200 mm
					3. After processing, deterioration on the outer diameter was 0.25 mm
3	Cut-off disk mill No. 3 ((TiAl)N + ion-nitriding + ion-alloying (NbHf) covering)	350	4.0	150	1. Before processing, the cutting tool and the outer diameter of the cutter were $\varnothing 100$ mm
					2. Depth of cut 4 mm for a length of 200 mm
					3. After processing, deterioration on the outer diameter was 0.2 mm
4	Cut-off disk mill No. 4 ((TiAl)N covering)	350	4.0	150	1. Before processing, the cutting tool and the outer diameter of the cutter were $\varnothing 99.5$ mm
					2. Depth of cut 4 mm for a length of 200 mm
					3. After processing, deterioration on the outer diameter was 0.5 mm
5	Cut-off disk mill No. 5 ((TiAl)N + ion-nitriding covering)	350	4.0	150	1. Before processing, the cutting tool and the outer diameter of the cutter were $\varnothing 99.6$ mm
					2. Depth of cut 4 mm for a length of 200 mm

(continued)

Table 3 (continued)

No	Name of the tool	Cutting modes			Tool durability T, min
		N, rpm	t, mm	S, mm/min	
					3. After processing, deterioration on the outer diameter was 0.3 mm
6	Cut-off disk mill No. 6 ((TiCr)N-(TiAl)N-(CrAlSi)N (nATCRo ³) covering)	350	4.0	150	1. Before processing, the cutting tool and the outer diameter of the cutter were Ø100.7 mm
					2. Depth of cut 4 mm for a length of 200 mm
					3. After processing, deterioration on the outer diameter was 0.3 mm
7	Cut-off disk mill No. 7 (without covering)	350	4.0	150	1. Before processing, the cutting tool and the outer diameter of the cutter were Ø99.5 mm
					2. Depth of cut 4 mm for a length of 200 mm
					3. After processing, deterioration on the outer diameter was 0.6 mm

Fig. 6 Complicated machined surface. 1-tool steel, 2-adhesive heat-resistant nitrided layer, 3-alloyed base, 4-covering



the formation of components of a new phase has been determined. The implementation of such complex processing processes, ion nitriding, ion alloying of the base casting of cutting tools reduces its plastic deformation.

There are a large number of methods for obtaining coverings on the working surfaces of cutting tools. Physical precipitation, the covering of this machining on the

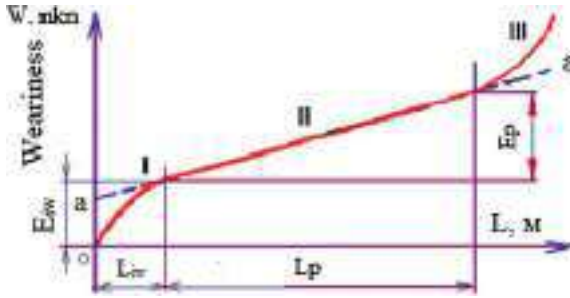


Fig. 7 Graph of cutting tool wear versus cutting path. L_{iw} -initial wear path, E_{iw} -initial wear, L_p -proportional length, E_p -proportional weariness

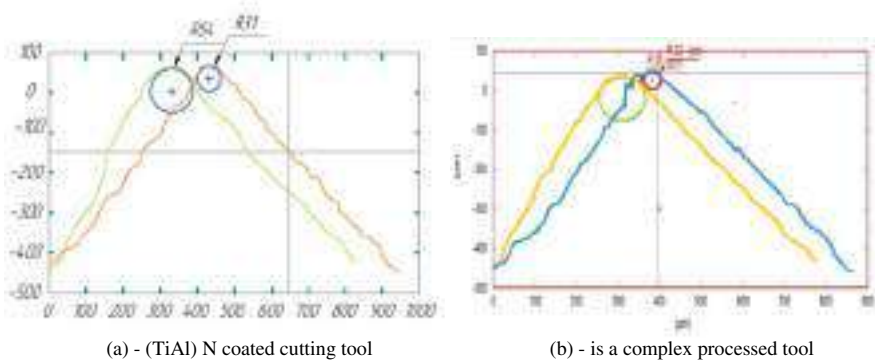


Fig. 8 Change in the radius of penetration of the cutting blade ρ after 5 min of operation of the gasket. (3D scanner GFM)

surface of a tool material, which significantly differs in its crystal-chemical, physical-mechanical and thermal-physical properties from the corresponding properties of the tool material (base), significantly improves the properties of the latter.

Ion-nitriding and microalloying may also be recommended. In particular, such treatment, which is recommended to be carried out before applying a wear-resistant coating, makes it possible to influence the wear processes of not only high-speed but also high-speed tools, which makes it possible to increase the wear resistance of the tool by 3–4 times.

This surface slows down the growth process in the cutting zone during processing with complex cutting tools and helps to remove the generated heat without absorbing it. The relevance of the study lies in the fact that one of the factors affecting the quality of the manufactured product is the inaccuracy of cutting tools, which in many cases, is transferred directly to the workpiece, causing systematic errors in the shape and size of the surfaces of the workpieces. Based on the main task of the research, the plastic deformation of the coating on the surface of cutting tools working at high loads was reduced by chemical-thermal treatment and coating.

References

1. Fedorov SV, Aleshin SV, Swe MH, Abdirova RD, Kapitanov AV, Egorov SB (2017) Comprehensive surface treatment of high-speed steel tool. *Mech Indus* 18:711
2. Sharipov J, Barakayev F, Fozilov S, Karimova Z, Zaripov M (2022) Increasing the resistance of the cutting tool during heat treatment and coating. *AIP Conf Proc* 2432:050042
3. Fedorov S, Sharipov J, Abrorov A (2021) Increasing the surface stability of the cutting tool through complex machining. *J Phys Conf Ser* 1889:022079
4. Vereschaka AA, Grigoriev SN (2017) Study of cracking mechanisms in multi-layered composite nano-structured coatings. *Wear* 378–379:43–57. <https://doi.org/10.1016/j.wear.2017.01.101/>
5. Vereschaka A, Volosova M, Chigarev A, Sitnikov N, Ashmarin A, Sotova C, Bublikov J, Lytkin D (200) Influence of the thickness of a nanolayer composite coating on values of residual stress and the nature of coating wear. *Coatings* 10:63. <https://doi.org/10.3390/coatings10010063>
6. Xu YX, Riedl H, Holec D, Chen L, Du Y, Mayrhofer PH (2017) Thermal stability and oxidation resistance of sputtered TiAlN coatings. *Surf Coat Technol* 324:47–57
7. Abrorov A, Kuvoncheva M, Rajabov O, Mukhammadov M, Jumaev S (2020) Method of thermal treatment of saw disk teeth of fiber-processing machines by laser quenching. *IOP Conf Ser Mater Sci Eng* 862:032034
8. Li WZ, Liu HW, Evaristo M, Polcar T, Cavaleiro (2013) A Influence of Al content on the mechanical properties and thermal stability in protective and oxidation atmospheres of Zr-Cr-Al-N coatings. *Surf Coat Technol* 236:238–246
9. Holec D, Rachbauer R, Chen L, Wang L, Luef D, Mayrhofer PH (2011) Mayrhofer phase stability and alloy-related trends in Ti–Al–N, Zr–Al–N and Hf–Al–N systems from first principles. *Surf Coat Technol* 206:1698–1704
10. Tabakov VP, Sagitov DI (2015) The performance of the cutting tool with Wear-resistant coatings in conditions of constrained cutting. *UIGTU, Ulyanovsk*, p. 179
11. Tabakov VP (2008) Formation of wear-resistant ion-plasma coatings of cutting tools. *M, Mashinostroenie*, p. 311
12. Vereshchaka AA (2010) Improving the cutting properties of carbide tools by rational choice of the composition, structure and properties of nanosized wear-resistant complexes: Dis. for the competition uch. step. cand. tech. Sciences. *GOU VPO MSTU “Stankin”, M*, p. 254
13. www.mdpi.com
14. Rakhmonov K, Fayziev S, Rakhimov K, Kazakova D (2021) Relative speed and temperature effect investigation of the of the drying agent on the moisture content of cotton. *E3S Web Conf* 264:04008
15. Díaz-Guillén JC, Naeem M, Hdz-García HM, Acevedo-Davila JL, Díaz-Guillén MR, Khan MA, Iqbal J, Mtz-Enriquez AI (2020) Duplex plasma treatment of AISI D2 tool steel by combining plasma nitriding (with and without white layer) and post-oxidation. *Surf Coat Technol* 385:125420
16. Krysinina OV, Prokopenko NA*, Ivanov YF, Tolkachev OS, Shugurov VV, Petrikova EA (2020) Multi-layered gradient (Zr,Nb)N coatings deposited by the vacuum-arc method. *Surf Coat Technol* 393:125759
17. Yamamoto K, Sato T, Takahara K, Hanaguri K (2003) Properties of (Ti,Cr,Al)N coatings with high Al content deposited by new plasma enhanced arc-cathode. *Surf Coat Technol* 174–175:620–626
18. Huang F, Wei G, Barnard JA, Weaver ML (2001) Microstructure and stress development in magnetron sputtered TiAlCr(N)films. *Surf Coat Technol* 146–147:391–397
19. Donohue LA, Smith IJ, Munz W-D, Petrov I, Greene JE (1997) *Surf. Coat Technol* 94–95:226
20. Tam PL, Zhou ZF, Shum PW, Li KY (2008) Structural, mechanical, and tribological studies of Cr-TiAl-N coating with different chemical compositions. *Thin Solid Films* 516(16):5725–5731

21. Xu YX, Riedl H, Holec D, Chen L, Du Y, Mayrhofer PH (2017) Thermal stability and oxidation resistance of sputtered Ti-si-n hard coatings. *Surf Coat Technol* 324:48–56
22. Vereschaka A, Volosova M, Chigarev A, Sitnikov N, Ashmarin A, Sotova C, Bublikov J, Lytkin D (2020) Influence of the thickness of a nanolayer composite coating on values of residual stress and the nature of coating wear. *Coatings* 10:63. <https://doi.org/10.3390/coatings10010063>

Chapter 7

Nano-Severe Plastic Deformation Process on Aluminum Alloy and Composites: An Overview



K. G. Sagar

Abstract Material when subjected to severe plastic deformation at the nanoscale level in a process known as nano-severe plastic deformation (NSPD), which produces a nanostructured material. Materials with ultrafine grain sizes, high strength, and enhanced mechanical properties can now be created employing NSPD processes. To create nanocrystalline and ultrafine-grained materials, the process involves subjecting the material to high plastic strains to cause deformation at the sub-micron level. Mechanical and thermo-mechanical processes are the two broad groups into which NSPD approaches can be categorised. High-pressure torsion, equal channel angular pressing, repeating corrugation, and straightening are examples of mechanical processes, while accumulative roll bonding and cyclic extrusion compression are examples of thermo-mechanical processes. A variety of nanostructured materials, including metals, alloys, and composites, have been created using NSPD. These materials may find use in a variety of industries, including those that call for high-strength and lightweight materials, like aerospace, automotive, and biomedical engineering. High plastic strains, often between 100 and 1000%, are applied to the material during NSPD, which causes the production of dislocations, grain boundary movement, and deformation twinning. As a result, mechanical qualities such as high strength, ductility, and fatigue resistance are enhanced. In this work, a review of the effect of NSPD on aluminium and aluminium metal matrix composites have been dealt.

Keywords Severe plastic deformation · Nano severe plastic deformation · Grain refinement · Mechanical and tribological properties

K. G. Sagar (✉)
Department of Mechanical Engineering, Cambridge Institute of Technology, Bengaluru,
Karnataka, India
e-mail: sagar.mech@cambridge.edu.in

1 Introduction

A class of materials known as aluminum alloys includes aluminium as the main component as well as silicon, copper, magnesium, zinc, and other alloying elements. Because of their low density, high strength-to-weight ratio, excellent corrosion resistance, and superior formability, these alloys are widely employed in a wide range of applications. Cast alloys and wrought alloys are the two basic categories of aluminium alloys. Cast alloys are created by pouring the molten metal into a mold, whereas wrought alloys are created by rolling, extruding, forging, or other forming techniques [1].

These pure aluminium alloys, known as the 1000 family, are frequently employed for their exceptional formability and corrosion resistance. They are frequently employed in the production of cooking utensils, electrical conductors, and packaging materials. Copper serves as the main alloying element in the 2000 series alloys, which are renowned for their high strength and superior fatigue resistance [2–8]. They are frequently utilised for structural components in the aircraft sector. Manganese is the main alloying element of the 3000 series alloys, which are renowned for their good corrosion resistance and average strength. They are frequently employed in the production of automobile components and heat exchangers. Magnesium is the main alloying element of the 5000 series alloys, which are renowned for their high strength and superior corrosion resistance [2–8]. They are frequently employed in the production of maritime applications and automotive parts. Magnesium and silicon serve as the principal alloying components in the 6000 series alloys, which are renowned for their good strength, corrosion resistance, and formability. They are frequently employed in the production of automotive and architectural elements. Zinc serves as the main alloying element in the 7000 series alloys, which are renowned for their high strength and superior fatigue resistance. They are frequently utilised for structural components in the aircraft sector. A wide range of industries, including aerospace, automotive, construction, and consumer goods, employ aluminium alloys extensively. Current studies are concentrated on creating novel alloys with enhanced characteristics, streamlining production methods, and investigating new uses for these materials [2–8].

1.1 Aluminum Metal Matrix Composites (AMMCs)

Aluminum serves as the matrix material for aluminium metal matrix composites (AMMCs), a class of materials that also include one or more reinforcement materials such as ceramic particles, fibres, or whiskers. AMMCs combine high stiffness, strength, and wear resistance of the reinforcement elements with the beneficial features of aluminium, such as high strength-to-weight ratio and good corrosion resistance. Ceramic particles, fibres, and whiskers are the three main categories for the reinforcement materials utilised in AMMCs [9–13]. The most popular type of

reinforcement material in AMMCs is ceramic particles because of their low price, convenient availability, and superior mechanical qualities. On the other hand, fibres and whiskers are more expensive but have better mechanical qualities. The preparation of the reinforcement material, mixing of the reinforcement material with the aluminium matrix material, and consolidation of the mixture are all phases in the manufacture of AMMCs. Many methods, including powder metallurgy, casting, and infiltration, can be used to consolidate. AMMCs have stronger stiffness, strength, and wear resistance than typical aluminium alloys, among other benefits. They are frequently utilised in areas including aerospace, automotive, and military, where strong mechanical characteristics and wear resistance are necessary [9–13]. AMMCs are frequently used in the manufacture of brake discs, engine parts, and structural elements for airplanes [9–13]. The goal of the ongoing study is to enhance the properties of AMMCs while also studying new types of reinforcing materials, developing innovative processing methods, and expanding the scope of their industrial uses. So, in this work, the author is discussing the nano-SPD of aluminum and aluminium metal matrix composites.

1.2 Nano-Severe Plastic Deformation (NSPD)

A material is subjected to severe plastic deformation in the nanoscale range in a process known as nano-severe plastic deformation (nano-SPD). By reducing the grain size to the nanoscale range, this method aims to enhance the material's mechanical and physical characteristics, such as strength, ductility, and wear resistance. High-pressure torsion (HPT), equal channel angular pressing (ECAP), and friction stir processing are just a few of the methods employed for nano-SPD (FSP) [14]. To achieve the appropriate nanoscale grain structure, each of these methods deforms the material under intense pressure and shear strain. Improved strength and ductility, greater wear resistance, and higher thermal stability are all advantages of nano-SPD [14, 15]. These enhancements result from the finer grain size, which increases the density of grain boundaries and dislocations and lessens the likelihood of material faults. Aerospace, automotive, and biomedical are just a few of the numerous areas where nano-SPD could find useful. Nano-SPD can be utilised, for instance, to make stronger and more resilient structural elements for cars and airplanes, as well as to increase the wear resistance of medical implants. The mechanical and tribological characteristics of aluminium alloys have been discovered to be significantly impacted by nanoscale severe plastic deformation (nano-SPD). Strength, ductility, wear resistance, and fatigue life are all enhanced by the nanoscale grain refinement achieved with nano-SPD. One study looked at how ECAP affected an aluminium alloy's mechanical characteristics. The scientists discovered that after ECAP, the material's strength and hardness greatly enhanced, while its ductility remained mostly unchanged. The increase in strength was attributable to the nanoscale grain size refinement, which raised the density of dislocations by increasing the number of grain

boundaries. Another study investigated how HPT affected the tribological characteristics of an aluminium alloy. The creation of a homogenous, refined microstructure with a high density of dislocations and grain boundaries after HPT was found to greatly boost the material's wear resistance. The development of a stable tribolayer on the material's surface was also noted by the researchers as a decrease in the friction coefficient and wear rate [14, 15]. Nano-SPD can increase the thermal stability of aluminium alloys in addition to enhancing their mechanical and tribological characteristics. For instance, one study discovered that ECAP increased the thermal stability of the grain boundaries, which in turn improved the high-temperature stability of an aluminium alloy. Fatigue life improvement: Nano-SPD has been found to significantly improve the fatigue life of aluminium alloys [14, 15]. One study found that after ECAP, the fatigue strength of an aluminium alloy increased by up to 60%. The improvement in fatigue life was attributed to the refinement of the grain size, which led to a greater number of dislocations and a higher density of grain boundaries, both of which contribute to improved fatigue resistance. Corrosion resistance: Nano-SPD has also been found to improve the corrosion resistance of aluminium alloys. One study found that after HPT, the corrosion resistance of an aluminium alloy was significantly improved due to the formation of a homogenous and refined microstructure with a high density of grain boundaries and dislocations. Microstructure refinement: One of the primary effects of nano-SPD on aluminium alloys is the refinement of the microstructure to the nanometre scale. This refinement leads to a more uniform distribution of the alloying elements and a higher density of grain boundaries and dislocations, which in turn leads to improvements in mechanical and tribological properties. Strain hardening: Nano-SPD induces a high level of strain hardening in aluminium alloys, which further contributes to improvements in mechanical and tribological properties. Strain hardening is the process by which the material becomes stronger and more resistant to deformation because of plastic deformation. Grain boundary strengthening: Using nano-SPD to refine the grain size to the nanoscale, the quantity of grain boundaries in the material is increased. The strengthening action that follows, known as grain boundary strengthening, helps to improve the mechanical properties of aluminium alloys. Aluminum alloys' texture, or the preferred orientation of the grains within the substance, can be changed through nano-SPD. The material's anisotropy, or directional dependency of characteristics, can be impacted by texture. A more random texture produced by nano-SPD may result in improved isotropic characteristics. Recrystallisation suppression: The material may recrystallise during typical plastic deformation, such as rolling or extrusion, which can result in coarsening of the grain size and a decrease in the strengthening effect. Yet, it has been discovered that nano-SPD inhibits recrystallisation, preserving the fine grain size and the strengthening effect. Fabrication of composites: Aluminum matrix composites with enhanced mechanical properties can also be created using nano-SPD. For instance, one study discovered that adding ceramic nanoparticles to an aluminium matrix via nano-SPD resulted in appreciable gains in strength and wear resistance. Surface modification: Nano-SPD can be used to modify the surface properties of aluminium alloys. For example, one study found that after HPT, the surface hardness of an aluminium alloy increased significantly, which was attributed

to the refinement of the grain size and the increase in the density of dislocations. Improved wear resistance: Nano-SPD has been found to significantly improve the wear resistance of aluminium alloys. One study found that after ECAP, the wear resistance of an aluminium alloy increased by up to 300%, which was attributed to the refinement of the grain size and the increase in the density of dislocations and grain boundaries. Improved mechanical properties at high temperatures: Nano-SPD can also improve the mechanical properties of aluminium alloys at high temperatures. One study found that after HPT, the yield strength and tensile strength of an aluminium alloy increased significantly at high temperatures, which was attributed to the refinement of the microstructure and the suppression of recrystallisation. Improved formability: Nano-SPD can also improve the formability of aluminium alloys, which is their ability to be shaped into complex geometries without cracking or rupturing. One study found that after ECAP, the formability of an aluminium alloy increased significantly due to the refinement of the microstructure and the increase in the density of dislocations. Nano-SPD can also enhance the joining characteristics of aluminium alloys. For instance, one study discovered that the improvement in the microstructure and the rise in dislocation density during HPT considerably boosted the joint strength of an aluminium alloy. Improved electrical and thermal conductivity: Aluminum alloys continue to have strong electrical and thermal conductivities despite the grain refinement caused by nano-SPD, making them a desirable material for a variety of applications [15].

Aluminum metal matrix composites (AMMCs) can use a variety of reinforcing types, such as: Ceramic particles: Due to their high strength and stiffness, ceramic particles including silicon carbide (SiC), alumina (Al₂O₃), and titanium diboride (TiB₂) are frequently employed as reinforcement in AMMCs. Metallic particles: AMMCs can also be reinforced with metallic particles including copper (Cu), nickel (Ni), and aluminium oxide (Al₂O₃). Carbon fibres: Carbon fibres are an appealing reinforcement for AMMCs because of their lightweight and excellent tensile strength [16–23]. Graphene: Because of its distinct mechanical, thermal, and electrical characteristics, graphene is a desirable reinforcement material for AMMCs. Nanoparticles: AMMCs can be reinforced with nanoparticles including carbon nanotubes (CNTs), graphene oxide (GO), and titanium oxide (TiO₂). The mechanical and tribological characteristics of AMMCs can be greatly enhanced by these particles, which have a large surface area to volume ratio. Fibers: AMMCs can also be reinforced with fibres, including glass, aramid, and carbon fibres. These fibres can increase the stiffness and strength of AMMCs, which makes them perfect for applications requiring high strength. Whiskers: Long, thin fibres, like silicon carbide whiskers, can be employed as reinforcement in AMMCs. The mechanical qualities of AMMCs can be considerably enhanced by whiskers, which have high strength and stiffness [16–23].

High-pressure torsion (HPT) and equal channel angular pressing are the two most popular nano-SPD processes that can be utilised to process AMMCs (ECAP). In HPT, a sample is subjected to high pressure and torsion deformation, which causes a severe plastic deformation that can improve the material's microstructure. ECAP includes running a sample through a die that has two channels that cross at a precise angle.

This causes a significant plastic deformation that can also improve the material's microstructure. It has been discovered that processing different kinds of AMMCs with HPT and ECAP greatly enhances their mechanical and tribological properties. Several research have investigated the impact of nano-SPD on aluminium alloys reinforced with different types of reinforcements. These are a few instances.

Carbon nanotube-reinforced aluminium matrix composites: Scientists have discovered that introducing carbon nanotubes (CNTs) and then subjecting the composite to nano-SPD can greatly improve its mechanical characteristics.

Graphene oxide has also been employed as a reinforcement in aluminium matrix composites, and its utilisation is described below. Researchers have discovered that applying nano-SPD to Al6061/GO composites can greatly enhance their mechanical characteristics. It is an emerging method.

1.3 Advantages and Limitations of Nano-SPD

Increased strength, ductility, and hardness are just a few examples of the mechanical attributes that nano-SPD can help materials possess. The creation of ultrafine or even nanocrystalline structures in materials because of nano-SPD might enhance their microstructure and, consequently their mechanical characteristics. Versatility: Metals, alloys, and composites are just a few of the many materials to which nano-SPD can be used. Cost-effectiveness: Nano-SPD does not require expensive equipment or supplies, making it a comparatively inexpensive approach to enhancing the mechanical characteristics of materials.

1.3.1 Limitations of Nano-SPD

In summary, the SPD process has some limitations that can affect its scalability, cost-effectiveness, and accessibility. However, with continued research and development, some of these limitations can be addressed, leading to the development of new and improved SPD techniques for manufacturing materials with tailored properties.

1.4 Nano-SPD

The use of nano-SPD on a wider variety of materials, such as metals, ceramics, polymers, and composites, may be investigated by researchers. Customised microstructures: To maximise the characteristics of materials for purposes, researchers may concentrate on creating novel techniques for controlling and modifying the microstructure of materials utilising nano-SPD. Multi-scale processing: To produce materials with multi-scale microstructures, which might result in superior mechanical

and functional properties, researchers may investigate the use of nano-SPD in combination with other processing methods. **Large-scale manufacturing:** To enable the commercial manufacture of high-performance materials, researchers may concentrate on creating large-scale manufacturing techniques for nano-SPD. **Improved characterisation:** To better understand the underlying principles and optimise the procedure for particular applications, researchers may develop novel approaches for assessing the microstructure and characteristics of materials made via nano-SPD. **Simulation and modelling:** To simulate and forecast the microstructural evolution and mechanical properties of materials produced with nano-SPD, researchers may create computational models. **Advanced applications:** Researchers might concentrate on creating cutting-edge uses for materials created via nano-SPD, like energy storage, aeronautical, and biological ones. **Integration with additive manufacturing:** Nano-SPD and additive manufacturing can be used together to produce materials with intricate geometries and microstructures, opening new design options for high-performance parts. **Materials with various functions:** To support the creation of cutting-edge technology, researchers may investigate the use of nano-SPD to produce materials with traits like high strength, thermal conductivity, and electrical conductivity. **Environmental factors:** Future studies may concentrate on enhancing the environmental sustainability of nano-SPD, for example, by lowering the amount of energy consumed and waste produced during the procedure. **Commercialisation:** As nano-SPD develops, there may be a greater interest in making the technology available for industrial uses, which could result in the creation of new markets and products. **Integration with Industry 4.0:** The combination of nano-SPD with Industry 4.0 technologies, including as artificial intelligence, machine learning, and the internet of things, may make it possible to optimise process parameters and boost the final product's quality and reproducibility. High-pressure torsion and accumulative roll bonding are two SPD techniques that could be combined with nano-SPD to develop hybrid processing methods that give distinctive microstructures and enhanced characteristics.

2 Conclusions

Nano-SPD is an effective method for enhancing the mechanical and tribological characteristics of aluminium alloys and composites made of aluminium metal matrix. The strength, ductility, hardness, and wear resistance of these materials can be considerably increased by nano-SPD through grain refinement and the creation of sub microscopic structures. These qualities can be improved even more by using other reinforcements, like nanoparticles and fibres. Although there are significant drawbacks and difficulties with nano-SPD, such as the requirement for specialised tools and the possibility of processing-induced errors, continuing research is resolving these problems and enhancing the technique's capabilities. In general, nano-SPD

holds the promise of revolutionising the creation of innovative materials for a variety of industries, including aerospace, automotive, and biomedical engineering. We may anticipate many exciting new advancements in the field as researchers work to fully utilise this technology.

References

1. Types of Aluminum and Aluminum Alloy You Should Know | MachineMfg (2022) August 31, 2022. [www.machinemfg.com](https://www.machinemfg.com/series-of-aluminum-and-aluminum-alloy/). <https://www.machinemfg.com/series-of-aluminum-and-aluminum-alloy/>
2. Aluminum and Aluminum Alloys nd. <https://doi.org/10.1361/autb2001p351>.
3. Dhanasekaran S, Sunilraj S, Ramya G, Ravishankar S (2015) SiC and Al₂O₃ reinforced aluminum metal matrix composites for heavy vehicle clutch applications. *Trans Indian Inst Met* 69(3):699–703. <https://doi.org/10.1007/s12666-015-0542-8>
4. Edalati K, Bachmaier A, Beloshenko VA, Beygelzimer Y, Blank VD, Botta WJ, Bryla K et al (2022) Nanomaterials by severe plastic deformation: review of historical developments and recent advances. *Mater Res Lett* 10(4):163–256. <https://doi.org/10.1080/21663831.2022.2029779>
5. Moona G, Walia R, Rastogi V, Sharma R (2018) Aluminium metal matrix composites: a retrospective investigation. *Indian J Pure Appl Phys*. <https://www.semanticscholar.org/paper/Aluminium-metal-matrix-composites%3A-A-retrospective-Moona-Walia/52820d12159b65f427f1f96f1ccec6b830b8230>
6. Garg P, Jamwal A, Kumar D, Sadasivuni KK, Hussain CM, Gupta P (2019) Advance research progresses in aluminium matrix composites: manufacturing & applications. *J Market Res* 8(5):4924–4939. <https://doi.org/10.1016/j.jmrt.2019.06.028>
7. Georgantzia E, Gkantou M, Kamaris GS (2021) Aluminium alloys as structural material: a review of research. *Eng Struct* 227(January):111372. <https://doi.org/10.1016/j.engstruct.2020.111372>
8. Joseph OO, Olubambi PA, Joseph OO, Edun BM, Okeniyi JO, Abioye OP (2021) Effects of alloying on aluminium-silicon alloys—a review. *IOP Conf Ser Mater Sci Eng* 1107(1):012116. <https://doi.org/10.1088/1757-899x/1107/1/012116>
9. Kottedda TK, Kumar M, Kumar P, Chekuri RBR (2022) Metal matrix nanocomposites: future scope in the fabrication and machining techniques. *Int J Adv Manuf Technol*. <https://doi.org/10.1007/s00170-022-09847-0>
10. Kumar H, Devade K, Singh DP, Giri JM, Kumar M, Arun V (2023) Severe plastic deformation: a state of art. *Mater Today Proceed*. <https://doi.org/10.1016/j.matpr.2023.02.194>
11. Mavhungu ST, Akinlabi ET, Onitiri MA, Varachia FM (2017) Aluminum matrix composites for industrial use: advances and trends. *Proced Manuf* 7:178–182. <https://doi.org/10.1016/j.pro.mfg.2016.12.045>
12. Metal Matrix Composite-an Overview | ScienceDirect Topics. nd. [www.sciencedirect.com](https://www.sciencedirect.com/topics/materials-science/metal-matrix-composite#:~:text=Aluminum%E2%80%93matrix%20composites%20are%20most%20commonly%20studied%20MMC%20as). Accessed April 14, 2023. <https://www.sciencedirect.com/topics/materials-science/metal-matrix-composite#:~:text=Aluminum%E2%80%93matrix%20composites%20are%20most%20commonly%20studied%20MMC%20as>
13. Pasha MBA, Kaleemulla M (2018) Processing and characterization of aluminum metal matrix composites: an overview. *Rev Adv Mater Sci* 56(1):79–90. <https://doi.org/10.1515/rams-2018-0039>
14. Rajaganapathy C, Vasudevan D, Selvakumar N (2020) Investigation on tribological and mechanical behaviour of AA6082—graphene based composites with Ti particles. *Mater Res Express* 7(7):076514. <https://doi.org/10.1088/2053-1591/aba508>
15. Saini P, Singh PK (2022) Fabrication and Characterization of SiC-reinforced Al-4032 metal matrix composites. *Eng Res Express* 4(1):015004. <https://doi.org/10.1088/2631-8695/ac4831>

16. Santos MC, Machado AR, Sales WF, Barrozo MAS, Ezugwu EO (2016) Machining of aluminum alloys: a review. *Int J Adv Manuf Technol* 86(9–12):3067–3080. <https://doi.org/10.1007/s00170-016-8431-9>
17. Singh L, Kumar S, Shivam SR, Badhani P (2021) Aluminium metal matrix composites: manufacturing and applications. *IOP Conf Ser Mater Sci Eng* 1149(1):012025. <https://doi.org/10.1088/1757-899x/1149/1/012025>
18. Subramanian C (2010) Wear properties of aluminium-based alloys. *Surf Eng Light Alloys* 40–57. <https://doi.org/10.1533/9781845699451.1.40>
19. Sundar G, Rajesh Jesudoss Hynes N (2019) Reinforcement in aluminium metal matrix composites. *Advances in basic science (ICABS 2019)*. <https://doi.org/10.1063/1.5122398>
20. Types of Aluminum: Types, Uses, Features and Benefits nd. Accessed April 14, 2023. www.iqsdirectory.com. <https://www.iqsdirectory.com/articles/aluminum-metal/types-of-aluminum.html#:~:text=The%201000%20series%20is%20non-heat%20treatable%20and%20contains>
21. Vijaya Ramnath B, Parswajinan C, Dharmaseelan R, Thileepan K, Nithin Krishna K (2021) A review on aluminium metal matrix composites. *Mater Today Proceed* 46:4341–43. <https://doi.org/10.1016/j.matpr.2021.03.600>
22. Yashpal S, Jawalkar CS, Verma AS, Suri NM (2017) Fabrication of aluminium metal matrix composites with particulate reinforcement: a review. *Mater Today Proceed* 4(2):2927–2936. <https://doi.org/10.1016/j.matpr.2017.02.174>
23. Zhang A, Li Y (2023) Thermal conductivity of aluminum alloys—a review. *Materials* 16(8):2972. <https://doi.org/10.3390/ma16082972>

Chapter 8

Review of Mechanized Garbage-Picking Machines: Challenges and Advancements in Sweeping and Handling of Trash



Nihal Wargantiwar, V. N. Bhaiswar, and V. W. Khond

Abstract The purpose of this paper is to study various mechanized garbage-picking machines with the view to overcome the challenges associated with roadside garbage picking, various sweeping machines, sweeping processes, handling garbage, and transportation of garbage. This study article summarizes the findings of numerous patents and studies done to improve various garbage-picking mechanisms. Garbage can be collected using a manual, electric motor-powered, or power-operated method. The first manually operated device is typically utilized to collect trash from minor roadways. To work, a second-powered mechanism needs gasoline or diesel. Electric battery power is used to operate the third electric power mechanism. Each mechanism has advantages and limitations. Comparative analyses of various mechanisms are carried out using prior research papers and patents. The majority of patents and researchers indicated enhanced performance and optimized mechanisms employing manual, electric, or other forms of power. These solutions have substantial maintenance costs as well, which raises the overall cost. The revised in this review article.

Keywords Sweeping machine · Garbage collection · Rotary brush · Trash · Trash container

N. Wargantiwar (✉) · V. N. Bhaiswar · V. W. Khond
Department of CAD/CAM, G H Raisoni College of Engineering, MTech, Nagpur,
Maharashtra 440016, India
e-mail: wargantiwarnihal@gmail.com

V. N. Bhaiswar
e-mail: vinod.bhaiswar@raisoni.net

V. W. Khond
e-mail: vivek.khond@raisoni.net

© The Author(s), under exclusive license to Springer Nature Singapore Pte Ltd. 2023
V. Bindhu et al. (eds.), *Proceedings of Sixth International Conference on Inventive Material Science Applications*, Advances in Sustainability Science and Technology,
https://doi.org/10.1007/978-981-99-4189-6_8

1 Introduction

In India, garbage cleaning is one of the major problems which covers all major cities and villages, especially on roads, railway stations, airports, and bus stops [1]. Managing garbage in the nation is a huge challenge. Owing to increasing urbanization. The 62 million tons of rubbish are produced annually by over 377 million urban residents of 7,935 towns and localities [2]. That dust is not commonly cited as a cause of road accidents in police reports, making data linking the two scarce. However, studies suggest that if dust contributes to 10% of accidents in developing countries, it could cost up to \$800 million annually and account for 0.02% of GDP, with 40% of dust emissions stemming from vehicle activities on the road [3]. Municipal corporations have been assigned by the government to handle critical services. India's trend is inconsistent. Few local government agencies decide to clean the roadways by themselves. Other municipal authorities desire to give sweeping private companies the entire contract for sweeping. Early in the morning, they hire employees to sweep the roadside trash, bottles, and leaf litter. However, there are numerous health and safety-related issues at the moment. Road sweeping is currently carried out by contractors in large urban areas. Indian road sweeping industry is still in its infancy, as seen by the effectiveness of the country's native roads. Road sweeping machines have given the impression that they are not appropriate for the relatively particular demands of Indian roads [4]. In India, cleaning roads with brooms and hand-held devices is time-consuming and unhealthy for operators due to dust inhalation and dehydration. The "Clean India Mission" has created a need for a more efficient and healthy trash-picking device [5]. Improper waste management due to rising population is a major issue. A planned system using ZigBee, GSM, and RFID technologies is designed for indoor floor waste collection in high-rise buildings [6].

Street sweeping is performed by 9231 regular employees of the Municipal Corporation of Greater Mumbai (MCGM), although this number must be significantly greater across all of India. Studies have found a link between occupational exposure to sweeping and the onset of chronic respiratory illnesses, skin conditions, eye irritation, asthma, TB, and hypertension among employees. Musculoskeletal injuries make up the majority of the other non-fatal injuries that were found [7]. Cleaners frequently labor hunched over and with their backs bowed. They carry out several repetitive activities every day [4].

Pain, soreness, or discomfort in any of the anatomical regions of the body, including the neck, shoulders, upper back, lower back, elbows, wrists, or hands, as well as the hips or thighs, knees, ankles, or feet, are referred to as musculoskeletal disorders (MSDs) [8]. Regular cleaning and sanitizing not only protect human health but also prevents pest infestations and improve the durability of surfaces [9].

- **Sweeping machines generally work on the following three principles**

The regenerative air sweeper: It is typically used for residential purposes on streets, parking lots, and back roads. It uses a closed loop of air without venting or fumes. It is the most adaptable advancement for getting ordinary street junk like overpowering

earth, rocks, sand leaves, and whip. To clean, regenerative air sweepers use a closed-loop “cyclonic effect.” They share a vacuum inlet with vacuum sweepers in the same location on one side of the sweeping head. However, in contrast to vacuum machines, regenerative air sweepers continuously regenerate their internal air supply [10].

Broom Sweeper Machines: Mechanical broom sweepers have a main drum-like broom that runs transversely from one side of the sweeper to the other so that the broom bristles contact the paved surface throughout the sweeper unit’s width. This technology can be compared to cleaning with a broom and parker. An attached refuse collector or bucket is used to collect swept debris for subsequent delivery to the dump site [10].

Vacuum Sweepers: This may be likened to a household vacuum system. The blow that creates the necessary vacuum and suction pressure is powered by a motor. A relatively recent technology is the high-efficiency sweeper. It uses a variety of fugitive dust loss controllers and a wide range of diverse devices, including vacuums, regenerative air systems, and at least one well-known mechanical broom machine. These devices are made to limit fugitive dust losses in addition to removing a significant amount of collected material of all sizes, particularly small-micron particles of less than 60 μ [10].

- **Most commonly used method of waste disposal in India**

In India, the most commonly used method of waste disposal is still landfilling, although efforts are being made to shift towards more sustainable practices. According to a report by the Central Pollution Control Board, around 75% of the country’s solid waste is still disposed of in landfills.

However, due to the increasing amount of waste generated and the limited availability of land for new landfills, the Indian government is encouraging the use of alternative waste management practices such as waste-to-energy, composting, and recycling.

Waste-to-energy involves converting waste into energy through various processes such as incineration or anaerobic digestion. Composting involves the decomposition of organic waste into nutrient-rich soil, which can be used as a fertilizer. Recycling involves processing waste materials into new products.

In recent years, various initiatives and policies have been implemented by the Indian government to promote sustainable waste management practices and reduce the amount of waste generated. For example, the Swachh Bharat Abhiyan (Clean India Mission) launched in 2014 aims to achieve the goal of a clean India by 2022 by promoting sustainable waste management practices and improving sanitation infrastructure.

- **Best disposal method for garbage that is eco-friendly**

The most eco-friendly method of waste disposal is to reduce the amount of waste generated in the first place, followed by reusing, recycling, and composting as

much waste as possible. However, when waste cannot be reduced, reused, recycled, or composted, the following disposal methods are considered to be the most eco-friendly:

- (1) **Waste-to-energy (WTE):** Waste-to-energy involves converting waste into energy through various processes such as incineration, gasification, and pyrolysis. These processes generate heat or electricity from the waste, which can then be used to power homes or businesses. While waste-to-energy has some environmental impacts, such as air emissions, it can reduce the amount of waste sent to landfills and offset the use of fossil fuels.
- (2) **Anaerobic digestion:** Anaerobic digestion is a biological process that breaks down organic waste, such as food and yard waste, into biogas and nutrient-rich soil. The biogas can be used to generate electricity or heat, while the soil can be used as a fertilizer. Anaerobic digestion has a lower environmental impact than incineration and can help to reduce greenhouse gas emissions.
- (3) **Land application:** Land application involves applying treated wastewater and biosolids to land for agricultural purposes. This method can provide a beneficial use for waste products while improving soil quality and reducing the need for chemical fertilizers. However, land application can also have negative environmental impacts, such as contaminating groundwater.

Overall, the most eco-friendly method of waste disposal will depend on the specific waste stream, local regulations, and available infrastructure. It is important to prioritize waste reduction, reuse, recycling, and composting, and to only use disposal methods that have been proven to be safe and effective.

Orders of waste handling methods:

The waste handling methods can be ordered in a hierarchy known as the “waste management hierarchy.” This hierarchy lists the preferred methods for managing waste in order of priority, from the most to least environmentally friendly options. The waste management hierarchy typically includes the following methods, listed in the order of preference:

1. **Source Reduction and Waste Prevention:** This involves reducing the amount of waste generated in the first place by changing consumer behavior, redesigning products, and reducing packaging.
2. **Reuse:** This involves using materials and products multiple times before they are discarded, such as by repairing, refurbishing, or repurposing them.
3. **Recycling and Composting:** This involves processing waste materials to recover valuable resources, such as paper, plastic, and metals, or to turn organic waste into compost.
4. **Recovery of Energy:** This involves recovering energy from waste through processes such as incineration, gasification, and anaerobic digestion.
5. **Treatment:** This involves treating waste to reduce its volume and make it less hazardous before disposal.

6. Landfilling: This involves burying waste in a landfill, which is typically the least environmentally friendly waste management option.

The waste management hierarchy is a useful tool for guiding waste management decisions and promoting environmentally sustainable waste management practices. By following this hierarchy, we can prioritize the most sustainable waste management practices and reduce the amount of waste that ends up in landfills.

2 Literature Review

1. Manually operated sweeper

Michaels [11] invented the manual sweeping machine. This machine is an entirely manually operated and semi-automatic machine. This machine has a rotary brush, hopper, and large trash container. The sweeping mechanism is connected to a bicycle, and the operator needs to push the pedal of the bicycle to run this machine. As the operator moves the bicycle by pushing the sweeping pedal mechanism also moves in the same direction. As the machine moves, wheels are rotated, and a rotary brush is connected with the wheels from gears. As the wheels rotate, the rotary brush rotates anticlockwise direction and pushes entrapped garbage to the hopper, and the hopper conveys that garbage to a large collecting tank [11]. A schematic drawing of the machine shows in Fig. 1.

Limitations:

- (1) This machine cannot pick the big type of garbage like water bottles, cans, cardboard, papers, etc.
- (2) Hard to maneuver, handling this machine a very complicated task.
- (3) Turning off this machine is very hard.

Fig. 1 Manual sweeper machine (Abraham Michaels, US3947912A) [11]

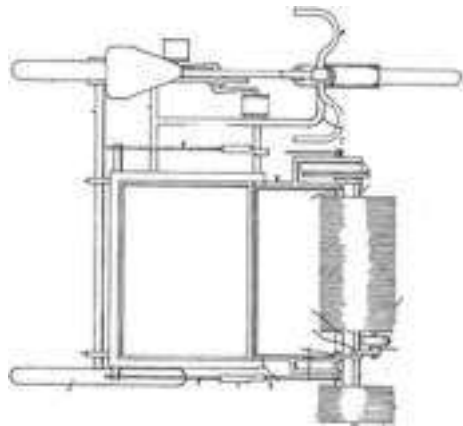
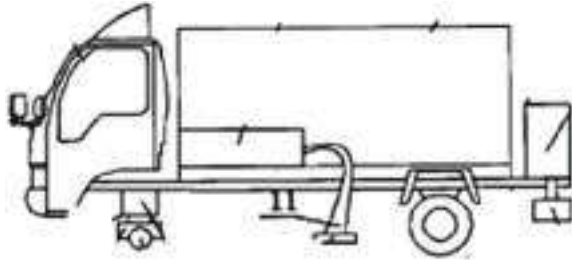


Fig. 2 Road refuse sweeping vehicle (项侠风(Xiang Xiaofeng), CN203514238U) [12]



- (4) Apart from garbage picking, many challenges to face the operator while moving in actual work conditions because maneuver is a very complicated task.

2. Road refuse sweeping vehicle

A 项侠风”(Xiang Xiaofeng) invented the automobile that sweeps up road debris as seen in the utility model. The road refuses sweeping vehicle is made up of a chassis, a vehicle head, and a refuse tank, both of which are mounted to the chassis. On the front part of the chassis, there is a removal mechanism. In the middle of the chassis is a dust collection system. On the back of the chassis, there is a water spraying system. The removal device may successfully remove refuse that has stuck to the road. The dust collection device is capable of effectively sucking up road debris and dust, the debris can be sucked and collected in the collecting chamber. The water spraying mechanism efficiently maintains a clean surface on which dust has been vacuumed up. Additionally, the water spraying system may stop dust from scattering. The vehicle used for road waste sweeping keeps city streets tidy and appropriate for use and popularization [12]. A schematic drawing of the machine is shown in Fig. 2.

Limitations:

- (1) Main disadvantage of this machine is that the operating cost of this machine is high.
- (2) It is too big and it can cause traffic issues.
- (3) Not compatible to work on narrow roads.
- (4) Much power is required to move the entire sweeping mechanism.

3. A kind of road that dust is dust removal integrated cleaning trolley

A 郑佳 (Zheng Jia) [13] invented a kind of road that dust is a dust removal integrated cleaning trolley. The invention describes a type of roadway where the removal of dust is integrated with cleaning the trolley, including the locomotive and the placement of the disposal box inside the locomotive. Both a trash can and a water tank, moving pulleys are fitted in the locomotive’s lower part. Pushing hands hold the locomotive’s right end in place. The water tank, garbage collection box, and disposal box are gradually positioned from left to right inside the locomotive. The equipment collects trash that can be cleaned up. It is simple to use and increases the effectiveness of road cleaning, garbage is delivered to the device’s garbage collection box using a

rubbish conveyer belt. The leftover trash is gathered in a secondary garbage collection container. The disposal box gathers microscopic dust, water can be sprayed from a tank after cleaning with the water sprayer hole on the watering plate to the ground. The phenomenon that prevents dust from flying upward and is pollution-free. This machine improves the effectiveness of cleaning the road and is suitable for more smooth road surfaces. It replaces the manual sweeping of roads [13]. A schematic drawing of the machine is shown in Fig. 3.

Limitations:

- (1) Main disadvantage of this machine is that the operating cost of this machine is high.
- (2) Machine cost is high as it is constructed on locomotives.
- (3) Much power is required to move the entire sweeping mechanism.

4. Sweeping machine tractor attachment for sports grounds

This mechanism was invented by Derek Burt Hargreaves Adlington, near Macclesfield; Eric Stanforth, Macclesfield; Edward Hobbs, Poynton, all of England [14]. The frame of the sweeper attachment can be connected to a tractor's hydraulic lifting equipment. A cable is provided to tip the open-fronted collector within the frame, which is pivotally mounted. The collector swings back into position to receive litter due to gravity and is secured there by a releasable lock. The litter is swept into the collector by a rotating brush in front of it. The sweeper attachment is supported by relatively big wheels near the brush, and the attachment's back is supported by smaller casters. Adjustable ground wheels' height about the frame.

Sweepings collector tilt is ably mounted as a unit on the frame rearward of the sweeping mechanism and is movable relative to the frame between a normal or receiving position and a tilted position for discharging collected sweepings forwardly in the ground-engaging means; sweepings mechanism supported by the frame and provided with driving means; A sweeping apparatus for mounting on a tractor is also

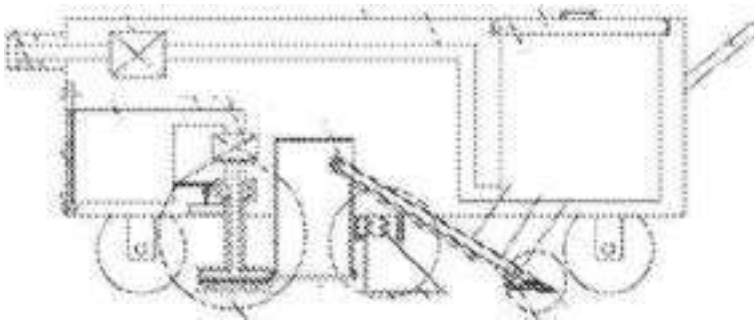


Fig. 3 A kind of road that dust is dust removal integrated cleaning trolley (郑佳 (Zheng Jia) CN108755529A) [13]

included in the invention. This apparatus has a frame with a front part and a rear part, a sweeping mechanism including a brush mounted on the front part and rotatable about an axis of rotation, ground wheels on the front part for providing support from the ground to the part adjacent to the brush, the coupling means for connecting the front part to the tractor, and ground wheels. Engagement mechanisms on the frames are in the back portion.

The rear half of the frame can move up and down in proportion to the front half as the sweeping machine is pushed across the uneven ground without appreciably affecting the height of the brush's axis of rotation above the ground [14]. A schematic drawing of the machine is shown in Fig. 4.

Limitations:

1. This machine is only used for dust sweeping.
2. Unable to pick up big types of garbage.
3. This machine can be operated by a toying tractor.
4. Large amount of power is required to operate this machine.
5. Not able to work on narrow areas.
6. Dust coming out while sweeping.

5. Litter pickup vehicle

Flemming [15] presented a garbage-picking mechanism that could be put on a moving vehicle. When the vehicle moves quickly, the waste becomes more and more entangled surface. There is an articulated arm in the mechanism. The arm has a waste pickup head at the end of it. The arm also has conveyor equipment to carry the picked-up litter that is installed on and made to fit the arm. The litter pickup head is made to move along the surface it is supporting while picking up any litter that comes into touch with it. The operator may search for and collect litter that is within arm's reach by fully controlling the head's position and operation from inside the vehicle's cab. The operation machine is represented schematically in Fig. 5.

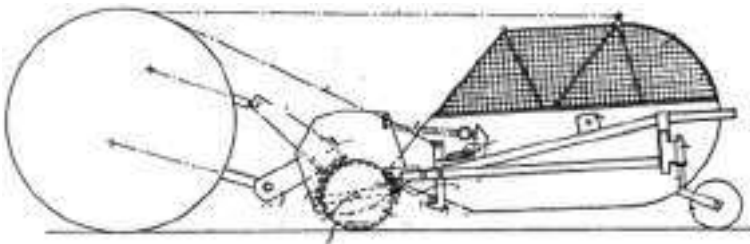
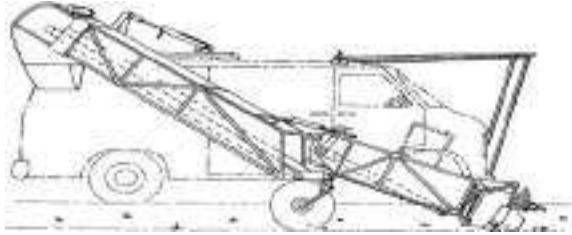


Fig. 4 Sweeping machine tractor attachment for sports grounds (Derek Burt Hargreaves Adlington, near Macclesfield; Eric Stanforth, Macclesfield; Edward Hobbs, Poynton, all of, England, US3594844) [14]

Fig. 5 Litter pickup machine (Jerry A. Flemming from Northeast Bellevue on 09 April 1975) [15]



Limitations:

The mechanism's limited waste pickup function is the litter pickup head. Because of this, very little trash was trapped. Litter within arm's reach may be sought out and collected by the operator. The load must be picked up using a vehicle and an arm. The machine has a smaller mechanical power advantage since moving requires more energy. Because a separate motor was needed to power the entire garbage picking system, it was pricey.

6. Bottle and can picker including rotatable flexible loops

Marsh and Johnson [16] showed off the next invention. Its structure is explained. The flexible loops come into sweeping contact with the ground as the carrier frame is moved over the surface, and the rotatable element is spun, dislodging the litter and pushing it upward and rearward into the waste container.

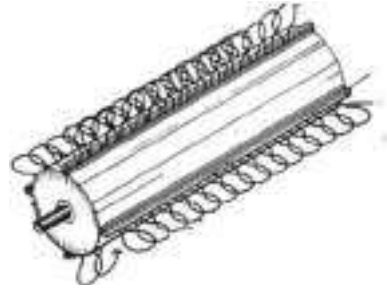
Working and Description:

A portable carrier frame, a rotatable member installed on the carrier frame, and several flexible loops attached to the rotatable member and extending radially are all components of a bottle and can picking equipment. There is a drive motor therefrom for collecting up the bottles, cans, and other garbage, and the rotatable member and a garbage container for collecting and holding the trash the loops have collected. The device consists of many circuits made of flexible materials such as padded vinyl or plastic and thin metal. These rings have two links and can be adjusted in length by loosening the screws, changing the size of the ring, and tightening the screws. These rings are designed to support the effect of collecting bottles and other garbage. The job of the loop is relative to the soil and ground to remove debris. Bottle and Can Picker is shown in Fig. 6.

Limitations of the Machine:

The machine employs several sets of flexible loops that are adjustable, but the loops are actually at a 90-degree angle from one location to the next. This means that the machine was designed to pick up larger objects, such as bottles and small cans; it is unable to pick up smaller items or waste other than bottle-sized waste. When a drum with attached flexible loops rotates, a power source motor is utilized. It operates with

Fig. 6 A plurality of sets of flexible loops [16]



an electric motor, increasing the cost of maintenance, and it only collects large types of trash.

7. Manually operated path cleaner machine

A manually operated path-cleaning machine is the subject of study by Ramesh et al. [17]. This device has wheels with a cylindrical nylon brush 120 mm in diameter outside. 12 mm for the inner diameter, aluminum pulleys 52 mm is the size of the big pulley. The small pulley diameter is 26 mm, and the length of the V belt's center distance is 330 mm. V belt angle = 40, the inner diameter of a ball bearing is 12 mm. 32 mm for the outside diameter [17].

Working Description: A 26 mm-diameter aluminum tiny pulley is attached to a nylon cylindrical brush. The back wheel, which has an outside diameter of 120 mm, is attached to a 52 mm big pulley via a V-belt. The back wheel revolves with a larger-diameter aluminum pulley when the operator pushes the machine. Smaller pulley turns the nylon brush anticlockwise as the bigger pulley rotates in the other way. Anytime a nylon brush in a container is used to sweep up dust, the container has an inclined slope on the front side that collects the dust and other microscopic particles [17]. The design and fabrication of a manually powered path cleaner using pulley drives is shown in Fig. 7.

Fig. 7 Bottle and Can Picker Marsh. A. Johnson, New York on 16 February 1993 [16]

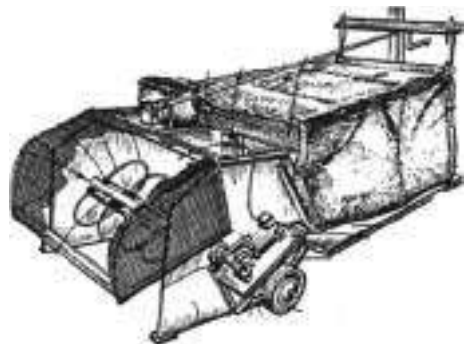


Fig. 8 Design and fabrication of manually powered path cleaner using pulley drives” international journal of engineering and advanced technology (IJEAT) Volume-9 Issue-1, October 2019 [16]



Limitations:

1. Only dust and small particles can be picked from this machine.
2. If any big type of garbage comes the machine will get stuck.
3. Less working area, the operator needs to run for longer time.
4. High energy is required for deep cleaning.
5. Less Storage Capacity.

3 Conclusion

Numerous methods for sweeping and gathering trash have been discussed and explained in this study. It also covered manual, electric, and gasoline-powered mechanisms. The future of sweeping has a very broad market to grab; all that remains is to remove the challenges and make garbage picking easier for operators to use and more cost-effective. The main consideration while constructing a machine is ergonomics. Whether or whether the operator uses it has a significant impact. By looking at all the patents that are mentioned in this paper, we can conclude that every machine has some limits that prevent us from using them, thus we create machines that transcend those limitations.

References

1. Aman khan, Anurag Pannase, Amol Sharnagat, Gaurav Gohane (2017) Study of multipurpose road cleaning machine. Int Res J Eng Technol 04(02)
2. www.iitmandi.ac.in
3. Chakraborty A, Bansal A (2013) Design of dust collector for rear wheel of four-wheeler. Int J Emerg Technol Adv Eng 3(7)

4. www.osha.europa.eu
5. Brijesh K, Karthik, Adarsh, Githin, Kevin Xavier (2019) Design and fabrication of waste collecting machine. *Int Res J Eng Technol* 06(05)
6. Amaljith, Kannan, Vaisakh, Vaishnav, Balakrishnan (2020) Automatic trash collector robot. *Int J Sci Res Publ* 10(4). 40 ISSN 2250–3153
7. National Center for Biotechnology Information. www.ncbi.nlm.nih.gov
8. www.worldsweepers.com
9. Ranjit Kumar M, Kapilan N (2015) Design and analysis of manually operated floor cleaning machine. *Int J Eng Res Technol* 4(04)
10. Adedeji KA, Adebesein E, Adekunle A (2020) Design and construction of a street sweeping machine. *Int J Eng Appl Sci Technol* 5(2). 2455–2143
11. Michaels A Manually operated sweeper. US Patent US3947912A. from 638 spruce st, philapedia, pa9106
12. Xiaofeng X Road refuse sweeping vehical. Worldwide Patent CN203514238U, “项侠风”
13. Jia Z A kind of road that dust is dust removal integrated cleaning trolley. Worldwide Patent CN108755529A. 郑佳
14. Hargreaves DB Adlington, near Macclesfield, Eric Stanforth M, Edward Hobbs P, all of, England Sweeping machine tractor attachment for sports grounds. US Patent US3594844
15. Jerry A Flemming from northeast Bellevue, Litter pickup machine. US Patent, 09 April 1975
16. Johnson MA 16550 County Lind Rd., Newark, Ill. 60541, Bottle and can picker including rotatable flexble loops. US Patent
17. Ramesh P, Balaji DS, Gnanasekaran V, Gopi P (2019) Design and fabrication of manually powered path cleaner using pulley drives. *Int J Eng Adv Technol (IJEAT)* 9(1)

Chapter 9

Study of Leakage Currents in FinFET SRAM Cells



David Gavini, E. Pallavi, B. Kiran Kumar, and Pavankumar Bikki

Abstract Static Random Access Memory (SRAM) is an essential component in modern electronic devices, and its performance parameters need to be continually improved to keep up with advances in technology. However, the memory design with traditional CMOS has many issues in terms of density and leakage current. In this paper, we analyze a FinFET-based SRAM architecture that addresses leakage current problems. The various designs were simulated through the Cadence Virtuoso. The simulation results show that the FinFET design achieves a reduction in leakage current. FinFETs have a better gate control over the channel, which reduces threshold voltage variability, enabling better scalability. The design features a leakage controlling sleep transistor that significantly reduces leakage power. Moreover, FinFET designs has reduced subthreshold leakage, which results in lower standby power consumption. This is important for scaling because it enables the use of smaller devices, which are essential for integration the integraon density of SRAM arrays.

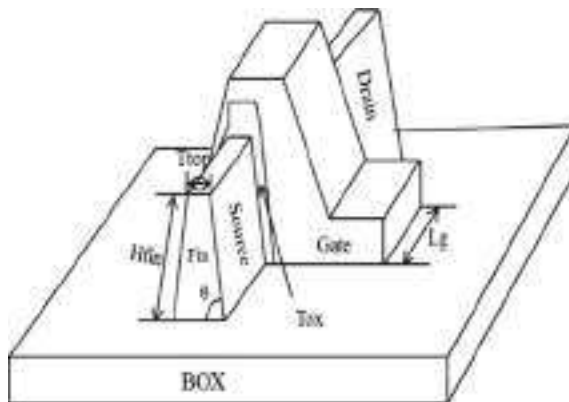
Keywords Complementary metal–oxide–semiconductor · Fin-shaped field-effect transistor · Leakage current · Power dissipation · Static random-access memory

1 Introduction

Static Random Access Memory (SRAM) is an important component in many electronic devices, including microprocessors, cache memories, and wireless communication devices. However, as technology continues to evolve, SRAM faces challenges such as power consumption, leakage current, and speed limitations. The FinFET (Fin-shaped Field-Effect Transistor) is a promising alternative to traditional MOSFETs (Metal–Oxide–Semiconductor Field-Effect Transistors) for SRAM designs due to its superior electrostatic control and reduced short-channel effects. Therefore, there

D. Gavini (✉) · E. Pallavi · B. Kiran Kumar · P. Bikki
Department of ECE, B V Raju Institute of Technology, Narsapur, India
e-mail: 19211a0448@bvrit.ac.in

Fig. 1 Basic FinFET transistor



is a need to explore new designs and techniques for improving the performance of FinFET-based SRAM. Figure 1 shows the basic structure of FinFET [1].

The FinFET transistor has a fin-like structure that improves electrostatic control and reduces short-channel effects. FinFET SRAM offers several advantages over traditional SRAM, such as reduced power consumption, improved performance, and higher stability. However, FinFET SRAM also faces challenges, such as leakage current, which can significantly affect its performance [2].

As we previously indicated, the preceding graphic makes it very evident that FinFETs have a “fin”-like structure. Thus, L_g is the physical height of the silicon fin, and H_{fin} . Gate length of the FinFET, where T_{top} is the silicon fin’s thickness. In single-gate devices, the short-channel effect kicks in after the channel length reaches a certain point. If the channel length is then reduced after that, the device’s performance starts to suffer because of the short channel effect. This is the single-gate device’s primary flaw. Initially, double-gate FinFETs were introduced to successfully lessen the short channel effect and overcome it; however, they required two power supplies for each gate. Then, short-gate FinFETs were developed, which significantly reduced the short-channel effect only needed a single power source [3].

The main objectives of this paper are to propose a FinFET-based design that addresses leakage current issues and improves read and write functions, and to investigate the effectiveness of this design through simulation. Specifically, we propose a leakage-controlling sleep transistor inserted over a pull-up and pull-down network to significantly reduce leakage power. We also explore various techniques for improving reading and writing efficiency. The contributions of this paper are twofold; First, we present a novel FinFET-based SRAM design that addresses leakage current issues and improves performance. Second, we provide insights into the effectiveness of various performance optimization techniques for FinFET SRAM through simulation analysis [4, 5].

2 Literature Review

Several studies have explored the use of FinFET transistors in SRAM design. Monica et al. proposed a FinFET-based 8 T SRAM cell that showed improved read stability and reduced write voltage compared to traditional 6 T SRAM [6]. Gao et al. presented a FinFET-based SRAM design that demonstrated lower power consumption and improved stability compared to bulk-SI technology [7]. N Kuar et al. proposed a FinFET-based 10 T SRAM design that showed improved read and write performance and reduced leakage compared to traditional 6 T SRAM [8].

Leakage current is a major challenge in FinFET SRAM design. Several studies have analyzed the sources and impacts of leakage current in FinFET SRAM. For example, Kim et al. investigated the impact of gate-induced drain leakage (GIDL) on FinFET SRAM performance and proposed a method to mitigate this effect [9]. Yang et al. studied the impact of subthreshold current on FinFET SRAM performance and proposed a FinFET-based SRAM design that minimized subthreshold current [10].

Various techniques have been proposed to improve the performance of FinFET SRAM. One common approach is to insert a sleep transistor over the pull-up and pull-down networks to reduce leakage, which improves write stability and reduces write voltage. A sense-amplifier-based read-assist technique that improves read speed and reduces read power. Other techniques, such as adaptive body biasing and supply voltage scaling, have also been explored for FinFET SRAM performance improvement [11, 12].

An extra transistor is included in the 7 T SRAM cell for write operation than the standard 6 T cell, giving it a higher level of stability in noisy conditions. The extra transistor increases the SRAM cell's dependability and helps to prevent data loss. In Fig. 2, a 7 T SRAM cell with a FinFET is displayed [13].

The 9 T FinFET SRAM cells in Fig. 3 can aid in increasing stability and lowering power consumption. The reduced leakage current and better control over the flow of current offered by FinFETs can help to ensure that data is retained even in the presence of noise and other environmental factors. The additional pass gate transistor can also help to reduce power consumption by allowing for more efficient read and write operations. Overall, FinFET-based 9 T SRAM cells can be used for high-performance and low-power memory designs [14].

From Fig. 4, the FinFETs in 10 T SRAM cells provide several structural advantages that can lead to improved performance, lower power consumption, and smaller chip sizes, making it an attractive option for a wide range of applications [8].

A 12 T SRAM cell is shown in Fig. 5; there are three access transistors and nine storage transistors arranged in a cross-coupled configuration. The three access transistors are used to read and write data to the cell, while the nine storage transistors are used to store the data. The use of FinFETs in 12 T SRAM cells allows for better performance, lower power consumption, and smaller chip sizes. This makes FinFET-based 12 T SRAM cells ideal for use in a wide range of applications, including high-performance computing, mobile devices, and the Internet of Things (IoT) [15].

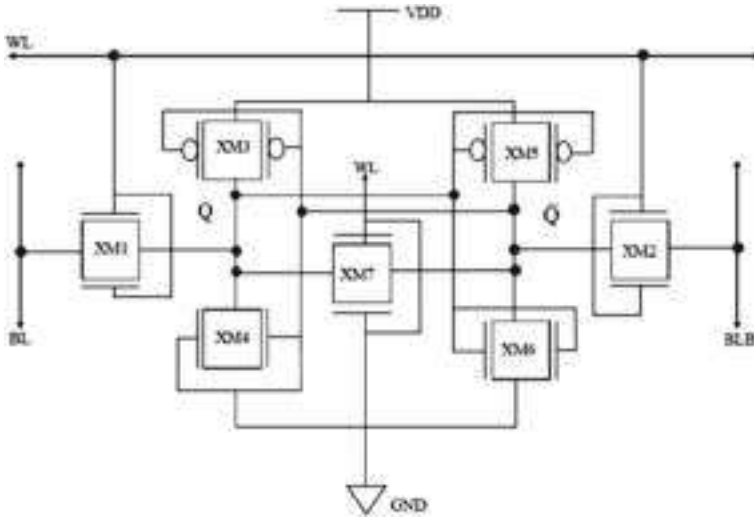


Fig. 2 7 T SRAM cell

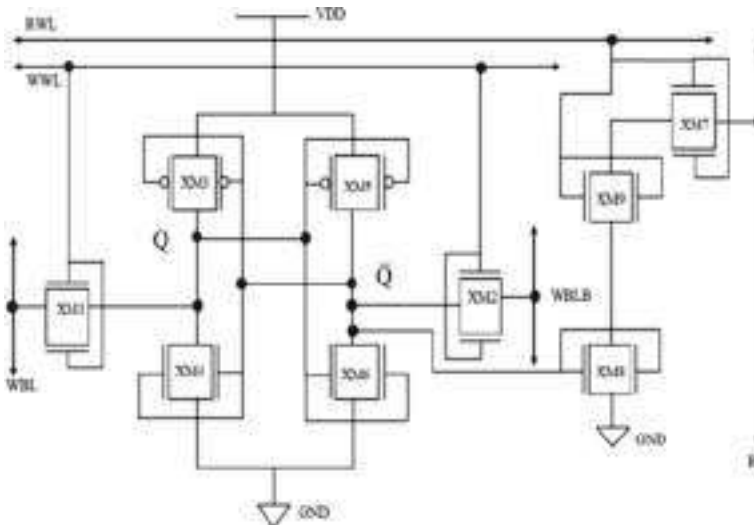


Fig. 3 9 T SRAM cell

In this paper, we build on prior work by proposing a novel FinFET-based SRAM design that addresses leakage current issues and improves read and write functions. We also investigate the effectiveness of various techniques for improving FinFET

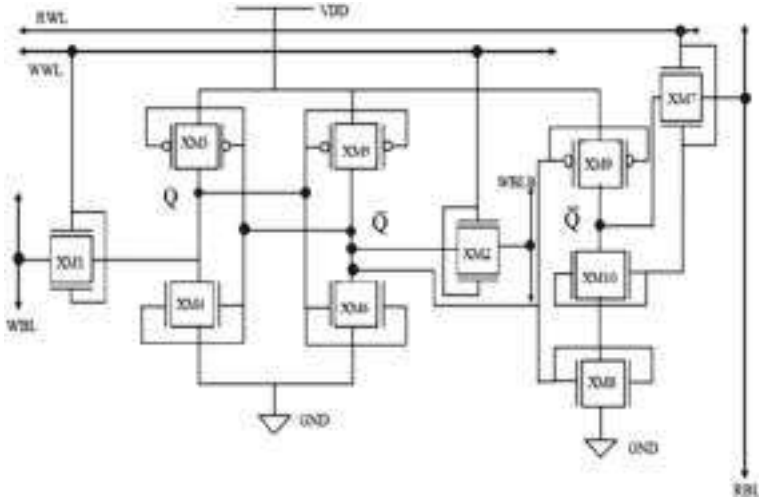


Fig. 4 10 T SRAM cell

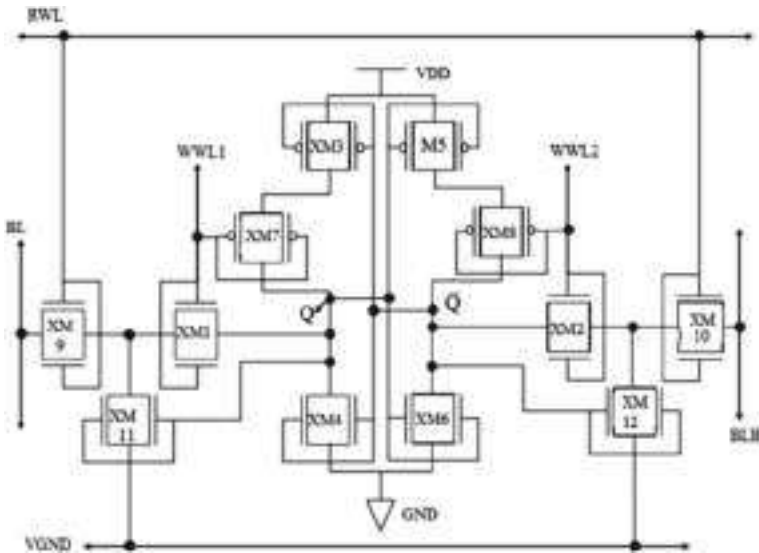


Fig. 5 12 T SRAM cell

SRAM performance, including the use of a leakage-controlling sleep transistor and other read-and-write optimization techniques. Our simulation-based analysis provides new insights into the potential for achieving improved efficiency in FinFET SRAM design.

3 FinEFT SRAM Architecture

The FinFET SRAM architecture is based on an 8 T cell design. The cell consists of four access transistors and four memory transistors, with two of each connected to the bit lines and the other two connected to the complementary bit lines. A leakage-controlling sleep transistor is inserted over the pull-up and pull-down networks to reduce leakage power.

To maintain the data integrity and usefulness of 6 T and 7 T SRAM cells, there are precise limits on the size of transistors. An 8 T SRAM, as shown in Fig. 6, is utilized to maintain read stability. The proportion of pull-down to access transistors describes the stability of 6 T and 7 T SRAM cells. A higher ratio results in improved data stability for 6 T and 7 T SRAM cells [11, 16]. A higher ratio results in improved data stability at the price of greater cell area and increased leakage power. An 8 T-cell solution was utilized to solve the issue of data storage destruction during read operations. With this implementation, the data output elements were read/write bits and word signal lines. The access transistors are designed with a gate length of 25 nm and a gate width of 180 nm, while the memory transistors have a gate length of 40 nm and a gate width of 120 nm. The FinFET SRAM cell is simulated and analyzed for its read and write functions, leakage current, power dissipation, and stability [17, 18]. Memories that need quick access times, little power consumption, and tolerance are implemented using SRAM cells shown in Fig. 7.

The leakage-controlling sleep transistor significantly reduces the leakage power, while the dynamic write assist technique improves write stability and reduces write voltage. Additionally, the FinFET SRAM cell achieves improved read and write functions, as demonstrated by simulation-based analysis. The use of FinFET technology also provides benefits such as improved scalability and reduced power consumption [19].

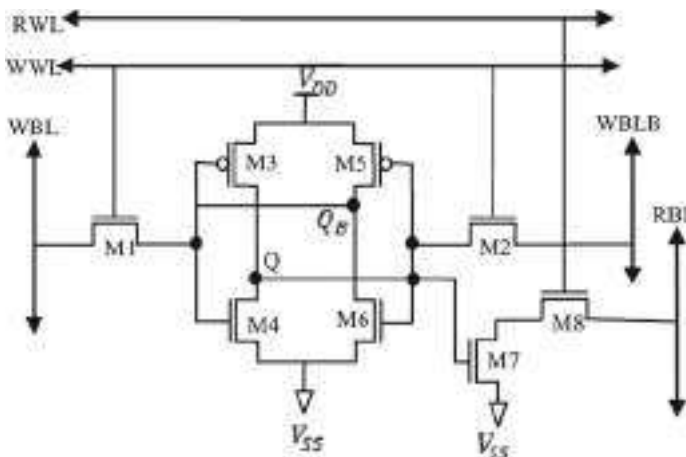


Fig. 6 8 T SRAM cell

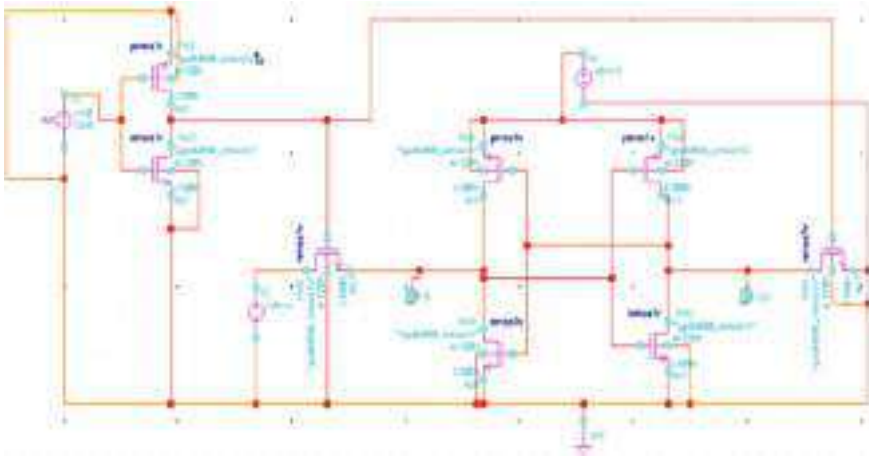


Fig. 7 Implementation of 8 T SRAM

4 Simulation Results Analyses

The simulation results were used to analyze the junction leakage currents, gate leakage currents, and sub-threshold currents of the FinFET SRAM cell. The analysis showed that the proposed design with the sleep transistors over the pull-up and pull-down networks significantly reduced the leakage power. Furthermore, the analysis revealed that the studied design resulted in a sub-threshold current reduction of 80% compared to the previous design. The reduction in sub-threshold current was achieved by optimizing the transistor size and using the sleep transistor.

The leakage current that passes through a transistor when it is operating in the subthreshold zone, when the gate voltage is lower than the threshold voltage, is known as the subthreshold current. Particularly for low-power applications, this current can have a considerable impact on the power consumption of integrated circuits. The subthreshold current is a crucial element in circuit design and optimization since it is greatly influenced by temperature and device characteristics like channel length and doping concentration. To decrease subthreshold current and increase power efficiency, a variety of methods can be used, including transistor stacking and threshold voltage modulation.

SRAM gate leakage current is a serious problem that may affect the memory cell's stability and dependability. Data flipping in an SRAM cell can result from gate leakage current, resulting in mistakes during data storage and retrieval. Low-power SRAM designs, where the operational voltage is decreased to reduce power consumption, worsen this issue by increasing gate leakage current. Designers can use a number of methods to alleviate this problem, including transistor stacking and body-biasing, to lessen the effect of gate leakage current on the SRAM cell. High-k gate dielectrics and metal gate electrodes are examples of sophisticated process

methods and materials that can be used to decrease gate leakage current and enhance SRAM.

Various techniques have been proposed in the literature to improve the read and write efficiency of FinFET SRAM cells. These include voltage scaling, data-dependent write assist, and assist techniques such as column redundancy, block redundancy, and assist write. The write assist technique was implemented by adding an additional write driver circuit that provides extra voltage to the bit line when the data is written as “0”. This technique improves the write efficiency of the SRAM cell. This results in faster write times and lower power consumption. The circuit design of the FinFET SRAM cell is implemented in Cadence Virtuoso using 32 nm FinFET technology at 25 °C and 110 °C with a load capacitance of 1 pF at a frequency of 100 MHz. The simulation results showed that the implementation of the data-dependent write assist technique improved the write efficiency of the proposed FinFET SRAM cell. The leakage current for 7 T SRAM is $5.38e-06$, the leakage current for 8 T SRAM is $1.82e-05$, the leakage current for 9 T SRAM is $1.82e-05$, the leakage current for 10 T SRAM is $1.17e-06$ and the leakage current for 12 T SRAM is $3.48e-06$. The leakage current for the 7 T FinFET SRAM is $13.2e-09$, 8 T FinFET SRAM is $12.82e-09$, 9 T FinFET SRAM is $11.34e-09$, 10 T FinFET SRAM is $10.43e-09$ and 12 T FinFET SRAM is $8.11e-09$. Overall, the FinFET SRAM architecture and circuit design, along with the implementation of the data-dependent write assist technique, result in a low-power SRAM cell with improved performance characteristics. These FinFET designs can serve as a reference for future FinFET SRAM designs. The V–I characteristics of the FinFET 8 T SRAM, 9 T SRAM, and 10 T SRAM designs are shown in Figs. 8 and 9.

The study of FinFET SRAM design was compared to traditional CMOS SRAM designs. The comparison showed that the FinFET design achieved significant improvements in terms of read and write delay and leakage power reduction. For instance, the FinFET SRAM cell achieved a read delay of 0.85 ns, while previous

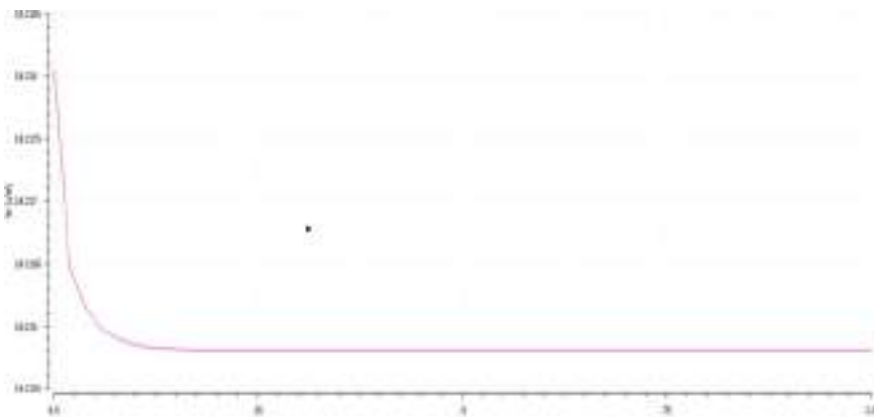


Fig. 8 V–I characteristics of FinFET 8 T SRAM



Fig. 9 V–I characteristics of FinFET 10 T SRAM

Table 1 Comparison of leakage current of various designs

Parameter	7 T	8 T	9 T	10 T	12 T
Supply voltage	1 V	1 V	1 V	1 V	1 V
Leakage power using CMOS	5.38E-06	1.82E-05	1.82E-05	1.17E-06	3.48E-06
Leakage power using FinFET	13.2E-09	12.82E-09	11.34E-09	10.43E-09	8.11E-09

designs achieved read delays in the range of 1.0–1.5 ns. Similarly, the FinFET design achieved a leakage power of 8.11 nW, while CMOS designs had leakage power in the range of 3.48 uW. The simulation results demonstrate the effectiveness of the FinFET SRAM design and the performance optimization techniques employed. The design achieves improved performance in terms of read and write delay and reduced leakage power, making it a promising candidate for low-power SRAM applications. A comparison of leakage current of various designs is shown in Table 1.

5 Conclusions

In this paper, we studied various FinFET SRAM architecture that incorporates several techniques for reducing leakage currents. Through simulations using Cadence Virtuoso, we were able to analyze and optimize the power dissipation, leakage current, and performance of the proposed design. Our analysis showed that the FinFET designs significantly reduced the leakage current compared to CMOS designs, while also improving read and write efficiency. Specifically, FinFET 12 T SRAM design achieves a 199% reduction in leakage current compared to the 12 T SRAM CMOS design. Hence, there is room for further exploration of techniques

for reducing leakage currents in FinFET SRAM, such as the use of sleep transistors and dynamic voltage scaling. Second, there is potential for exploring novel FinFET SRAM architectures that incorporate emerging technologies, such as resistive random-access memory (RRAM) and spin-transfer torque magnetic random-access memory (STT-MRAM). Finally, there is a need for further investigation into the tradeoffs between power dissipation, leakage current, and read and write efficiency in FinFET SRAM, as well as the impact of scaling on these parameters. Finally, this paper presents a promising design for FinFET SRAM that achieves significant improvements in performance and leakage current reduction. Future work in this area can build on this design and explore new techniques and architectures to continue pushing the boundaries of FinFET SRAM performance and efficiency.

References

1. Park J, Lee S, Jeong H (2023) Voltage boosted fail detecting circuit for selective write assist and cell current boosting for high-density low-power SRAM. *IEEE Trans Circuits Syst I Regul Pap* 70(2):797–805
2. Turi MA, Delgado-Frias JG (2020) Effective low leakage 6T and 8T FinFET SRAMs: using cells with reverse-biased FinFETs, near-threshold operation, and power gating. *IEEE Trans Circ Syst II Express Briefs* 67(4):765–769
3. Bikki P, Annapurna M, Vujwala S (2019) Analysis of low power SRAM design with leakage control techniques. In: 2019 TEQIP III sponsored international conference on microwave integrated circuits, photonics and wireless networks (IMICPW). IEEE
4. Raj B, Saxena AK, Dasgupta S (2011) Nanoscale FinFET based SRAM cell design: analysis of performance metric, process variation, underlapped FinFET, and temperature effect. *IEEE Circuits Syst Mag* 11(3):38–50
5. Bikki P, Annapurna M (2019) Analysis of low power novel SRAM design with self-biasing approach for ultra-low power applications. In: 2019 TEQIP III sponsored international conference on microwave integrated circuits, photonics and wireless networks (IMICPW). IEEE
6. Monica M, Chandramohan P (2016) Characterization of 8T SRAM cells using 16 nm FinFET technology. In: 2016 international conference on signal processing and communication (ICSC). IEEE
7. Gao R, Wang H, Xie Y (2015) Optimization and analysis of a FinFET-based 8T SRAM cell for low power applications. In: 2015 IEEE international conference on electron devices and solid-state circuits (EDSSC). Chengdu, pp. 1–2
8. Kaur N, Gupta N, Pahuja H, Singh B, Panday S (2016) Low power FinFET based 10T SRAM cell. In: 2016 Second international innovative applications of computational intelligence on power, energy and controls with their impact on humanity (CIPECH). Ghaziabad, India, pp. 227–233
9. Kim Y et al (2019) A 12T SRAM with improved read and write margins for low-power applications. *IEEE Trans Circuits Syst II Express Briefs* 66(6):1067–1071
10. Lakshmi TV, Kamaraju M (2021) A review on SRAM memory design using FinFET technology. *Int J Syst Dyn Appl (IJSDA)* 11.6:1–21
11. Li H, Zhao Y, Li X (2014) A low-power and high-speed 8T SRAM cell for FinFET technology. In: 2014 IEEE international conference on electron devices and solid-state circuits (EDSSC). Hong Kong, pp. 1–2
12. Alioto M (2015) Ultra-low voltage, ultra-low power FinFET SRAM design. In: Proceedings of IEEE International Symposium on Circuits and Systems (ISCAS), pp. 1557–1560

13. Sneha G, Krishna BH, Kumar CA (2017) Design of 7T FinFET based SRAM cell design for nanometer regime. In: 2017 International conference on inventive systems and control (ICISC). Coimbatore, India, pp. 1–4
14. Yang Y, Park J, Song SC, Wang J, Yeap G, Jung S-O (2015) SingleEnded 9T SRAM cell for near-threshold voltage operation with enhanced read performance in 22-nm FinFET technology. *IEEE Trans Very Large Scale Int (VLSI) Syst* 23(11):2748–2752.
15. Karamimanesh M et al (2021) A robust and write bit-line free sub-threshold 12T-SRAM for ultra low power applications in 14 nm FinFET technology. *Microelectron J* 118: 105185
16. Kumar TS, Tripathi SL (2022) Comprehensive analysis of 7T SRAM cell architectures with 18nm FinFET for low power bio-medical applications. *Silicon* 14.10:5213–5224
17. Yang JP, Song SC, Wang J, Yeap G, Jung S-O (2015) Single ended 9T SRAM cell for near-threshold voltage operation with enhanced read performance in 22-nm FinFET technology. *IEEE Trans Very Large Scale Int (VLSI) Syst* 23(11):2748–2752
18. Pal S, Bhattacharya A, Islam A (2014) Comparative study of CMOS-and FinFET-based 10T SRAM cell in subthreshold regime. In: 2014 IEEE international conference on advanced communications, control and computing technologies. IEEE
19. Raushan RK et al (2021) Implementation of 12T and 14T SRAM bit cell using FinFET with optimized parameters. *Trans Electr Electron Mater* 22:328–334

Chapter 10

Advanced Characterization of Estolides from Coconut, Sunflower and Karanja Oils



P. V. Maneesh Kumar and T. Jagadeesha

Abstract Cold flow properties of vegetable oils are generally subpar to industrial lubricants. This is one major drawback that limits the usage of otherwise abundant vegetable oil. Estolides belong to the class of esters synthesis from naturally occurring oils as carboxylic acid functionality of a fatty acid reacts, forming ester linkage on an unsaturated site of another fatty acid. Estolide number tells the mean number of fatty acids attached to the base fatty acid that varies with respect to synthesis temperature, reacting saturated fatty acids, and other parameters. Though vegetable oils show excellent biodegradability, their cold flow properties are poor compared to functional lubricants. In this present study, three vegetable oils have been synthesized to obtain their estolides, they are coconut, sunflower, and karanja oils to analyze the variations. Lubricating machines with mineral-based lubricants have become a major cause of pollution now. To use natural oils for making lubricants instead of petroleum is something mainstream researchers have been looking at for a few decades. Though vegetable oils show excellent biodegradability, their cold flow properties are poor compared to functional lubricants. Biodegradable lubricant oils must have excellent cold flow properties as well as competitive costs in order to be accepted widely as a base stock for industrial lubricants.

Keywords Estolides · SPARTAN · Saturated fatty acids · Pour point

1 Introduction

Vegetable oil belongs to the family of fats and lipids. Coconut oil is an abundant natural oil. It is mentioned among the lubricants used in the pre-mineral era. Coconut oils show good lubricating properties in many aspects like good viscosity index, fine lubrication, above average flash point, and lower evaporative losses [1, 2]. A major

P. V. Maneesh Kumar (✉) · T. Jagadeesha
Department of Mechanical Engineering, National Institute of Technology, Kerala, 673 601
Calicut, India
e-mail: maneesh_p210081me@nitc.ac.in

© The Author(s), under exclusive license to Springer Nature Singapore Pte Ltd. 2023
V. Bindhu et al. (eds.), *Proceedings of Sixth International Conference on Inventive Material Science Applications*, Advances in Sustainability Science and Technology,
https://doi.org/10.1007/978-981-99-4189-6_10

demerit of coconut oil is that it exhibits very poor cold-flow properties. It is due to the predominance of saturated fatty acids that are present. The pour point of coconut is 23 °C. Significant reduction in pour point is essential for considering coconut oil as base stock of lubricants in cold climatic and temperate conditions. Sunflower oil is another abundant oil that can be utilized. Sunflower oil is highly unsaturated in nature. Sunflower oil exhibits better cold-flow properties than coconut oil (−17 °C), but it also needs improvement in comparison with commercial lubricants. Karanja oil is also an abundantly available natural oil with a pour point in the range of 4 °C. Karanja oil contains fatty acids of saturation and unsaturation [3]. Synthesizing estolides has proven to be improving the cold flow properties of natural oils [3].

Esterified oligomers are further reacted to 2-ethylhexanol to increase molecular weight, the degree of oligomerization results in a better pour point [4]. The fatty acids attached to the double bonds cause the formation of estolides resulting in better cold flow characters. Generally, plant base oils exhibit pour points in the range of around 10 to 20 °C. Surprisingly, estolides clot at 5 °C to 45 °C that are comparable with commercial lubricants, viscosities are also improved with oligomerization [5]. Estolide number is an indicator of the physical properties of the synthesized estolides. The characteristics can be further improved by capping the estolides with 2-ethyl hexanol for additional improvements [5].

A lubricant's main purpose is to reduce the friction acting between the mating surfaces that causes deformation, deterioration, and stress induction. For this, any material that can act as a protective layer between the surfaces that can also reduce the interlocking of mating surfaces causing stress buildup can be employed. An ideal lubricant should have good viscosity to maintain a strong film, good viscosity index, good flash point to withstand heat in mating surfaces, and low volatility along with other properties. Based on the operating conditions, a lubricant is selected for application, in cold working conditions, only a lubricant with very good pourpoint can be used otherwise, the lubricant will solidify causing all possible problems. A refrigeration lubricant must be thermally stable over a wide range of temperatures and must be chemically inert too. This work is an attempt to produce a good lubricant from coconut oil by eliminating one of its major defects, which is the pour point of around 20 °C that makes it obsolete in cold conditions.

2 Experimental Procedure

2.1 Materials

Coconut, sunflower, karanja, and castor oils were procured locally as they are readily available for cooking purposes. Oleic acid, perchloric acid, 2-ethyl hexanol, KOH, ethanol, and silica gel were obtained from SIGMA ALDRICH Chemical Company, supplied by Alpha Chemicals Ernakulam, Kerala.



Fig. 1 Estolides synthesized from coconut, sunflower, and karanja oils

2.2 Preparation of Estolides

Estolides were synthesized from coconut, sunflower, and karanja oils through condensation reactions that are catalyzed by acids. The synthesis is in a 750 ml 3-necked flask at atmospheric pressure. The reactant mixture for estolide contains 90 g base oil, 10 g of castor oil with 20.3 g of oleic acid. The mixture was heated in a Rota mantle to a temperature of 60 ± 0.1 °C. A magnetic stirrer was used for mixing. When the required temperature was attained, 3 g of perchloric acid (HClO_4) was added drop by drop. Then the reactants were heated for 24 h at atmospheric pressure for obtaining estolides. After 24 h, 56.5 g of 2-ethyl hexyl alcohol was added to the reactant flask and the reactants were further heated for 2 h to get estolide esters. For quenching, 2 g potassium hydroxide (KOH) mixed through ultrasonic stirring for 180 s in 90% ethanol–water mixture was added. The completed reactions were cooled for an additional 30 min. The reactant mixture was transferred to a separating funnel and 100 g hexane was added for extracting the organic layer. The estolide synthesized was then further water-washed with warm water at 60 °C till the pH of washed water obtained equals the pH of normal water. For further water removal, the estolides were kept in an open beaker surrounded by silica gel in a closed vessel for 24 h. Commercially available coconut, sunflower, and karanja oils were used for experiments (as in Fig. 1).

2.3 FTIR Analysis

Fourier-transform infrared spectroscopy helps to understand the infrared spectrum of the emission and absorption of matter. An FTIR spectrometer deals with high-resolution spectral data across a vast range of spectra. This mechanism gives better results than a dispersive spectrometer, which only measures the intensity over a small

spectra of wavelengths at one point of time. We can confirm estolide synthesis if the results from FTIR show peaks at desired points.

2.4 Tribological Study

Tribological studies were conducted on a DUCOM 4 ball tester as per ASTM D 4172-B standards with a load of 392 N, temperature of 75 °C, and speed of 1200 RPM for 3600 s. The obtained friction coefficient values and wear scar diameters are analyzed to evaluate the improvements in estolides synthesized over base oils. The variation of frictional characteristics was analyzed between base fluids and their estolides for comparison.

2.5 Viscosity Analysis

The viscosity of samples was analyzed on a BROOKFIELD viscometer as per ASTM D 2983 standards. The samples were analyzed at constant torque and varying speed rates on rotating a spindle immersed in an oil sample between 50 and 200 RPM in temperature ranging from 40 to 100 °C at 10 °C intervals. The value of kinematic viscosities at 40 and 100 °C are obtained from the viscometer. The viscosity index was identified as per ASTM D2270 to compare with commercial lubricants.

3 Results and Discussion

3.1 FTIR Analysis

FTIR analysis is a spectroscopy in which infrared rays are passed through the sample to evaluate the properties of the sample being tested. Based on the absorption of certain wavelengths by the sample, now we are able to characterize the bonds present in the sample. From the samples tested, the following results were obtained. The peaks at 2922/cm are C–H bonds representing fatty acid structure. The peaks at 1734/cm are representing ester functional groups (2-ethylhexyl ester). The peaks at 1041/cm are indicating C = O bond. From this, we can confirm that the synthesis of estolides is successful. FTIR analysis of Coconut, Sunflower, and Karanja estolides are shown in Figs. 2, 3 and 4. DSC Analysis of estolides of Coconut, Sunflower, and Karanja is shown in Fig. 5.

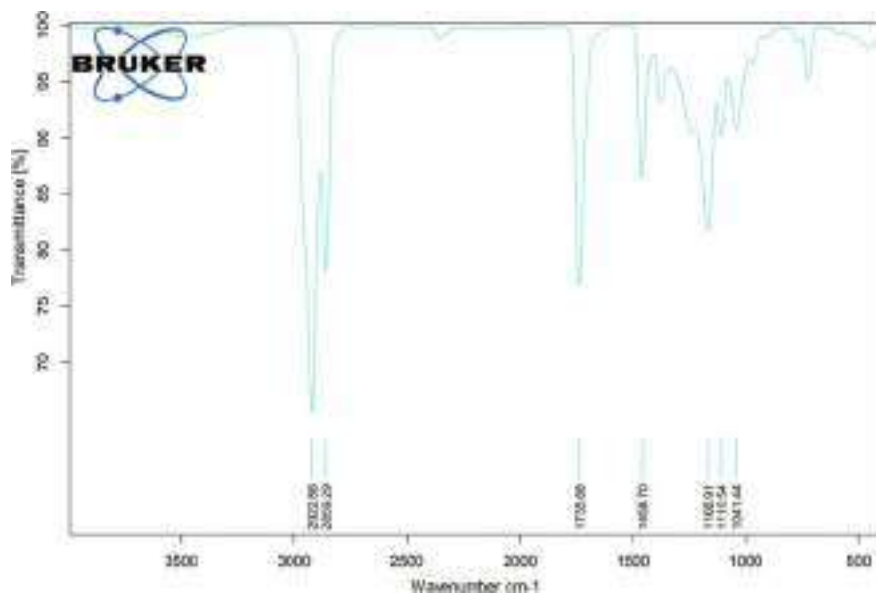


Fig. 2 FTIR of coconut estolide

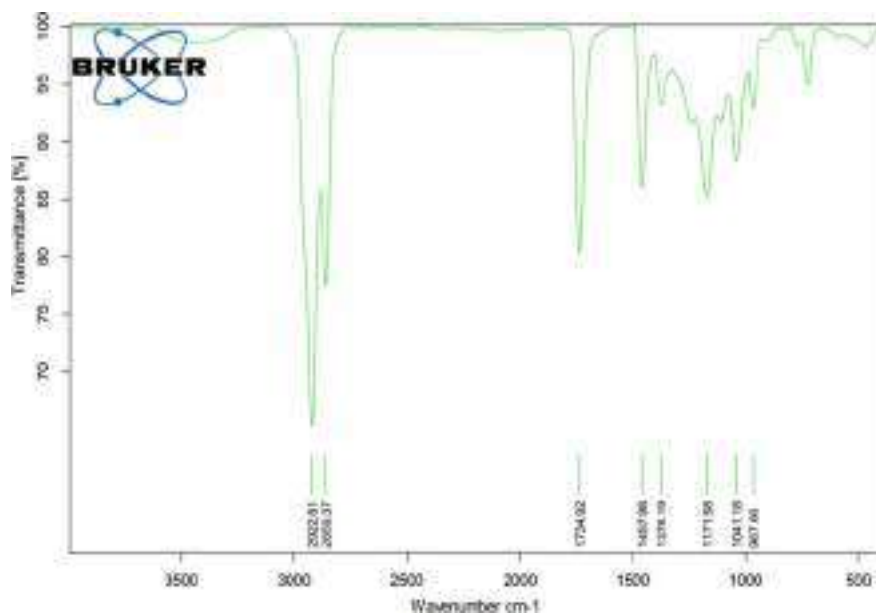


Fig. 3 FTIR of sunflower estolide

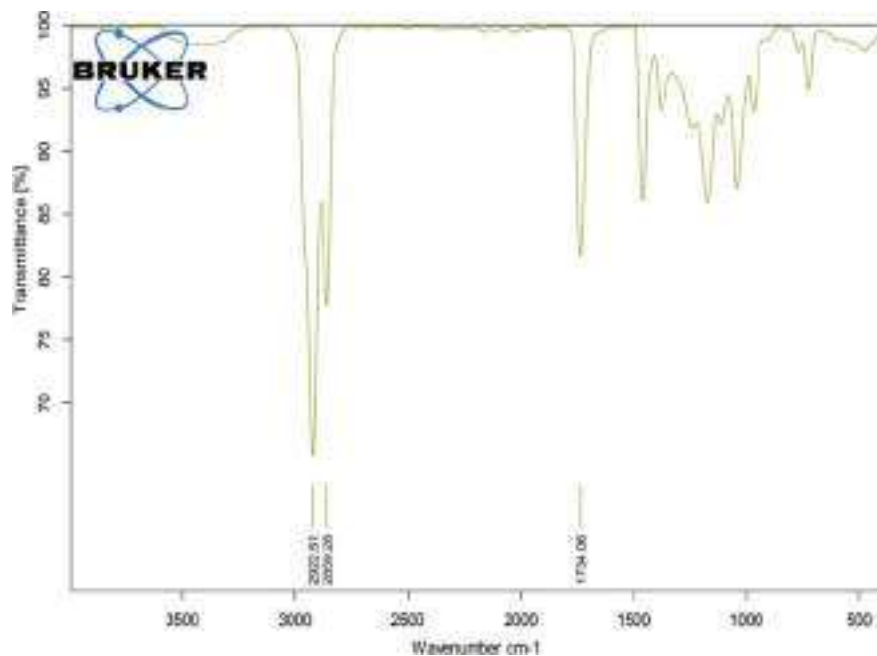


Fig. 4 FTIR of karanja estolide

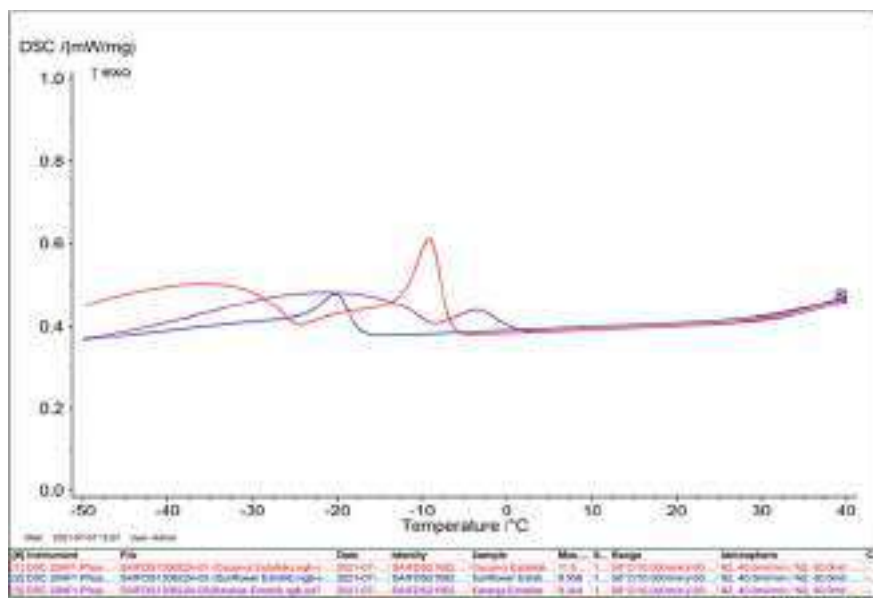


Fig. 5 DSC analysis of estolides of coconut, sunflower, and karanja

3.2 *Pour Point Analysis—DSC*

Pour point is one major aspect of lubricants and is one area where natural oils show poor properties. Pour point is also the major demerit of coconut oil as a lubricant because it will solidify at a temperature as low as 22 °C, which makes it unusable for lubricant applications even though it has many other merits. Though pour point could have been evaluated from the pour point apparatus, for more precise results the samples were sent for DSC. The samples were sent to STIC (Sophisticated Testing and Instrumentation Center, Cochin) for DSC—Differential Scanning Calorimetry testing to determine their crystallization parameters. Cloud points are determined from the college laboratory, pour point values are obtained from DSC. Oligomers with branching have complex structures resulting in lower Pour points [6]. Coconut oil shows a significant decrease in pour point from 22 °C to −3 °C. Sunflower oil's pour point decrease from −18 °C to −21 °C. Karanja oil's pour point decreased from 9 °C to −12 °C as per the ASTM D97 test and according to DSC thermograms, the pour points have been lowered to −9 °C, −20 °C and −3 °C for coconut, sunflower and karanja estolides, respectively. Estolides are known for their improved cold-flow properties, and the results also state the same.

3.3 *Viscosity Analysis*

Viscosity can be considered the major property of lubricating oils as it is the property that reduces the friction acting upon the mating surfaces. Most natural oils have good viscosity characteristics due to the presence of large molecules in them. Here, the variation of viscosity between natural oils and their estolide samples is shown in the graph (Fig. 6). Coconut estolide is showing reduced viscosity compared to pure coconut oil. Sunflower estolide shows improved viscosity at 40 °C but is showing reduced viscosity at 100 °C. Karanja estolide shows reduced viscosity compared to karanja oil. It is to be inferred that estolides show poor Viscometric properties compared to their base oil properties. The viscosity variations of coconut oil are from 25 cP at 40 °C to 8.4 cP when the temperature is 100 °C with a viscosity index of 152. Whereas the estolide shows a viscosity of 11.2 cP when the temperature is 40 °C to 4.07 cP at 100 °C with a VI value of 224. The viscosity variations of sunflower oil are from 35.9 cP when the temperature is 40 °C to 15.566 cP at 100 °C with a VI of 167, whereas the viscosity of estolides is 53.6 cP at 40 °C to 13.96 cP at 100 °C with a VI value of 130. The variations in karanja oil are from 46.5 cP at 40 °C to 14.2 cP at 100 °C with a VI of 101, and the estolides are showing a viscosity of 22.2 cP at 40 °C to 13.96 cP at 100 °C with a VI of 134. Variation of VI of oils, and their estolides compared with SAE20W40 are tabulated in Table 1.

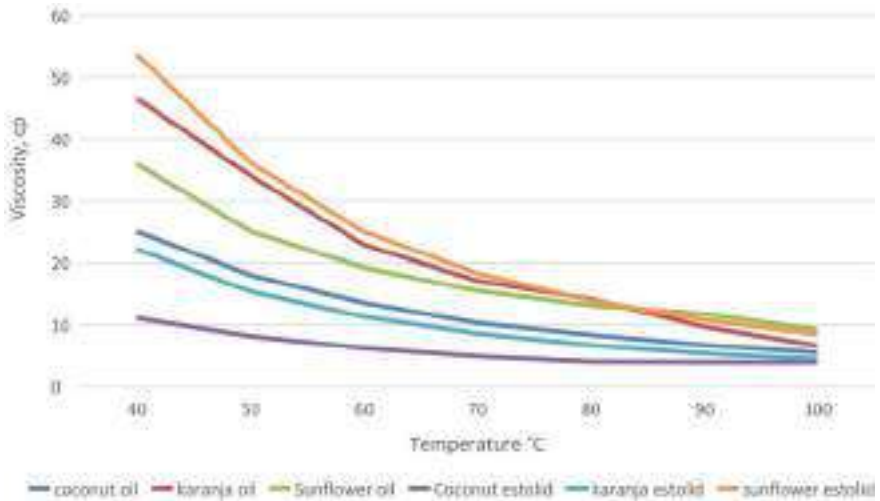


Fig. 6 Viscosity variation of base oils and their estolides

Table 1 Variation of VI of Oils, their estolides compared with SAE20W40

Sl no	Sample	Viscosity index
1	Coconut oil	152
2	Coconut estolide	224
3	Sunflower oil	167
4	Sunflower estolide	130
5	Karanja oil	101
6	Karanja estolide	134
7	SAE 20W40	125

3.4 Coefficient of Friction

Friction characters of the base oils and their estolides were analyzed on a Ducom 4 ball tester to evaluate their coefficient of friction and these balls were used for the examination of the wear scar diameters to evaluate properties and to compare with their base oils (Figs. 7, 8, 9, 10, 11 and 12).

From Table 2, coconut estolide shows a reduction in the coefficient of friction over the base oil. Sunflower estolide shows increased coefficient of friction over its base oil. Karanja estolide shows an increase in the coefficient of friction over its base oil. The wear scar diameter of coconut estolide has increased from 591.48 to 600.78 μm . The wear scar diameter of sunflower estolide has increased from 723 to 745 μm . The scar diameter of karanja oil is reduced from 524 to 544 μm . Coefficients of friction and wear scar diameter show insignificant variations between the base oil and estolide forms.



Fig. 7 Wear scar using coconut oil



Fig. 8 Wear scar using coconut estolide



Fig. 9 Wear scar using sunflower oil



Fig. 10 Wear scar using sunflower estolide



Fig. 11 Wear scar using karanja oil



Fig. 12 Wear scar using karanja estolide

Table 2 Variation of CoF and WSD of oils and their estolides

Sl no	Sample	COF	WSD
1	Coconut oil	0.0779	591.48
2	Coconut estolide	0.0509	600.78
3	Sunflower oil	0.0743	732.85
4	Sunflower estolide	0.0825	745.67
5	Karanja oil	0.0530	524.52
6	Karanja estolide	0.0702	544.8

4 Conclusion

Though estolides have insignificant improvements over their base oils in terms of viscosity and coefficient of friction, their cold-flow properties show significant improvements. Vegetable oils make macro-crystalline figures through ordered arrangements of triacylglycerol, with branching at possible unsaturation sites like oligomerization and alkoxylation can improve the cold flow characters [3]. Pour point, which is a major demerit of vegetable oils, can be improved to a lower value with branching at possible locations on unsaturated sites with chemical modification. As the estolides are formed, the branching at the unsaturated sites leads to a slower uniform stacking of these molecules, slowing down their solidification [6]. The alcohol part from the ester attached also helps in reducing the pour-point. So the synthesized estolides were further converted to 2-ethylhexyl estolide esters by reacting them with 2-ethylhexanol for an additional 2 h for a further lower pour-point. Nature has an abundant source of fatty acids that can satisfy the raw material requirements of most needs [7]. Recent developments in this area are confirming the possibilities of natural industrial oils [8]. Another promising bio-derived lubricants are polyols showcasing good lubrication properties [9]. Adding more molecular weight to component molecules can help improve properties further [10]. Estolide esters can also be converted into biofuel rather than bio-lubricants is another ray of hope [11]. The cold-flow characteristics of thus produced biofuels can also be improved to industrial standards [12]. There are many methods to improvise the cold flow characteristics of the fluids to industrial requirements [13]. Polymers and vegetable oil-based composites are replacing major industrial fluids in most applications [14]. Another advantage of estolides is that all synthesis processes happen at temperatures as low as 60 °C, which means the cost of production of samples is low compared to other processes. Further improvements are to be made to make it a proper industrial-grade lubricant. Blending with other oils, addition of nanomaterial, etc. are some methods to improve the characteristics.

References

1. Isbell TA, Edgcomb MR, Lowery BA (2001) Physical properties of estolides and their ester derivatives. *Ind Crops Prod* 13:11–20
2. Sajeeb A, Rajendrakumar PK (2019) Comparative evaluation of lubricant properties of biodegradable blend of coconut and mustard oil. *J Clean Produc* 240:118255
3. Ajithkumar G (2009) Analysis of the pour point of coconut oil as a lubricant base stock using differential scanning calorimetry. *Lubric Sci* 01
4. Ho CK, McAuley KB, Peppley BA (2019) Biolubricants through renewable hydrocarbons: A perspective for new opportunities. *Renew Sustain Energy Rev*
5. Cermak SC, Isbell TA (2002) Physical properties of saturated estolides and their 2-ethylhexyl esters. *Indust Crops Produc*
6. Greco-Duarte J, Collaço ACA, Costa AMM, Silva LO, Da Silva JAC, Torres AG, Fernandez-Lafuente R, Freire DMG (2019) Understanding the degree of estolide enzymatic polymerization and the effects on its lubricant properties. *Fuel*
7. Ray AK, Stark RE (1998) Isolation and molecular structure of an oligomer produced enzymatically from the cuticle of lime fruit, phytochemistry, vol 48, no 8, pp 1313–1320
8. Perera M, Yan J, Xu L, Yang M, Yan Y (2022) Bioprocess development for biolubricant production using non-edible oils, agro-industrial byproducts and wastes. *J Clean Produc* 357:131956
9. Åkermana CO, Gaber Y, Ghani NA, Lämsä M, Hatti-Kaul R (2011) Clean synthesis of biolubricants for low temperature applications using heterogeneous catalysts. *J Molec Catalys B Enzymatic* 72:263–269
10. Bantchev GB, Cermak SC (2022) Correlating viscosity of 2-ethylhexyl oleic estolide esters to their molecular weight. *Fuel* 309:122190
11. de Haro JC, del Prado Garrido M, Perez A, Carmona M, Rodríguez JF (2018) Full conversion of oleic acid to estolides esters, biodiesel and choline carboxylates in three easy steps. *J Clean Produc* 184:579e585
12. Smith PC, Ngothai Y, Nguyen QD, O'Neill BK (2010) Improving the low-temperature properties of biodiesel: methods and consequences. *Renew Energy* 35:1145–1151
13. Sierra-Cantora JF, Guerrero-Fajardo CA (2017) Methods for improving the cold flow properties of biodiesel with high saturated fatty acids content: a review. *Renew Sustain Energy Rev* 72:774–790
14. Zhang C, Garrison TF, Madbouly SA, Kessler MR (2017) Recent advances in vegetable oil-based polymers and their composites. *Progress Polym Sci* 71:91–143

Chapter 11

Manufacturing of AlSi₁₀Cu₂ Foam Using Centrifugal Casting Route and LiAlH₄ Foaming Agent



Anandarao S. Kashid and Abhijit A. Patil

Abstract Foams are intentionally produced porous lightweight materials useful in structural, mechanical, acoustic, thermal, and domestic applications. Aluminum and its alloy foams are gaining importance due to lower melting temperatures, lower densities, and ease of manufacturing by a variety of techniques, light in weight, good strength-to-weight ratio, good anticorrosive properties, and aesthetic in appearance. Powder metallurgy route of foam manufacturing is used to check the suitability of hydrides like LiAlH₄ as foaming agents. LM2 (AlSi₁₀Cu₂) alloy is cold compacted at 200 MPa for 5 s, and at 6000C hydrogen release is observed for a minimum 5% weight of lithium containing blowing agents. This is an alternative for TiH₂ foaming agent by powder metallurgy route. The foam production can be analyzed by visual observation, microstructure observation and nondestructive testing methods like X-ray diffraction analysis. A new approach of centrifugally cast powder metallurgy precursor method is introduced in this paper which can generate 45 to 60% porosity for batch production requirements at low cost.

Keywords Foaming agents · Foaming process · Metal foam · Powder metallurgy · Centrifugal casting

1 Introduction

Material Science is gaining the attention of all branches of engineering as a tool of development in the product and manufacturing areas. The development of composites, nanomaterials, and on-demand composites are satisfying complex property

A. S. Kashid (✉)

Department of Mechanical Engineering, N K Orchid College of Engineering & Technology, Solapur, Maharashtra, India
e-mail: askashid@gmail.com

A. A. Patil

Department of Mechanical Engineering, S. G. University, Kolhapur, Maharashtra, India
e-mail: abhijit.patil@sanjayghodawatuniversity.ac.in

© The Author(s), under exclusive license to Springer Nature Singapore Pte Ltd. 2023
V. Bindhu et al. (eds.), *Proceedings of Sixth International Conference on Inventive Material Science Applications*, Advances in Sustainability Science and Technology,
https://doi.org/10.1007/978-981-99-4189-6_11

127

requirements of design and production streams. Foams and cellular materials are basically intentionally produced porous materials for lightweight applications of metals, plastics, and ceramic materials family. The porous products are manufactured conventionally by powder metallurgy process with required quality and property combinations. But the cost of manufacturing is high as well as it is suitable for mass-scale production only. Metal foams are an important group of materials having applications in structural, mechanical, acoustic, thermal, and domestic applications. Aluminum and its alloy foams are gaining importance due to lower melting temperatures, lower densities, and ease of manufacturing by a variety of techniques [1]. Aluminum foams are light in weight, good strength-to-weight ratio, good anti-corrosive properties, and are aesthetic in appearance. Open-grain and close-grain aluminum foams are mostly used in automotive, aerospace, building and construction, healthcare, and energy industries [1]. A centrifugally cast powder metallurgy precursor in a stationary furnace is a new approach. It combines centrifugal casting and powder metallurgy precursor methods of foam manufacturing.

The paper is divided into five sections. Section 2 is related to literature review of methods available for foam manufacturing. Section 3 gives details of the experimental procedure and observations. Conclusion of the experiment is given in Sect. 4

2 Literature Review

Currently, there are six methods of use for commercial manufacturing of metal foam.

- **Bubbling gas in molten alloy** [2, 3]: In this method, foams are made by injecting gas bubbles into molten aluminum. It can produce highly porous foam having a large pore size. It is a low-cost method as compared with the power compact and Alporas method.
- **Stirring of foaming agent in molten alloy** [2, 4]: It is also called as ‘Alporas’ method. Metal powders and blowing agents are mixed at 6800C to 7200C and stirred for 6 min to increase viscosity. Due to the decomposition of blowing agent, gas gets released, which causes the foaming process.
- **Consolidation of metal powder with particulate foam powder** [5, 6]: To produce aluminum foam, aluminum powder or alloys of aluminum are mixed with foam agents and compacted. The foaming agent gets uniformly distributed in the foam obtained. The density of metal foam depends on foaming parameters and agents.
- **Vapor phase deposition of metal on polymer foam precursor** [7, 8]: Foaming take place by galvanically depositing polymer in ionic state of metal. Ions of metal and vapors are deposited on polymer and then the polymer is removed to obtain the foam.

- **Sintering of metal powder with a leachable foam powder** [9, 10]: In manufacturing of metal foams using sintering, thermal treatment is used to entrap the gas in the first step, and it is expanded in the second step. It forms uniform porous metal due to creep expansion.
- **Hydrogen gas dissolution in hot liquid metal under pressure** [11–13]. A pore-free melt having completely solved hydrogen is prepared at high pressure and pressure. Now, two-phase region solid and gas is formed by reducing temperature and pressure. The gas gets accumulated in the form of fine bubbles and forms foam if the cooling rate and pressure profile are selected correctly.

From the literature survey, it is observed that there is a scope for combining two of the existing manufacturing processes and to develop a new technique.

3 Experimental Setup

A small, batch production machine is developed for designing and testing for aluminum and its alloys as shown in Fig. 1.

A machine is fabricated, consisting of a rotating vertical mechanism for metallic die of mild steel mounted on a disc. This setup is fitted in an electrical resistance furnace having a maximum temperature of 800 °C having a heating rate of 11.5 °C / min [4]. The die is rotated by the electric motor at 1440 rpm. The total cycle time for the 250 gm batch is 50–60 min. The variables like rotational speed, weight of foaming agent, temperature of melting can be studied on this setup. The chemical analysis

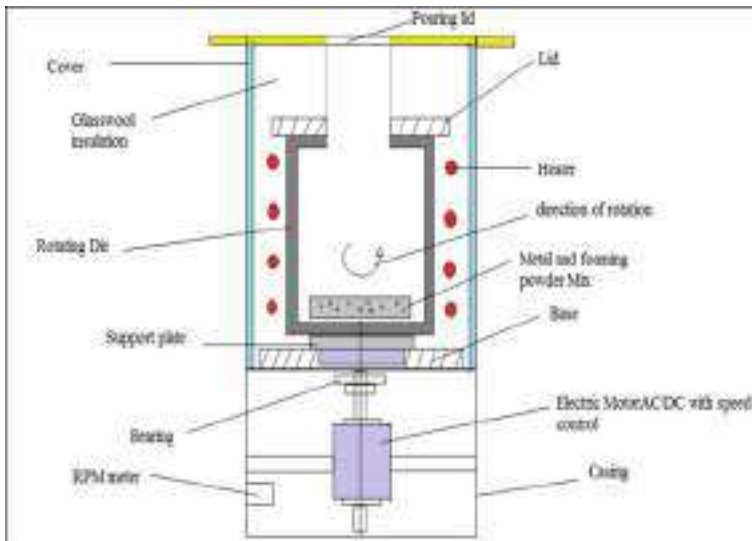


Fig. 1 Machine designed for small batch production of aluminum and its alloys

Table 1 Chemical analysis of aluminum alloy

Sr. no	Element name	Element %
1	Mn	0.16
2	Si	9.64
3	Cu	1.34
4	Fe	0.8
5	Zn	0.89
6	Ni	0.07
7	Pb	0.3
8	Al	Balance

Fig. 2 Al melting process

of aluminium alloy is shown in Table 1. Spectroscopic analysis of raw material is done and chemical analysis confirms to BS1490:1988 LM2 (AlSi10Cu2) EN AB-46100. This raw material is used for the foaming experiment by adding foaming agent LiAlH_4 in proportions like 5, 10, and 15% to find the effect of foaming agent on void formation. LiAlH_4 is in the powder form having an assay value of Min.96% is added in the alloy LM2. Figure 2 shows the Al melting process.


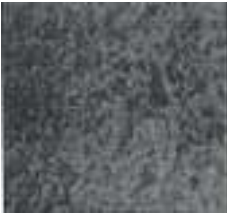

4 Sample Preparation for Microscopic Observation

Standard metallurgical sample preparation involves rough cutting and polishing, dry polishing with silicon carbide emery papers having mesh sizes 200, 400, 600, 800, 1000. Wet polishing was performed with Al_2O_3 powder on a wet polishing machine and etching with NH_4OH .

From the experimentation work, following are the observations:

- A vertical axis centrifugal casting process is a very common casting process. Effect of centrifugal force during foam cell formation, expansion, and cell size are obtained.
- Microstructural analysis shows the morphology of the cell and the presence of voids. It is shown in Table 2.
- X-ray diffraction is a non-destructive method used to provide detailed information about the chemical composition, crystallographic structure, and physical properties of a material [14, 15]. Optical microscope observation reported at 250X and 400X magnification. Microstructure is used to confirm the crystalline phases present in a material and reveal chemical composition information. The confirmation is done by using XRD data for aluminum and aluminum alloy available from standard resources as shown in Figs. 3, 4 and 5. The specifications of the machine are Goniometer Ultima IV Attachment Sample Rotation (with Z) Att. Scanning Mode 2Theta/Theta Scanning Type Continues Scanning X-Ray.40 kV/40 mA.

Table 2 Microstructure observation

Sr. no	Microstructure	Details	Remarks
1		LM2 alloy + 5% LiAlH ₄ (Foaming Agent) at 400X magnification and NaOH etchant	35% voids
2		LM2 alloy + 10% LiAlH ₄ (Foaming Agent) at 400X magnification and NaOH etchant	55% voids
3		LM2 alloy + 15% LiAlH ₄ (Foaming Agent) at 400X magnification and NaOH etchant	65% voids

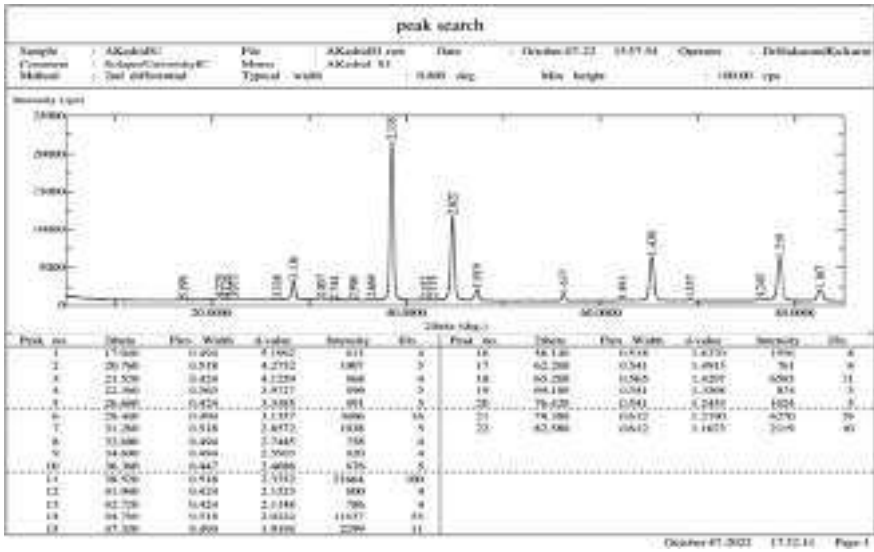


Fig. 3 XRD pattern for LM2 alloy + 5% LiAlH₄

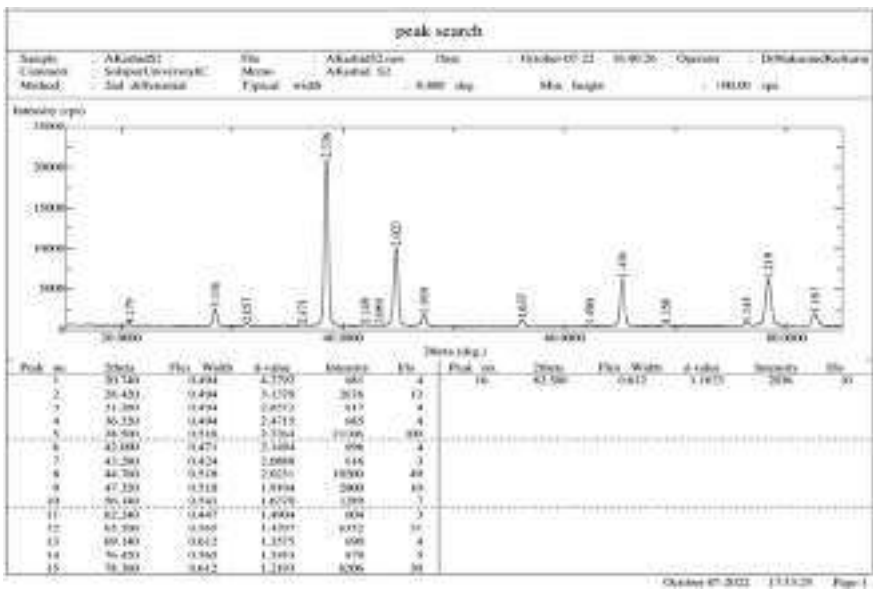


Fig. 4 XRD pattern for LM2 alloy + 10% LiAlH₄

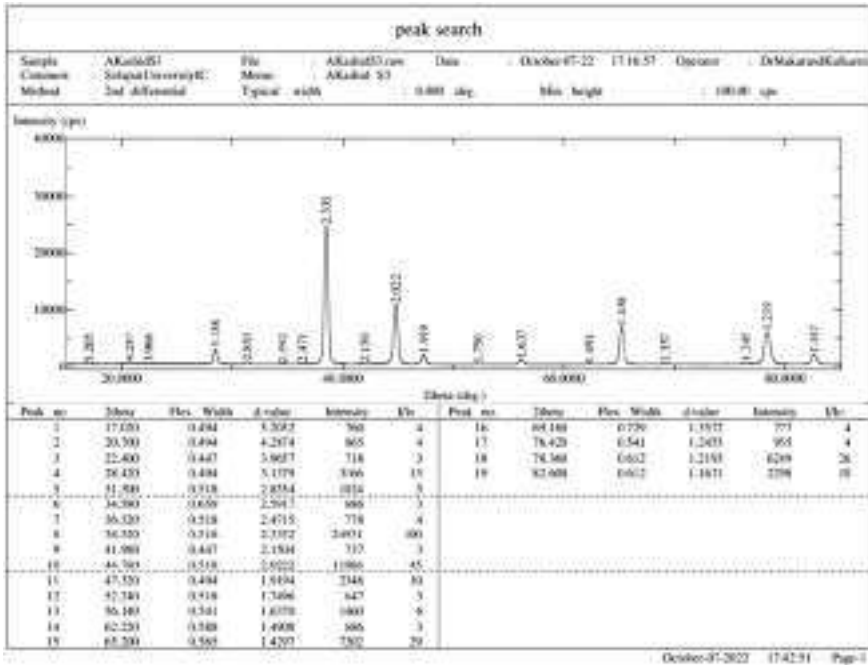


Fig. 5 XRD pattern for LM2 alloy + 15% LiAlH₄

5 Conclusions

- A centrifugal casting method can be combined with the powder metallurgy precursor method of foam manufacturing. Powder metallurgy precursor method is a commonly used foam manufacturing process. The centrifugal force offered during centrifugal casting evenly distributes the melt and prevents floating of lighter phases upward. This combination leads to new technology in foam manufacturing.
- A low-cost LiAlH₄ foaming agent can replace TiH₂ foaming agent.
- This method is suitable for batch production of cylindrical-shaped products in less time.
- The overall cost of production is less compared to the bubbling method, which is a commonly used method. Precursor of the desired composition can be produced on a mass scale in less time. These can be stored in plastic bags for long shelf life. Melting is done in a rotating mold electric muffle furnace, which is energy efficient and of low energy cost.

- Performance: Material composition is exactly obtained as powder metallurgy precursor. Melting is uniform and homogenous. High foaming rate is obtained at 60–90 rpm.
- Accuracy: The chemical composition, dimensions, melting temperature, and rotational speed can be monitored and controlled precisely using sensors for desired foam density.

References

1. Neu TR, Pfretzschner B, Garcia-Moreno F, Banhart J (2017) Influence of the heating rate on the foaming behaviour of various aluminium alloys. *Metals* 7(2017):323. <https://doi.org/10.3390/met7090323>
2. Banhart J (2001) Manufacture, characterization and application of cellular metals and metal foams. *Prog Mater Sci* 46:559–632
3. Liu X, Li Y, Chen X, Yuan L, Fan X (2010) Foam stability in gas injection foaming process. *J Mater Sci* 45:6481–6493. <https://doi.org/10.1007/s10853-010-4736-5>
4. Sánchez-Martínez A, Cruz A, González-Nava M, Suárez MA (2016) Main process parameters for manufacturing open-cell Zn-22Al-2Cu foams by the centrifugal infiltration route and mechanical properties. *Mater Design* 108:494–500
5. Deng-wei H, Juan Y, Xiang-yang Z, Hui W, Zhang T (2012) Preparation of open-celled aluminum foams by counter-gravity infiltration casting, *Trans Nonferrous Met Soc China* 22:85–89
6. Goodall R, Despois OJF, Marmottant A, Salvo L, Mortensen A (2006) The effect of preform processing on replicated aluminium foam structure and mechanical properties. *Scripta Mater* 54:2069–2073
7. Rajak DK, Kumaraswamidhas LA (2017) Technical overview of aluminum alloy foam. *Rev Adv Mater Sci* 48
8. Banhart J (2006) Metal foams: production and stability. *Adv Eng Mater* 8(9):781–794
9. Banhart J, Baumeister J (1998) Production methods for metallic foams. *Mat Res Soc Symp Proc* 521:121–133
10. Matijasevic B, Banhart J (2006) Improvement of aluminum foam technology by tailoring of blowing Agent. *Scripta Mater* 54(4):503–508
11. Wannasin J, Flemings MC (2005) Fabrication of metal matrix composites by a high-pressure centrifugal infiltration process. *J Mater Process Technol* 169:143–149
12. Baltatescu O, Axinte M, Barbu G, Manole V (2015) New approach for porous material obtaining using centrifugal casting. *Modern technologies in industrial engineering (MedTech 2015) 10P Conf. Series: Material science and engineering* 95
13. Baumgartner F, Durate I, Banhart J (2000) Industrialization of powder compact foaming process. *Adv Eng Mater* 2(4):168–174
14. Gibson LJ (2000) Metallic foams: structure, properties and applications annual review of material science. In: Aref H, Phillips JW (eds) *Mechanics for a new Millennium*. Springer, Dordrecht, pp 57–74. https://doi.org/10.1007/0-306-46956-1_4
15. Banhart J, Baumeister J, Weber M (1995) Powder metallurgical technology for the production of metallic foams. In: *Proceedings of the European conference on advanced PM materials (PM'95) Birmingham (UK), 23.-25.10.1995* (European Powder Metallurgy Association, Shrewsbury), pp. 201–208

Chapter 12

Synthesis and Characterization of Nano-CuO Complexed HPMC:PVA Polymer Blend Electrolytes



N. Sandhya Rani, Sunil Kumar, B. Vinod, C. S. Dileep, C. Manasa,
and N. Srikantamurthy

Abstract Polymerelectrolyte films of polyvinylalcohol (PVA)/hydroxypropyl methylcellulose (HPMC) complexed with copper oxide (CuO) nanoparticles (1%–4% wt.%) were synthesized by adopting casting solution technique. X-ray diffraction results showed a reduced percentage of crystallinity with the increase in CuO concentration. Scanning electron microscopy (SEM) showed the different morphology of all the samples. Differential scanning calorimetry (DSC) analysis shows the increase in glass transition as well as in melting temperature for all samples. This is because the presence of CuO nanoparticles in the host polymer blend matrix makes them more thermally stable. The tensile strength and modulus nano-CuO complexed samples show improvement when compared with HPMC:PVA blends. The AC conductivity also increases with frequency and CuO concentration. All the experimental studies showed that 3 wt% nano-CuO complexed HPMC:PVA polymer electrolyte samples are more thermally stable and exhibit high conductivity at room temperature.

Keywords Nanocomposite polymer electrolytes · X-ray diffraction · DSC

N. Sandhya Rani (✉)
Department of Applied Physics, VVCE, Mysore, India
e-mail: sandhya.phy@vvce.ac.in

S. Kumar
Department of Physics, S.S Arts College and T.P Science Institute, Sankeshwar,
Belagavi 591313, India

B. Vinod
Department of Mechanical Engineering, VVCE, Mysore, India
e-mail: vinod@vvce.ac.in

N. Sandhya Rani · C. S. Dileep · C. Manasa · N. Srikantamurthy
Department of Applied Chemistry, VVCE, Mysore, India
e-mail: srijmn@vvce.ac.in

1 Introduction

One of the key constituents of the electrochemical cell devices is polymer electrolyte [1–4]. It is made by dissolving metal salt in a polymer host [5–7]. Here, an environmentally friendly polymer mixture of HPMC and PVA is employed as the host polymer matrix to boost electrical conductivity and give extra sites for ion hopping and ion transfer as hydrogen bonds are formed between the polymer chains [8–12]. To improve the thermal, structural, mechanical, and electrical conductivity qualities of the synthesized polymer electrolyte films, CuO nanoparticles are added to the polymer mixture [13–18].

2 Experimental Work

2.1 Materials and Sample Preparation Method

The HPMC and PVA solutions (5:5 wt%) were made separately, combined, and stirred continuously. This blend solution was gradually added with CuO nanoparticles (1–4 wt%), which were then continuously swirled for two hours at 380 rpm using a magnetic stirrer. After being evaporated in a vacuum chamber for a period of ten minutes, the liquid was placed into flat plates to cool down at the ambient temperature for four to five days. Film samples were coded as HPMC:PVA blend (S1), HPMC:PVA—1% CuO (S2), HPMC:PVA—2% CuO (S3), HPMC:PVA—3% CuO (S4), HPMC:PVA—4% CuO (S4).

2.2 Instrumentation

X-ray diffractometer with CuK radiation (1.5406), a Rigaku Miniflex-II was used to obtain the XRD patterns on a scale of 10° – 80° . The SEM studies were done by using an electron microscope (JEOL 840) with a resolution of 20 kV. DSC-Q20, Universal V4.5 A was used to create the DSC thermograms. The tensile test was done on the test specimens prepared as per ASTM D-638 (165*19*6) type 1 standard (Fig. 4). The AC conductivity was measured using an LCR meter ZM2376 at operating frequencies ranging from 50 Hz to 1 MHz. Using Eq. 1, the electrical conductivity is determined.

$$\nu = \left(\frac{1}{R_b}\right)\left(\frac{t}{A}\right) \quad (1)$$

where ‘A’ is the area mm^2 , ‘t’ is the thickness in mm, and ‘ R_b ’ is the resistance in $M\beta$.

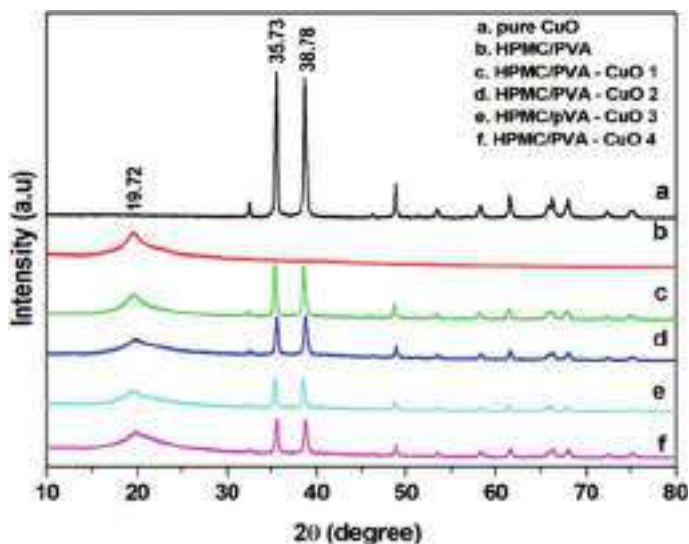


Fig. 1 XRD pattern of all samples

3 Results and Discussion

3.1 X-Ray Diffraction Studies

Figure 1 displays the XRD graphs of all samples. According to well-reported literature, the electrical conductivity of the polymer electrolyte sample is higher in the amorphous area [19–23]. Peaks for pure CuO are more powerful and distinct at about 34.72° , 38.82° and 47.70° . While the HPMC:PVA blends show a visible broad peak at 19.69° . The sharp peak of pure CuO and the broad peak of polymer blends reduce in all other polymer electrolyte samples; hence, the percentage of crystallinity also reduces (Table 1). Percentage of crystallinity is calculated using Eq. 2.

$$\text{Crystallinity}(\%) = \frac{\text{crystalline peaks area}}{\text{crystalline peaks area} + \text{amorphous haloes area}} \times 100 \quad (2)$$

3.2 Morphological Studies

Figure 2 displays the film morphologies of the reported polymer electrolyte sample. Due to the absence of discernible crystalline regions, pure HPMC and pure PVA

Table 1 Crystalline parameters

Sample	X_C (%)
Pure CuO	58.66
S1	18.52
S2	56.60
S3	49.20
S4	31.43
S5	43.22

display semi-crystallinity [21, 22, 24]. SEM picture (Fig. 2c) reveals an evenly dispersed microporous structure. This demonstrates that one of the key elements affecting the polymer blend performance is the similarity of the interfaces between the segments [25]. Figure 2d–g shows that overall the CuO nanoparticles are widely disseminated throughout the polymer mixtures and interacted with them [26, 27]. This clearly demonstrates the viability of this approach to create a uniform layer of well-distributed nanoparticles [28–30].

3.3 DSC Studies

The thermal characteristics of the reported samples are displayed in Fig. 3. Table 2 provides an overview of the thermal properties obtained from these thermograms. Nano-CuO complexing with HPMC:PVA blends affects the melting temperature as well as the crystallization behavior of the polymer electrolytes. From XRD, a drop in the percentage of crystallinity was also observed for all the CuO complexed samples. It is clear from the DSC plots that the glass transition temperature T_g and melting temperature T_m increases slightly, whereas crystallization temperature T_c decreases slightly [31, 32]. All the values showed that the 3wt% CuO complexed polymer blend had got high thermal stability.

3.4 Tensile Properties

Figure 4 shows the test specimen used for tensile test according to ASTM standards. Figure 5 displays the stress–strain curves of the reported samples. Table 3 shows the test results. The tensile strength of PVA:HPMC blend is 3.477 Mpa. The highest tensile strength of 13.533 Mpa is obtained for 3% CuO complexed sample. Therefore, its strength is almost 3.89 times greater than the pure polymer blend. Similarly, the modulus of the 3% CuO complexed sample is 0.162 Gpa, which is 65% greater than the polymer blends. It is evident that when the nano-CuO concentration rises, both the tensile strength and the modulus also rise and reaching to their maximum

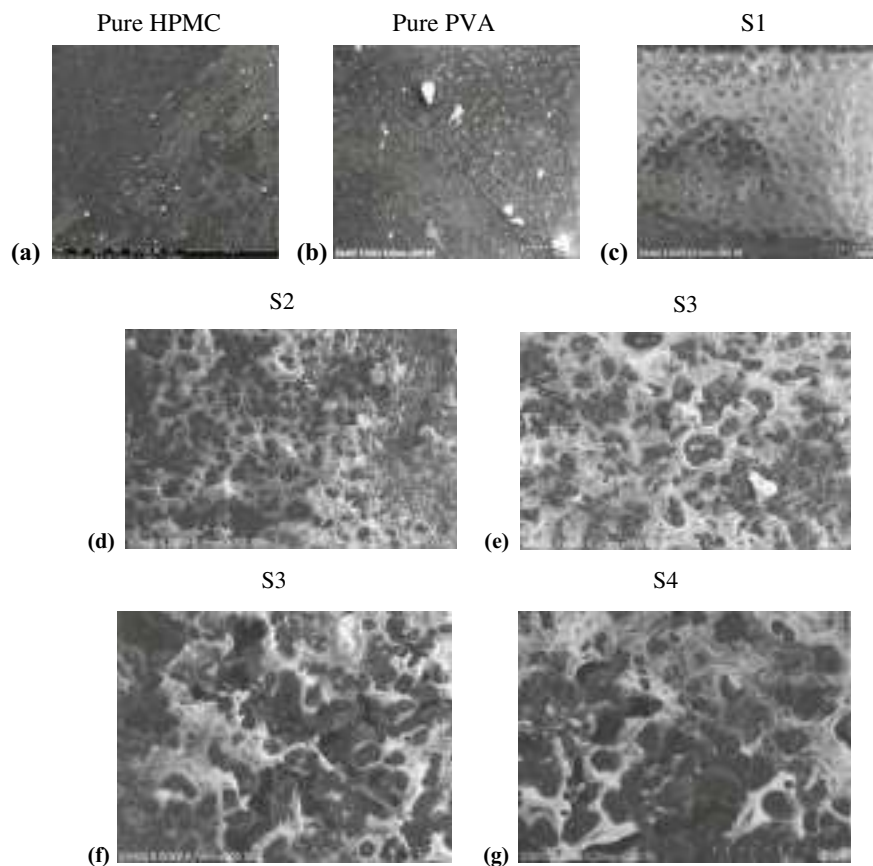


Fig. 2 SEM photographs of the samples

values at 3% CuO complexed HPMC:PVA blends. Whereas a higher concentration, i.e., for HPMC:PVA—CuO 4%, both tensile strength and modulus start to reduce. This exhibits that the nanocomposite sample of HPMC:PVA—CuO 3% has got more strength than other ratios of nano-CuO complexed samples.

3.5 *Electrical Conductivity Studies*

Figure 6 clearly displays enhancement in the conductivity up to 3 wt% CuO and then decreases. It can also be seen that the HPMC:PVA—3 wt% CuO sample exhibits the highest ionic conductivity of 1.23×10^{-4} S/cm at room temperature. According to

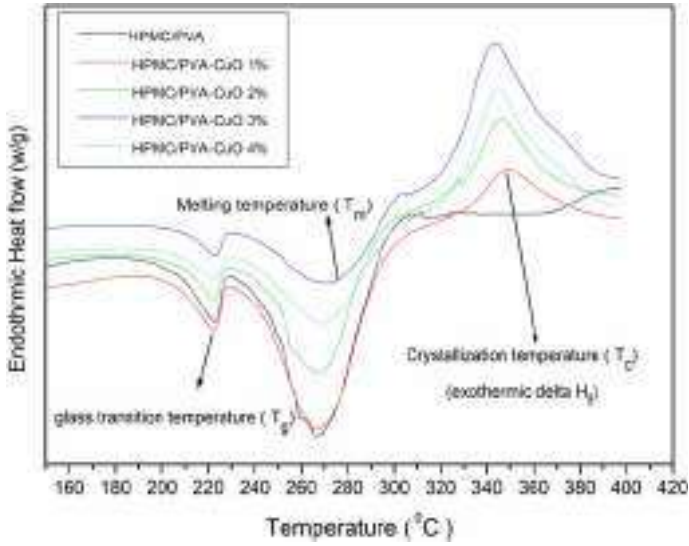


Fig. 3 DSC curves of all samples

Table 2 DSC parameters

Sample	T_g (°C)	T_m (°C)	θH_m (J/g)	T_C (°C)
S1	220.11	264.17	328	–
S2	221.1	269.89	265	349.882
S3	223.18	268.78	222	347.20
S4	223.48	272.51	274	344.06
S5	222.43	269.56	270	344.83

Table 3 Tensile properties of the samples

Sample	Tensile strength (Mpa)	Modulus (Gpa)	Peak load (kN)	Stiffness kN/mm
S1	3.477	0.097	0.105	0.02
S2	3.659	0.102	0.107	0.02
S3	10.259	0.123	0.494	0.039
S4	13.533	0.162	1.021	0.082
S5	10.41	0.125	0.795	0.064

this, an increase in nano CuO dissociation is what is responsible for the increase in ionic conductivity as it produces more mobile ions. On the other hand, at larger salt concentrations, the dissociated ions start to recombine to create neutral salt, which reduces electrical conductivity [33, 34].

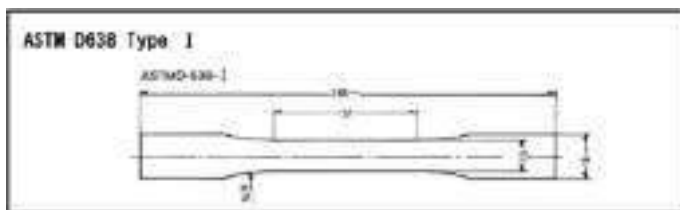


Fig. 4 Test specimen for tensile test (ASTM D638)

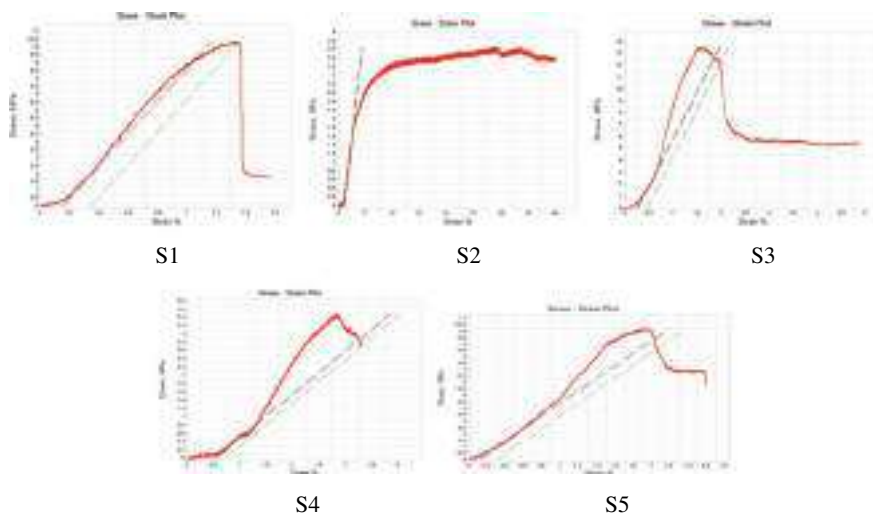
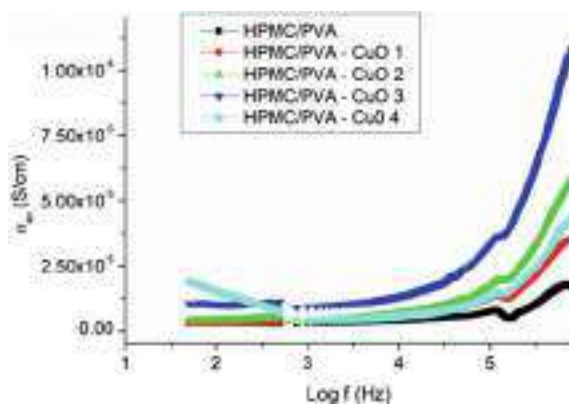


Fig. 5 Stress–strain curves of the samples

Fig. 6 Ionic conductivity behaviour of HPMC:PVA—CuO films



4 Conclusion

HPMC:PVA polymer blends complexed with different ratios (wt%) of nano-CuO were successfully synthesized using solution cast technique. From XRD studies, it is evident that adding nano-CuO to the host polymer matrix has an impact on the polymer matrix and hence decreases the percentage of crystallinity. The samples' rise in amorphous domain leads to an increase in the polymer electrolytes' electrical conductivity. SEM image of all the samples showed a microporous structure that is equally distributed. DSC studies show that the glass transition temperature, as well as melting temperature improved after nano-CuO complexing in the polymer mix, making them more thermally stable. Tensile and modulus studies showed good improvement in all the polymer electrolyte samples. The electrical conductivity also increases with increasing nano-CuO concentration. From all the studies, it was observed that the sample HPMC:PVA—CuO 3% shows more thermal stability, less crystallinity, and high conductivity of 1.28×10^{-4} S/cm at room temperature; hence it can become useful in electrochemical device applications.

Acknowledgements The authors are thankful to the LCR metre and computerized universal testing machine facilities provided by the Engineering Physics and Mechanical Engineering department of VVCE in Mysore for the investigation of mechanical characteristics.

References

1. Parameswaran V, Nallamuthu N, Devendran P, Nagarajan ER, Manikandan A (2017) Electrical conductivity studies on ammonium bromide incorporated with zwitterionic polymer blend electrolyte for battery application. *J Phys B* 515:89–98
2. Senthil RA, Theerthagiri J, Madhavana J, Arof AKM (2016) High performance dye-sensitized solar cell based on 2-mercaptobenzimidazole doped poly(vinylidene fluoride-co-hexafluoropropylene) based polymer electrolyte. *J Macromol Sci A* 53:245–251
3. Senthil RA, Theerthagiri J, Madhavan J (2015) Hematite Fe₂O₃ nanoparticles incorporated polyvinyl alcohol based polymer electrolytes for dye-sensitized solar cells. *J Mater Sci Forum* 832:72–83
4. Hafiza MN, Bashirah ANA, Bakar NY, Isa MIN (2014) Electrical properties of carboxyl methyl-cellulose/chitosan dual-blend green polymer doped with ammonium bromide. *J Int J Polym Anal Charact* 19:51–58
5. Shukur MF, Ithnin R, Illias HA, Kadir MFZ (2013) Proton conducting polymer electrolyte based on plasticized chitosan-PEO blend and application in electrochemical devices. *J Opt Mater* 35(18):34–41
6. Abdullah OG, Hanna RR, Salman YAK (2017) Structural, optical, and electrical characterization of chitosan: methylcellulose polymer blends based film. *J Mater Sci Mater Electron* 28(102):83–94
7. Acosta JL, Morales E (1996) Structural morphological and electrical characterization of polymer electrolytes based on PEO/PPO blends. *J Solid State Ionics* 85:85–90
8. Yang CC, Wu GM (2009) Study of microporous PVA/PVC composite polymer membrane and its application to MnO₂ capacitors. *J Mater Chem Phys* 114:948–955

9. Sandhya Rani N, Sannappa J, Demappa T, Mahadevaiah (2014) Structural, thermal, and electrical studies of sodium iodide (NaI)-doped hydroxypropyl methylcellulose (HPMC) polymer electrolyte films. *J Ionics* 20(2):201–207
10. N. Sandhya Rani, J. Sannappa, T. Demappa, Mahadevaiah (2015) Effects of CdCl₂ concentration on the structural, thermal and ionic conductivity properties of HPMC polymer electrolyte films. *J Ionics* 21:133–140
11. Nouh SA, Abdel-Kader MH, Mohamed MB (2017) Structural and optical modifications in polyvinyl alcohol due to Cr₂O₃ nanoparticles additives concentration, and gamma irradiation. *J Adv Polym Technol* 3:1–5
12. Mohammed G, Morsi WM (2018) Spectroscopic, thermal and electrical properties of MgO/PVP/PVA nanocomposites. *J Phys Chem Solids* 115:238–247
13. Tamgadge YS, Talwatkar SS, Sunatkari AL, Pahurkar VG, Muley GG (2015) Studies on nonlocal optical nonlinearity of Sr–CuO–polyvinyl alcohol nanocomposite thin films. *J Thin Solid Films* 595:48–55
14. Sivasubramanian R, Biji P (2016) Preparation of copper (I) oxide nanohexagon decorated reduced graphene oxide nanocomposite and its application in electrochemical sensing of dopamine. *J Mater Sci Eng* 2(10):10–18
15. Souza SD, Hidembregue O, Sanches EA (2018) Polyaniline–CuO hybrid nanocomposite with enhanced electrical conductivity. *J Mol Struct* 1153:20–27
16. Jundale DM, Navale ST, Khuspe GD, Dalavi DS (2013) Polyaniline–CuO hybrid nanocomposites: synthesis, structural, morphological, optical and electrical transport studies. *J Mater Sci Mater Electron* 24:3526–3535
17. Alghunaim NS (2019) Effect of CuO nanofiller on the spectroscopic properties, dielectric permittivity and dielectric modulus of CMC/PVP nanocomposites. *J Mater Resea Technol* 8(4):3596–3602
18. Ali Alhazime A (2020) Effect of nano CuO doping on structural, thermal and optical properties of PVA/PEG blend. *J Inorg Organ Polym Mater* 157:7–8
19. Ahmed HT, Abdullah OG (2020) Structural and ionic conductivity characterization of PEO:MC-NH4I proton-conducting polymer blend electrolytes based films. *J Resul Phy* 16:102861
20. Abdullah OG, Aziz SB, Rasheed MA (2016) Structural and optical characterization of PVA:KMnO₄ based solid polymer electrolyte. *J Resul Phys* 6(110):3–8
21. Ahmed HT, Abdullah OG (2019) Preparation and composition optimization of PEO:MC polymer blend films to enhance electrical conductivity. *J Polym* 11:853
22. Singh NL, Shah S, Qureshi A, Tripathi A, Singh F, Dkavasthi. *J. Bull. Mater. Sci.* 34, 81–88 (2011)
23. Mohamada AH, Abdullah OG, Saeed SR (2020) Effect of very fine nanoparticle and temperature on the electric and dielectric properties of MC-PbS polymer nanocomposite films. *J Resul Phys* 16(102898):1–9
24. Bianchia SE, Angelia VW, de Souzaa KCB (2011) Evaluation of the solubility of the HPMC/PVA blends in biological fluids in vitro. *J Mater Resea* 14(2):166–171
25. Jundale D, Pawar S, Chougule M, Godse P, Patil S, Raut B (2011) Nanocrystalline CuO thin films for H₂S monitoring microstructural and optoelectronic characterization. *J Sens Technol* 36–46
26. Jundale DM, Joshi PB, Sen S, Patil VB (2012) Nanocrystalline CuO thin films: synthesis, microstructural and optoelectronic properties. *J Mater Sci Mater Electron* 23:1492–1499
27. Lee KH, Kim HY, La YM, Lee DR, Sung NH (2002) Influence of a mixing solvent with tetrahydrofuran and N, N-dimethylformamide on electrospun poly(vinyl chloride) nonwoven mats. *J Polym Sci Polym Phys* 40:2259–2268
28. Han YG, Kusunose T, Sekino T (2009) One-step reverse micelle polymerization of organic dispersible polyaniline nanoparticles. *J Synth Mater* 159:123–131
29. Jundale DM, Navale ST, Khuspe GD, Dalavi DS, Patil PS, Patil VB (2013) Polyaniline–CuO hybrid nanocomposites: synthesis, structural, morphological, optical and electrical transport studies. *J Mater Sci Mater Electron* 24:3526–3535

30. Sahoo S, Hajra S, Mohantha K, Choudhary RNP (2018) Processing dielectric and impedance spectroscopy of lead free. *J Alloy Comp* 766:25–32
31. Falqi FH, Bin-Dahman OA (2018) Preparation of miscible PVA/PEG blends and effect of graphene concentration on thermal, crystallization, morphological, and mechanical properties of PVA/PEG (10wt%) blend. *J Hindawi Int J Polym Sci* 1–10
32. Ali ZI, Eisa WH (2014) Characterization of electron beam irradiated poly vinyl alcohol/poly ethylene glycol blends. *J Sci Res* 6:29–4
33. Alakanandana A (2017) Structural and electrical characterization of PVA doped malonic and succinic acid polymer electrolytes. *J Int J Sci Tech Eng* 3(7):30–36
34. Schantz S, Torell LM (1993) Evidence of dissolved ions and ion pairs in dilute poly (propylene oxide)-salt solutions. *J Solid State Ionics* 60:47–53

Chapter 13

Study on Effect of Pista Shell as Filler Material on Mechanical Performance of Banana Fiber Reinforced Polymer Composite



**B. Vinod, L. J. Sudev, B. B. Ganesha, K. N. Arunkumar,
and C. S. Thammegowda**

Abstract Recently, more research efforts have been initiated to improve the performance of composite materials due to their ever-increasing demand. A range of pre- and post-processing processes may be used to modify the biological, chemical, physical, and mechanical properties of any material. As a result, the primary goal of this study is to investigate the effect of powdered pistachio shells as a filler on the mechanical performance of banana fiber-reinforced polymer composites. The 10 wt.% of filler material, 30 wt.% of fiber and 60 wt.% of epoxy resin were used to prepare composite laminates using compression mould technique for rigid compaction of fiber and filler material. From experimental investigation, it was observed that the use of filler material improved the hardness and stiffness of the composite. The tensile stress was reduced to 22.97 MPa from 25.34 MPa and flexural strength was reduced to 36.76 MPa from 43.66 Mpa, respectively. The Young's modulus was increased to 4.96 GPa from 3.23 GPa and flexural modulus was increased to 7.38 GPa from 6.21 Gpa, respectively.

Keywords Banana · Filler · Epoxy Resin · Hardness · Stiffness · Strength

B. Vinod (✉) · L. J. Sudev · B. B. Ganesha · K. N. Arunkumar · C. S. Thammegowda
Department of Mechanical Engineering, VVCE, Mysuru, India
e-mail: vinod@vvce.ac.in

L. J. Sudev
e-mail: sudevjl@vvce.ac.in

B. B. Ganesha
e-mail: bbganesha.bbg@vvce.ac.in

K. N. Arunkumar
e-mail: arunkn.10@vvce.ac.in

C. S. Thammegowda
e-mail: thammegowda.cs@vvce.ac.in

1 Introduction

When it comes to Fiber Reinforced Polymers (FRP) composites, there may be a possibility of an interstitial space between the fibers and the matrix material. This interstitial space may act as a void or inner crack, thereby reducing the performance ability of composite material. Therefore, it is essential to reduce the space between the fibers and matrix material through various processes during manufacturing. Applying the compressive force during manufacturing is one of the effective methods to reduce the inner voids in composite. At the same time, application of compressive force may generate internal stress in the composite material, which further reduces the load-bearing ability of the composite. Therefore, one of the best methods to reduce the space between matrix and fiber is the utilization of filler materials. These materials can either be available naturally or it could be manmade. Most commonly used natural fillers are from agricultural waste like pistachio shell, rice husk, wheat husk, ash and coconut coir, etc. There are certain inorganic materials that are used as filler materials like calcium carbonate, calcium sulfate, alumina trihydrate and kaolin (hydrated aluminum silicate) etc. [1].

Iskender Ozsoy et al. [2] made an investigation on the effect of micro- and nanofillers such as Al_2O_3 , TiO_2 , clay and fly ash on epoxy composite for 10–30wt.% by weight ratios. From experimental investigation, it was examined that the tensile and flexural strength of the composite decreases with increasing micro- and nanofiller content ratio. However, the modulus of elasticity during tensile and bending tests improves with the increase of the content ratio of micro- and nanofillers. Hardness of the composite increased with the addition of filler material and thus making the composite brittle. Zaman et al. [3] analysed the micro- and nano-ZnO-stuffed polypropylene composites for different weight ratios ranging between 2 and 8wt.%. The study inferred that nano-filled composites exhibits better strength than micro-filled composites for the same filler ratios. The 5 wt.% filler content was found to be an optimum ratio for which the dispersion of particles was better. A stronger interfacial bonding between the matrix and fillers was observed with the help of morphology images. Gao et al. [4] examined an effect of nano-sized CaCO_3 as filler on the mechanical strength of polystyrene composites. The stiffness starts to increase with increasing the filler ratio up to a certain extent, beyond which the filler starts to agglomerate, thereby reducing the adhering ability between matrix and fiber material. Thus, the strength of the composite starts to decrease. Agubra et al. [5] studied the impacts of nano-clay distribution procedures on the mechanical performance glass fiber epoxy composites. Magnetic dispersion, planetary centrifugal mixing and ultrasonication are some of the commonly used dispersion methods to attain moderate dispersion of nanoparticles in polymer matrix. In this research, the influence of the three roll milling method for nano-clay dispersion into epoxy matrix was analyzed. The paper concluded that significant clay dispersion in the epoxy matrix was accomplished by merging the magnetic stirring and tinky mixing followed by three roll milling method. Yasmin et al. [6] investigated the structural, mechanical, viscoelastic and thermal behavior of graphite-filled epoxy composites of filler

weight ratios between 2.5 and 5 wt.%. The tensile strength, glass transition temperature and modulus increased with increasing graphite platelets up to 5 wt.% filler ratios. However, above which, the agglomeration of fillers occurred. The coefficient of thermal expansion was reduced with the increase of graphite platelets and also there was an improvement in the thermal stability of the composite. Sayer [7] studied the effect of ceramic fillers like SiC, Al₂O₃, and B₄C on the elastic- and load-carrying ability of e-glass fiber reinforced epoxy resin. The filler weight ratios were varied from 5 to 15% wt. The article concluded that the 10% Wt. attained as the optimal value the composite exhibiting maximum load-bearing ability and elastic moduli. Apart from the weight percentage, it was also reflected that the particle size also plays a major role to improve the strength of the composite. Smaller the particle size greater will the elastic moduli and load-carrying ability of the composite. Asi [8] studied the mechanical properties of glass fiber-reinforced epoxy composites filled with various proportions of Al₂O₃. Experimental results showed that the tensile and shear strengths decreased with the increasing addition of Al₂O₃ particles. However, the flexural strength of the composite was increased by 33% and flexural modulus by 78% with an increase in Al₂O₃ particles up to 10% wt. beyond which it starts to decrease. Yang et al. [9] analyzed the effect of lignocellulosic material (rice husk flour) as fillers on the mechanical properties of thermoplastics composite (polypropylene). The composite was prepared for different filler loading of 10, 20, 30 and 40% weight ratios. The paper concluded that interfacial area improves with an increase in filler ratios and thereby increasing the stiffness, hardness, and brittleness of the composite.

The comprehensive literature survey on the pertaining topic has revealed enormous information related to filler materials and helps to identify the gap that exists and to move in the right path. Therefore, in the current work, the effect of the powdered pistachio shell as filler material for weight ratios ranging from 0 to 10% wt. on the mechanical properties of banana fiber reinforced epoxy composites was studied. The tensile, flexural and hardness tests were performed, and the results were analyzed.

2 Materials and Methodology

The details on materials, processing and the experimental procedures followed in the present work are discussed below.

2.1 *Banana Fiber*

Banana fibers are well-known natural fibers to mankind from past decades. India is the world's largest producer of banana fruit, followed by China, Brazil, the Philippines and Ecuador. The excellent blending ability of banana fibers have extended its value-added applications in various fields [10]. It is a lignocellulosic fiber with very good

Table 1 The chemical compositions of banana fiber [10]

Chemical composition	Range in percentage
Cellulose	63–64
Hemicellulose	16–19
Lignin	5
Moisture content (%)	10–11
Density (g/cc)	1.35
Microfibrillar angle (deg)	11

strength obtained from the stem of the banana plant (*Musa sepientum*). The cellulose in the fiber acts as a cement or binder that gives the fiber its strength. Together with cellulose, the lignin content of the cell wall increases its stiffness and hemicellulose strengthens the cell wall due to its interaction with lignin and cellulose [11]. Table 1 shows the chemical compositions of banana fiber. A small variation in the assessments of these properties may be noted due to the difference in the source from where the fibers are available, the process of fiber extraction, age of the plant and climatic conditions, etc.

2.2 *Pistachio Shell (Filler)*

Pistachio is a small tree originating from Central Asia which belongs to the cashew family. After extraction of nuts, pistachio shells are commonly used for mulching, potted plant fillers, pest deterrent, fire kindling and compost, etc. Pistachio shells possess high stiffness, strength and hardness. Even though it is least considered as filler/reinforcing material in the case of fiber reinforced polymer composite materials [12].

2.3 *Lapox L12 Epoxy Resin*

Lapox L12 is an unmodified epoxy resin of medium viscosity, also known as poly-epoxides based on Diglycidyl Ethers of Bisphenol A (DGEBA). Diethylene triamine (DETA) was used to cure lapox L12, which is a light-yellow aliphatic polyamine. The reaction of the poly-epoxide with the multifunctional curing agent forms a thermoset polymer with excellent mechanical properties, adhering ability, dimensional stability, thermal insulator, fire retardance, low cure shrinkage, resistance to corrosion and water ingress, etc. [13]. Lapox L12 is commonly used for marine coating, flooring, aerospace, automobile and packaging industries, etc.

2.4 Methodology

The raw banana fibers were extracted from the trunk of the banana plant by retting process. The obtained raw fibers contain impurities and fatties at its surface. Therefore, in order to remove these impurities, a pretreatment operation of fibers such as an alkali treatment and drying the fibers using a hot air oven has been performed [14]. In the case of alkaline chemical treatment, the fibers were immersed in 5% NaOH solution for 1 h and then completely dried in a hot air oven at 60 °C to remove internal moisture. The finished fiber is spun into a mat and laminated by hand with a constant volume fraction of 30% fiber and 60% resin. The composite laminates were prepared by a 2% increase in the weight fraction of filler material up to 10%.

Test specimens were prepared according to American Society for Testing and Materials (ASTM) standards D638 and D790 for tensile and flexural tests, respectively. Similarly, hardness and impact testing were carried out according to ASTM D2240 and D256, respectively. High-speed waterjet cutting is used to cut samples into desired shapes [15]. Testing was performed using a computerized universal testing machine (UTM) with a constant load of 1kN and with a rate of elongation of 0.3 mm/min until the specimen broke. The detailed dimension of ASTM D638 and ASTM D790 are shown in Figs. 1 and 2, respectively.

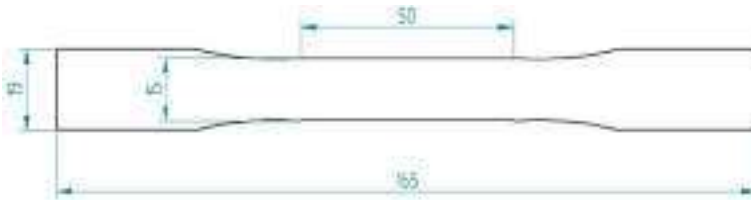


Fig. 1 Dimensions of tensile test specimen as per ASTM D638 (in mm)

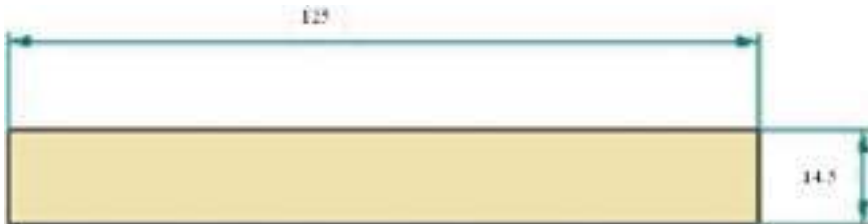


Fig. 2 Dimensions of flexural test specimen as per ASTM D790 (in mm)

3 Results and Discussion

The specimen with different combinations of fiber and filler materials were subjected to tensile, flexural, impact and hardness test. The specimen with 70% wt. of Resin (R), 30% wt. of fiber (F) and 0% wt. of filler material was represented as sample A and similarly as B, C, D, E and F for the combinations as mentioned in Table 1, respectively. From experimental investigation, it is very much clear that the mechanical behavior of composite material varies by varying the amount of filler material. Table 2 shows the tensile, flexural, impact and hardness test results of the specimen with and without filler material. The values given in Table 2 are the average of 5 tests and the tests were conducted until failure of the sample occurred. Figure 3 shows the variation of tensile strength and tensile modulus of the specimens.

The test results clearly show that the percentage of filler material greatly influences the tensile strength and Young's modulus of the composite material. The maximum tensile strength of 41.76 MPa was achieved for sample A (i.e., 70% of resin, 30% of fiber and 0% of filler material). The tensile stress of the composite laminate starts to decrease gradually with the increase in the percentage of filler material, as shown in Fig. 3a. The tensile loading ability of the composite was reduced by 3.11%, with a

Table 2 Mechanical properties of composites with and without filler material

Sample	Combinations	Volume %	Tensile strength (MPa)	Young's modulus (GPa)	Flexural strength (MPa)	Flexural modulus (GPa)	Impact strength (KJ/m ²)	Hardness
A	Resin	70	41.76	2.98	84.56	3.69	6.41	114
	Fiber	30						
	Filler	0						
B	Resin	70	40.46	3.01	78.62	3.84	4.11	116
	Fiber	28						
	Filler	2						
C	Resin	70	38.45	3.15	75.02	3.97	3.52	119
	Fiber	26						
	Filler	4						
D	Resin	70	36.08	3.65	69.48	4.65	3.05	126
	Fiber	24						
	Filler	6						
E	Resin	70	32.53	3.67	65.39	5.52	2.63	129
	Fiber	22						
	Filler	8						
F	Resin	70	30.60	3.86	62.96	5.65	2.09	131
	Fiber	20						
	Filler	10						

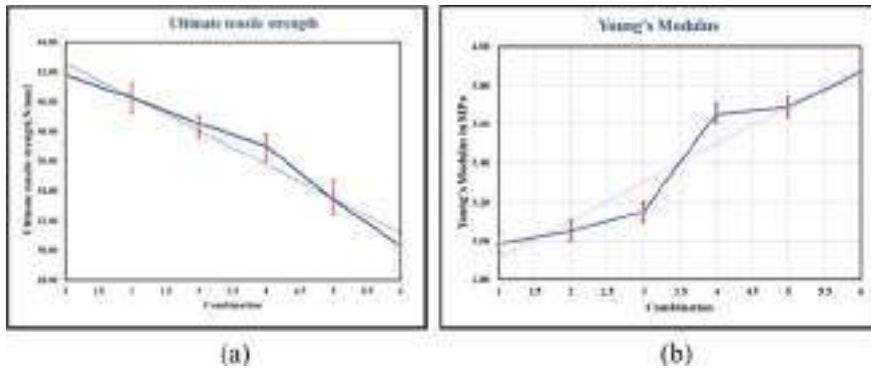


Fig. 3 Variation of tensile strength and modulus of the specimen

2% increase in the filler material. Similarly, the tensile strength is reduced by 7.95, 13.6, and 22.01% for samples 'C', 'D' and 'E', respectively. The least tensile strength of 30.60 MPa was attained for sample 'F' (i.e., 70% of resin, 20% of fiber with 10% of filler material), which is 26.72% lesser than sample 'A'.

The increase in the proportion of filler material increases the stiffness of the composite material [16]. Thus, Young's modulus of a composite material increases as the filler proportion increases, as shown in Fig. 3b. The Young's modulus of 2.98 GPa was obtained for sample 'A' and keeps on increasing gradually with a gradual increase in the filler material. The maximum Young's modulus of 3.86 GPa was achieved for sample 'F', which is 29.5% greater than sample 'A'. Figure 4 shows the variation of flexural strength and flexural modulus of the specimens.

Figure 4 clearly shows the effect of the percentage of filler material on the three-point bending strength and modulus of the composite. The maximum three-point bending strength of 84.56 MPa was achieved for sample 'A'. The bending ability of the composite material decreases gradually with the increase in the percentage

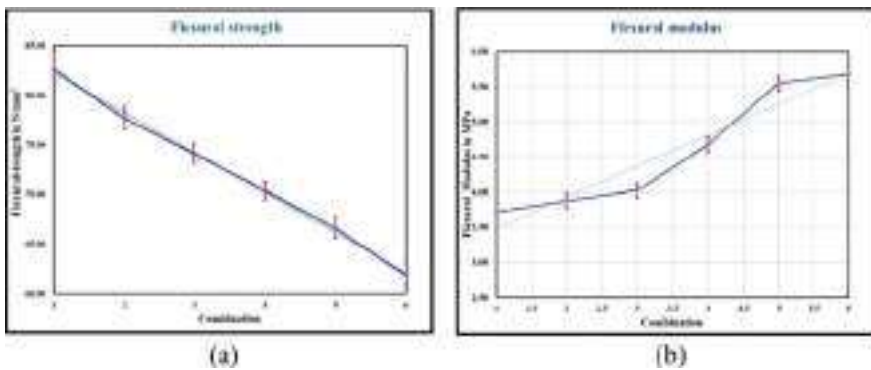


Fig. 4 Variation of flexural strength and modulus of the specimen

of filler material, as shown in Fig. 4a. The bending strength of the composite was reduced by 7.02% for sample 'B' (i.e., 70% of resin, 28% of fiber with 2% of filler material). Similarly, the bending strength reduced is by 11.28, 17.8, and 22.67% for samples 'C', 'D', and 'E' respectively. The least bending strength of 62.96 MPa was obtained for sample 'F', which is 25.54% lesser than the base material.

It can be seen that the stiffness of the composite increases as the filler proportion increases. Thus, the flexural modulus (bending modulus) of the composite improves with an increase in the percentage of filler material, as shown in Fig. 4b. The flexural modulus of 2.72 GPa was obtained for sample 'A' and its value increases gradually with a gradual increase in the filler material. The maximum flexural modulus of 5.65 GPa was achieved for sample 'F', which is 53.11% greater than sample 'A'.

It is evident from the results that the tensile and flexural strengths of the Pistachio shell filled banana fiber reinforced composite reduces with an increase in the percentage of filler material. The increase in filler content may lead to weaker bonding between fibers and the matrix material. In addition, at a high percentage of filler, non-uniform distribution of filler can cause agglomeration and stress concentration zones to appear. Thus, it reduces the tensile and flexural strength of the composite material. Figure 5a shows the SEM image of sample 'A' and figure (b) shows the SEM image of sample 'F' where the agglomeration of filler material can be observed. Figure 6 shows the variation in hardness and impact strength of the specimens.

From Fig. 6a, the hardness of the samples gradually increases as the percentage of filler increases. Sample 'F' exhibits a maximum hardness, which is 14.91% greater than sample 'A'. Increasing the filler concentration increases the fragility of the composite. And also, the increase in the concentration of filler material reduces the ability of the matrix to absorb energy and thereby reducing the toughness [17], thus reducing the impact strength from 6.41 to 2.09 kJ/m² as shown in Fig. 6b.

The reduction in the elongation of the test specimen containing filler material at the point of failure can be explained by the fact that the elastic properties of the composites depend on the polymer matrix exhibiting brittle behavior in the presence

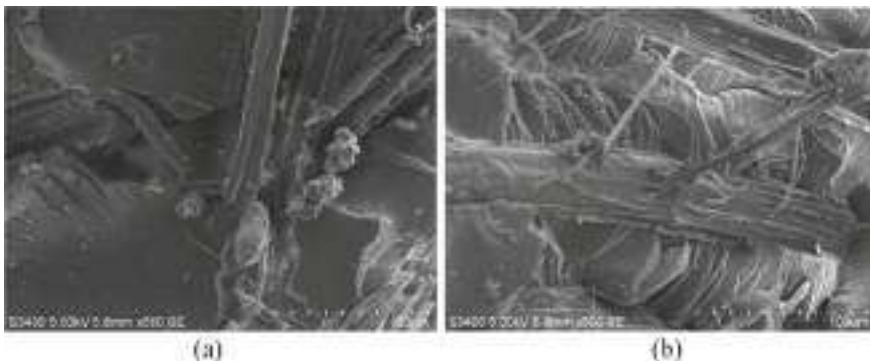


Fig. 5 SEM images of base material and composite with filler material

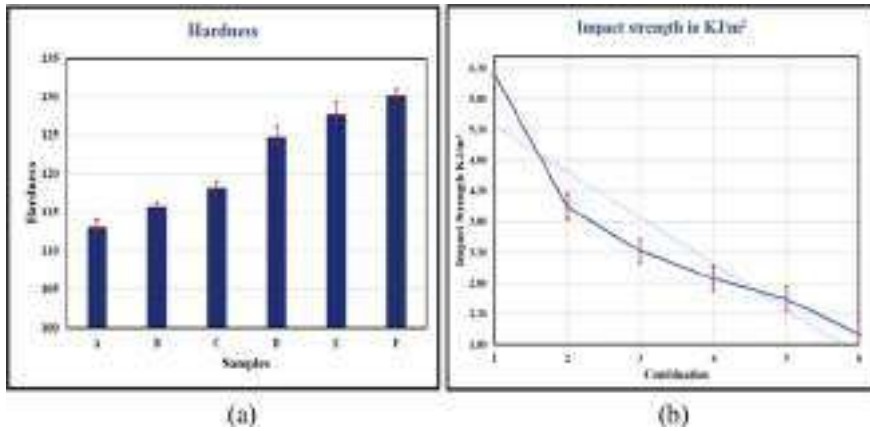


Fig. 6 Variation of the hardness of the specimen

of fillers. This is because the existence of filler material restricts the mobility of the polymer. Higher the filler content in the composites, higher will be the brittleness in the composites [18].

4 Conclusion

The experimental investigations on the effect of Pistachio shell as filler material on banana fiber reinforced composite clearly show that the mechanical performance of the composite varies with respect to the percentage of filler material. In general, the increase in the percentage of filler material decreases the tensile and flexural strength of the composite. The tensile and flexural strength of the composite is almost reduced by 26.72 and 25.54%, respectively, lesser than the base material. The maximum Young's and flexural modulus of 3.86 and 5.65 GPa, respectively, was achieved for sample 'F', which is 29.5 and 53.11%, respectively, greater than sample 'A'. At the same time, the stiffness of the composite increases as the filler proportion increases. Thus, increases the Youngs and flexural modulus of the composite. The intensification in the brittle behavior of the composite indicates an increase in the hardness of the composite. And also, an increase in the concentration of filler material reduces the capacity of the matrix to absorb energy and thus reduces the toughness of the material; therefore, the impact strength was reduced from 6.41 to 2.09 kJ/m². Thus, the pistachio shell as filler material on banana fiber reinforced composite influences the mechanical behavior of the composite material.

References

1. Rustemeyer T, Elsner P, John S-M, Maibach HI (eds) (2012) *Kanerva's occupational dermatology*. Springer, Berlin Heidelberg
2. Ozsoy I, Demirkol A, Mimaroglu A, Unal H, Demir Z (2015) The influence of micro- and nano-filler content on the mechanical properties of epoxy composites. *Strojnicki Vestnik/J Mech Eng* 61(10)
3. Zaman HU, Hun PD, Khan RH, Yoon KB (2012) Morphology, mechanical, and crystallization behaviors of micro- and nano-ZnO filled polypropylene composites. *J Reinf Plast Compos* 31(5):323–329. <https://doi.org/10.1177/0731684411436126>
4. Gao Y, Liu L, Zhang Z (2009) Mechanical performance of nano-CaCO₃ filled polystyrene composites. *Acta Mech Solida Sin* 22(6):555–562. [https://doi.org/10.1016/S0894-9166\(09\)60386-4](https://doi.org/10.1016/S0894-9166(09)60386-4)
5. Agubra VA, Owuor PS, Hosur MV (2013) Influence of nanoclay dispersion methods on the mechanical behaviour of e-glass/epoxy nanocomposites. *Nanomaterials* 3(3):550–563. <https://doi.org/10.3390/nano3030550>
6. Yasmin A, Daniel IM (2004) Mechanical and thermal properties of graphite platelet/epoxy composites. *Polymer* 45(24):8211–8219. <https://doi.org/10.1016/j.polymer.2004.09.054>
7. Sayer M (2014) Elastic properties and buckling load evaluation of ceramic particles filled glass/epoxy composites. *Compos B Eng* 59:12–20. <https://doi.org/10.1016/j.composites.2013.11.016>
8. Asi O (2009) Mechanical properties of glass-fiber reinforced epoxy composites filled with Al₂O₃ particles. *J Reinf Plast Compos* 28(23):2861–2867. <https://doi.org/10.1177/0731684408093975>
9. Yang HS, Kim HJ, Son J, Park HJ, Lee BJ, Hwang TS (2004) Rice-husk flour filled polypropylene composites; mechanical and morphological study. *Compos Struct* 63(3–4):305–312. [https://doi.org/10.1016/S0263-8223\(03\)00179-X](https://doi.org/10.1016/S0263-8223(03)00179-X)
10. Uma Devi L, Bhagawan SS, Thomas S (1997) Mechanical properties of pineapple leaf fiber-reinforced polyester composites. *J Appl Poly Sci* 1739–1748
11. Kannan G, Thangaraju R, Kayaroganam P, Davim JP (2022) The combined effect of banana fiber and fly ash reinforcements on the mechanical behavior of polyester composites. *J Nat Fibers* 19(15):11384–11403
12. Salasinska K, Ryszkowska J (2015) The effect of filler chemical constitution and morphological properties on the mechanical properties of natural fiber composites. *Compos Interfaces* 22(1):39–50
13. Rami N, Meghraoui H, Ziraoui R, El khoukhi T, Mouhib M, El Harfi A (2010) Influence of gamma irradiation on the chemical and physical properties of DGEDDS/PDA and DGEDDS / MDA epoxy resins. *J Mater Environ Sci* 1(4):277–288
14. Bhattacharya A, Misra BN (2004) Grafting: a versatile means to modify polymers: techniques, factors and applications. *Prog Polym Sci* 29(8):767–814
15. Form and Style for ASTM Standards, © By American Society for Testing and Materials edition approved in 2010 as D638–10. <https://doi.org/10.1520/D0638-14>
16. Cho D, Lee J (2008) Effect of quasi-carbonization processing parameters on the mechanical properties of quasi-carbon/phenolic composites. *J Appl Polym Sci* 107(5):3350–3357
17. Sathees Kumar S, Kanagaraj G (2016) Investigation of characterization and mechanical performances of Al₂O₃ and SiC reinforced PA6 hybrid composites. *J Inorgan Organometal Polym Mater* 26:788–798
18. Haque MM, Hasan M (2021) TiO₂ and zeolite nanopowder enhanced mechanical properties of hybrid polymer composites. *J Thermoplast Compos Mater* 34(3):382–395

Author Index

A

Abhijit A. Patil, 127
Abhishek Kumar, 43
Afnaan Ali Khan, 1
Anandarao S. Kashid, 127
Aravind, S. L., 1
Arunkumar, K. N., 145

B

Bhaiswar, V. N., 89

C

Chetan, B. G., 1

D

David Gavini, 101
Dileep, C. S., 135

G

Ganesha, B. B., 145

J

Jagadeesha, T., 43, 53, 113

K

Khond, V. W., 89
Kiran Kumar, B., 101

L

Lallianmawii, 13

M

Manasa, C., 135
Maneesh Kumar, P. V., 53, 113
Mohondas Singh, N., 13

N

Nihal Wargantiwar, 89

P

Pallavi, E., 101
Pavankumar Bikki, 101
Poornananda, H., 1
Prashanth, 1

R

Ranjit Wadkar, 29
Ravikiran, 1

S

Sagar, K. G., 79
Sandhya Rani, N., 135
Sathvik, K. S., 1
Sharipov, J. O., 63
Shiyekar, S. M., 29
Shriharsha, K., 1
Srikantamurthy, N., 135
Sudev, L. J., 145

Sunil Kumar, [135](#)

V
Vinod, B., [135](#), [145](#)

T
Thammegowda, C. S., [145](#)



RESEARCH ARTICLE



OPEN ACCESS

Received: 02-12-2022

Accepted: 05-01-2023

Published: 07-02-2023

Citation: Dongre S, Kumar S, Suresh S, Sannappa J (2023) Estimation of Inhalation and Ingestion Dose Due to Radon Concentration in Drinking Water Samples of Shankaraghatta Forest Environment, Karnataka, India. Indian Journal of Science and Technology 16(5): 367-376. <https://doi.org/10.17485/IJST/v16i5.2321>

* **Corresponding author.**

sannappaj2012@gmail.com

Funding: None

Competing Interests: None

Copyright: © 2023 Dongre et al. This is an open access article distributed under the terms of the [Creative Commons Attribution License](https://creativecommons.org/licenses/by/4.0/), which permits unrestricted use, distribution, and reproduction in any medium, provided the original author and source are credited.

Published By Indian Society for Education and Environment ([iSee](https://www.isee.org/))

ISSN

Print: 0974-6846

Electronic: 0974-5645

Estimation of Inhalation and Ingestion Dose Due to Radon Concentration in Drinking Water Samples of Shankaraghatta Forest Environment, Karnataka, India

Sandeep Dongre¹, Sunil Kumar^{1,2}, S Suresh³, J Sannappa^{1*}

¹ Department of PG Studies and Research in Physics, Jnana Sahyadri, Kuvempu University, Shankaraghatta, 577451, India

² Department of Physics, S.S Arts College and T.P Science Institute, Sankeshwar, 591313, India

³ Department of Physics, M.P.E Society's S.D.M College, Honnavara, 581334, India

Abstract

Objectives: To estimate inhalation and ingestion doses due to radon concentration in rural areas of Shankaraghatta forest environment, India.

Methods: In this study, the risk due to radon concentration in underground drinking water samples of the Shankaraghatta region has been estimated using emanometry technique. The 44 drinking water samples were collected from different water sources in sample bottles (500 ml) and were carefully sealed to ensure there is no air gap and were analysed within 24 hours by radon bubbler technique using a Lucas cell. **Findings:** The radon (²²²Rn) concentration in underground and surface water samples of the entire region varies from $1.10 \pm 0.25 \text{ Bq l}^{-1}$ to $30.67 \pm 5.10 \text{ Bq l}^{-1}$ with an average value of $13.10 \pm 2.2 \text{ Bq l}^{-1}$, is higher than the USEPA proposed maximum contamination threshold of 11 Bq l^{-1} . The Annual Effective Dose Equivalent (AEDE) ranges from $3.86 \mu\text{Sv y}^{-1}$ to $83.80 \mu\text{Sv y}^{-1}$ with an average value of $36.35 \mu\text{Sv y}^{-1}$, which is slightly higher than the global average value. **Novelty:** The present work focuses on the public health of the study area where such estimation was not carried out. The estimated annual effective, inhalation and ingestion doses due to radon in underground drinking water samples are found to be substantially below the $100 \mu\text{Sv y}^{-1}$ recommended by WHO and EC. Hence, public of the study area won't receive any serious health hazard due to radon in drinking water and the water is fit for drinking without any additional treatment.

Keywords: Radon Concentration; Underground and Surface water; Emanometry Technique

1 Introduction

The measurement of radon in the environment matrix is important all over the world due to the fact that inhalation of radon and its progeny contribute more than 55% of

the total natural background radiation dose to the human being^(1,2). Testing its level of contamination, monitoring its concentration, assessment of dose due to inhalation and ingestion in underground drinking water is became a priority aspect for purpose of public health awareness but it is challenging to estimate the radiation doses that living things are exposed to as a result of radon and its progeny because of the complex interactions between radon's radioactive progeny, chemical forms, and its attachment to aerosols, as well as the intake, deposition, and retention of radon-related radioactivity in living things. Hence, addressing the existing problems all over the globe, several studies have been carried out by many researchers using both active and passive methods such as CR-39, RAD7, and Lucas Cell⁽³⁾. Regulated levels of this radon in drinking water have been set by numerous international organizations. 11 Bq l^{-1} is the maximum contamination limit (MCL) for radon in drinking water⁽⁴⁾.

In Malaysia Penang region Najeba F. Salih (2021) investigated the radon concentration in drinking water using both active and passive methods (CR-39 & RAD7) and their results show that there is a strong and significant correlation found in both active and passive techniques⁽⁵⁾. In their study, they estimated radon activity concentration in water samples by using both active and passive methods (CR-39). In the passive method to establish equilibrium between the radium and radon the sample is kept in a tube for about 60 days, which is a prolonged period of time (60 days) during this weighting period there is a possibility of samples getting destructed even at the time of etching process or there might be chances of getting back diffusion of radon even though the tube is airtight and care is taken. There is always a bit of risk involved in maintaining the samples for such a long period. Hence, the passive method turns out to be a time-consuming and inconvenient method.

While the active method was implemented by many researchers. Biljana Vuckovic' et al. (2022) in the north of Kosovo region had investigated the radon in drinking water samples of north Kosovo using RAD7 and their results show that radon in drinking water was found to be $12.4 \pm 2.0 \text{ Bq l}^{-1}$ ⁽⁶⁾. In their study, the author studied only two types of water samples and the geological formation predominantly consists of neogenic, sediments, and magmatic rocks.

Suresh et al. (2022) in Uttar Kannada, India investigated the radon concentration in different types of groundwater samples in the Uttar Kannada district using the active method (Emanometry-Lucas cell method) and their result shows that the radon concentration in groundwater samples is $26.23 \pm 0.65 \text{ Bq l}^{-1}$ ⁽⁷⁾. The study area predominantly consists of Lithological formations such as granites, metabasalt, and granitic gneiss. Hence Biljana Vuckovic' et al and Suresh S et al. observed different results because radionuclide content varies with the type of rock system⁽⁸⁾. Therefore, the radon concentration in water samples purely depends upon the local geology and geography of the study area. The present study area consists of Migmatite rock, Granodiorites-Tonalitic gneiss, and Ultramafic Schist. Hence, one can expect variations in radon concentration.

In the present study measurement of activity concentration and annual effective dose of radon in groundwater was carried out using emanometry technique (Lucas cell methods) because Mostafa et al. (2022) used RAD7 for the measurement of radon in water and observed measurements with RAD7 affected by various factors including the sampling method, sample size, counting interval, temperature, relative humidity, and background⁽⁹⁾. This causes errors in the measurement of radon concentration. Hence, in the current study, we have used the Lucas cell method. The key component of the procedure is the washing of radon from a large sample of water (0.75l) to a small volume of air (0.6l), which results in a high radon concentration in the air and gives a significant increase in measurement sensitivity compared to RAD7. Moreover, this method is a convenient, economical, and efficient method, giving almost comparable results recommended by various international research organizations such as UNSCEAR, USEPA, ICRP, EC, and WHO.

In view of this importance and to reduce the possible adverse health effects on human beings. The present study involves the measurement of activity concentrations of radon in 44 water samples from 6 different water resources and the annual effective dose of radon in groundwater samples for different age groups were also estimated. The purpose of the present study focuses on the estimation of radon concentration in drinking water, inhalation, and ingestion dose to the public, to reduce possible health risks, to take preventive measures, and also to provide baseline data for further epidemiological studies in future research work.

2 Methodology

2.1 The Study Area

Shankaraghatta region, which is hilly and rich in natural history, is located between $75^{\circ}39' 30''$ East longitude and $13^{\circ}45' 30''$ North latitude. It is the jewel of the Western Ghats because of its lush hills and high elevation. This area is abundant in biodiversity and is home to numerous endemic species. The districts of Shivamogga and Chikkamagaluru in the state of Karnataka are included in the study region. The region is covered in deep forests, and has steep, hilly Malnad in the west, sparsely forested tablelands, and semi-malnad in the east. It also has several natural water sources, including the Bhadra River, a major supply of portable water, as well as hand pumps and bore wells. The study area is comprised of lithology which includes the rock formations made up of Migmatite rock, Granodiorites-Tonalitic gneiss, and Ultramafic Schist. These rock systems contain radionuclides⁽⁸⁾. The three main types of soil that can be found in the study region are clay, red sandy clay loam, and

habitat masks. Due to this reason, one can expect a higher concentration of radon in this region and in the underground water. Moreover, the Shankaraghatta region in Badhravathi taluk has a population of around 13000 and this region is the hub for higher education, it includes 3500 students 600 teaching and non-teaching staff⁽⁸⁾. This reason the study area is chosen because of the importance of water and public health. Also, this study aims to estimate the inhalation and ingestion doses due to radon in groundwater and to monitor the quality of drinking water from underground and surface water resources. The investigations and collection of samples were carried out during the period of November 2022.

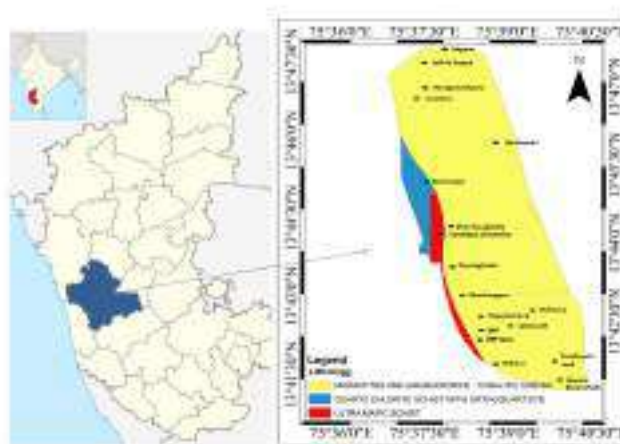


Fig 1. Geological Map of measurement of radon concentration in drinking water samples in the environment of Shankaraghatta

Measurements are carried out using the portable Lucas cell with a programmable alpha counting system and a radon bubbler chamber and it is discussed below.

Drinking water samples were collected from 44 distinct places in the Badhravathi taluk of Shivamogga district's Shankaraghatta and adjacent villages. The bore well, open well, hand pump, and public tap water samples are collected. Four samples were obtained from each site to determine the repeatability of radon concentrations. Water samples were collected (500ml) in an airtight plastic bottle. The plastic bottles were carefully packed to ensure that there was no air gap. Within 24 hours, all of the samples collected were analyzed. The emanometry technique was used to determine the concentration of ²²²Rn in drinking water Figure 2^(1,9). Once when, all the water samples using the aforementioned conventional approach, samples were transported to the laboratory, PSI-RBS-1 model is specially designed for Radon Bubbler, which is made up of corning glass with a leak-free sintered disc, airtight joints and PTFE bore-glass stop cocks^(7,10). Leak-free coupling for gassing and degassing of samples as well as radon sampling to Lucas cells are provided. A radon bubbler is often used to measure the radon concentration of liquid samples. Figure 3 shows the experimental setup of the Emanometry technique.

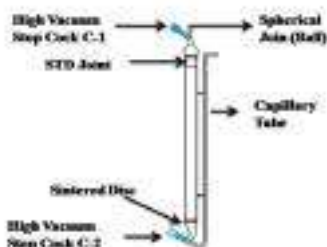


Fig 2. An illustration of a Radon-bubbler



Fig 3. Experimental setup of Emanometry technique

In the bubbler, approximately 70 ml of the water is filled, and the dissolved radon in the water is transported to a Lucas cell that had been pre-evacuated and counted for background counts. Radon is allowed to reach equilibrium with its daughter products for about 3 hours in the Lucas cell.

Lucas Cell: It consists of cylindrical chamber, which is coated internally with ZnS (Ag), has a maximum wavelength of 4500Å with scintillating property. A photomultiplier tube detects the light signal created when an alpha particle collides with the ZnS phosphor and converts it into an electrical count. It's having a radius of 2.2 cm and an interior height of 7 cm. To sample or evacuate radon, one end of it is attached to a Swagelok quick connector, while the opposite window is sealed with transparent glass to couple with a counting device.

Later it is connected to the PMT (photomultiplier) tube and an alpha counting assembly and counted for 17 minutes. The formula used to calculate the radon concentration in the groundwater sample is given in equation (1) below^(10,11).

$$^{222}\text{Rn} (\text{Bql}^{-1}) = \frac{6.97 \times 10^{-2} \times C_B}{E \times V \times (1 - e^{-\lambda\theta_t})e^{-\lambda\theta_t}} \tag{1}$$

Where: C_B is the total Counts above background, V is the volume of water (in L), E represents the Efficiency of the Scintillation/Lucas cell (74%), λ represents decay constant for radon ($2.098 \times 10^{-6} \text{ s}^{-1}$), θ_t , is the delay time after sampling.

2.2 Estimation of Inhalation dose and Ingestion dose due to ²²²Rn in drinking water

The annual effective doses of radon in water for inhalation and ingestion were determined using the formula UNSCEAR (2000) criterion, as given by

$$E_{in} (\mu\text{Svy}^{-1}) = R_{CW} \times R_{aw} \times E_q \times A_{int} \times DCF \tag{2}$$

Where: E_{in} represents the effective dose for inhalation, R_{CW} represents the radon concentration in water (Bql^{-1} or Bqm^{-3}), R_{aw} represents the radon in air to water ratio (10^{-4}), E_q represents the equilibrium factor of radon and its progenies (0.4), A_{int} represents the average indoor occupancy time per individual (7000 ha^{-1}), DCF represents the conversion factor for radon exposure dose [$9 \text{ nSv} (\text{Bqhm}^{-3})^{-1}$].

The following formula is used to calculate the ingestion dose:

$$D_{ing} = R_{CW} \times W_C \times E_D \tag{3}$$

Where: D_{ing} → the effect dose for ingestion, R_{CW} represents the radon concentration levels in drinking water (Bql^{-1}), W_C represents estimated water consumptions (60 la^{-1}), E_D represents the effective ingestion dose (3.5 nSvBq^{-1}).

$$TD_{ing} (\mu\text{Svy}^{-1}) = R_{CW} \times DWC \times C_F \times E_T \tag{4}$$

TD_{ing} Represents total effective dose, R_{CW} represents the radon concentration levels in drinking water (Bql^{-1}), DWC represents daily water consumption E_T exposure time. Table 2 provides the DWC for the public of various age groups, including

infants, children, males, females, pregnant women, and lactating women, for use in determining doses from drinking water consumption^(10,11).

$$\text{Effective Dose } (\mu\text{Svy}^{-1}) = T_{WF} \times D_{In} \cdot D_{Ing} \tag{5}$$

Where: T_{WF} represents the tissue weighting factor (Lungs, Stomach; $T_{WF}=0.12$)

3 Result and Discussion

3.1 Radon concentration in the drinking water

Table 1 shows the average radon concentration of 44 drinking water samples collected from different locations of the Shankaraghatta. The average values of radon concentration in drinking water samples vary from $1.41 \pm 0.25 \text{ Bq l}^{-1}$ to $30.67 \pm 5.10 \text{ Bq l}^{-1}$, with an average value of $13.10 \pm 2.2 \text{ Bq l}^{-1}$. The drinking water samples collected from groundwater sources such as bore wells and hand pumps have shown higher radon concentrations among all the samples that are analyzed. This may be due to its increased depth, which allows water to interact with a thicker aquifer, resulting in higher levels of radon in hand pumps and bore wells^(7,12).

The higher concentration of radon in the drinking water was found at locations such as the Farmland, Teacher’s Quarters, Ladies hostel Lakkavalli Five Light Circle, Karkucchi road, Sogane and Ranganathpura. This may be due to the presence of a granodiorite gneiss rock system (Figure 1). This region consists of the geology of quartz chlorite Schist with orthoquartzite which consists of mineral composition, the depth of groundwater sources also plays a predominant role for higher concentration^(7,10). A granitoid is a 90 percent coarse-grained material. It has a quartz content of 20–60% and a plagioclase content of 65–90%. The roughly analogous intrusive rock to rhyodacite is composed of coarse-grained plutonic rocks that contain quartz, plagioclase (oligoclase or andesine), and minerals like subordinate potassium feldspar. Mafic components may also include biotite, hornblende, or, less frequently, pyroxene.⁽¹³⁾ The lower concentration is observed at B.R.P Gramapachayath, Singanamane village bore wells, this may be due to the less depth of bore well. Migmatite and granodiorite dominate the research region. These rocks contain quartz, clays, orthoclays, biotite, amphibol, hornblend, and silicate as their main minerals⁽⁸⁾. The mineral makeup of feldspar and other minerals affects the radionuclides⁽¹⁴⁾. The lower concentration was found for surface water at locations such as Gonibeedu, Channel, BRP Dam water, and Shanthinagara pond. This may be due to diffusion losses to the atmosphere⁽¹⁵⁾.

The maximum radon contamination limit (MRCL) in groundwater has been proposed by the US Environmental Protection Agency to be 11.1 Bq l^{-1} ⁽¹⁶⁾. It is clear from this that among all the samples 75 percent of bore wells and hand pumps contain radon concentration values of more than 11.1 Bq l^{-1} . The United Nations Scientific Committee on the Effects of Atomic Radiation recommends a radon concentration in drinking water vary from 4 to 40 Bq l^{-1} for human consumption⁽¹⁷⁾. It is clear from the data (Table 1) that all the water samples of the study area contained radon values of less than 40 Bq l^{-1} . The average measured radon concentration in drinking water samples of the Shankaraghatta region was found to be 13.10 Bq l^{-1} , which is higher compared to the US Environmental Protection Agency⁽¹⁶⁾ for public protection against radon exposure in drinking water supplies, and lower compared to the WHO’s recommended radon in drinking water limit, which advises a 100 Bq l^{-1} action level for public water supplies⁽¹⁸⁾. When these data are compared, it is clear that the major source of health risk in the case of water is radon inhalation. Our average annual effective doses of $2.80 \mu\text{Svy}^{-1}$ and $33.57 \mu\text{Svy}^{-1}$ from radon in water owing to ingestion and inhalation respectively, which are marginally higher than average annual effective doses of 2 and $25 \mu\text{Svy}^{-1}$ due to ingestion and inhalation⁽¹⁹⁾. The findings show that the total annual ingestion dose exposure from the water samples was significantly below the WHO standard threshold of $100 \mu\text{Svy}^{-1}$, indicating that the ^{222}Rn dosages ingested by water in the study locations does not pose any health risks.

When compared to radon gas inhalation, the radiation dosage from radon in drinking water is modest. Both of these radon sources, however, should be treated with caution and should take appropriate precautions to reduce radon exposure through drinking water. As a result, according to state legislation, any new supply of drinking water must undergo radon and another radioactive testing before being utilized for public use⁽²⁰⁾.

Table 1. The average ^{222}Rn concentration in 44 drinking water samples of different locations in Shankaraghatta region

Sl. No	Name of the Locations	Type of water Source	^{222}Rn Conn. (Bq l^{-1})	Annual Effective Dose Equivalent Total Dose (μSvy^{-1})				
				Inhalation (a)	Lung	Ingestion (b)	Stomach	Total (a+b)

Continued on next page

Table 1 continued

1	Shankaraghatta	OW	03.24 ± 0.50	08.05	1.00	0.67	0.10	08.72
2	Kuvempu University-1	BW	17.94 ± 0.95	45.07	5.41	3.76	0.50	48.82
3	Kuvempu University-2	TW	02.41 ± 1.29	06.08	0.73	0.51	0.10	06.59
4	Teachers Quarters	BW	28.21 ± 2.00	71.00	8.50	5.90	0.70	77.50
5	Ladies hostel	BW	25.10 ± 0.50	63.20	7.60	5.30	0.59	68.50
6	Kuvempu Nagara	BW	09.37 ± 1.29	23.78	2.85	1.98	0.24	25.76
7	Tipperudrappa layout	BW	12.22 ± 2.57	30.79	3.69	2.57	0.31	33.35
8	Kudremukh Layout	BW	14.08 ± 0.95	35.60	4.27	2.97	0.36	38.57
9	Tavaraghatta-1	BW	10.06 ± 3.90	25.41	3.05	2.12	0.25	27.52
10	Tavaraghatta-2	HP	11.29 ± 2.89	28.41	3.41	2.37	0.30	30.78
11	Malenahalli-1	BW	10.24 ± 4.10	25.79	3.10	2.15	0.30	27.94
12	Malenahalli-2	HP	12.44 ± 2.76	31.25	3.75	2.60	0.31	33.85
13	Sompura Road-1	HP	14.67 ± 1.29	37.05	4.45	3.09	0.40	40.13
14	Sompura Road-2	BW	16.86 ± 0.75	42.51	5.10	3.54	0.43	46.05
15	Gonibeedu-1	HP	11.67 ± 3.30	29.41	3.53	2.45	0.30	31.86
16	Gonibeedu-2	BW	13.29 ± 3.50	33.63	4.04	2.80	0.30	36.43
17	Gonibeedu-3	CW	1.41 ± 0.25	03.57	0.43	0.30	0.04	03.86
18	Tammadi Halli	HP	12.29 ± 2.70	31.10	3.73	2.59	0.31	33.69
19	Farm Land	BW	30.67 ± 3.30	77.30	9.30	6.40	0.80	83.80
20	Junction-1	BW	15.24 ± 5.10	38.19	4.58	3.18	0.38	41.37
21	Junction-2	HP	16.45 ± 0.95	41.50	4.98	3.46	0.41	44.96
22	Umble bailu road	HP	12.01 ± 2.20	30.27	3.63	2.59	0.30	32.80
23	Ranganathpura	HP	23.08 ± 2.10	58.32	7.00	4.86	0.58	63.18
24	Lakkin Koppa -1	BW	19.78 ± 4.25	49.92	5.99	4.16	0.50	54.08
25	Lakkin Koppa-2	TW	1.80 ± 0.45	04.60	0.55	0.38	0.03	04.98
26	Kallihalu	BW	9.50 ± 1.50	23.93	2.87	1.99	0.24	25.93
27	Sogane	BW	23.22 ± 3.25	58.57	7.03	4.88	0.59	63.45
28	Shanthinagara-1	HP	11.50 ± 3.10	28.87	3.46	2.41	0.29	31.28
29	Shanthinagara-2	PW	1.57 ± 0.25	04.06	0.50	0.33	0.04	04.31
30	BRP	HP	10.18 ± 2.80	25.61	3.07	2.13	0.26	27.75
31	B.R.P.Grama panchayath	BW	8.06 ± 1.57	20.54	2.46	1.71	0.21	22.25
32	Singanamane-1	BW	8.89 ± 2.45	22.42	2.69	1.87	0.22	24.29
33	Singanamane-2	HP	13.29 ± 3.50	33.52	4.02	2.79	0.34	36.31
34	Bhadra Dam -1	RW	1.57 ± 0.25	04.06	0.49	0.34	0.04	04.40
35	Bhadra Dam -2	BKW	1.73 ± 0.57	04.24	0.51	0.35	0.04	04.60
36	Garage camp	HP	10.19 ± 2.19	25.73	3.09	2.14	0.26	27.88
37	Vadiyuru	HP	10.56 ± 1.81	26.60	3.19	2.22	0.27	28.81
38	Lakkavalli Five Light Circle	HP	28.37 ± 3.38	71.61	8.59	5.97	0.72	77.58
39	Lakkavalli Canara bank	HP	14.11 ± 4.30	35.48	4.26	2.96	0.35	38.44

Continued on next page

Table 1 continued

40	Uppara beerana Halli	HP	15.50 ± 2.85	39.01	4.68	3.25	0.39	42.26
41	Nellisara-1	BW	18.61 ± 3.75	46.86	5.62	3.91	0.47	50.77
42	Nellisara-2	HP	16.24 ± 3.25	40.73	4.89	3.39	0.41	44.12
43	Karkucchi Road	BW	23.29 ± 2.50	58.59	7.03	4.88	0.59	63.47
44	Someshwara temple	OW	4.37 ± 1.57	11.18	1.34	0.93	0.11	12.111
	MAX		30.67 ± 5.10	77.30	9.30	6.40	0.80	83.80
	MIN		1.41 ± 0.25	3.57	0.43	0.30	0.03	3.86
	AVG		13.10 ± 2.20	33.54	4.03	2.80	0.34	36.35
	GM		10.20 ± 1.70	26.27	3.16	2.19	0.27	28.45
	SD		7.50 ± 1.30	18.88	2.26	1.57	0.19	20.49

(Note: OW=Open Well; BW=Bore Well; HP = Hand Pump; TW= Tank Water; PW=Pond Water; RW=River Water= Channel water; BKW= Back Water)

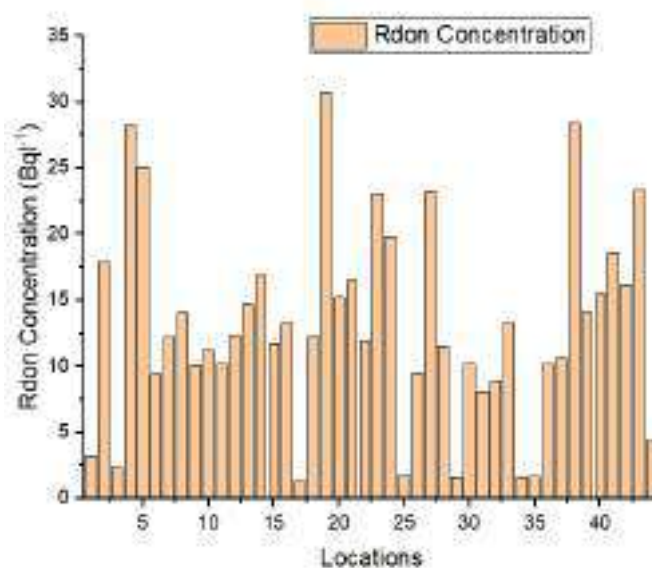


Fig 4. Radon Concentration v/s different locations

Figure 4 shows the variation of wide variation of ^{222}Rn concentration in 44 different locations of the Shankaraghatta forest environment. This might be because radionuclides like ^{238}U and ^{226}Ra , which are present in soil and rocks in various concentrations are present⁽⁷⁾. As a result, radon can easily pass through porous rocks that are beneath saturated underground aquifers. The radon that is present in the soil and rocks may readily dissolve into the water when it comes from these pores and be carried there with it⁽⁷⁾. Various factors influence the radon concentration in water such as geology, the type of aquifer found in those particular locations⁽¹²⁾. The higher radon concentration is indeed mostly due to the deeper wells and hand pumps. The hand pumps and deeper bore wells enable more water to interact with the aquifer’s substantial thickness^(7,10).

Figure 5 shows the variation of radon concentration in different sources of drinking water samples, the graph clearly shows that the radon concentration from groundwater samples such as bore well, hand pumps, and open well has shown higher concentrations than the surface water samples. This may be due to the fact that the depth of the bore well and hand pump, greater the depth means it allows water to interact with the aquifers significantly, and also this may be due to the radionuclides present in the soil and rock system^(7,10,12,18). But the radon concentration in the tap water (TP), backwater (BKW), and pond (P) have shown lower radon concentration this may be due to dissolved radon being disrobed and later released along the path water body source and the sample collection point. Also, surface water shows lower radon concentration⁽¹²⁾, because of variations in atmospheric temperature, moreover surface water is well exposed to the atmosphere therefore dissolved radon gets easily discharged. Hence, lower concentrations can be found⁽¹⁰⁾.

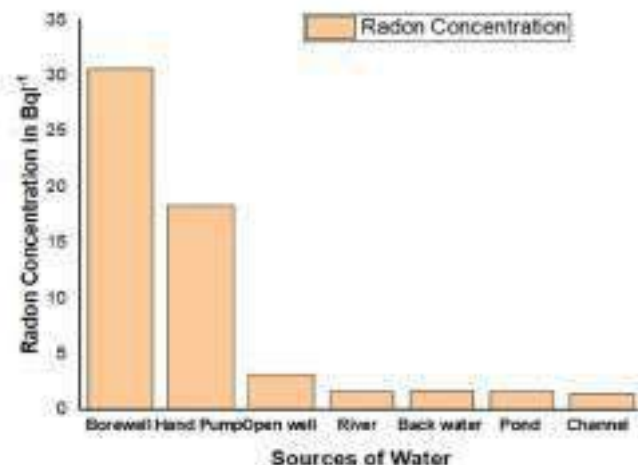


Fig 5. Variation of radon concentration in different sources of drinking water sample

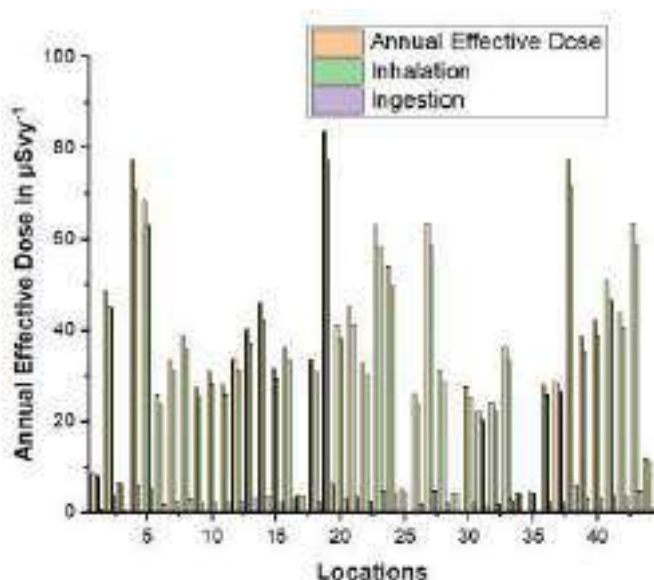


Fig 6. Variation of Inhalation, Ingestion & Annual effective dose equivalent with different Alocations of Shankaraghatta

3.2 Annual effective dose equivalent

Figure 6 shows the variation of the total dose, inhalation, and ingestion dose with locations. The inhalation dose of the study area varies from $3.57 \mu\text{Sv y}^{-1}$ to $77.30 \mu\text{Sv y}^{-1}$ with an average of $33.54 \mu\text{Sv y}^{-1}$. The ingestion dose received varies from $0.30 \mu\text{Sv y}^{-1}$ to $6.40 \mu\text{Sv y}^{-1}$ with an average of $2.80 \mu\text{Sv y}^{-1}$. The quantity of radon reaching the lung varies from $0.43 \mu\text{Sv y}^{-1}$ to $9.30 \mu\text{Sv y}^{-1}$ with an average of $4.03 \mu\text{Sv y}^{-1}$. The quantity of radon from these sources reaching the stomach varies from 0.03 to 0.80 with an average of 0.34 and the total annual effective dose rate due to both inhalation and ingestion varies from 3.86 to $83.80 \mu\text{Sv y}^{-1}$ with a mean of $36.35 \mu\text{Sv y}^{-1}$, which is less than the $100 \mu\text{Sv y}^{-1}$ of global average value as per the European Commission (EC) and World Health Organization (WHO)^(12,21,22). The estimated radon inhalation and ingestion doses from water are higher than the recommendations^(1,9).

For people of various ages, the ingestion dose was calculated based on annual water intake in order to determine the potential harmful effects of radon on health. Table 2 provides a summary of the calculated total annual ingestion doses to individuals in various age groups. The fact that infants and children drink less water than adults may be the reason why the mean ingestion

dose exposure to ^{222}Rn in drinking water is significantly below the UNSCEAR and WHO recommended limit of $100(\mu\text{Svy}^{-1})$. The average adult radon ingestion dosage exposures were a little bit higher than the UNSCEAR and WHO-recommended limit^(7,10).

Table 2. Annual effective dose equivalent estimated due to ingestion of radon in drinking water of different age groups

Life Stage	Age Group	DWI(L/day)	(Annual Effective Ingestion Dose(μSvy^{-1}))				
			Min	Max	GM	Avg.	SD
Infants	0-6months	0.7	3.45	75.14	24.99	32.10	18.38
	7-12months	0.8	3.94	85.87	28.56	36.68	21.00
Children	1-3	1.3	6.41	139.54	46.41	59.61	34.13
	4-12	1.7	8.38	182.48	60.69	77.95	44.63
Males	9-13	2.4	11.84	257.62	85.68	110.04	63.00
	14-18	3.3	16.28	354.23	117.81	151.31	86.63
	Adults	3.7	18.25	397.17	132.09	169.65	97.13
Females	9-13	2.1	10.36	225.42	74.97	96.29	55.13
	14-18	2.3	11.35	246.89	82.11	105.46	60.38
	Adults	2.7	13.32	289.83	96.39	123.80	70.88
Pregnancy	17-18	3	14.80	322.03	107.10	137.55	78.75
	19-50	3	14.80	322.03	107.10	137.55	78.75
Lactation	14-18	3.8	18.75	407.91	135.66	174.23	99.75
	19-50	3.8	18.75	407.91	135.66	174.23	99.75

4 Conclusion

Airborne radon is a significant source of natural radiation. Because it dissolves quickly in water, it poses a risk of radiation exposure. In places with granite deposits, high quantities of radon are found in the water. Water seeping through ore deposits carries away Radon and Radium generated by the decay of Uranium found in Granite, and it ends up in well water. The radon concentration in (^{222}Rn) all samples actually utilized by the residents of the study area is higher than the USEPA proposed maximum contamination threshold of 11Bql^{-1} , according to previous study⁽¹⁶⁾. It is clear from this study that 75 percent of bore well and hand pump water samples contain radon values of more than 11Bql^{-1} . The entire study area's annual effective dose equivalent value is very much less than the safe limit of $100\mu\text{Svy}^{-1}$ ^(7,12,22). The exposure to radon from drinking water will not pose any health effects to the public of the study area. When compared to lung tissues exposed to airborne waterborne radon by breathing, the annual effective dose equivalent absorbed by stomach walls through ingestion was much lower. Therefore, there is no need for additional treatment because the water is fit for drinking. But the groundwater sources such as Borewell, and Handpump which exceed the maximum contamination limit should be treated with granular activated carbon (GAC) filters (which use activated carbon to remove the radon). Radon exposure has been linked to an increased risk of developing stomach and lung cancer. Additionally, epidemiological studies must be conducted to determine the prevalence of stomach and lung cancer in the research area and other locations of Shankaraghatta where the highest concentration is observed.

Acknowledgement

Authors thank the Department of PG Studies and Research in Physics, Jnana Sahyadri Kuvempu University, and Shankaraghatta-577451 for providing laboratory facility.

References

- 1) UNSCEAR 2019 report United Nations Scientific Committee on the Effects of Atomic Radiation. . Available from: <https://www.unscear.org/unscear/en/publications/2019.html>.
- 2) Harrison JD, Marsh JW. ICRP recommendations on radon. *Annals of the ICRP*. 2020;49(1_suppl):68–76. Available from: <https://doi.org/10.1177/0146645320931974>.
- 3) Abojassim AA. Comparative study between active and passive techniques for measuring radon concentrations in groundwater of Al-Najaf city, Iraq. *Groundwater for Sustainable Development*. 2020;11:100476. Available from: <https://doi.org/10.1016/j.gsd.2020.100476>.

- 4) Suresh S, Rangaswamy DR, Srinivasa E, Sannappa J. Measurement of radon concentration in drinking water and natural radioactivity in soil and their radiological hazards. *Journal of Radiation Research and Applied Sciences*. 2020;13(1):12–26. Available from: <https://doi.org/10.1080/16878507.2019.1693175>.
- 5) Salih NF. Determine the Contaminations of Radon in the Drinking Water Using NTDs (CR-39) and RAD7 Detectors. *Arabian Journal for Science and Engineering*. 2021;46(6):6061–6074. Available from: <https://doi.org/10.1007/s13369-020-05267-y>.
- 6) Vučković B, Kurilić SM, Nikolić-Bujanović L, Todorović N, Nikolov J, Živković Radovanović J, et al. Radon in drinking water from alternative sources of water supply in the north of Kosovo. *Radiation Protection Dosimetry*. 2023;199(1):44–51. Available from: <https://doi.org/10.1093/rpd/ncac222>.
- 7) Suresh S, Srinivasa E. Study on Estimation of Inhalation and Ingestion Dose due to 222 Rn Concentrations in Different Types of Ground Water of Some Taluks of. *Journal of Scientific Research*. 2022;14(3):891–900. Available from: <https://doi.org/10.3329/jsr.v14i3.57163>.
- 8) Dongre S, Kumar S, Suresh S, Rangaswamy DR, Sannappa J. Assessment of natural radiation levels in the forest ecosystem of Shankaraghatta-Shivamogga District, India. *Journal of Radioanalytical and Nuclear Chemistry*. 2022;331(7):2825–2847. Available from: <http://dx.doi.org/10.1007/s10967-022-08354-6>.
- 9) Mostafa M, Olaoye MA, Ademola AK, Jegede OA, Saka AA, Khalaf H. Measurement of Radon Concentration in Water within Ojo Axis of Lagos State, Nigeria. *Analytica*. 2022;3(3):325–334. Available from: <https://doi.org/10.21203/rs.3.rs-1397022/v2>.
- 10) Suresh S, Srinivasa E. Study on Estimation of Inhalation and Ingestion Dose due to 222 Rn Concentrations in Different Types of Ground Water of Some Taluks of. *Journal of Scientific Research*. 2022;14(3):891–900. Available from: <https://doi.org/10.3329/jsr.v14i3.57163>.
- 11) Hidayath M, Chandrashekar MS, Rani KSP, Namitha SN. Studies on the concentration of 226Ra and 222Rn in drinking water samples and effective dose to the population of Davanagere district, Karnataka state, India. *Journal of Radioanalytical and Nuclear Chemistry*. 2022;331(4):1923–1931. Available from: <http://dx.doi.org/10.1007/s10967-022-08240-1>.
- 12) Yashaswini T, Ningappa C, Niranjana RS, Sannappa J. Radon Concentration Level in Ground and Drinking Water around Kabini River Basin, Karnataka. *Journal of the Geological Society of India*. 2020;95(3):273–278. Available from: <https://doi.org/10.1007/s12594-020-1425-0>.
- 13) Orosun MM, Ajibola TB, Akinyoshe FC, Osanyinlusi O, Afolayan OD, Mahmud MO. Assessment of ambient gamma radiation dose and annual effective dose associated with radon in drinking water from gold and lead mining area of Moro, North-Central Nigeria. *Journal of Radioanalytical and Nuclear Chemistry*. 2021;328(1):129–136. Available from: <https://doi.org/10.1007/s10967-021-07644-9>.
- 14) Nagabhushana SR. Study on Radon Concentration in ground water and Physicochemical parameters of Tumkur industrial areas, Karnataka State, India. *International Journal of Scientific Research in Physics and Applied Sciences*. 2019;7(2):44–54. Available from: <http://dx.doi.org/10.26438/ijrps/v7i2.4454>.
- 15) Srinivasamoorthy K, Ponnunani G, Prakash R, Gopinath S, Saravanan K, Vinnarasi F. Tracing groundwater inputs to Bay of Bengal from Sankarabarani River Basin, Pondicherry, India, using continuous radon monitoring. *International Journal of Environmental Science and Technology*. 2019;16(10):5513–5524. Available from: <http://dx.doi.org/10.1007/s13762-018-1938-x>.
- 16) Srinivasa E, Rangaswamy DR, Sannappa J. Measurement of Radon Concentration and Evaluation of Total Dose in Drinking Water of Chikmagalur City, Karnataka. *Journal of the Geological Society of India*. 2019;94(1):100–104. Available from: <http://dx.doi.org/10.1007/s12594-019-1273-y>.
- 17) Kumar V, Gudennavar P, Chandrashekar SB, Bubbly MS, Hamsa SG, S K. Radon in groundwater of Magadi Taluk, Ramanagara district in Karnataka. 2019. Available from: <https://doi.org/10.1093/rpd/ncy176>.
- 18) Singh B, Kant K, Garg M. Ingestion/inhalation dose due to intake of 222Rn in the water of district Gurugram, Southern Haryana, India, measured by alpha scintillometry technique. *International Journal of Environmental Analytical Chemistry*. 2022;p. 1–12. Available from: <https://doi.org/10.1080/03067319.2022.2115893>.
- 19) Kumar M, Kumar P, Agrawal A, Sahoo BK. Radon concentration measurement and effective dose assessment in drinking groundwater for the adult population in the surrounding area of a thermal power plant. *Journal of Water and Health*. 2022;20(3):551–559. Available from: <https://doi.org/10.2166/wh.2022.265>.
- 20) Opoku-Ntim I, Andam AB, Akiti TT, Fletcher JJ, Roca V. Annual effective dose of radon in groundwater samples for different age groups in Obuasi and Offinso in the Ashanti Region, Ghana. *Environmental Research Communications*. 2019;1(10):105002. Available from: <https://doi.org/10.1088/2515-7620/ab42d8>.
- 21) Water Sanitation and Health. . Available from: <https://www.who.int/teams/environment-climate-change-and-health/water-sanitation-and-health/water-safety-and-quality/publications>.
- 22) Guidelines for drinking-water quality. . Available from: <https://www.who.int/publications-detail-redirect/9789240045064>.

Modification of Optical Parameters of Solid Polymer Electrolyte Films for Optoelectronic Device Applications

Sunil Kumar^{1,2} and Sannappa J^{1*}

¹Department of PG Studies and Research in Physics, Jnana Sahyadri, Kuvempu University Shankaraghatta, India

²Department of Physics, S.S Arts College and T.P Science Institute, Sankesbwar, India

*Correspondence to:

Sannappa J
Department of PG Studies and Research in
Physics, Jnana Sahyadri, Kuvempu University
Shankaraghatta, India
E-mail: Sannappaj2012@gmail.com

Received: October 28, 2022

Accepted: February 17, 2023

Published: February 20, 2023

Citation: Kumar S, Sannappa J. 2023. Modification of Optical Parameters of Solid Polymer Electrolyte Films for Optoelectronic Device Applications. *NanoWorld J* 9(1): 8-14.

Copyright: © 2023 Kumar and Sannappa. This is an Open Access article distributed under the terms of the Creative Commons Attribution 4.0 International License (CCBY) (<http://creativecommons.org/licenses/by/4.0/>) which permits commercial use, including reproduction, adaptation, and distribution of the article provided the original author and source are credited.

Published by United Scientific Group

Abstract

In this work, a time saving, and economical solution cast approach was applied to make solid polymer electrolyte films using hydroxypropyl methylcellulose and sodium bromide. A range of techniques was used to characterize the films, such as Ultraviolet-Visible (UV-Vis) spectroscopy and X-ray diffraction (XRD). The optical factors like refractive index (n), dielectric properties including real and imaginary parts (ϵ_1 and ϵ_2), optical conductivity and extinction coefficient were investigated. The absorption edge (E_g) was relocated with increase of salt to a province of lower photonic energy. This caused the rapid decrease of direct and indirect optical bandwidth gaps from 5.59 to 2.57 eV and 4.61 to 2.44 eV. The optical dielectric loss approach was successfully adopted as a stand-in method for determining the optical band gap. The optical dielectric constant variation with change in optical band gap verified Penn's model. The XRD spectra was used to examine the structural variation, the extent of interaction was evidenced by the relatively wide amorphous phase of the hydroxypropyl methylcellulose (HPMC) polymer with an increase of the NaBr salt. Finally, Tauc's approach was used to specify different kinds of electrical transitions within the polymer matrix. The solid polymer electrolyte with an expanded amorphous percentage is key factor for application in optoelectronic devices.

Keywords

Solid polymer electrolyte, Optical band gap, Penn's model, Optical dielectric function, Dielectric loss method

Introduction

Nowadays energy conversion and storage devices generally use solid polymer electrolytes (SPEs). Because they are environmentally friendly, leakage-free, combustion-free, flexible, lightweight, solvent-free, forms films, and importantly it has good ion transport property compared to the liquid ionic solution [1-3]. Moreover, these SPE qualities may be tailored to any desired shape, making them appropriate for mass manufacture. The first SPE was reported based on poly (ethylene oxide) complexed with alkali metal salts in the year 1973 by Fenton et al. [4]. Later, Vashishta et al. [5] showed that ionic conductivity of such complexations could reach 10^{-5} S/cm under room temperature, this promised the development SPEs. Later, a number of studies took place on SPEs showing good results on optical and conductivity parameters. The easy processing and low-cost production of polymer-based optical communications are attracting more attention than silica-based optical materials [6, 7]. Previous research has shown that functional materials and biopolymer composites with appropriate optical band gaps are ideal for optoelectronic devices and organic light-emitting diodes [8-12]. However, one of the most difficult jobs for photovoltaic and optoelectronic applications is

establishing a suitable band gap material [13]. The majority of conjugated polymers are reported to be narrow-band gap polymers. However, conjugated polymers have some disadvantages, such as poor performance and rapid decomposition [14, 15]. Instead, polar polymers such as cellulose and chitosan are relatively inexpensive with good film-forming and long-life properties. The current study used HPMC as a host polymer. Because of its distinct advantages over other cellulose-based polymers. It is thermally stable and forms stable thin films, making it the preferred host polymer. It is frequently used in the biomedical and pharmaceutical fields since it is environmentally safe and non-toxic. In addition to this, nowadays HPMC is used in various industries because it is water soluble and dissolves a variety of metal salts [16, 17]. Here the dopant used is Sodium bromide because recently sodium-based solid polymer electrolytes are attracting more attention than lithium. Because sodium ion is readily available, economic and more moisture resistant than lithium [18-21]. However, the energy density of sodium would not exceed that of lithium, but this is not a significant concern in the sphere of large-scale production, where operating costs and durability are the most essential factors [22, 23].

The optical spectrum is a valuable resource for understanding band structure and optical parameters of polymers [6]. In this work, we incorporated NaBr into an HPMC polymer in order to achieve the desired optical properties. In this report, it is shown that the amorphous segment of HPMC improved, and the optical band gap energy decreased. The solution cast methodology and small optical energy gap show the significance of the current study.

Materials and Methods

The solution cast method was used to make HPMC-based polymer electrolytes. All analytic grade NaBr and HPMC chemicals were furnished from Sigma Aldrich. The pure film was prepared by mixing 3 gm of HPMC powder in 100 ml of triple distilled water (3 wt%) and stirring the liquid for many hours at room temperature with a magnetic stirrer until the HPMC is completely dissolved. Furthermore, NaBr with a suitable weight percentage ratio (0.2 wt%, 0.4 wt%, and 0.8 wt%) was added to each generated 3 wt% (100 ml) of HPMC polymeric solution for 10 - 12 h under constant stirring. After that, solutions were put in a flattened glass slab/petri dish and allowed to evaporate for 5 days. Finally, the film samples were maintained in desiccators for further study.

Following film preparation, samples were tested by XRD and UV-Vis spectroscopy. The structural analysis of the produced polymer film was performed using the Rigaku Mini-flex-II X-ray diffractometer with Ni filtered, $\text{CuK}\alpha$ radiation ($\lambda = 1.540 \text{ \AA}$). A double-beam UV-Vis spectrometer was used to evaluate the optical characteristics of all samples (Lambda 35).

Results and Discussion

Absorption and transmittance study

The addition of NaBr profoundly affected the polymer's optical response. Figure 1 shows absorbance spectra between

200 and 800 nm. The methyl groups $n-\pi^*$ transition might be responsible for the 270 nm absorption band [24-26]. This band is shifted to a higher wavelength and an increase of absorbance takes place with salt concentration due to intermolecular stacking. The intensity of absorption is determined by the number of absorbing molecules. This is in agreement with previous studies and findings [27-30].

Figure 2 shows a transmittance plot. In the visible range,

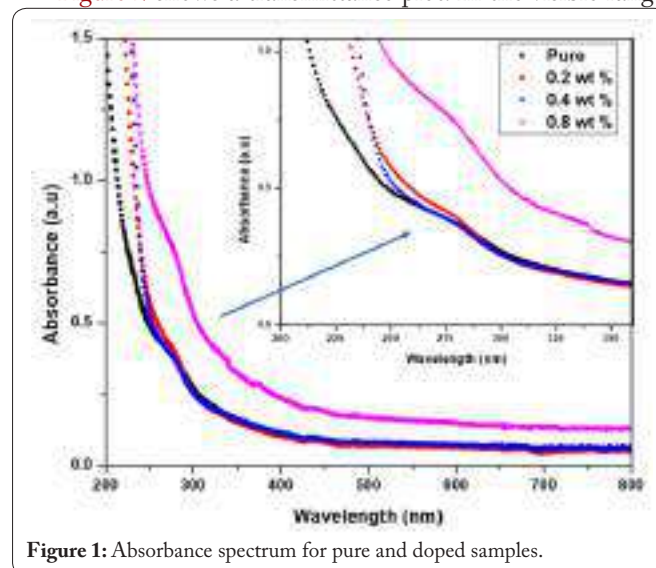


Figure 1: Absorbance spectrum for pure and doped samples.

pure HPMC exhibits accountable transparency of around 90%. HPMC is a transparent polymer [31]. However, increasing the salt content reduces transparency due to changes in the refractive index. This occurs as a result of scattering within the doped layers, which alters the refractive index [32]. However, maintaining the transparency of doped films is challenging. Significantly, the visible range transparency of the doped samples was observed to be greater than 70%.

Refractive index analysis (n)

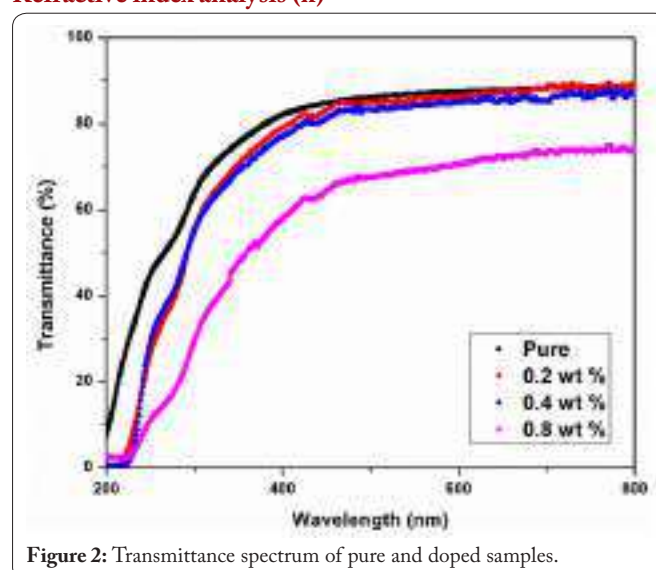


Figure 2: Transmittance spectrum of pure and doped samples.

The optical refractive index (n) of the medium, is one of the crucial parameters that can be obtained by equation (1) [33]. Figure 3 illustrates the proper dispersion behaviour, as

the wavelength rises, the refractive index falls [34]. This dispersion behavior is key for the design of optical systems [32]. In the visible zone, n is non-dispersive and does not equal zero. This alteration in the n value is proof that interactions between photons and electrons are taking place in the films.

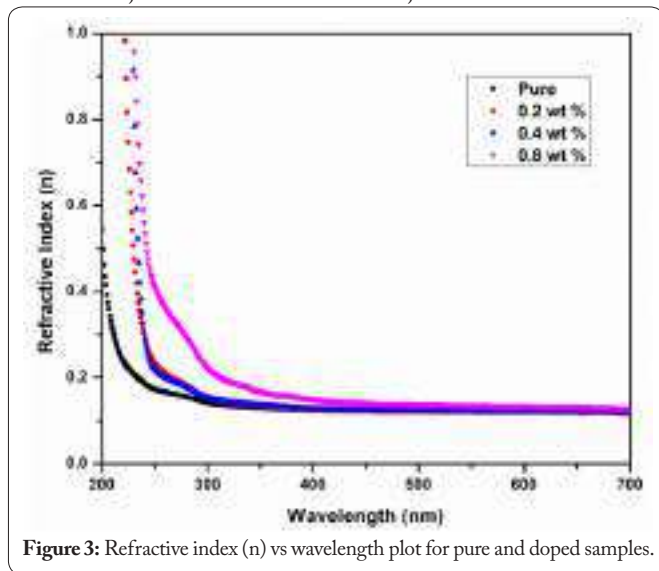
$$n = \frac{1}{T_s} + \sqrt{\frac{1}{T_s} - 1} \quad (1)$$

Where, T_s is the percentage transmission coefficient.

The absorption coefficient (α) is obtained by the equation (2) [35].

$$\alpha = \frac{1}{d} \ln\left(\frac{1}{T}\right) = \frac{2.303 A}{d} \quad (2)$$

Where, d denotes film thickness, A denotes absorbance,



and T denotes transmittance.

The absorption edge obtained from the absorption coefficient is used to classify the material [30]. The absorption edge is obtained by extrapolating the linear segment of the curves to zero absorption ($\alpha = 0$). The pure film absorption edge (E_e) was 4.84 eV; however, it was reduced to 2.53 eV for 0.8 wt% NaBr films (shown in Table 1). The increase in intermolecular stacking and intramolecular charge transfer is responsible for the substantial change in the absorption edge in doped films [17].

Band gap study

The Tauc and Davis-Mott equation (3) [36] was used to assess the band gap of the samples.

$$\alpha = A(h\nu - E_g)^r \quad (3)$$

Where, E_g is optical energy bandgap, r is the exponent factor takes the values of $1/2$, 2, $3/2$ and 3 for direct and indirect allowed and forbidden electron excitations, respectively [37] (Figure 4).

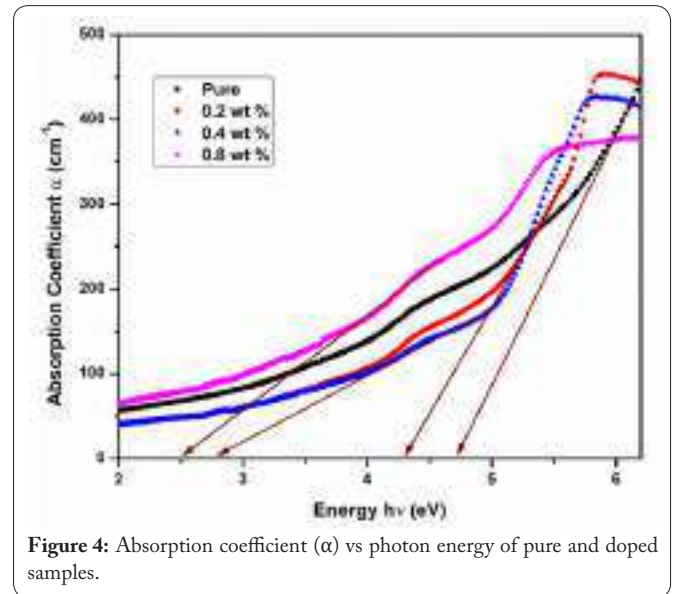


Figure 4: Absorption coefficient (α) vs photon energy of pure and doped samples.

The fluctuation of $(\alpha h\nu)^2$ and $(\alpha h\nu)^{1/2}$ as a function of the photon energy ($h\nu$) at ambient temperature is shown in figures 5 and 6, respectively. The linear area of curves may be connected to the shifts between the valence and conduction bands via the direct energy band gap (E_d) and indirect energy band gap (E_{ind}) transitions [38]. These values are calculated by extrapolating the linear section to zero absorption are shown in Table 1. The values E_d and E_{ind} fell from 5.59 to 2.57 eV and 4.61 to 2.44 eV, respectively. This illustrates that when the salt level increases, the samples become more semiconducting [39]. This would be due to an increase in the valence and conduction band shift. Furthermore, the existence of unsaturated defects enhances the density of localized states in the band gap, resulting in a decrease in the optical energy gap [40, 41].

Extinction coefficient (K)

The extinction coefficient (K) is the amount of light that is lost due to scattering and absorption per unit distance of penetrating medium. The increase in extinction coefficient with increasing photon energy shown in Figure 7 indicates that a fraction of light is reduced due to scattering and absorption increases. This is because absorption decreases at lower energy when the

Table 1: Absorption edge, direct bandgap, indirect bandgap, and estimated band gap at room temperature.

Sl. No.	HPMC/NaBr wt%	Absorption edge (E_e) eV	Direct bandgap (E_d) eV	Indirect bandgap (E_{ind}) eV
1.	Pure HPMC	4.84	5.59	4.61
2.	0.2	4.28	3.72	4.25
3.	0.4	2.75	3.44	2.64
4.	0.8	2.53	2.57	2.44

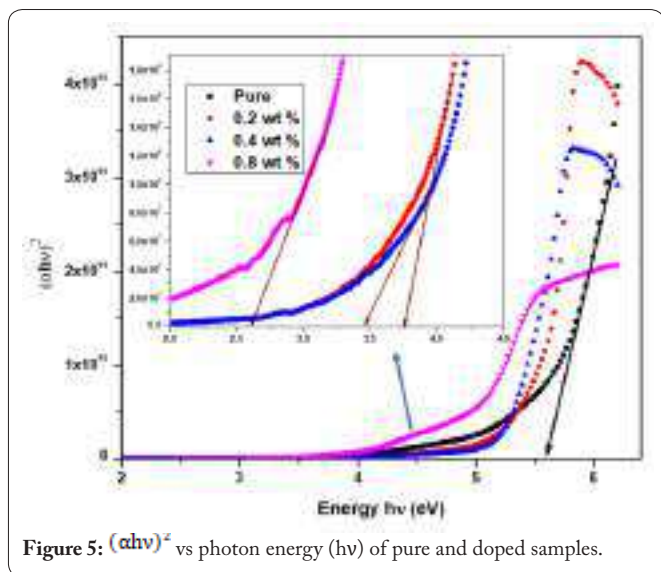


Figure 5: $(\alpha hv)^2$ vs photon energy (hv) of pure and doped samples.

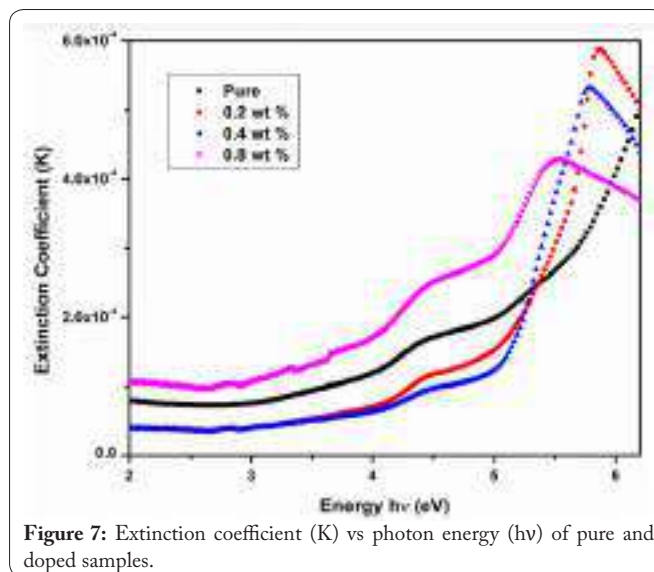


Figure 7: Extinction coefficient (K) vs photon energy (hv) of pure and doped samples.

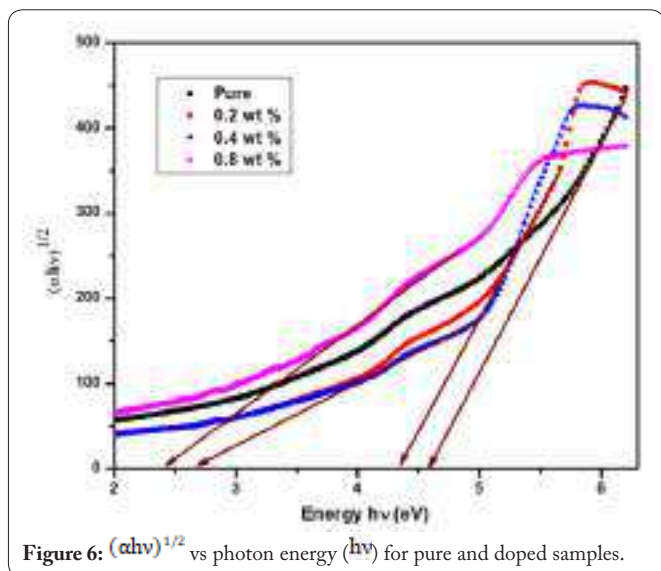


Figure 6: $(\alpha hv)^{1/2}$ vs photon energy (hv) for pure and doped samples.

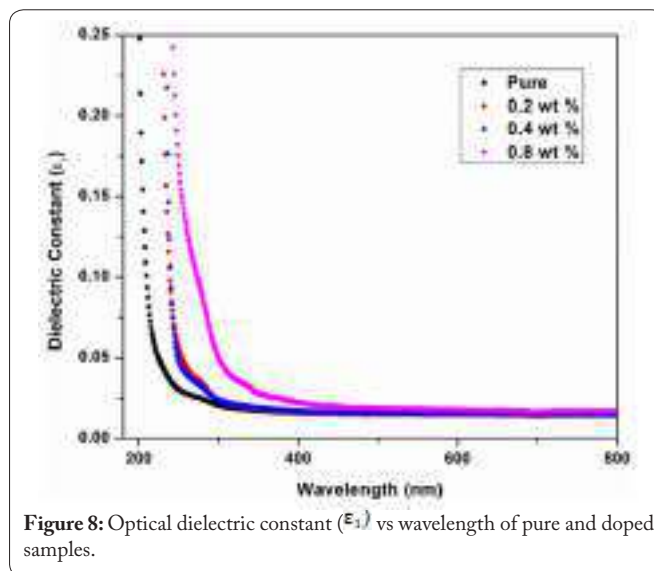


Figure 8: Optical dielectric constant (ϵ_1) vs wavelength of pure and doped samples.

falling photon energy is smaller than the energy gap [42].

$$K = \frac{\lambda \alpha}{4\pi} \quad (4)$$

Optical dielectric function (ϵ^*)

The dielectric function is highly dependent on the band structure of the material. The dielectric function is essential; the real component (ϵ_1) of the dielectric function relates to an electronic part, and the imaginary part (ϵ_2) pertains to the optical absorptions of the materials and has a direct correlation to the valence and conduction band [43]. Figure 8 depicts an optical dielectric constant (ϵ_1) vs. wavelength graph, with the vertex of the curve shifting towards the higher wavelength as salt content increases. The well-known Penn's model [44] is validated by the greatest value of the optical dielectric constant (ϵ_1) for the smallest optical band gap. Figure 9 depicts the optical dielectric loss as a function of photon energy. The absorption edge was shown to be reallocated to lower photon energy in doped films. It has been found that the dielectric loss absorption edge should be fairly comparable to Tauc's relation anticipated values [45]. Table 1 displays the band gap values computed using both methodologies (optical

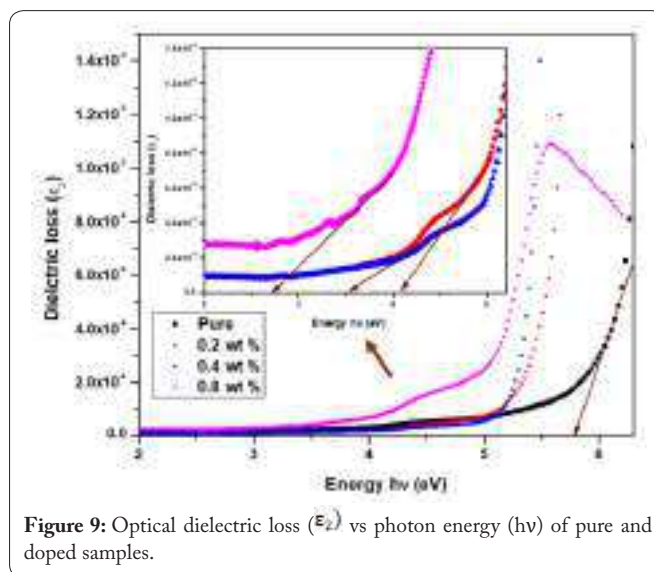


Figure 9: Optical dielectric loss (ϵ_2) vs photon energy (hv) of pure and doped samples.

dielectric loss and Tauc). Previous studies already have shown that Tauc's and optical dielectric loss models can be used to fix the mode of electronic transition and band gap respectively

[46, 47].

The real and imaginary components of the dielectric function can be calculated by equation (5) and (6)

$$\epsilon_1 = n^2 - K^2 \quad (5)$$

$$\epsilon_2 = 2nK \quad (6)$$

Optical conductivity (σ_{opt})

One of the most important parameters that affect a material's optical properties is its optical conductivity σ_{opt} . It is used to highlight the material's allowable interband optical transitions. The relationship between optical conductivity and photon energy is displayed in Figure 10. Optical conductivity improves with photon energy. The rise in absorption coefficient is accountable for the excitation of carriers from the valence to the conduction band.

The optical conductivity (σ_{opt}) is given by equation (7) [48].

$$\sigma_{opt} = \frac{\alpha n c}{4\pi} \quad (7)$$

Where, α is the absorption coefficient, n is the refrac-

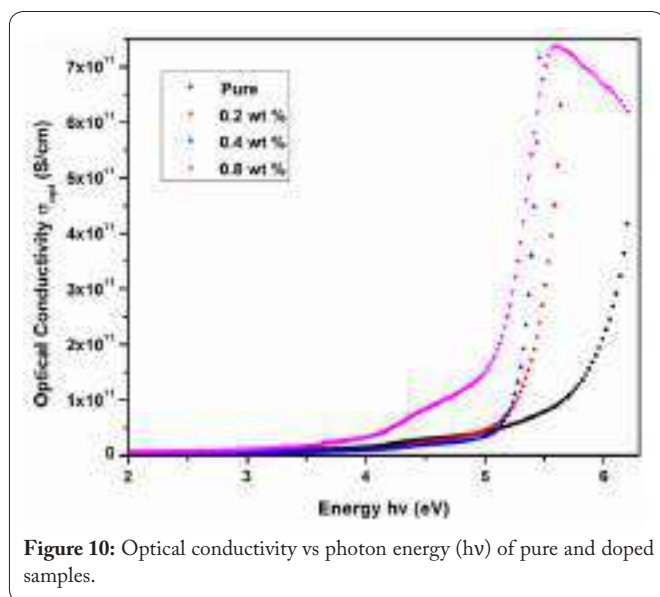


Figure 10: Optical conductivity vs photon energy (hv) of pure and doped samples.

tive index and c is the velocity of light.

XRD study

The XRD patterns of pure HPMC shows only two distinct peaks at 8° and 21° (Figure 10). Wang et al. reported comparable findings, who had created a hydrogel using chitosan, HPMC, and glycerol [49]. They also observed only two peaks at 7.9° and 20.3° . The intensity of the first peak almost vanished with salt concentration but the second broad peak broadened with the salt concentration this shows the decrease of the crystalline portion and increase of the amorphous portion which causes the reduction of the optical band gap. Similar outcomes were obtained by Nofal et al. who had prepared Co^{2+} -polyphenol with polyvinyl alcohol polymer to get desired optical parameters [50].

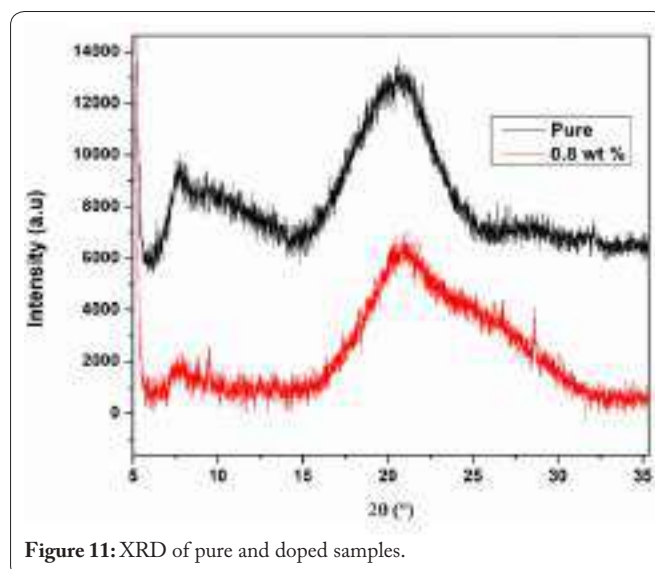


Figure 11: XRD of pure and doped samples.

Conclusion

The narrow bandgap solid polymer electrolyte films were successfully prepared by the solution casting method. The optical characteristics of the samples have been characterized. The optical absorption edge and optical energy gaps (indirect and direct) exhibit a significant decline as dopant salt concentration increases. On doping, these values moved to lower energies. This suggests that the doped HPMC films become semiconducting nature. This is owing to the significant population of carriers in the valence and conduction bands, which promotes carrier-carrier interaction and shifts the valence and conduction band. Also, the existence of unsaturated defects also aids in a reduction in the optical band gap. The optical band gap was precisely measured using the optical dielectric loss graph, and the nature of electronic transition was established using Tauc's method. The results of the highest optical dielectric constant for the shortest optical band gap obeyed Penn's model. The XRD measurements confirm the semicrystalline phase of HPMC and the amorphous area expanded with dopant concentration, which narrows the optical band gap. The observed narrow bandgap demonstrates its potential for optoelectronic devices.

Acknowledgement

Sunil Kumar expresses gratitude to S. D. V. S. Sangh's S. Arts College and T. P. Science Institute for their financial support.

Conflict of Interest

The authors declare that they have no conflict of interest.






References

1. Asnawi A, Hamsan M, Aziz S, Kadir M, Matmin J, et al. 2021. Impregnation of [Emim] Br ionic liquid as plasticizer in biopolymer electrolytes for EDLC application. *Electrochim Acta* 375: 137923. <https://doi.org/10.1016/j.electacta.2021.137923>
2. Aziz S, Nofal M, Kadir M, Dannoun E, Brza M, et al. 2021. Bio-based plasticized PVA based polymer blend electrolytes for energy storage EDLC devices: ion transport parameters and electrochemical properties. *Materials* 14(8): 1994. <https://doi.org/10.3390/ma14081994>

3. Wang H, S Li, Yasin G, W Li, Xu H, et al. 2020. Reviewing the current status and development of polymer electrolytes for solid-state lithium batteries. *Energy Storage Mater* 33: 188–215. <https://doi.org/10.1016/j.ensm.2020.08.014>
4. Fenton DE, Parker JM, Wright PV. 1973. Complexes of alkali-metal ions with poly(ethylene oxide). *Polymer* 14(11): 589–589. [https://doi.org/10.1016/0032-3861\(73\)90146-8](https://doi.org/10.1016/0032-3861(73)90146-8)
5. Vashishta P, Mundy JN, Shenoy GK. 1979. Fast ion transport in solids electrodes and electrolytes. Elsevier North Holland Inc, Lake Geneva, New York, USA.
6. El-Kader KMA, Orabi AS. 2002. Spectroscopic behavior of poly(vinyl alcohol) films with different molecular weights. *Polym Test* 21(5): 591–595. [https://doi.org/10.1016/S0142-9418\(01\)00129-5](https://doi.org/10.1016/S0142-9418(01)00129-5)
7. Hamad TK. 2013. Refractive index dispersion and analysis of the optical parameters of (PMMA/PVA) thin film. *Journal of Al-Nabrain University* 16(3): 164–170.
8. Li W, Hendriks KH, Wienk MM, Janssen RA. 2016. Diketopyrrolopyrrole polymers for organic solar cells. *Acc Chem Res* 49: 78–85. <https://doi.org/10.1021/acs.accounts.5b00334>
9. Meng D, Sun D, Zhong C, Liu T, Fan B, et al. 2016. High-performance solution-processed non-fullerene organic solar cells based on selenophene-containing perylene bisimide acceptor. *J Am Chem Soc* 138(1): 375–380. <https://doi.org/10.1021/jacs.5b11149>
10. Aziz SB, Abdullah OG, Hussein AM, Abdulwahid RT, Rasheed MA, et al. 2017. Optical properties of pure and doped PVA:PEO based solid polymer blend electrolytes: two methods for band gap study. *J Mater Sci: Mater Electron* 28: 7473–7479. <https://doi.org/10.1007/s10854-017-6437-1>
11. Abdullah OG, Aziz SB, Rasheed MA. 2016. Structural and optical characterization of PVA:KMnO₄ based solid polymer electrolyte. *Results Phys* 6: 1103–1108. <https://doi.org/10.1016/j.rinp.2016.11.050>
12. Badry R, El-Khodary S, Elhaes H, Nada N, Ibrahim M. 2021. Optical, conductivity and dielectric properties of plasticized solid polymer electrolytes based on blends of sodium carboxymethyl cellulose and polyethylene oxide. *Opt Quant Electron* 53: 3. <https://doi.org/10.1007/s11082-020-02649-2>
13. Wu Y, Wadia C, Ma W, Sadtler B, Alivisatos AP. 2008. Synthesis and photovoltaic application of copper(I) sulfide nanocrystals. *Nano Lett* 8(8): 2551–2555. <https://doi.org/10.1021/nl801817d>
14. Ito S, Hirose A, Yamaguchi M, Tanaka K, Chujo Y. 2017. Synthesis of aggregation-induced emission-active conjugated polymers composed of group 13 diiminate complexes with tunable energy levels via alteration of central element. *Polymers* 9(2): 68. <https://doi.org/10.3390/polym9020068>
15. Mallajosyula AT, Srivastava N, Iyer SSK, Mazhari B. 2010. Characterization of matrix and isolated organic solar cells. *Sol Energy Mater Sol Cells* 94(8): 1319–1323. <https://doi.org/10.1016/j.solmat.2008.09.027>
16. Ryusuke T, Maurer R, Jacob L, Stowasser F, Stillhart C, et al. 2020. Formulating amorphous solid dispersions: impact of inorganic salts on drug release from tablets containing itraconazole-HPMC extrudate. *Mol Pharmaceutics* 17(8): 2768–2778. <https://doi.org/10.1021/acs.molpharmaceut.9b01109>
17. Kumar S, Demappa T, Sannappa J. 2022. Influence of KI salt concentration on the hydroxypropyl methylcellulose films: optical study. *Opt Mater* 129: 112474. <https://doi.org/10.1016/j.optmat.2022.112474>
18. Kim H, Kim H, Ding Z, Lee MH, Lim K, et al. 2016. Recent progress in electrode materials for sodium-ion batteries. *Adv Energy Mater* 6(19): 1600943. <https://doi.org/10.1002/aenm.201600943>
19. Kim SM, Seo DH, Ma X, Ceder G, Kang K. 2012. Electrode materials for rechargeable sodium-ion batteries: potential alternatives to current lithium-ion batteries. *Adv Energy Mater* 2(7): 710–721. <https://doi.org/10.1002/aenm.201200026>
20. Yabuuchi N, Kubota K, Dahbi M, Komaba S. 2014. Research development on sodium-ion batteries. *Chem Rev* 114(23): 11636–11682. <https://doi.org/10.1021/cr500192f>
21. Fuentes I, Andrio A, Teixidor F, Viñas C, Compañ V. 2017. Enhanced conductivity of sodium versus lithium salts measured by impedance spectroscopy. Sodium cobaltacarboranes as electrolytes of choice. *Phys Chem Chem Phys* 19(23): 15177–15186. <https://doi.org/10.1039/C7CP02526B>
22. Pan H, Hu YS, Chen L. 2013. Room-temperature stationary sodium-ion batteries for large-scale electric energy storage. *Energy Environ Sci* 6: 2338–2360. <https://doi.org/10.1039/C3EE40847G>
23. Bella F, Colò F, Nair JR, Gerbaldi C. 2015. Photopolymer electrolytes for sustainable, upscalable, safe, and ambient-temperature sodium-ion secondary batteries. *Chem Sus Chem* 8(21): 3668–3676. <https://doi.org/10.1002/cssc.201500873>
24. Rao BL, Shivananda CS, Shetty GR, Harish KV, Madhukumar R, et al. 2018. Influence of UV irradiation on hydroxypropyl methyl cellulose polymer films. *AIP conference proceedings* pp 080011. <https://doi.org/10.1063/1.5032817>
25. Chen Z, Zheng Y, Yan H, Facchetti A. 2009. Naphthalenedicarboximide- vs perylene dicarboximide-based copolymers. Synthesis and semiconducting properties in bottom-gate n-channel organic transistors. *J Am Chem Soc* 131(1): 8–9. <https://doi.org/10.1021/ja805407g>
26. Ahmed E, Ren G, Kim FS, Hollenbeck EC, Jenekhe SA. 2011. Design of new electron acceptor materials for organic photovoltaics: synthesis, electron transport, photophysics, and photovoltaic properties of oligothiophene-functionalized naphthalene diimides. *Chem Mater* 23(20): 4563–4577. <https://doi.org/10.1021/cm2019668>
27. Al-Taa'y WA, Abdul Nabi MT, Al-Rawi TK. 2011. The MR affect on optical properties for poly (vinyl alcohol) films. *Baghdad Sci J* 8(2): 543–550.
28. Lobo B, Ranganath MR, Chandran TR, Rao GV, Ravindrachary V, et al. 1999. Iodine-doped polyvinyl alcohol using positron annihilation spectroscopy. *Phys Rev B* 59(21): 13693–13698. <https://doi.org/10.1103/PhysRevB.59.13693>
29. El-Deen HZ, Hafez AI. 2009. Physico-chemical stability of PVA films doped with Mn²⁺ ions against weathering conditions. *Arab J Sci Eng* 34(1A): 13–26.
30. Guirguis OW, Moselhey MT. 2011. Optical study of poly (vinyl alcohol)/hydroxypropyl methylcellulose blends. *J Mater Sci* 46: 5775–5789. <https://doi.org/10.1007/s10853-011-5533-5>
31. Sanderson GR. 1981. Polysaccharides in foods. *Food Technol* 35(7): 50–57.
32. Aziz SB, Abdulwahid RT, Rsaul RA, Ahmed HM. 2016. *In situ* synthesis of CuS nanoparticle with a distinguishable SPR peak in NIR region. *J Mater Sci Mater Electron* 27: 4163–4171. <https://doi.org/10.1007/s10854-016-4278-y>
33. Ditta MA, Farrukh MA, Ali S, Younas N. 2017. X-ray peak profiling, optical parameters and catalytic properties of pure and CdS doped ZnO–NiO nanocomposites. *Russ J Appl Chem* 90(1): 151–159. <https://doi.org/10.1134/S1070427217010220>
34. Sharma P, Katal SC. 2007. Determination of optical parameters of a-(As₂Se₃)₉₀Ge₁₀ thin film. *J Phys D Appl Phys* 40(7): 2115. <https://doi.org/10.1088/0022-3727/40/7/038>
35. Juma AO, Arbab EA, Muiva CM, Lepodise LM, Mola GT. 2017. Synthesis and characterization of CuO–NiO–ZnO mixed metal oxide nanocomposite. *J Alloy Comp* 723: 866–872. <https://doi.org/10.1016/j.jallcom.2017.06.288>
36. Bakr NA, Funde AM, Waman VS, Kamble MM, Hawaldar RR, et al. 2011. Determination of the optical parameters of a-Si:H thin films deposited by hot wire-chemical vapour deposition technique using transmission spectrum only. *Pramana - J Phys* 76: 519–531. <https://doi.org/10.1007/s12043-011-0024-4>

37. Ibrahim S, Ahmad R, Johan MR. 2012. Conductivity and optical studies of plasticized solid polymer electrolytes doped with carbon nanotube. *J Lumin* 132(1): 147–152. <https://doi.org/10.1016/j.jlumin.2011.08.004>
38. Kumar GV, Chandramani R. 2009. Investigations on Fe³⁺ doped polyvinyl alcohol films with and without gamma (γ)-irradiation. *App Surfac Sci* 255(15): 7047–7050. <https://doi.org/10.1016/j.apsusc.2009.03.038>
39. Siddaiah T, Ojha P, Gopal NO, Ramu C, Nagabhushana H. 2018. Thermal, structural, optical and electrical properties of PVA/MAA:EA polymer blend filled with different concentrations of lithium perchlorate. *J Sci Adv Mater Devices* 3(4): 456–63. <https://doi.org/10.1016/j.jsamd.2018.11.004>
40. Bhunia R, Ghosh D, Ghosh B, Hussain S, Bhar R, et al. 2015. Free-standing flexible nanocrystalline-ZnO-impregnated polyvinylidene fluoride composite thin films. *J Compos Mater* 49(25): 3089–3101. <https://doi.org/10.1177/0021998314559756>
41. Sheela T, Bhajantri RF, Ravindrachary V, Rathod SG, Pujari PK, et al. 2014. Effect of UV irradiation on optical, mechanical and microstructural properties of PVA/NaAlg blends. *Rad Phys Chem* 103: 45–52. <https://doi.org/10.1016/j.radphyschem.2014.05.036>
42. Nadeem MY, Ahmed W. 2000. Optical properties of ZnS thin films. *Turk J Phys* 24(5): 651–659.
43. Biskri ZE, Rached H, Boucheur M, Rached D, Aida MS. 2016. A comparative study of structural stability and mechanical and optical properties of fluorapatite (Ca₅(PO₄)₃F) and lithium disilicate (Li₂Si₂O₅) components forming dental glass–ceramics: first principles study. *J Electron Mater* 45: 5082–5095. <https://doi.org/10.1007/s11664-016-4681-4>
44. Ravindra NM, Ganapathy P, Choi J. 2007. Energy gap–refractive index relations in semiconductors—an overview. *Infrared Phys Technol* 50(1): 21–29. <https://doi.org/10.1016/j.infrared.2006.04.001>
45. Yu L, Li D, Zhao S, Li G, Yang K. 2012. First principles study on electronic structure and optical properties of ternary GaAs:Bi alloy. *Materials* 5(12): 2486–2497. <https://doi.org/10.3390/ma5122486>
46. Aziz SB, Ahmed HM, Hussein AM, Fathulla AB, Wsw RM, et al. 2015. Tuning the absorption of ultraviolet spectra and optical parameters of aluminium doped PVA based solid polymer composites. *J Mater Sci Mater Electron* 26: 8022–8028. <https://doi.org/10.1007/s10854-015-3457-6>
47. Aziz SB. 2016. Modifying poly(vinyl alcohol) (PVA) from insulator to smallband gap polymer: a novel approach for organic solar cells and optoelectronic devices. *J Electron Mater* 45: 736–745. <https://doi.org/10.1007/s11664-015-4191-9>
48. Yakuphanoglu F, Cukurovali A, Yilmaz I. 2005. Refractive index and optical absorption properties of the complexes of a cyclobutane containing thiazolyl hydrazone ligand. *Opt Mater* 27(8): 1363–1368. <https://doi.org/10.1016/j.optmat.2004.09.021>
49. Wang T, Chen L, Shen T, Wu D. 2016. Preparation and properties of a novel thermo-sensitive hydrogel based on chitosan/hydroxypropyl methylcellulose/glycerol. *Int J Biol Macromol* 93: 775–782. <https://doi.org/10.1016/j.ijbiomac.2016.09.038>
50. Nofal MM, Aziz SB, Hadi JM, Karim WO, Dannoun EM et al. 2021. Polymer composites with 0.98 transparencies and small optical energy band gap using a promising green methodology: structural and optical properties. *Polymers* 13(10): 1648. <https://doi.org/10.3390/polym13101648>

Dielectric and Conductivity Study of Salt-Doped HPMC Solid Polymer Electrolyte Films

Sunil Kumar^{1,2} , Sandhya Rani Nagarajaiah³ , Raghu S⁴ , Sandeep Dongre¹ ,
Demappa Thippaiah⁵ , Sannappa Jادیappa^{1,*} 

¹ Department of P G Studies and Research in Physics, Jnana Sahyadri, Kuvempu University, Shivamogga 577451, India; sannappaj2012@gmail.com (S.J.);

² Department of Physics, S.S Arts College and T.P Science Institute, Sankeshwar, Belagavi 591313, India; sunil11111kumar@gmail.com (S.K.);

³ Department of Physics, Vidyavardhaka College of Engineering, Mysore 57002, India; sandhya.phy@vvc.ac.in (R.N.S.);

⁴ Department of Physics, KLE Society's, Basavaprabhu Kore Arts, Science and Commerce College, Chikodi 591201, India; raghu.mona@gmail.com (R.S.);

⁵ Department of Polymer Science, Sir M V, P G Centre, University of Mysore, Mandya 571402, India; demappa@uni-mysore.ac.in (D.T.);

* Correspondence: sannappaj2012@gmail.com (S.J.);

Scopus Author ID 6508209624

Received: 27.08.2022; Accepted: 7.10.2022; Published: 5.02.2023

Abstract: This study reports the solid polymer electrolyte films of hydroxypropyl methylcellulose (HPMC) doped with different sodium bromide (NaBr) salt concentrations. The test samples were prepared using the solution cast method, and their structural characterization was done using XRD, SEM, and FTIR. Sharp crystalline peaks of pure NaBr salt disappeared completely in all the HPMC:NaBr polymer electrolyte systems revealing the reduced crystallinity, which greatly influences the dielectric and conductivity of the polymer electrolytes. Fourier transform infrared spectral (FTIR) reports subjected to vibrational changes that appeared due to the result of dopant salt in the host polymer. The samples were analyzed using a pc-based impedance analyzer (Wayne Kerr 6510B) in the frequency scale of 50 Hz to 1 MHz. As the frequency increases, the constant dielectric declines, and the AC electrical conductivity rises. The AC conductivity curves in the high-frequency area follow the Jonscher Power Law. The electrolyte's non-Debye behavior was supported by its relaxation time and dielectric property. According to the reported polymer electrolyte systems, the distribution of relaxation time is influenced by the presence of conducting ions in an amorphous formation. All assessed outcomes of these polymer electrolytes are assuring their use for electrochemical cell drives.

Keywords: solid polymer electrolyte; dielectric constant; ac conductivity; impedance analysis.

© 2022 by the authors. This article is an open-access article distributed under the terms and conditions of the Creative Commons Attribution (CC BY) license (<https://creativecommons.org/licenses/by/4.0/>).

1. Introduction

Supercapacitors (SCs), fuel cells, batteries, and other energy conversion and storage technologies primarily employ solid polymer electrolytes (SPEs) [1-4]. SPEs are composed of dissolved salts in high molecular mass polymer matrices. Compared to other liquid ionic solutions, the ionic-conducting phase of SPEs has a better transport property. Additionally, they are flexible, light in weight, relatively high in ionic conductivity, solvent-free, and capable of forming films. Likewise, they are risk-free and also leakage free. In 1973, poly(ethylene oxide) (PEO) that had been combined with alkali metal salts was the first ion-conducting polymer to be reported [5]. J Koliyoor *et al.* studied Magnesium ion-doped methyl cellulose

electrolyte system and found the highest ionic conductivity of 1.02×10^{-4} S/cm at room temperature for 25 wt% Mg [6]. Bashir A.A. *et al.* reported the highest conductivity of 5.30×10^{-4} S/cm for Poly (vinyl alcohol) (PVA) and cellulose acetate (CA) in 80:20 with 20 wt% potassium carbonate [7]. N. M. Khan *et al.* reported AL-NH₄Cl BE's highest ionic conductivity of 3.18×10^{-8} S/cm for an NH₄Cl content of 8 wt%. However, when plasticized with 4 wt% of EC, an increased optimum value of 1.46×10^{-6} S/cm was obtained [8]. Maheshwari *et al.* reported a maximum conductivity of 1.66×10^{-3} S/cm at room temperature for the composition 700 mg_{Dextran}:300 mg_{PVA}:450 mg_{NH₄NO₃} [9]. The ion transport property depends on various factors, including a degree of ion aggregation, salt concentration, degree of salt dissociation, polymer chain mobility, etc. Even though the SPEs have good conductivity, the analysis of dielectric studies gives additional information for understanding ion transport actions and getting data on molecular/ionic interface in polymer electrolytes [10]

In contrast to other cellulose derivatives (carboxymethylcellulose, hydroxyethyl cellulose (HEC), and methylcellulose (MC)), HPMC is more thermally stable, making it the preferred host polymer. It is widely utilized in the textile, biomedical, and pharmaceutical industries because it is biodegradable and non-toxic [11-13]. According to earlier research, HPMC can dissolve various metal salts and produce thin films with exceptional stability [12,13]. Compared to other inorganic salts, the benefit of using sodium metal particles is their abundance and accessibility at a low cost [14-18]. The inorganic compound sodium bromide (NaBr) is a white crystalline solid with a high melting point. It is a widely used source of bromide ions in pharmaceutical preparations [19]. As a result, the sodium-ion battery has gained popularity as the next-generation secondary battery because it is much less expensive than a lithium-ion battery. Several research findings have found that Na⁺ ions bring better or comparable ionic conductivity to Li⁺ ions in the same primary host source [20-21]. This presented a chance to develop a battery using Na⁺ ions instead of lithium. NaBr does have narrow lattice energy of 747 kJ/mol, that's a little less than NaCl (786 kJ/mol) because Br (182 pm) is larger than Cl (167 pm) [22]. The lattice energy of salts and the crystalline percentage of sodium salts used in PEs can significantly impact the synthesized electrolyte's conductivity. As a result, this study looks into the effect of NaBr salt on the dielectric and electrical conductivity properties of HPMC-based solid polymer electrolytes.

2. Materials and Methods

The electrolyte film samples are prepared by the standard casting method. The samples in pure form are purchased from Sigma-Aldrich. Here water is used as a base solvent, and different percentages of samples are prepared. Initially, the pure film is prepared by adding 3 grams of HPMC in 100 ml double distilled water, and it is let to stir for 24 hours. The prepared solution is poured into the glass slab (14x14 cm), and it is dried for 7-10 days. Finally, the film samples are peeled from the glass slab and kept in the desiccators to avoid moisture.

Similarly, different percentages of salt are added to the pure solution. Experiments like XRD, FTIR, and SEM assessed the synthesized pure HPMC and doped HPMC polymer electrolyte films. These samples' dielectric and AC conductivity were measured using a PC-based impedance analyzer at frequencies from 50 Hz to 1 MHz (Wayne Kerr 6510B).

3. Results and Discussion

3.1. Structural study.

Our previous paper described the structural evaluation of the prepared polymer electrolyte films. According to Figure 1, the Virgin HPMC film showed a pronounced peak that occurred at 22.17° , revealing the semi-crystalline character of HPMC, and this broad peak disappeared in the NaBr salted HPMC films. The crystallinity decreased with salt content in doped films, indicating a decrease in intermolecular interaction (crystalline phase) [23].

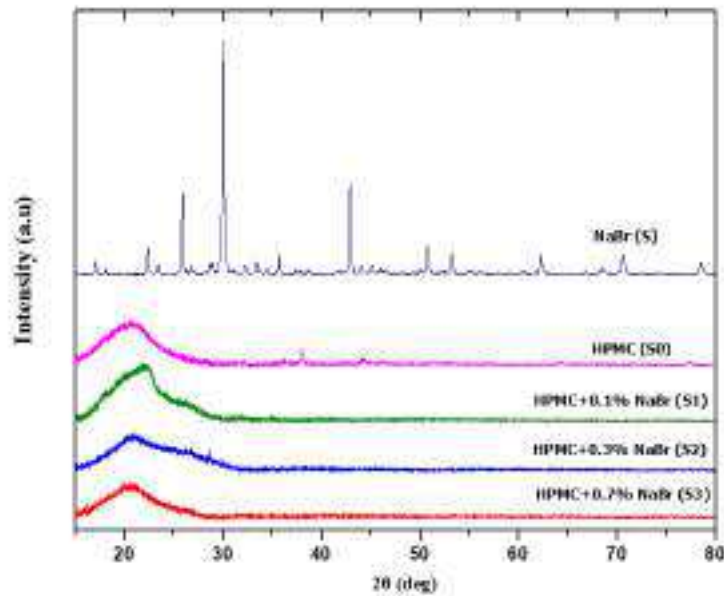


Figure 1. XRD Spectrum of pure and NaBr doped samples [23].

3.2. FTIR studies.

In our earlier paper, we reported on the evaluation of the IR spectra of the prepared composite film samples.

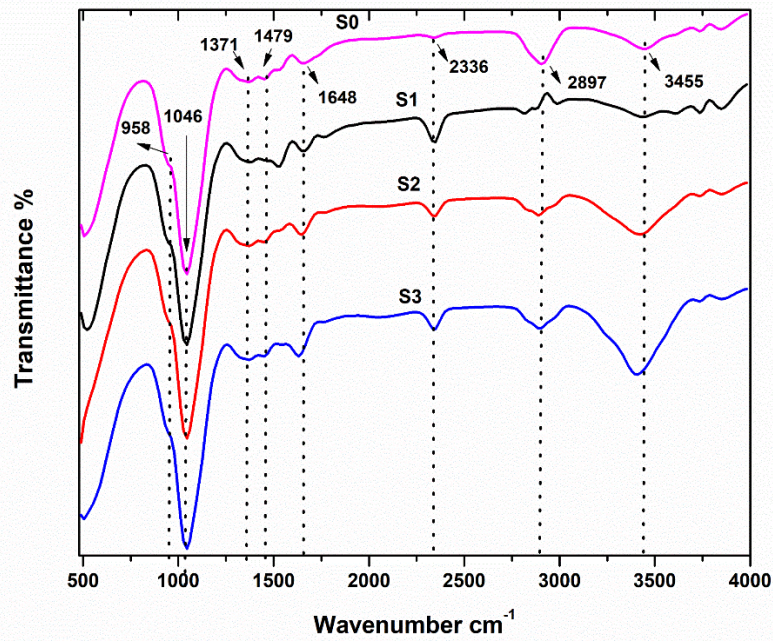


Figure 2. FTIR Spectrum of pure and NaBr doped samples [23].

The effect of the dopant on the vibration modes was observed in the IR spectra as a decrease in intensities, a widening of the bands, and repositioning of the bands to shorter wavenumbers. All of these variations in the FTIR spectra are dependable signs of polymers-ion complexes. The OH groups are vital for ensuring the crystalline packing of the polymer [24]. The large shift and variation in the OH group's intensity in complex films causes a break of the crystalline phase and simultaneously increases amorphous content [23].

3.3. SEM studies.

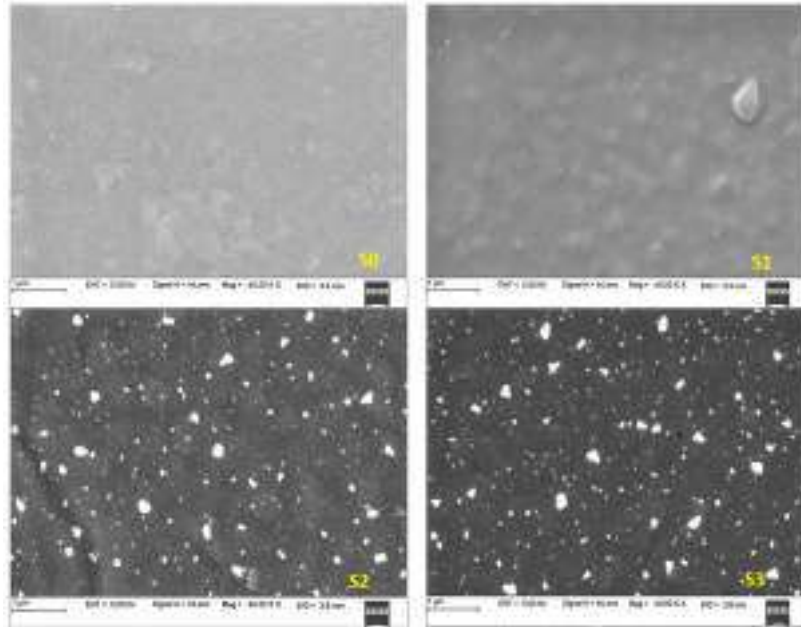


Figure 3. SEM Spectrum of pure and NaBr doped samples [20].

The SEM results of the ready composite film sample were reported in our earlier paper. Pure HPMC film can show plane morphology [12]. The complex film samples display varying degrees of roughness, which shows the dopant has segmented in the host polymer matrix and broken up its crystalline phase [23].

3.4. Conductivity and dielectric studies.

3.4.1. Room temperature study of complex impedance spectroscopy analysis.

The following equation 1 [25] gives the complex impedance (z^*) based on impedance modulus (Z' and Z'').

$$Z^* = Z' + iZ'' \tag{1}$$

where Z' represents the real part of the impedance modulus and Z'' represents the imaginary part, as given by equations 2 and 3

$$Z' = \frac{1}{2\pi f C_o} \left[\frac{\epsilon''}{\epsilon''^2 + \epsilon'^2} \right] \tag{2}$$

$$Z'' = \frac{1}{2\pi f C_o} \left[\frac{\epsilon'}{\epsilon''^2 + \epsilon'^2} \right] \tag{3}$$

where C_0 is the vacuum capacitance, and f is the frequency. The ϵ' and ϵ'' are real and imaginary parts of dielectric permittivity, respectively.

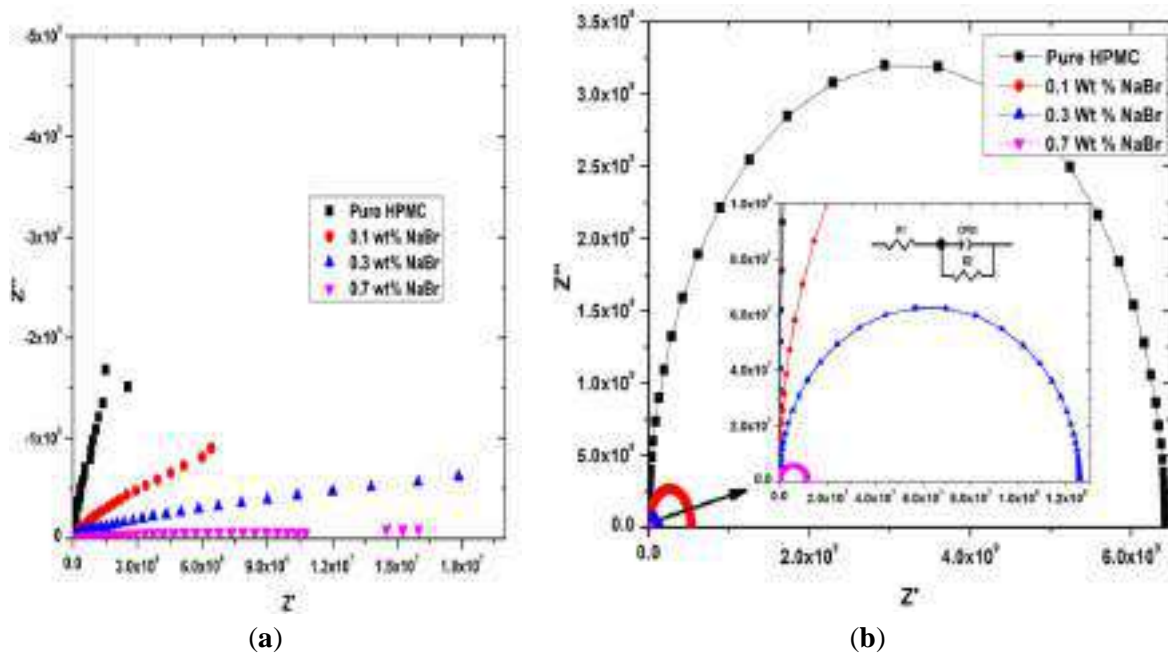


Figure 4. (a) Plot of Complex impedance Nyquist. (b) electrical equivalent circuit for pure and doped electrolyte samples at room temperature.

Figure 4 (a) shows the complex impedance plots of Z^* (known as Nyquist plot) at room temperature for pure and doped samples. The complex impedance Figure 4a shows an inclined spike which shows the interaction of two blocking electrodes, which triggers the formation of double-layer capacitance of HPMC:NaBr film [26-28]. Figure 4 (b) displays the experimental data fitted plots that were developed using an equivalent circuit consisting of a resistance R_1 (grain resistance R_g) in series with a fixed phase impedance (Z_{CPE}) and resistance R_2 (grain boundary resistance R_{gb}) in parallel. The analogous composition is of the form $\left(R_1 + \left(R_2 / Z_{CPE} \right) \right)$. Table 1 displays the values of all fitted parameters. From the plots, it is clear that the R_b value declines with increasing NaBr salt. All samples display a high-frequency semi-circle arc that is connected to the bulk conduction process [26,27].

The assessment of Argand sketches with a complete semi-circular arc on the real impedance (Z') axis discloses that relaxation time varies for charge carriers [28]. From Table 1, the R_g value declines with the rise of NaBr concentration and achieves the lowest value ($1.607 \times 10^7 \Omega$) for HPMC/NaBr 0.7 wt % sample. Hence, 0.7 wt % NaBr content composite polymer electrolyte has a significant ionic conductivity. The density and mobility of charge carriers both contribute to the variation in the ionic conductivity of electrolyte samples [29].

3.4.2. Dielectric analysis.

A detailed study of the dielectric constant is required to design and advance electrical and electronic components. It exposes more knowledge about the polymer's physical and chemical state. When contrasted to ceramic materials, it is possible to create polymers with good dielectric constants and small dielectric losses [30]. Figure 5 depicts the room temperature dielectric constant (real part ϵ') and $\text{Log}(f)$ plots for pure and doped electrolyte systems for frequencies stretching from 100 Hz to 1 MHz.

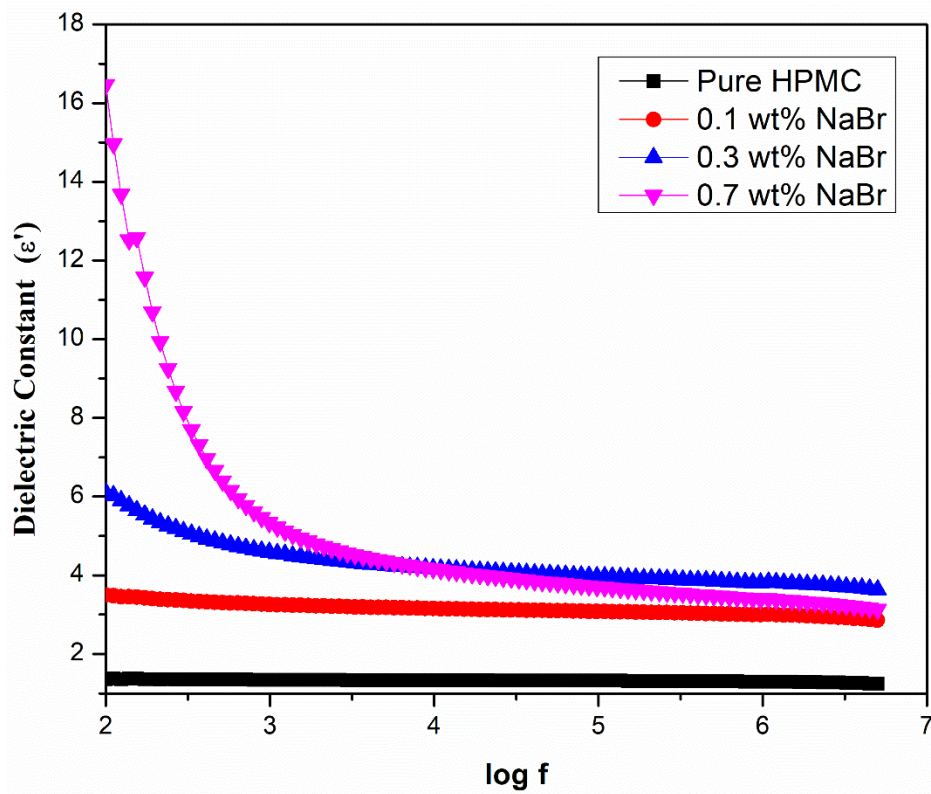


Figure 5. Variation of Dielectric constant (ϵ') with frequency.

The relationship used to calculate the dielectric constant is given by equation 4

$$\epsilon' = \frac{Cd}{\epsilon_0 A} \tag{4}$$

where 'C' stands for equivalent capacitance, 'd' for sample thickness, ϵ_0 for free-space permittivity, and "A" for sample area.

Figure 5 plots clearly show that the dielectric constant falls as frequency rises. NaBr salt has a noticeable impact on the dielectric constant at room temperature, resulting in an increase in total charge carriers, dielectric constant, and ionic conductivity. The outcome displays that the host polymer electrolyte complexed with 0.7 wt % NaBr salt reports a high dielectric constant and shows the maximum ionic conductivity. The increase in the dielectric constant at short frequencies is caused by the space charge polarization at the electrode-electrolyte junction. This charge growth displays relaxation behavior resembling dipolar relaxation [31]. Due to the presence of space charge polarisation at the electrode-electrolyte junction, there is a high dielectric constant at low frequencies. This shows that the applied electric field periodically reverses that no longer be followed by the dipoles [32,33]. As a result, as the frequency rises, the charge carriers' contribution to polarisation also declines, which results in a continuous decline in the ϵ' - values.

3.4.3. AC electrical conductivity.

The scaling of dielectric properties with frequency under conditions of alternating current (AC) is given by Power law equation 5.

$$\sigma(\omega) = \sigma_{dc} + A\omega^S \tag{5}$$

Here, $A\omega^s$ is the only dispersive AC conductivity factor that appears in the power law form of angular frequency (ω), and s is the power element ($0 \leq s \leq 1$), denotes how well mobile ions interface with the lattices surrounding those. A is a constant that determines the strength of polarizability. Exponent factor s $\sigma(\omega)$ is the total conductivity, and σ_{dc} is the DC conductivity of the sample. Table 1 shows the room temperature assessment of parameters attained from JPL fit (Equation 7) with the experiment records of electrolyte samples. Figure 6 displays that the AC conductivity at room temperature rises with frequency and reaches a maximum for the highest doped electrolyte of 0.7 wt % HPMC-NaBr. The frequency-dependent electrical conductivity of polymer-electrolyte obeys Jonscher Power Law (JPL) [34-36]. The JPL fitting and the experimental values match each other well. The plateau region in the low frequency relates to σ_{dc} . The conductivity in the large-frequency province obeys $A\omega^s$. Jonscher claims that the cause of the frequency dependency of conductivity is the cause of mobile charge carriers payable to the relaxation existences of the ionic atmosphere. In the host polymer matrix, ions jump from one vacant site to an adjacent vacant site, contributing to DC conductivity at lower frequencies. This effective ion hopping occurs at a shorter frequency than the hopping frequency. The figure shows higher frequencies exhibit more dispersive conductivity due to the ions' backward and forward hopping motion [37].

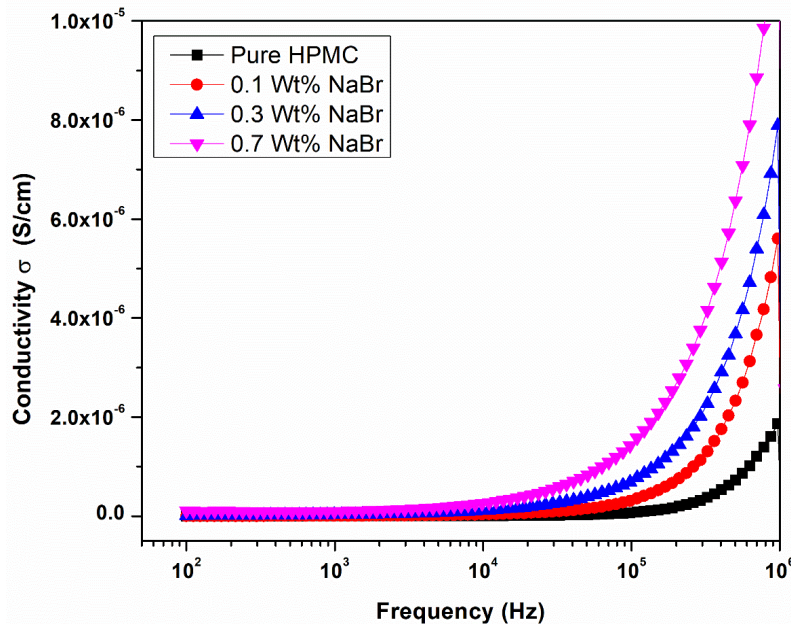


Figure 6. Variation of AC conductivity versus frequency.

Table 1. Variation of Grain resistance, capacitance, relaxation time, ac conductivity, and dc conductivity with salt concentration at room temperature.

Parameters	Pure HPMC	0.1 wt% NaBr	0.3 wt% NaBr	0.7 wt% NaBr
R_g (k Ω)	6.4325×10^9	5.314×10^8	1.255×10^8	1.607×10^7
C (F)	8.348×10^{-12}	1.632×10^{-11}	1.927×10^{-11}	2.645×10^{-11}
τ (s)	1.591×10^{-3}	1.427×10^{-3}	1.279×10^{-3}	3.45×10^{-4}
σ (S/cm)	1.87005×10^{-6}	5.60342×10^{-6}	7.8932×10^{-6}	1.23638×10^{-5}
S	1.01374	0.86887	0.69948	0.51776
σ (dc)	1.5019×10^{-10}	1.629×10^{-9}	1.1154×10^{-8}	1.094×10^{-7}

3.4.4. Complex electrical modulus analysis at room temperature.

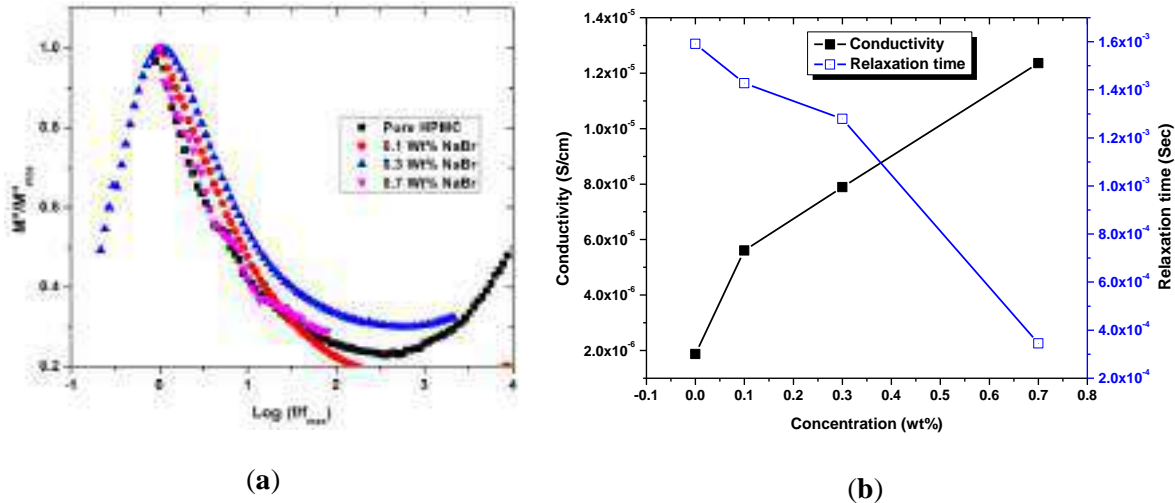


Figure 7. (a) Normalized plot of M''/M''_{max} versus $\log (f/f_{max})$; (b) Variation of relaxation time with dopant concentration.

Theoretically, the complex electrical modulus is derived from the complex permittivity M^* using equation 6 [38].

$$M^* = M' + iM'' \tag{6}$$

The real M' and imaginary M'' parts of the dielectric modulus can be calculated from ϵ' and ϵ'' using equation 7 and 8 as follows:

$$M' = \left[\frac{\epsilon'^2}{\epsilon'^2 + \epsilon''^2} \right] \tag{7}$$

$$M'' = \left[\frac{\epsilon''^2}{\epsilon'^2 + \epsilon''^2} \right] \tag{8}$$

The relaxation time can be calculated from the peak position of M'' using equation 9:

$$\tau = \frac{1}{2\pi f_{max}} \tag{9}$$

where f_{max} is the frequency corresponding to the maximum peak position of the plot.

From Figure 7 (a), all samples' curve peaks overlap, suggesting the relaxation shows the same mechanism. The peak shifts slightly towards a higher frequency as the dopant salt concentration increases, indicating a decrease in relaxation time and resulting in maximum ionic conductivity. The spread of relaxation and non-Debye-type behavior in these electrolyte film samples is confirmed by the asymmetric broadening of the peak [39]. Figure 7 (b) shows the room temperature variation of relaxation time. The relaxation time decreases with the dopant. The lowest relaxation time was observed in the highest wt% film sample.

4. Conclusions

The chemical and physical parameters of polymer electrolytes are dependent on the degree of crystallinity. XRD and FTIR characterizations confirmed the complexation of salt in the host polymer. The structural results showed a significant decrease in crystallinity in the

host polymer with salt concentration because additional salt prevents polymer chains from crystallizing. SEM images of composite films show more degree of roughness compared to the host polymer. The intensity variation and shift in the band were observed through functional studies, which signifies the host polymer's interaction with NaBr. It has been found that increases in AC electrical conductivity depend on frequency. The AC conductivity plots in the high-frequency region show Jonscher's power law. The dielectric property and relaxation time confirmed the non-Debye behavior of the electrolyte system. The distribution of relaxation times is related to the presence of conducting ions in an amorphous structure of the reported polymer electrolyte systems. The estimated outcomes strongly support the use of these polymer electrolytes in electrochemical cell electronic applications.

Funding

This research received no external funding.

Acknowledgments

The author, Sunil Kumar, is thankful to the Physics department, Kuvempu University and S S Arts College, and T P Science Institute for providing sample preparation and characterization facilities.

Conflicts of Interest

The authors declare no conflict of interest. The authors declare that they have no known competing financial interests or personal relationships that could have appeared to influence the work reported in this paper.

References

1. Asnawi, A.; Hamsan, M.; Aziz, S.; Kadir, M.; Matmin, J.; Yusof, Y. Impregnation of [Emim] Br ionic liquid as plasticizer in biopolymer electrolytes for EDLC application. *Electrochim. Acta.* **2021**, *375*, 137923, <https://doi.org/10.1016/j.electacta.2021.137923>.
2. Aziz, S.; Dannoun, E.; Hamsan, M.; Abdulwahid, R.; Mishra, K.; Nofal, M.; Kadir, M. Improving EDLC Device Performance Constructed from Plasticized Magnesium Ion Conducting Chitosan Based Polymer Electrolytes via Metal Complex Dispersion. *Membranes.* **2021**, *11*, 289, <https://doi.org/10.3390/membranes11040289>.
3. Aziz, S.; Nofal, M.; Kadir, M.; Dannoun, E.; Brza, M.; Hadi, J.; Abdullah, R. Bio-Based Plasticized PVA Based Polymer Blend Electrolytes for Energy Storage EDLC Devices: Ion Transport Parameters and Electrochemical Properties. *Materials.* **2021**, *14*, 1994, <https://doi.org/10.3390/ma14081994>.
4. Aziz, S.; Asnawi, A.; Kadir, M.; Alshehri, S.; Ahamad, T.; Yusof, Y.; Hadi, J. Structural, Electrical and Electrochemical Properties of Glycerolized Biopolymers Based on Chitosan (CS): Methylcellulose (MC) for Energy Storage Application. *Polymers* **2021**, *13*, 1183, <https://doi.org/10.3390/polym13081183>.
5. Agrawal, R.C.; Pandey, G.P. Solid polymer electrolytes: Materials designing and all-solid-state battery applications: An overview. *J. Phys. D Appl. Phys.* **2008**, *41*, 223001. <https://doi.org/10.1088/0022-3727/41/22/223001>.
6. Koliyoor, J.; Ismayil; Hegde, S.; Vasachar, R.; Sanjeev, G. Novel solid biopolymer electrolyte based on methyl cellulose with enhanced ion transport properties *J. Appl. Polym. Sci.* **2022**, *139*, 51826, <https://doi.org/10.1002/app.51826>.
7. Bashir, A.A.; John, O.D.; Abbas, A.A.; Yerima, M.H.; Nurrul, A.S.; Shukur, M.F. Preparation and characterization of solid biopolymer electrolytes based on polyvinyl alcohol/cellulose acetate blend doped with potassium carbonate (K₂CO₃) salt, *J. Electroanal. Chem.* **2022**, *919*, 116539, <https://doi.org/10.1016/j.jelechem.2022.116539>.

8. Khan, N.M.; Mazuki, N.M.; Abdul Majeed, A.P.P.; Samsudin, A.S. Interrelation Between Ionic Conduction and Ions Fraction of Biopolymer Electrolytes Based on Alginate Doped with NH₄Cl, *J. of Macromol. Sci, Part B*, **2021**, *60*, 631-646, <https://doi.org/10.1080/00222348.2021.1889126>.
9. Maheshwari, T.; Tamilarasan, K.; Selvasekarapandian, S.; Chitra, R.; Muthukrishnan, M. Synthesis and characterization of Dextran, poly (vinyl alcohol) blend biopolymer electrolytes with NH₄NO₃, for electrochemical applications, *Int. J. Green Energy*, **2022**, *19*, 314-330, <https://doi.org/10.1080/15435075.2021.1946811>.
10. Sengwa, R. J.; Priyanka, D.; Shobhna, C. Effects of plasticizer and nanofiller on the dielectric dispersion and relaxation behaviour of polymer blend based solid polymer electrolytes. *Current Applied Physics*. 2015, *15*, 135-143, <https://doi.org/10.1016/j.cap.2014.12.003>.
11. Ryusuke, T.; Reto, M.; Laurence, J.; Frank, S.; Cordula, S.; Susanne. Formulating Amorphous Solid Dispersions: Impact of Inorganic Salts on Drug Release from Tablets Containing Itraconazole-HPMC Extrudate. *Mol Pharm*. **2020**, *17*, 2768-2778, <https://doi.org/10.1021/acs.molpharmaceut.9b01109>.
12. Kumar, S.; Dongre, S.; Raghu, S.; Demappa, T.; Sannappa, J. Structural and Mechanical characteristic study of HPMC polymer composite films, Second International Conference on Physics of Materials and Nanotechnology, Mangalore University, India, 27/10/2021 - 30/10/2021, *IOP Conf. Ser.: Mater. Sci. Eng.* **2022**, *1221*, 012011, <https://doi.org/10.1088/1757-899X/1221/1/012011>.
13. Kumar, S.; Demappa, T.; Sannappa, J. Influence of KI salt concentration on the hydroxypropyl methylcellulose films: Optical study, *Opt. Mater.* **2022**, *129*, 112474, <https://doi.org/10.1016/j.optmat.2022.112474>.
14. Cyriac, V.; Ismayil, Noor, I.M.; Mishra, K.; Chavan, C.; Bhajantri, R.F.; Masti, S.P. Ionic conductivity enhancement of PVA: carboxymethyl cellulose poly-blend electrolyte films through the doping of NaI salt. *Cellulose*, **2022**, *29*, 3271–3291, <https://doi.org/10.1007/s10570-022-04483-z>.
15. Abdullah, A.M.; Aziz, S.B.; Saeed, S.R. Structural and electrical properties of polyvinyl alcohol (PVA): Methyl cellulose (MC) based solid polymer blend electrolytes inserted with sodium iodide (NaI) salt, *Arab. J. Chem.* **2021**, *14*, 103388, <https://doi.org/10.1016/j.arabjc.2021.103388>.
16. Shetty, S.K.; Ismayil; Hegde, S.; Ravindrachary, V.; Sanjeev, G.; Bhajantri R.F.; Masti, S.P. Dielectric relaxations and ion transport study of NaCMC:NaNO₃ solid polymer electrolyte films. *Ionics*, **2021**, *27*, 2509–2525, <https://doi.org/10.1007/s11581-021-04023-y>.
17. Bharati, D.C.; Rawat, P.; Saroj, A.L. Structural, thermal, and ion dynamics studies of PVA-CS-NaI-based biopolymer electrolyte films. *J Solid State Electrochem*, **2021**, *25*, 1727-1741, <https://link.springer.com/article/10.1007/s10008-021-04946-6>.
18. Shetty, S.K.; Ismayil, N.; Swathi, M.M.G.; Rashmitha, K. Sodium ion conducting PVA/NaCMC bio poly-blend electrolyte films for energy storage device applications. *Int. J. Polym. Anal. Charact.* **2021**, *26*, 411–424, <https://doi.org/10.1080/1023666X.2021.1899685>.
19. Michael, J.D.; Henry J.B.; Theodore J.B.; David C.S. "Bromine Compounds" in Ullmann's Encyclopedia of Industrial Chemistry Wiley-VCH, Weinheim, **2000**, <https://onlinelibrary.wiley.com/doi/book/10.1002/14356007>.
20. Fuentes, I.; Andrio, A.; Teixidor, F.; Viñas, C.; Compañ, V. Enhanced conductivity of sodium versus lithium salts measured by impedance spectroscopy. Sodium cobaltacarboranes as electrolytes of choice. *Phys. Chem. Chem. Phys.* **2017**, *19*, 15177–15186, <https://doi.org/10.1039/C7CP02526B>.
21. Rani, N.S.; Sannappa, J.; Demappa, T.; Mahadevaiah. Structural, thermal, and electrical studies of sodium iodide (NaI)-doped hydroxypropyl methylcellulose (HPMC) polymer electrolyte films. *Ionics*. **2014**, *20*, 201–207, <https://doi.org/10.1007/s11581-013-0952-8>.
22. Ravi, M.; Pavani, Y.; Kiran, K. K.; Bhavani, S.; Sharma, A. K.; Narasimha Rao, V.V.R. Studies on electrical and dielectric properties of PVP:KBrO₄ complexed polymer electrolyte films. *Materials Chemistry and Physics*, 2011, *130*, 442-448, <https://doi.org/10.1016/j.matchemphys.2011.07.006>.
23. Kumar, S.; Raghu, S.; Demappa, T.; Sannappa, J. Effect of NaBr on the Structural, Thermal and Mechanical Properties of HPMC:NaBr Composite Films. *Asian J. Chem.* **2022**, *34*, 305-310, <https://doi.org/10.14233/ajchem.2022.23507>.
24. Andrew, K. J. Relaxation in low-loss dielectrics. *Journal of Molecular Liquids*, 2000, *86*, 259-268. [https://doi.org/10.1016/S0167-7322\(99\)00147-6](https://doi.org/10.1016/S0167-7322(99)00147-6).
25. Jonscher, A. K. Dielectric Relaxation in low loss Solids. *J molec liqu.* **2000**, *86*, 259–268, [https://doi.org/10.1016/S0167-7322\(99\)00147-6](https://doi.org/10.1016/S0167-7322(99)00147-6).

26. Rani, M. S. A.; Mohamed, N. S.; Isa, M. I. N. (2015) Investigation of the Ionic Conduction Mechanism in Carboxymethyl Cellulose/Chitosan Biopolymer Blend Electrolyte Impregnated with Ammonium Nitrate. *International Journal of Polymer Analysis and Characterization*, 2015, 6, 491-503, <https://doi.org/10.1080/1023666X.2015.1050803>,
27. Kiran, K.K.; Ravi, M.; Pavani, Y.; Bhavani, S.; Sharma, A.K.; Rao, V.V.R.N. Investigations on the effect of complexation of NaF salt with polymer blend (PEO/PVP) electrolytes on ionic conductivity and optical energy band gaps, *Physica B*, **2011**, 406, 1706-1712, <https://doi.org/10.1016/j.physb.2011.02.010>.
28. Kim, C.; Lee, G.; Lio, K.; Ryu, K.S.; Kang, S.G.; Chang, S.H. Polymer electrolytes prepared by polymerizing mixtures of polymerizable PEO-oligomers, copolymer of PVDC and poly(acrylonitrile), and lithium triflate, *Solid State Ion*, **1999**, 123, 251-257, [https://doi.org/10.1016/S0167-2738\(99\)00119-8](https://doi.org/10.1016/S0167-2738(99)00119-8).
29. Lee, K. H.; Kim, H. Y.; La, Y. M.; Lee, D. R. Sung, N. H. Influence of a mixing solvent with tetrahydrofuran and N, N-dimethylformamide on electrospun poly(vinyl chloride) nonwoven mats. *J Polym Sci and Polym Phys*, **2002**, 40, 2259–2268, <https://doi.org/10.1002/polb.10293>.
30. Han, Y.G.; Kusunose, T.; Sekino, T. One-step reverse micelle polymerization of organic dispersible polyaniline nanoparticles. *J Synth Mater* **2009**, 159, 123–131, <https://doi.org/10.1016/j.synthmet.2008.08.011>.
31. Aziz, S.B.; Abdullah O.Gh.; Saeed S.R.; Hameed M.A. Electrical and dielectric properties of copper ion conducting solid polymer electrolytes based on chitosan: CBH model for ion transport mechanism, *Int. J. Electrochem. Sci.* **2018**, 13, 3812 – 3826, <https://doi.org/10.20964/2018.04.10>.
32. Sahoo, S.; Hajra, S.; Mohantha, K.; Choudhary, R. N. P. Processing dielectric and impedance spectroscopy of lead free BaTiO₃, BiFeO₃ CaSnO₃, *J. Alloy. Comp.* **2018**, 766, 25–32, <http://dx.doi.org/10.1016/j.jallcom.2018.06.284>.
33. Ibrahim, S.; Yasin, S.M.M.; Nee, N.M.; Ahmad, R.; Johan, M.R. Conductivity and dielectric behavior of PEO-based solid nanocomposite polymer electrolyte, *J. Soli. Sta. Commun*, **2012**, 152, 426-434, <https://doi.org/10.1016/j.ssc.2011.11.037>.
34. Jonscher, A.K. The Universal dielectric response, *J. Nature*, **1977**, 267, 673-679, <https://doi.org/10.1038/267673a0>.
35. Ramesh, S.; Liew, C.W. Exploration on nano-composite fumed silica-based composite polymer electrolytes with doping of ionic liquid, *J. Non-Cryst. Soli.* **2012**, 358, 931-940, <https://doi.org/10.1016/j.jnoncrysol.2012.01.005>.
36. Funke, K. Jump relaxation in solid electrolytes, *J. Prog. Solid State Chem*, **1993**, 22, 111-195, [https://doi.org/10.1016/0079-6786\(93\)90002-9](https://doi.org/10.1016/0079-6786(93)90002-9).
37. Maji; Pande, P.P.; Choudary, R.B. Effect of Zn(NO₃)₂ filler on the dielectric permittivity and electrical modulus of PMMA, *J. Bull. Mater. Sci.* **2015**, 38, 417-424, <https://doi.org/10.1007/s12034-015-0886-z>.
38. Ranjan, R.; Kumar, R.; Kumar, N.; Behera, B.; Choudhary, R. N. P. Impedance and electric modulus analysis of Sm-modified Pb(Zr_{0.55}Ti_{0.45})_{1-x/4}O₃ ceramics, *J. Alloy. Compd*, **2011**, 509, 6388-6394, <https://doi.org/10.1016/j.jallcom.2011.03.003>.
39. Aziz, S. B.; Rasheed, M. A.; Abidin, Z. H. Z. Optical and electrical characteristics of silver ion conducting nanocomposites solid polymer electrolytes based on chitosan, *J. Electron. Mater.* **2017**, 46, 6119-6130, <https://doi.org/10.1007/s11664-017-5515-8>.



Assessment of natural radiation levels in the forest ecosystem of Shankaraghatta-Shivamogga District, India

Sandeep Dongre¹ · Sunil Kumar^{1,2} · S. Suresh³ · D. R. Rangaswamy⁴ · J. Sannappa¹

Received: 4 November 2021 / Accepted: 28 April 2022
© Akadémiai Kiadó, Budapest, Hungary 2022

Abstract

The estimated mean value of activity of radionuclides (^{226}Ra , ^{232}Th , and ^{40}K) in the forest environment of Shankaraghatta are 11.52 ± 1.6 , 19.94 ± 2.08 and 164.67 ± 3.2 Bq kg⁻¹ for soil, and for building materials 48.53 ± 1.99 , 63.20 ± 2.48 and 470.47 ± 6.59 Bq kg⁻¹ respectively. The average indoor and outdoor Gamma Absorbed Dose rate and total Annual Effective Dose rate are less than the global average values. The forest ecosystem influenced in reducing the natural ambient gamma radiation levels. The constructions materials used for roads enhanced it. The entire measured hazard indices are far below the criterion limit of unity except pink granite and ceramic tiles contains higher activity of radionuclides.

Keywords Activity of ^{226}Ra ^{232}Th and ^{40}K · Gamma-radiation level · Forest ecosystem · Gamma-ray spectrometry · Hazard indices

Introduction

Natural gamma (γ)-radiation originated from the radionuclides (^{226}Ra , ^{232}Th , and ^{40}K) of uranium (^{238}U , ^{235}U), thorium (^{232}Th) series and singly radionuclide potassium (^{40}K), which are occur at the trace level in the environment matrices such as surface soil, rock, water and building materials. Where ^{40}K radioisotope is a single natural radionuclide that makes up 0.0118% of total potassium in the earth crust [1]. About 80% of radiation coming from radionuclides present in soil [2]. The concentrations of these radionuclides present in the soil of the earth differ from place to place since their levels rely on the origins of the soil and the type of rocks in the earth crust [1, 3, 4]. Soil is one of the most prominent natural resource available on the earth surface, which consists of minerals, organic components and radionuclides in

varying quantities known as NORM's (Naturally Occurring Radioactive Materials) which in turn depend on nature of the parent rock and soil [5]. The total radiation emitted by the NORM's is known as terrestrial background radiations [5]. Soil is one of the important natural resource and is the main source of natural radionuclides formed by the weathering of rocks in the environment. That is used for various purposes, including building materials. In order to assess the activity concentration of soil and building materials significantly, it is important to measure the background radiation levels. The cause of indoor and outdoor human exposure is mainly due to natural radiation levels in the soil and its derivatives, which in turn is the source of γ -exposure and radon gases [1, 3, 6, 7]. Exposure to such radionuclides will damage tissue or organ, and causes various health effects. The long term exposure to ionizing radiation has produced hereditary, leukemia; cancer of different organs such as kidney, lungs, stomach, bones, and the structure of DNA may be change and causes some biological effects [4, 8–10]. Measurement of natural radioactivity in soil and building material is important to understand the behavior of natural ecosystem, which also produces the information needed for assessment of probable health risk [2, 3, 6, 11], and epidemiological studies. This type of measurement increases the demands for policy making to radiation protections. The radionuclides such as ^{238}U , ^{226}Ra , ^{232}Th , and ^{40}K present in soil are

✉ J. Sannappa
Sannappaj2012@gmail.com

¹ Department of Studies and Research in Physics, Kuvempu University Sankaraghatta, Jnana Shayadri 577451, India

² Department of Physics, S.S Arts College and T.P Science Institute, Sankeshwar 591313, India

³ Department of Physics, M.P.E Society's S.D.M College, Honnavara 581334, India

⁴ Department of Physics, PES University, Bangalore 560100, India

distributed non uniformly, hence the understanding of their distribution in soil is very important for radiation safety [5].

In view of this importance, the measurement of radionuclides in the Shankaraghatta forest–ecosystem plays an important role because of different geophysical and geographical conditions, and also the soil is covered by rich vegetation and thick forest. Therefore the behavior of radionuclides in this region plays a major role in plant uptakes. The forest plays an important role in the epidural and temporal distribution of radionuclides in this environment. The radionuclides are absorbed into soil corresponds to organic matter, clay carbonate Fe/Mn oxides and take part in biogeochemical process, therefore this distribution of radionuclides in soil is essential for many environmental studies [12]. Due to this we are selected Shankaraghatta, which is located on the bank of river Bhadra. The study area is surrounded by both dense and partial forest ecosystem along with agricultural lands. As per the existing literature survey, there have been many radiological surveys to determine the background radionuclides levels in soil samples and their radiological hazards [13, 14]. However there are few data are available for this type of study area. The aims and objectives of the present study consists of measurement of distribution of radionuclides in soil and building materials by using gamma ray spectrometry, measurement of ambient gamma dose rate, annual effective dose, hazard indices and dose to the public of this study area by using environmental radiation survey meter. The data obtained by the experiment are analyzed and explained in detail.

About the study area

The study area Shankaraghatta including Kuvempu University lies in between 75°39'30" East longitude and 13°45'30" North latitude is a hilly and a natural heritage site as shown in Fig. 1a–c. The grassy hillocks and great altitude truly make it the crowning jewel of the Western Ghats. Rich in biodiversity, this region is home to many endemic species of fauna. The jurisdiction of the Kuvempu University spreads over the districts of Shivamogga and Chikkamagaluru. The dense forest high hilly Malnad in the west and sparsely forested tablelands, semi-Malnad in the east. To understand the distribution of radionuclides and external gamma radiation level, the study area is divided into three zones depending on the local geology and forest area covered. The first zone is partially covered by thin forest area consists of 15 different locations (Fig. 1a) and is comprises of Migmatite and Granodiorite. The second is covered by thick forest area and hillocks, it consists of 18 different locations and is attributed by Ultramafic Schist. The third zone is also covered by hills and thick forest it consists of only one location and is attributed by quartz, dolerite, schist and ortho quartzite. The major soil forms found in the study area are Clay; brown

clay loamy, Red Sandy clay loam Habitation Mask [15] as shown in Fig. 1b. The study area comprises of rock formations belongs Migmatite, Granodiorites–Tonalitic gnesis and Ultramafic Schist as shown in Fig. 1c. The University offers under-graduate, post-graduate and Ph.D. programmes in a wide range of disciplines. It has 35 Post-graduate Departments around 3500 students, 600 teaching and non teaching workers. The University has its headquarters at Jnana Sahyadri campus. It sprawls over an area of 230 acres of a lush green, picturesque locale providing the right ambience for higher education and research programs. The main buildings of the university have been constructed on small hillocks, thus blending naturally with the landscape.

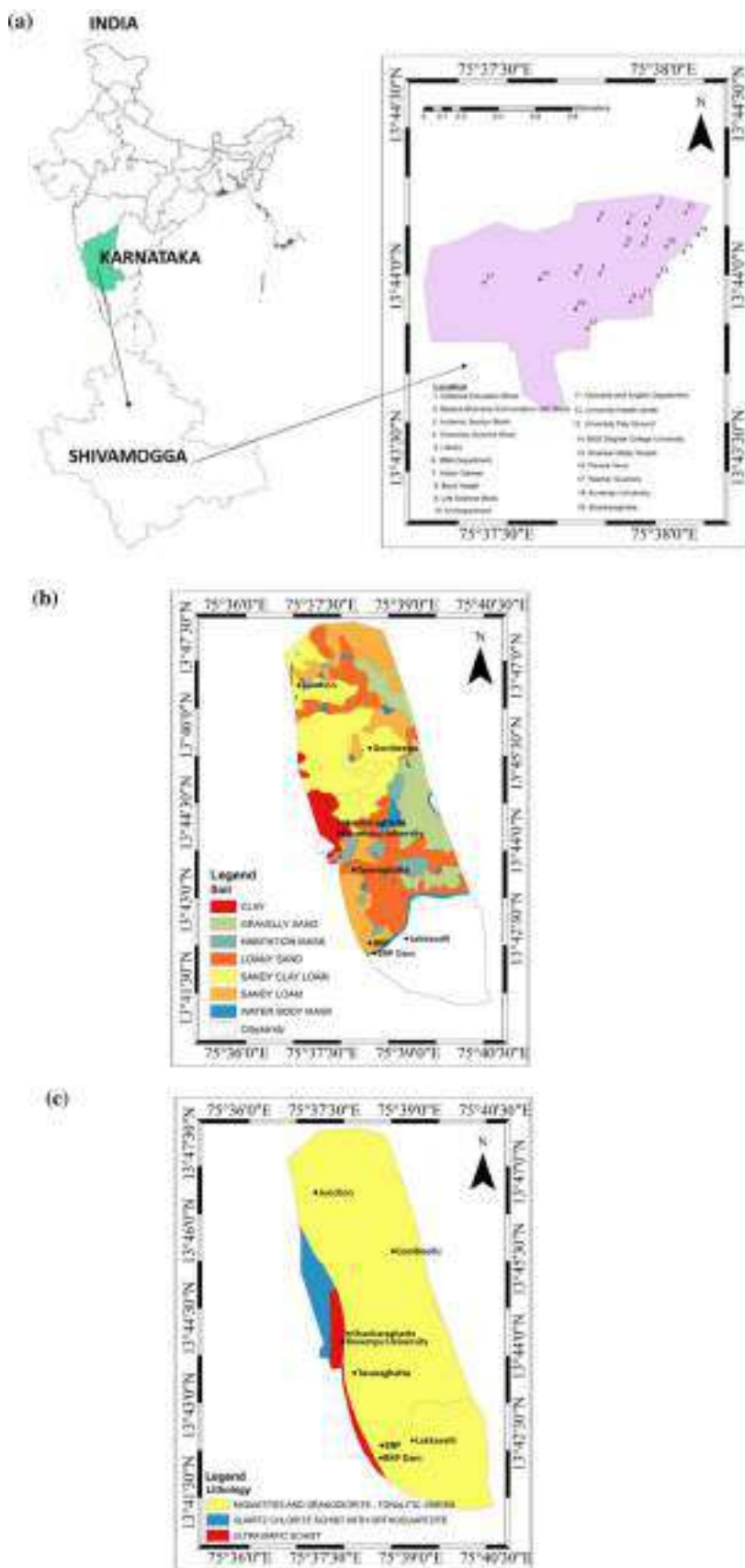
Materials and methods

The sample locations are chosen based on the preliminary survey of background gamma radiation. Soil samples are collected at random from various locations around the study area. At one location 6–8 points each of area 0.5 m² are identified. Upper layer of the soil containing vegetative materials and organic materials were removed. After the collection, all samples were thoroughly mixed, with all noxious substances like plants, detritus, hunks of stone, and pebbles eliminated [16].

Sample preparation

To begin, initially about 2 kg soil collected from each location, soil samples are collected over a 0.5 m² surface area, and once plants and roots have been removed, a location is marked. The marked spot was dug up to a depth of 15 cm, which was crushed into the finest powdered form possible before being sieved through 500 µm (0.5 mm) to remove the undesired particles. About 300 g of samples are subjected to air dry for several days in order to remove the moisture content in it. The cleansed and sieved samples then dried in an electric oven at temperature of 110 °C for 12 h make sure it has become moisture free and to achieve constant weight, thus formed powdered samples transferred to plastic containers and are stored in it, meanwhile care has taken that it is air tightened and are sealed externally using adhesive tapes. These homogenized samples were kept identical to that of reference materials as to their geometrical shapes, size and weight. Then kept aside for about a month (more than 7 times the half-lives of ²²²Rn, and ²²⁴Ra) at room temperature for to ensure that secular equilibrium has been established between radium and its daughter products further more; before being taken it to analysis using gamma ray spectrometry [17–20]. Similarly about 2 kg of each building materials samples such as cement, granite rocks, vitrified tiles, marbles, bricks collected locally and are powdered by

Fig. 1 **a** Natural ambient gamma radiation levels, distribution of radionuclides in soil and building materials in environment of Shankaraghatta (Zone-I). **b** Natural ambient gamma radiation levels, distribution of radionuclides in soil and building materials in environment of Shankaraghatta (Zone-II&III). **c** Natural ambient gamma radiation levels, distribution of radionuclides in soil and building materials in environment of Shankaraghatta (Zone-II&III)



using hammer and crushers. About 300 g of samples collected in polythene cover after that the same procedure is used for the preparation of building material samples as for soil.

Gamma-ray spectrometry

Gamma-ray Spectrometry provides a convenient, direct and non-destructive analytical method utilizing for the estimation of various gamma emitting radionuclides present in the environmental samples. It provides two types of detectors namely high efficiency scintillation detectors [NaI (Tl)] and high-resolution semiconductor detectors (HPGe detectors). There are numerous methods used for the detection of gamma emitting radionuclides in the environmental samples. However, the qualitative and quantitative gamma ray spectroscopy is one of the powerful techniques available for the non destructive estimation of samples in the environment matrix [21]. This techniques enables the use of large quantities of sample to be counted and this method reduces the extraneous background to very low values using suitable shielding arrangements and moreover due to its excellent separation capabilities it gives us much of information regarding all the radionuclides. Along with these features appropriate software codes that have now become available has made gamma spectroscopic technique one of the accurate method for estimating the activity concentration in the environmental samples and is cheaper when compared to other new methods; mass spectroscopy. In the present study $3' \times 3$ NaI (Tl) detector based gamma spectrometer was used for the estimation of gamma emitting radionuclides in soil, and building materials.

Calibration of gamma ray spectrometer system

In order to get an accurate measurement, it is must to calibrate the counting system with standard sources of the same geometry and composition as the sample under test measurement.

Basic requirements needed for calibration is as follows;

- The distance between detector and sample should be constant for particular given calibration
- In order to avoid frequency of changing the standards, the selected sources must be of longer half life

Energy calibration

To determine the energy of each channel and to ensure the linearity exists between the energy and number of channel corresponding to that energy calibration should be carried out. The gamma spectrometry has been calibrated for a wide range of energy up to 3 MeV in order to accommodate all the

natural radionuclides. The gamma energy emitter for ^{137}Cs has 661.65 keV, for ^{60}Co is 1173.24 and 1332.46 keV and 2614.5 keV gamma energy emitter of RG-Th (IAEA thorium standard) has been for the energy calibration purposes. The sources are kept at a distance of 5 cm and the spectrum was acquired for reasonable time so that photo peaks have sufficient counts for analysis, the region of interest (ROI) and centroid peak with channel number is identified. The spectrum analyzer has got provision to fit the peak in order to obtain the peak position in the channels. Energy of any channel is determined by using relation

$$E = (m \times \text{Channel number}) + b \quad (1)$$

where m —is the slope, b —is the intercept.

The energy calibration of the graph is as shown in Fig. 2a

Efficiency calibration

It is calibrated with the use of standard sources such as RGU-I (Uranium), RGTh-I (Thorium) and RGK-I (Potassium) produced from IAEA, these standard samples are filled in container which is similar to that of sample's

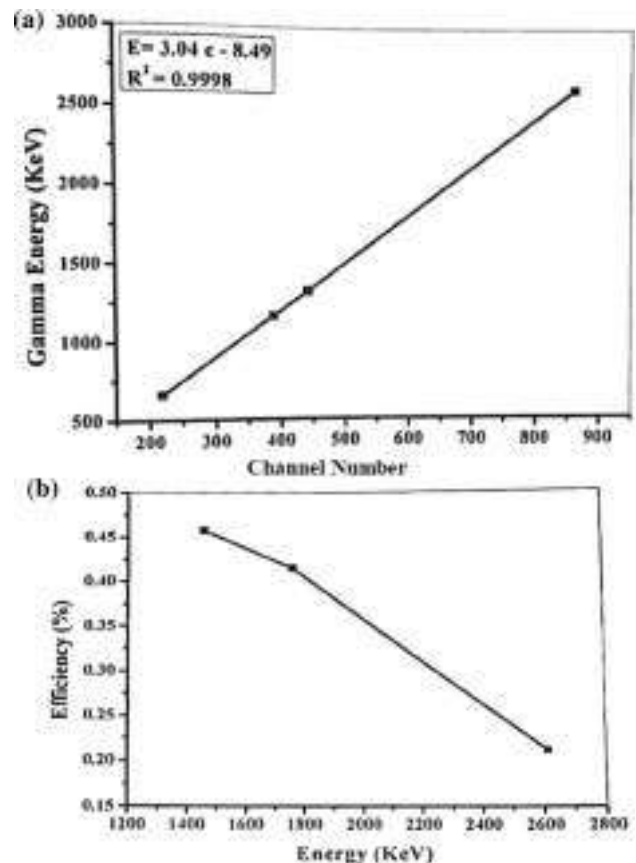


Fig. 2 **a** Energy Calibration graph of NaI(Tl) detector, **b** Efficiency calibration curve graphs

geometry. These samples were prepared as per the normal procedure and are kept for about month. The standard efficiency spectra were acquired for time period of 10,000 s, and the obtained spectrum is analysed for net counts under the photo peaks of gamma energies of interests using G-spec software.

The efficiency of gamma ray energies of various radionuclides can be determined with g use of following relation:

$$E(\%) = N \times \frac{100}{A_s} \times \frac{100}{G_a} \quad (2)$$

where N -represents background counts per second of the radionuclides, A_s -represents the activity of standard sources (Bq), G_a -represents the gamma abundance for particular energy.

The efficiency of calibration graph is as shown in Fig. 2b.

Estimation of activity of radionuclides present in soil and building materials

The activity of radionuclides of prepared samples was estimated by using Gamma ray spectrometry method. To obtain good statistics for activity of concentration of radionuclides (^{226}Ra , ^{232}Th , and ^{40}K) in soil and building materials GSPEC software is used. The Procedure is followed to estimate the activity.

To determine the activity of radionuclides, the formula has given by following equation [22]. (IAEA/RCA, 1989.)

$$A(\text{Bq kg}^{-1}) = (C \pm \text{SD}) \times \frac{100}{P_E} \times \frac{100}{A_\gamma} \times \frac{1000}{W} \quad (3)$$

where the notations ' C ' is the Compton corrected background subtracted counts per second, SD-Standard deviation due to counting, P_E -The detector's photo peak efficiency (%), A_γ -The Gamma ray abundance (%), W -The sample's weight (in grams).

Scintillometer (type SM 141D, ECIL)

The ECIL, Scintillometer, model SM 141D is used to measure gamma radiation levels in the environment. It's a radiometric, geophysical, and environmental reconnaissance scintillometer that's tough, light, and portable. The radiation levels are displayed on the 216 LCD modules with antiglare and backlight facilities, which provide better visibility under direct sunlight and even in low light conditions, thanks to the microcontroller-based design and the large crystal volume. The scintillometer was calibrated at regular intervals using standard ^{137}Cs and ^{60}Co sources by ECIL (Electronics Corporation of India limited) standards.

Ambient gamma radiation level

An ambient gamma radiation levels in the outdoor and indoor atmosphere of the study area was measured with the use of Scintillometer (Type SM 141D, ECIL). A thallium-activated sodium iodide crystal is optically connected to a photomultiplier as the detector. Every reading was taken at a height of 1 m above the ground. At each place, 4–5 readings have been taken and with the use of factor of conversion ($1 \mu\text{R h}^{-1} = 8.7 \text{ nGy h}^{-1}$), exposure rate ($\mu\text{R h}^{-1}$) is converted into an absorbed dose rate (nGy h^{-1}) [21, 23], and then it is converted into an equivalent effective dose rate using conversion factor 0.7 Sv y^{-1} [11].

Estimation of radiological hazard indices

Soil and building materials such as granite rocks, bricks, cement, sand, and tiles are utilised in the construction of the buildings. As a result, determining the radiation hazard level of these materials to mankind is essential. Radiation dangers arise from inhalation and ingestion of radioactive materials, which directly harm the living tissues and respiratory organs. Using the measured specific activity concentrations of radionuclides, the radiological hazard associated with soil and various construction materials were determined (^{226}Ra , ^{232}Th , and ^{40}K). Various forms of hazard indices have been defined previously [24–27].

The gamma index (I_γ)

The gamma index (I_γ) is radiation risk assessment parameter is used for identifying safe materials for construction purposes. I_γ has been introduced to account for the combined impact of ^{226}Ra , ^{232}Th , and ^{40}K as radiological hazard associated with soil and building material.

$$I_\gamma = \frac{S_{\text{Ra}}}{300} + \frac{S_{\text{Th}}}{200} + \frac{S_{\text{K}}}{3000} \quad (4)$$

where the notations S_{Ra} , S_{Th} , and S_{K} are the activity concentrations of ^{226}Ra , ^{232}Th and ^{40}K in Bq kg^{-1} respectively. Materials having $I_\gamma \leq \gamma \leq 2$ will make an increase of 0.3 mSv y^{-1} in the annual effective dose rate, whereas $2 \leq I_\gamma \leq 6$ correspond to an increase of 1 mSv y^{-1} [27, 28].

The alpha index (I_α)

The radiation risk assessment parameter alpha index (I_α) is defined by Righi and Bruzzi [29]. This parameter (I_α)

gives us the excess of alpha radiation due to radon inhalation which originated from soil and dwellings.

$$I_{\alpha} = \frac{S_{\text{Ra}}}{200} \quad (5)$$

where S_{Ra} is the specific activities of ^{226}Ra in Bq kg^{-1}

Radium equivalent activity (Ra_{eq})

Primeval radionuclides plays prominent role in our environment and they are not uniformly distributed, in order to know the exposure rate; the total exposure rate is defined in terms of Radium equivalent activity (Ra_{eq}) in Bq kg^{-1} , which in turn used to compare the specific activity of materials containing variable amounts of radionuclides (^{226}Ra , ^{232}Th and ^{40}K) [24, 26 and 28].

$$\text{Ra}_{\text{eq}} (\text{Bq kg}^{-1}) = S_{\text{Ra}} + 1.43 S_{\text{Th}} + 0.077 S_{\text{K}} \quad (6)$$

where the notations S_{Ra} , S_{Th} and S_{K} stand in for activity concentrations of ^{226}Ra , ^{232}Th , ^{40}K in Bq kg^{-1} , respectively.

External hazard index (H_{ex})

The index parameter external hazard index (H_{ex}) has been used to assess the indoor radiation dose due to the external exposure of human beings to hazardous gamma radiation from natural radionuclides. H_{ex} is a radiation hazard index defined by Beretka and Mathew [26]. As per the UNSCEAR [24], the external hazard index (H_{ex}) is calculated by using the equation.

$$H_{\text{ex}} = \frac{S_{\text{Ra}}}{370} + \frac{S_{\text{Th}}}{259} + \frac{S_{\text{K}}}{4810} \leq 1 \quad (7)$$

where the notations S_{Ra} , S_{Th} and S_{K} stand in for activity concentrations of ^{226}Ra , ^{232}Th , ^{40}K in Bq kg^{-1} respectively. H_{ex} Value must be less than unity to keep the radiation hazard insignificant [30]. The maximum value of H_{ex} equal to unity corresponds to the upper limit of Ra_{eq} (370 Bq kg^{-1}).

Internal hazard index (H_{in})

Internal organs exposure to carcinogenic radon and its short-lived progenies are estimated by the use of internal hazard index (H_{in}) parameter. The internal hazard index is also hazardous to the respiratory organs, which is given by the equation [26].

$$H_{\text{in}} = \frac{S_{\text{Ra}}}{185} + \frac{S_{\text{Th}}}{259} + \frac{S_{\text{K}}}{4810} \leq 1 \quad (8)$$

where the notations S_{Ra} , S_{Th} , and S_{K} stand in for the activity concentrations of ^{226}Ra , ^{232}Th and ^{40}K in Bq kg^{-1} ,

respectively. The safe use of a material in the construction of dwellings, H_{in} should be less than unity [31].

Indoor and outdoor gamma absorbed dose rate and annual effective dose rate

The absorbed dose rate (D) is measured using survey meter by holding it in the air at 1 m above the ground surface for the uniform distribution of the naturally occurring radionuclides (^{226}Ra , ^{232}Th and ^{40}K) and was calculated based on guidelines provided by [24, 32]. The absorbed dose rate (D_{out}) is calculated with the help of following formula:

$$D_{\text{out}} (\text{nGy h}^{-1}) = 0.462 S_{\text{Ra}} + 0.604 S_{\text{Th}} + 0.042 S_{\text{K}} \quad (9)$$

And, the indoor absorbed dose rate (D_{in}) can be calculated by avail oneself of the following formula

$$D_{\text{in}} (\text{nGy h}^{-1}) = 0.92 S_{\text{Ra}} + 1.1 S_{\text{Th}} + 0.08 S_{\text{K}} \quad (10)$$

where the notations S_{Ra} , S_{Th} and S_{K} stand in activity concentrations of ^{226}Ra , ^{232}Th , ^{40}K in Bq kg^{-1} , respectively. Where, D_{out} and D_{in} indicates the outdoor and indoor absorbed dose rate in nGy h^{-1} . The coefficients of S_{Ra} , S_{Th} and S_{K} are the activity concentration to dose rate conversion factors in $\text{nGy} \cdot \text{h}^{-1}$ per Bq kg^{-1} . It is given that the global mean value of the ambient gamma radiation absorbed dose rate for an outdoor is 59 nGy h^{-1} and 84 nGy h^{-1} for indoor [24]. The annual equivalent effective dose rate for both indoor and outdoor was estimated from the out and out external gamma radiation dose rate (D) by taking into an account of 'occupancy factor' (OF) 0.2 for outdoor and 0.8 for indoor environment and the conversion factor (CF) from the absorbed dose rate in air to effective dose is 0.7 Sv y^{-1} for the adults. The E_{out} is calculated by avail oneself of the following equation proposed by UNSCEAR [24].

$$E_{\text{out}} = (\text{mSv y}^{-1}) = D_{\text{out}} (\text{nGy h}^{-1}) \times 8760 \times 0.2 \times 0.7 \times 10^6 \quad (11)$$

where E_{out} is the outdoor annual effective dose rate expressed in $\text{mSv} \cdot \text{year}^{-1}$.

Likewise, the indoor annual effective dose rate (E_{in}) is calculated by avail oneself of following equation proposed by UNSCEAR [24].

$$E_{\text{in}} (\text{mSv y}^{-1}) = D_{\text{in}} (\text{nGy h}^{-1}) \times 8760 \times 0.8 \times 0.7 \times 10^6 \quad (12)$$

Annual gonadal dose equivalent (AGDE)

To estimate the dose received by different body organs and gonads UNSCEAR has formulated an equation and is given by;

$$AGDE = 3.09 \times S_{Ra} + 4.18 \times S_{Th} + 0.314 \times S_K \quad (13)$$

where the notations S_{Ra} , S_{Th} , and S_K stand in for the activity concentrations of ^{226}Ra , ^{232}Th and ^{40}K in Bq kg^{-1} , respectively.

Excess lifetime cancer risk (ELCR)

The excess lifetime cancer risk is defined as the tendency that a person will develop cancer over his lifetime of radiation exposure. The cancer cell development due to exposure to ionizing radiation is not an immediate effect. It takes several years of time to develop. The cancer occurs only when an individual has reached an advanced age [33]. Therefore based on the estimation of AEDE values ELCR was estimated by the Eq. (11).

$$ELCER = AEDE \times MDL \times RF \quad (14)$$

where MDL represents the mean duration of life in years for Indian citizens equal to 70 and 0.057 is the risk factor to the public exposure [25, 34, 35].

Results and discussion

(a) Distribution of radionuclides in soil

The activity concentration of radionuclides (^{226}Ra , ^{232}Th and ^{40}K), present in soil and building materials of the study area were determined by gamma ray spectrometry using NaI [TI] detector. The average values of the activity concentrations of radionuclides, gamma absorbed dose (GAD) rate and equivalent effective dose rate are given in the Table 1. The recorded values of radionuclides (^{226}Ra , ^{232}Th and ^{40}K) in the soil samples of the entire study area varies from $6.5 \pm 0.4 \text{ Bq kg}^{-1}$ to $15.25 \pm 2.6 \text{ Bq kg}^{-1}$, $10.49 \pm 0.6 \text{ Bq kg}^{-1}$ to $36.25 \pm 3.5 \text{ Bq kg}^{-1}$ and $50.16 \pm 1.5 \text{ Bq kg}^{-1}$ to $260.27 \pm 4.6 \text{ Bq kg}^{-1}$ with a median values of 11.52 ± 1.6 , 19.94 ± 2.08 and $164.67 \pm 3.2 \text{ Bq kg}^{-1}$ respectively. The higher values of radionuclides (^{226}Ra , ^{232}Th and ^{40}K) in soil was observed near the sports ground, chemical block, administrative office, nudi loka, social science block. These locations belong to second zone which consists mafic mineral schist, feldspar, kyanite, andalusite and staurolite and some garnet. These minerals contain higher activity of radionuclides [36, 37]. Slightly lesser activity concentration of radionuclides were observed at the prasanga, Biotech, Library science and computer Science block these locations are situated at the bottom of the hill towards the west. The rock system consists of ultramafic schist which is meta-igneous rocks with low silica content having

lesser activity of radionuclides. Slightly lower activities of radionuclides were also observed in some locations of the first zone, which consists of some villages with thin forest. This zone is comprised by migmatite and granodiorite. The mineral compositions of these rocks are quartz, clays ortho clays, biotite, amphibol, hornblend and silicate [28]. The radionuclides are depends on the mineral composition of the feldspar and other mineral content [29]. Due to which lesser activity of radionuclides is observed in this zone. The lower activity of radionuclides is noticed at university quarters, BRP Quarters and Bhadra Dam. The university quarters are comprised by quartz, tolerite, schist, and orthoquartzite. Mineral composition of the rocks is tolerite minerals, quartz, and epizoite. These minerals may contain lower activity of radionuclides [38]. Hence lower activity is observed in these locations. The activity concentration of ^{40}K was found to be higher than that of ^{226}Ra and ^{232}Th in soil of all the locations of the study area. The abundance of ^{40}K is proportional to the silica content of the rock to some extent [39]. The activity concentration of thorium is higher than that of radium at all locations. The ratio of thorium (^{232}Th) and radium (^{226}Ra) was in the range of 1.61 to 2.90 the medium value can be used to determine the relative abundance of uranium and thorium in a given area. In the present study the estimated average activity concentration of ^{226}Ra , ^{232}Th , ^{40}K are $11.52 \pm 1.60 \text{ Bq kg}^{-1}$, $19.94 \pm 2.04 \text{ Bq kg}^{-1}$ and $164.67 \pm 3.28 \text{ Bq kg}^{-1}$ respectively, these average values of radionuclides in the soil samples of the study area were found to be lower than the world average value 33, 45, 420 Bq kg^{-1} and Indian average value 29, 64, 400 Bq kg^{-1} [24]. The standard deviation, uncertainty and standard uncertainty in measurement of activity of radionuclides (^{226}Ra , ^{232}Th and ^{40}K) using Bayesian statistics for soil is shown in Table 1. The estimated data shows confidence level of 95.45% ($^{226}\text{Ra} = 3.66$, $^{232}\text{Th} = 2.59$ and $^{40}\text{K} = 25.50$) and with the help of 'T' table we found the coverage factor $k = 2$.

Figure 3a–c Shows correlation between the absorbed dose rate and activity of radionuclides (^{226}Ra , ^{232}Th , and ^{40}K) of soil. In comparison to ^{232}Th , the correlation between activity and total absorbed dose was determined to be ($R^2 = 0.90$), whereas the least relevant correlation was reported for ^{226}Ra ($R^2 = 0.70$) and ^{40}K ($R^2 = 0.78$). This is observed due to the fact that the major contribution is from Thorium content present in the soil [40]. Gamma absorbed dose is the energy imparted to a matter by ionizing radiation per unit mass of irradiated materials at the region of interest. The calculated activity concentration of radionuclides soil samples were used to estimate the GAD in air with the use of dose conversion coefficients of 0.46 nGy h^{-1} , 0.6 nGy h^{-1} and 0.042 nGy h^{-1} for ^{226}Ra , ^{232}Th , ^{40}K [24].

Table 1 Average activity of radionuclides and gamma absorbed dose rate of soil samples of the study area

S. no	Zones of location	Activity of Radionuclides (Bq kg ⁻¹)		²³² Th	⁴⁰ K	²³² Th/ ²²⁶ Ra	AEDE (mSv y ⁻¹)		
		²²⁶ Ra	²³² Th				GADR (mGy h ⁻¹)	E _{in}	E _{out}
<i>ZONE-I</i>									
1	Shankaraghatta	9.53 ± 0.50 ± 0.25	15.26 ± 2.00 ± 1.00	70.15 ± 2.50 ± 1.25	1.60	16.57	0.08	0.02	0.10
2	Tipperudrappa Layout	10.51 ± 2.50 ± 1.25	17.21 ± 2.50 ± 1.25	80.37 ± 2.00 ± 1.00	1.64	18.63	0.09	0.02	0.11
3	Kudremukh Layout	11.24 ± 1.6 ± 0.80	16.33 ± 1.50 ± 0.75	100.27 ± 3.00 ± 1.50	1.45	19.27	0.09	0.02	0.12
4	Shanthi Nagara	10.10 ± 1.29 ± 0.60	14.27 ± 0.75 ± 0.35	90.42 ± 2.50 ± 1.25	1.41	17.08	0.08	0.02	0.10
5	BR Project	8.25 ± 0.50 ± 0.25	12.24 ± 0.57 ± 0.30	50.16 ± 1.50 ± 0.75	1.48	13.31	0.07	0.02	0.08
6	Near Bhadra Dam	7.54 ± 0.81 ± 0.40	10.49 ± 3.50 ± 1.75	65.21 ± 1.80 ± 0.90	1.39	12.56	0.06	0.02	0.08
7	Singanmane	12.50 ± 1.6 ± 0.80	13.46 ± 2.10 ± 1.05	110.37 ± 2.60 ± 1.30	1.08	18.54	0.09	0.02	0.11
8	Fishery and Hand Post	11.52 ± 1.75 ± 0.85	15.52 ± 2.40 ± 1.20	95.79 ± 2.00 ± 1.00	1.35	18.72	0.09	0.02	0.11
9	River turn Lodge	70.12 ± 0.57 ± 0.30	18.34 ± 2.40 ± 1.20	86.47 ± 1.50 ± 0.75	0.26	47.10	0.23	0.06	0.29
10	Lakkavalli	08.50 ± 0.81 ± 0.40	15.14 ± 1.40 ± 0.70	80.42 ± 1.70 ± 0.85	1.78	16.45	0.08	0.02	0.10
11	Kuvempu Nagara	10.34 ± 1.50 ± 0.75	14.25 ± 1.29 ± 0.65	130.25 ± 2.80 ± 1.40	1.38	18.85	0.09	0.02	0.12
12	Tavaraghatta	10.52 ± 1.50 ± 0.75	11.33 ± 1.00 ± 0.50	120.46 ± 2.50 ± 1.25	1.08	16.76	0.08	0.02	0.10
13	Malenahalli	09.15 ± 0.50 ± 0.25	13.32 ± 1.50 ± 0.75	98.45 ± 3.50 ± 1.75	1.46	16.41	0.08	0.02	0.10
14	Gonibeedu	11.47 ± 1.60 ± 0.80	14.27 ± 2.30 ± 1.15	110.26 ± 4.50 ± 2.25	1.24	18.55	0.09	0.02	0.11
15	Junction	12.5 ± 1.8 ± 0.90	19.34 ± 1.7 ± 0.85	125.09 ± 4.00 ± 2.00	1.55	22.71	0.11	0.03	0.14
<i>ZONE-II</i>									
1	Sports Ground	12.25 ± 2.10 ± 1.05	17.52 ± 3.00 ± 3.00	185.53 ± 3.60 ± 2.18	1.43	24.03	0.12	0.03	0.15
2	BGS College	11.52 ± 2.00 ± 1.00	16.54 ± 2.60 ± 2.60	189.25 ± 3.50 ± 1.75	1.44	23.26	0.11	0.03	0.14
3	Chemical Science Block	14.24 ± 2.50 ± 1.25	35.27 ± 2.10 ± 2.10	200.00 ± 4.50 ± 2.25	2.48	36.28	0.18	0.04	0.22
4	Ladies Hostel	12.5 ± 1.74 ± 0.87	36.25 ± 2.20 ± 2.20	260.27 ± 4.20 ± 2.10	2.90	38.60	0.19	0.05	0.24
5	Guest House	14.12 ± 2.50 ± 1.25	30.15 ± 2.40 ± 2.40	215.11 ± 4.60 ± 2.30	2.14	33.77	0.17	0.04	0.21
6	Shankara mata Temple	14.52 ± 2.60 ± 1.30	35.45 ± 2.50 ± 2.50	220.25 ± 4.50 ± 2.25	2.44	37.37	0.18	0.05	0.23
7	Social Science Block	13.33 ± 2.00 ± 1.00	20.22 ± 2.30 ± 2.30	210.30 ± 3.60 ± 1.80	1.52	27.20	0.13	0.03	0.17
8	Prasaranga	12.50 ± 1.80 ± 0.90	18.25 ± 2.00 ± 2.00	200.15 ± 3.50 ± 1.75	1.46	25.20	0.12	0.03	0.15
9	Bio Science Block	13.50 ± 2.50 ± 1.25	25.15 ± 3.20 ± 3.20	180.10 ± 3.00 ± 1.50	1.86	28.99	0.14	0.04	0.18
10	Library Science Block	12.45 ± 1.90 ± 0.95	22.24 ± 3.00 ± 3.00	225.20 ± 3.40 ± 1.70	1.79	28.64	0.14	0.04	0.18
11	Computer Science Block	11.48 ± 1.50 ± 0.75	18.32 ± 2.60 ± 2.6	235.50 ± 3.50 ± 1.75	1.60	26.26	0.13	0.03	0.16
12	Mlib	11.53 ± 1.60 ± 0.80	19.38 ± 2.50 ± 2.50	250.24 ± 3.00 ± 1.5	1.68	27.54	0.14	0.03	0.17
13	Boys Hostel	10.52 ± 0.80 ± 0.40	20.42 ± 2.00 ± 2.00	240.25 ± 3.50 ± 1.75	1.94	27.28	0.13	0.03	0.17
14	Commerce & MBA Block	9.54 ± 0.50 ± 0.25	18.17 ± 2.50 ± 2.50	230.15 ± 4.10 ± 2.05	1.90	25.05	0.12	0.03	0.15
15	Administrative Block	15.25 ± 2.40 ± 1.20	27.12 ± 1.60 ± 1.60	250.49 ± 4.50 ± 2.25	1.78	33.95	0.17	0.04	0.21

Table 1 (continued)

S. no	Zones of location	Activity of Radionuclides (Bq kg ⁻¹)			²³² Th/ ²²⁶ Ra	AEDE (mSv y ⁻¹)	E _{in}	E _{out}	E _{Total}
		²²⁶ Ra Activity ± SD ± RUN	²³² Th Activity ± SD ± RUN	⁴⁰ K Activity ± SD ± RUN					
16	Distance Education	15.25 ± 2.40 ± 1.20	27.12 ± 1.60 ± 1.60	250.49 ± 4.50 ± 2.25	1.78	33.95	0.04	0.21	
17	Basava Bhavana	15.25 ± 2.40 ± 1.20	27.12 ± 1.60 ± 1.60	250.49 ± 4.50 ± 2.25	1.78	33.95	0.04	0.21	
18	Nudi Loka	14.54 ± 2.00 ± 1.00	30.15 ± 2.10 ± 2.10	240.30 ± 4.00 ± 2.00	2.07	35.02	0.04	0.21	
ZONE-III									
1	Teachers quarters	06.52 ± 0.40 ± 0.20	10.49 ± 0.6 ± 0.60	50.16 ± 1.5 ± 0.75	1.61	15.65	0.02	0.10	
	MAX	15.25 ± 2.60 ± 1.30	36.25 ± 3.5 ± 1.75	260.27 ± 4.6 ± 2.30	2.90	38.60	0.05	0.24	
	MIN	06.52 ± 0.40 ± 0.20	10.49 ± 0.6 ± 0.30	50.16 ± 1.50 ± 0.75	1.61	15.65	0.02	0.08	
	AV	11.52 ± 1.60 ± 0.79	19.94 ± 2.04 ± 1.02	164.67 ± 3.28 ± 1.62	1.72	24.28	0.03	0.15	
	GM	11.26 ± 1.40 ± 0.69	18.81 ± 1.90 ± 0.94	148.67 ± 3.12 ± 1.53	1.67	23.14	0.03	0.14	
	SD	2.38 ± 0.71 ± 0.35	7.21 ± 0.70 ± 0.35	68.83 ± 0.97 ± 0.51	0.42	7.61	0.01	0.05	
	RUN	0.41 ± 0.12 ± 0.06	1.24 ± 0.12 ± 0.06	11.80 ± 0.17 ± 0.09	0.07	1.31	0.00	0.01	
	SU	4.36 ± 1.10 ± 0.55	12.88 ± 2.45 ± 0.72	105.05 ± 1.55 ± 0.77	0.64	11.47	0.01	0.08	

AV Average, GM Geometric mean, SD standard deviation, RUN random uncertainty, SU standard uncertainty
 The bold representation in this tables are the minimum, maximum, average and uncertainty values that are given at the end of each table

The Fig. 4a–c shows correlation between ²²⁶Ra and ²³²Th ²²⁶Ra and ⁴⁰K and ²³²Th and ⁴⁰K present in soil samples. There exists is a strong and positive correlation between ²²⁶Ra and ²³²Th with correlation coefficient of R² = 0.57 and in between ²²⁶Ra and ⁴⁰K the correlation coefficient of R² = 0.46 and similarly for ²³²Th and ⁴⁰K it is observed R² = 0.51 respectively.

(a) Activity Concentration of radionuclides in Building materials:

About 17 building materials were collected from the study area. The activity of radionuclides (²²⁶Ra, ²³²Th, and ⁴⁰K) of the building material was estimated by gamma ray spectrometry. The activity concentration of radionuclides in building materials were summarized in Table 2. The activity concentration of ²²⁶Ra, ²³²Th, and ⁴⁰K varies from 8.12 ± 0.30 Bq kg⁻¹ to 150.27 ± 4.0 Bq kg⁻¹, 18.47 ± 0.2 Bq kg⁻¹ to 200.17 ± 4.5 Bq kg⁻¹ and 45.25 ± 2.0 Bq kg⁻¹ to 1500.24 ± 14.5 Bq kg⁻¹ with an average value of 48.53 ± 1.99 Bq kg⁻¹, 63.20 ± 2.48 Bq kg⁻¹ and 470.47 ± 6.59 Bq kg⁻¹ respectively. The higher values noticed in pink granite, slightly lower values in gray granite and lower values in the Black granite. This may be due to higher content of minerals compositions such as quartzite, silica, potassium feldspar is present in granite [34, 36]. The different colours of the granite are due to variation in their chemical compositions [41]. The activity of marbles is same as local sand black granite. Marble is metamorphic rock consists of calcite and other minerals such as clay, silt, mica, quartzite, phirite iron oxide, graphite. The colour of the marble is due to the different mineral composition. This mineral composition may be very less radioactive nuclides; hence it is observed that the lower activity of radionuclides in marbles. The activity of radionuclides in ceramic is higher than that of vitrified tiles. Ceramic is admixture of illicit white clay kaolin white clay, calcite dolomite, sodium feldspar perilte, and talc, quartz and sand granule [42]. But vitrified tiles are a mixture of 60% clay 40% some mineral compositions. The ceramic contains more radionuclides than vitrified tiles; hence activity of radionuclides in ceramic is higher than that of vitrified tiles. The activity concentration in cement brick is higher compared to soil brick because the cement brick made-up of cement and granite rock jolly, these rocks contains higher activity of radionuclides [43].

The activity concentration in different types of cement is slightly higher than that of marble, black granite and sand because cement is made up of chemical combination of calcium, silicon, aluminium, iron and other ingredients. common materials is used to manufacture cement include limestone, chalk or marl combined with clay and, shells,

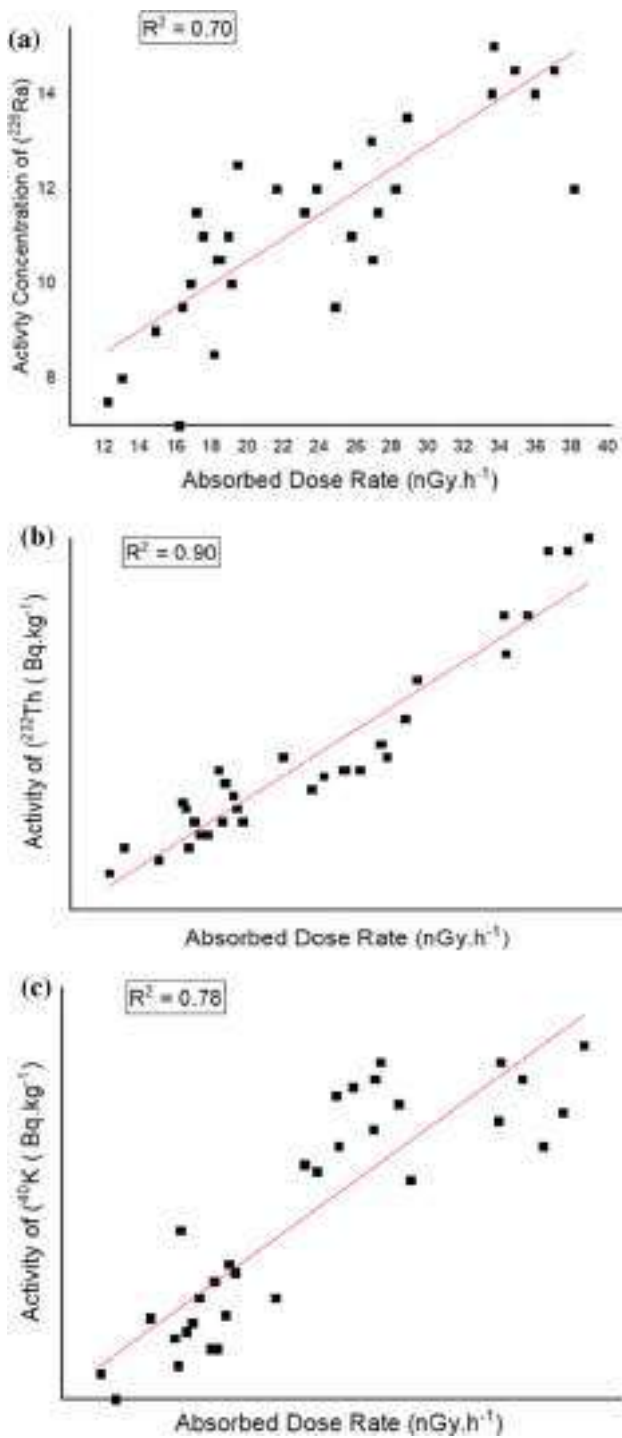


Fig. 3 **a** Correlation between calculated absorbed dose rate and ^{226}Ra concentration in soil samples of study area, **b** Correlation between calculated absorbed dose rate and ^{232}Th concentration in soil samples of study area, **c** Correlation between absorbed dose rate and ^{40}K concentration in soil samples of study area

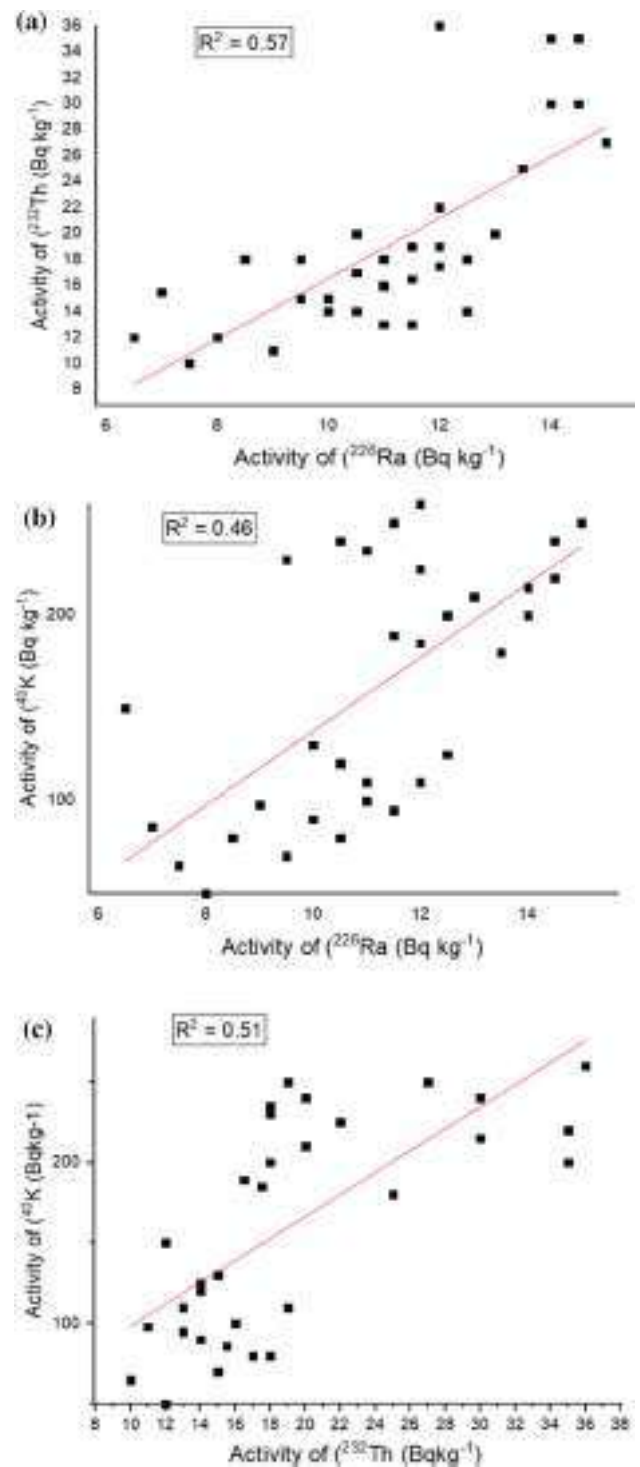


Fig. 4 **a** Correlation between the activity of ^{232}Th and ^{226}Ra in soil samples, **b** Correlation between the activity of ^{226}Ra and ^{40}K in soil samples, **c** correlation between the activity of ^{232}Th and ^{40}K in soil samples

Table 2 Average activity concentration of ^{226}Ra , ^{232}Th and ^{40}K , gamma absorbed dose and annual effective dose in building materials samples of Shankaraghatta

S. no	Building materials	Activity of radionuclides(Bq kg ⁻¹)			$^{232}\text{Th}/^{226}\text{Ra}$	GADR (Din) nGy h ⁻¹	AEDE (mSv y ⁻¹)		
		^{226}Ra Activity \pm SD \pm RUN	^{232}Th Activity \pm SD \pm RUN	^{40}K Activity \pm SD \pm RUN			E_{in}	E_{out}	E_{total}
<i>Granites</i>									
1	Pink granite	150.11 \pm 4.10 \pm 0.12	200.17 \pm 4.20 \pm 2.10	1500.24 \pm 10.10 \pm 5.05	1.33	478.30	2.34	0.60	2.93
2	Black granite	35.12 \pm 2.20 \pm 0.62	40.32 \pm 3.50 \pm 1.75	550.36 \pm 8.00 \pm 4.00	1.14	120.69	0.58	0.10	0.70
3	Gray granite	95.34 \pm 3.15 \pm 0.40	90.05 \pm 4.50 \pm 2.25	1350.2 \pm 12.10 \pm 6.05	0.94	294.78	1.49	0.36	1.80
4	Black mix grey	65.24 \pm 2.50 \pm 0.30	105.32 \pm 3.20 \pm 1.60	1010.27 \pm 6.2 \pm 3.10	1.62	256.43	1.25	0.31	1.60
5	Maple red	53.30 \pm 2.10 \pm 0.12	79.94 \pm 2.80 \pm 1.40	1200.12 \pm 14.5 \pm 7.25	1.50	232.97	1.14	0.30	1.42
<i>Marbles</i>									
6	Rajasthan marble	14.19 \pm 1.54 \pm 0.20	25.26 \pm 2.40 \pm 1.20	60.22 \pm 4.40 \pm 2.20	1.78	45.65	0.22	0.05	0.27
7	Andra marble Kadapa	12.26 \pm 1.62 \pm 0.40	20.33 \pm 1.80 \pm 0.90	50.22 \pm 3.20 \pm 1.60	1.66	37.65	0.18	0.04	0.22
<i>Tiles</i>									
8	Ceramic tiles	150.27 \pm 4.10 \pm 0.42	175.49 \pm 4.00 \pm 2.00	390.46 \pm 9.10 \pm 4.55	1.16	362.52	1.77	0.44	2.21
9	Vitrified tiles	80.43 \pm 3.50 \pm 0.15	135.42 \pm 3.20 \pm 1.60	450.37 \pm 13.00 \pm 6.50	1.68	258.98	1.26	0.31	1.60
10	Mosaic tiles	38.41 \pm 1.60 \pm 0.20	42.61 \pm 2.80 \pm 1.40	355.15 \pm 3.80 \pm 1.90	1.11	110.62	0.54	0.13	0.67
<i>Sand</i>									
11	Sand-1	11.47 \pm 1.45 \pm 0.37	18.47 \pm 1.60 \pm 0.80	70.26 \pm 5.00 \pm 2.50	1.63	36.49	0.17	0.04	0.21
12	Sand-2	21.41 \pm 1.20 \pm 0.37	41.33 \pm 1.80 \pm 0.90	365.72 \pm 3.20 \pm 1.60	1.91	94.41	0.46	0.11	0.57
<i>Cement</i>									
13	Penna cement	15.53 \pm 0.50 \pm 0.12	19.51 \pm 1.20 \pm 0.60	45.25 \pm 2.50 \pm 1.25	1.25	39.36	0.19	0.05	0.24
14	Zuari cement	18.43 \pm 0.30 \pm 0.40	20.58 \pm 0.20 \pm 0.10	55.46 \pm 2.80 \pm 1.40	1.11	44.03	0.21	0.05	0.26
15	Ultratech cement	8.12 \pm 0.40 \pm 0.45	19.15 \pm 0.90 \pm 0.45	67.34 \pm 5.50 \pm 2.75	2.34	33.92	0.16	0.04	0.20
<i>Bricks</i>									
16	Soil brick	15.27 \pm 1.80 \pm 0.52	30.25 \pm 2.50 \pm 1.25	100.24 \pm 4.10 \pm 2.05	2.00	55.35	0.26	0.07	0.33
17	Cement bricks	40.15 \pm 1.80 \pm 0.50	52.26 \pm 1.50 \pm 0.75	376.10 \pm 4.50 \pm 2.25	1.30	124.51	0.60	0.15	0.76
	MAX	150.27 \pm 4.1 \pm 0.62	200.17 \pm 4.50 \pm 2.25	1500.24 \pm 14.50 \pm 7.25	2.34	478.00	2.34	0.60	2.94
	MIN	8.12 \pm 0.30 \pm 0.12	18.47 \pm 0.20 \pm 0.10	45.25 \pm 2.50 \pm 1.25	0.95	33.70	0.17	0.04	0.21
	AV	48.53 \pm 1.99 \pm 0.33	63.20 \pm 2.48 \pm 1.23	470.47 \pm 6.59 \pm 3.29	1.50	154.00	0.76	0.19	0.94
	GM	32.46 \pm 1.59 \pm 0.29	44.98 \pm 2.06 \pm 1.03	245.17 \pm 5.66 \pm 2.83	1.46	104.90	0.51	0.13	0.64
	SD	46.01 \pm 1.17 \pm 0.15	58.40 \pm 1.22 \pm 0.60	491.31 \pm 3.84 \pm 1.91	0.40	109.80	0.54	0.13	0.67
	RUN	11.16 \pm 0.28 \pm 0.02	14.16 \pm 0.29 \pm 0.10	119.16 \pm 0.93 \pm 0.32	0.90	32.85	0.13	0.03	0.16
	SU	71.07 \pm 1.90 \pm 0.25	90.85 \pm 2.15 \pm 1.07	727.49 \pm 6.00 \pm 3.00	0.69	222.15	1.08	0.28	1.36

AV average, GM geometric mean, SD standard deviation, RUN random uncertainty, SU standard uncertainty

The bold representation in this tables are the minimum, maximum, average and uncertainty values that are given at the end of each table

blast furnace slag, silica sand and iron ore. These materials are contains most important naturally occurring radionuclides such as ^{226}Ra , ^{232}Th , ^{40}K and trace metals [43]. Hence, it is observed higher values of radionuclides compared to marbles and the activity concentration of radionuclides (^{226}Ra , ^{232}Th , ^{40}K) typically less than the world average value which is of 50, 50, 500 Bq kg⁻¹ respectively as mentioned in UNSCEAR 1993 reports [42–44]. The average activity concentration of the building materials varies from 48.53 \pm 1.99 Bq kg⁻¹, 63.20 \pm 2.48 Bq kg⁻¹; thorium (^{232}Th) concentration found to be higher than the world average values because granitic rocks contains higher concentration of ^{238}U and ^{232}Th [16, 30, 45] and for potassium (^{40}K) 470.47 \pm 6.59 Bq kg⁻¹ which is slightly less when compared to typical world average values of

50, 50 and 500 Bq kg⁻¹ respectively [46]. The standard deviation, uncertainty and standard uncertainty in measurement of activity of radionuclides (^{226}Ra , ^{232}Th and ^{40}K) using Bayesian statistics for building material sample is as shown in Table 2. The estimated data shows confidence level of 95.45% (^{226}Ra = 24.22, ^{232}Th = 30.25 and ^{40}K = 258.47) and with the of ‘T’ table we found the coverage factor $k = 2$.

The Fig. 5a–c shows correlation between ^{226}Ra and ^{232}Th , ^{226}Ra and ^{40}K and ^{232}Th and ^{40}K present in the building materials. There is a strong and positive correlation exists between ^{226}Ra and ^{232}Th with a correlation coefficient of $R^2 = 0.93$ and in between ^{226}Ra and ^{40}K the correlation coefficient of $R^2 = 0.51$ and similarly for ^{232}Th and ^{40}K it is observed $R^2 = 0.51$ respectively.

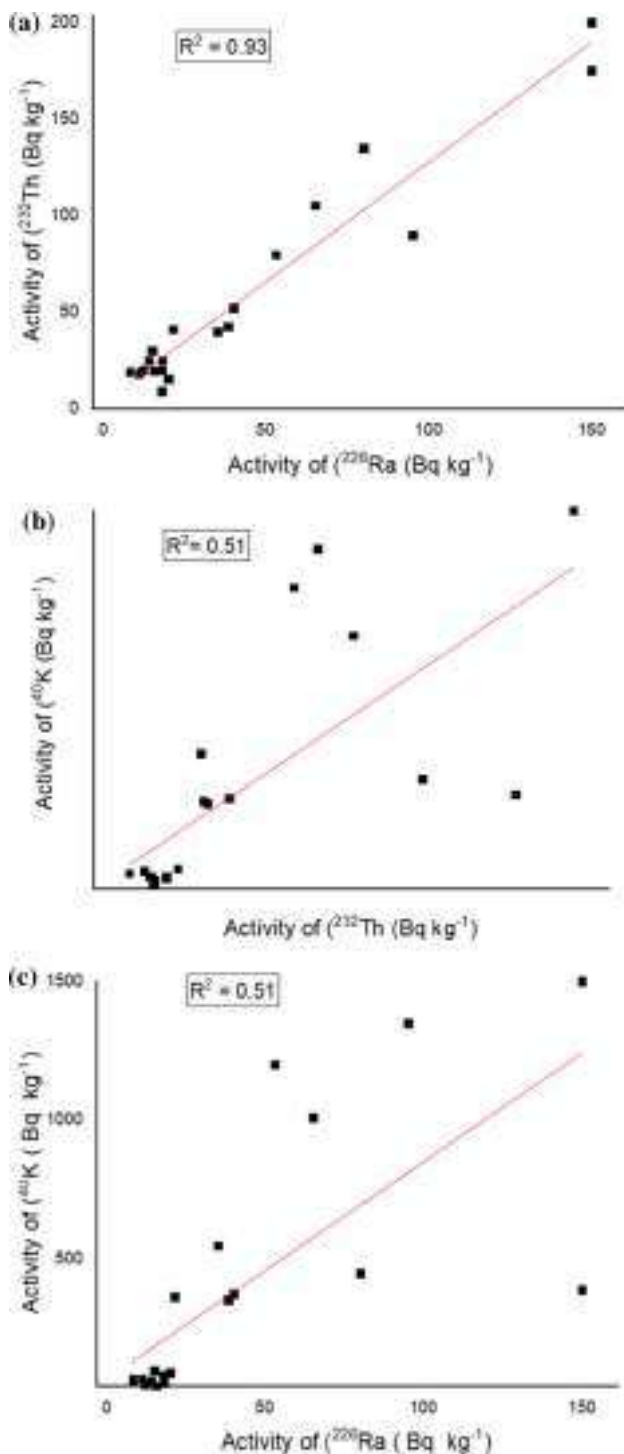


Fig. 5 **a** Correlation between the activity of ^{226}Ra and ^{40}K in Building material samples, **b** correlation between the activity of ^{232}Th and ^{40}K in Building material samples, **c** Correlation between the activity of ^{226}Ra and ^{40}K in Building material samples

(b) Distribution of gamma radiation levels in indoor and outdoor atmosphere:

The gamma absorbed dose rate for both in indoor and outdoor atmosphere have been calculated by estimating the activity of radionuclide in soil and building material and measured gamma exposure rate. The estimated absorbed dose rate can be converted into equivalent effective dose rate by using conversion factor 0.7 Sv y^{-1} and occupation factor i.e., the fraction of a time spent in indoor and outdoor atmosphere are 0.8 and 0.2 respectively. Were given in the Table 3 [24]. The indoor measured ambient GAD rate of entire location varies from $3.8 \pm 0.12 \text{ nGy h}^{-1}$, to $97.9 \pm 1.3 \text{ nGy h}^{-1}$, with a mean value of 33.6 nGy h^{-1} and average value of 42.8 ± 0.6 . The outdoor measured ambient GAD rate of the entire study area varies from $5.74 \pm 0.4 \text{ nGy h}^{-1}$ to $52.2 \pm 1 \text{ nGy h}^{-1}$ with a mean value of 17.3 and average value of 21.3 ± 0.8 . The higher values outdoor gamma absorbed dose rate and annual effective dose rate are observed in the location such as sports ground near, boys, ladies hostel, and Guest House administrative block. The Gamma exposure rate depends on the local geology formation of rocks, mineral compositions and activity of radionuclides present in soil, parent rocks [17, 34, 36, 45, 47]. These locations are attributed by ultramafic rocks. The activity of radionuclides in soil shows higher when compared to the other locations (Table 1) except for the bioscience, library science building and Prasaranga. These locations shows slightly less gamma absorbed and equivalent effective dose rates, because these locations are surrounded by thick forest and upper layer of soil is highly humous and it contains more organic materials and this may be acts as shielding for gamma radiation. Hence notice slightly low activity. Higher depth of the soil may be contains higher activity of radionuclides present in soil. In the first zone slightly low GAD and AED was also noticed at the some of the locations and villages, in this zone GAD and AED rates don't vary significantly. This is because entire zone is comprised by migmatite and granodiorite. The activity of radionuclides present in the soil of these locations are also doesn't vary significantly as given in the Table 2. The locations such as University Quarters, BRP quarter and Bhadra Dam show lower value of GAD and AED. This may be due to the lower activity values of radionuclide present in the soil of these locations (Table 1). When comes to second zone which is the university campus; Shankaramata cave and Indoor Games building found that the outdoor GAD and AED is higher when compared to indoor. Because the cave formed from ultramafic rock consists of dunite which indeed has the lowest content of radioactive minerals [48]. And an Indoor game building's flooring is made up of wood; which in turn may acts as shielding for gamma. The University campus area is quite different when compared to the all the locations of zone-I. Because 20 to 30% of the campus

Table 3 Average measured ambient Gamma exposure rate, absorbed dose, and equivalent effective dose rate of the study area (Zone-I)

S. no	Zones of location	Absorbed dose D (nGy h ⁻¹)		Annual effective dose E (mSv y ⁻¹)		
		Indoor GAD ± SD ± RUN	Outdoor GAD ± SD ± RUN	Indoor	Outdoor	Total
ZONE-I						
1	<i>Shankaraghatta</i>					
a	Black granite	71.77 ± 0.95 ± 0.48	30.45 ± 0.50 ± 0.25	0.25	0.04	0.39
b	Vitrified	41.32 ± 0.50 ± 0.25	30.45 ± 0.50 ± 0.25	0.25	0.04	0.24
c	Andra marble	39.15 ± 0.57 ± 0.29	30.45 ± 0.50 ± 0.25	0.25	0.04	0.23
d	State highway	–	71.77 ± 1.29 ± 0.65	0.65	0.35	0.35
2	<i>Tipperudrappa layout</i>					
a	Pink granite introduced by gray	82.65 ± 0.50 ± 0.25	32.62 ± 1.29 ± 0.65	0.65	0.04	0.44
b	Black Mix pink	73.95 ± 0.57 ± 0.25	32.62 ± 1.29 ± 0.65	0.65	0.04	0.40
c	Red-oxide	47.85 ± 0.57 ± 0.28	32.62 ± 1.29 ± 0.65	0.65	0.04	0.27
3	<i>Kudremukh layout</i>					
a	Andra marble	36.97 ± 1.0 ± 0.50	28.71 ± 0.57 ± 0.29	0.29	0.04	0.22
b	Cement	47.85 ± 0.57 ± 0.29	28.71 ± 0.57 ± 0.29	0.29	0.04	0.27
c	Gray granite	65.25 ± 0.57 ± 0.29	28.71 ± 0.57 ± 0.29	0.29	0.04	0.36
4	<i>Shanthi nagara</i>					
a	Red-oxide	45.67 ± 1.0 ± 0.50	26.10 ± 1.50 ± 0.75	0.75	0.03	0.25
b	Cement	47.85 ± 0.6 ± 0.29	26.10 ± 1.50 ± 0.75	0.75	0.03	0.26
c	Mosaic tiles	50.03 ± 0.50 ± 0.25	26.10 ± 1.50 ± 0.75	0.75	0.03	0.28
d	Vitrified	43.50 ± 0.81 ± 0.41	26.10 ± 1.50 ± 0.75	0.75	0.03	0.24
5	<i>BRP quarters</i>					
a	Red oxide	45.67 ± 1.0 ± 0.50	17.40 ± 0.40 ± 0.20	0.20	0.02	0.24
b	Cement	43.50 ± 0.81 ± 0.41	17.40 ± 0.40 ± 0.20	0.20	0.02	0.23
c	Magna tiles	50.03 ± 0.50 ± 0.25	17.40 ± 0.40 ± 0.20	0.20	0.02	0.27
6	<i>Near Bhadra Dam</i>					
a	Cement	43.50 ± 0.81 ± 0.25	26.10 ± 0.50 ± 0.25	0.25	0.03	0.24
7	<i>Singana Mane</i>					
a	Black Granite	69.60 ± 0.81 ± 0.41	32.19 ± 0.81 ± 0.41	0.41	0.04	0.38
b	Pink Mix Gray	82.65 ± 0.57 ± 0.29	32.19 ± 0.81 ± 0.41	0.41	0.04	0.44
c	Cement	56.55 ± 0.81 ± 0.43	32.19 ± 0.81 ± 0.41	0.41	0.04	0.32
8	<i>Fishery office and hand post</i>					
a	Kadapa	41.32 ± 0.50 ± 0.25	34.80 ± 1.50 ± 0.75	0.75	0.04	0.24
b	Red-oxide	43.50 ± 0.81 ± 0.41	34.80 ± 1.50 ± 0.75	0.75	0.04	0.25
c	Vitrified tiles	45.67 ± 1.0 ± 0.50	34.80 ± 1.50 ± 0.75	0.75	0.04	0.26
9	<i>River turn lodge</i>					

Table 3 (continued)

S. no	Zones of location	Absorbed dose D (nGy h ⁻¹)		Annual effective dose E (mSv y ⁻¹)		
		Indoor GAD ± SD ± RUN	Outdoor GAD ± SD ± RUN	Indoor	Outdoor	Total
a	Wood and cement	50.03 ± 0.50 ± 0.25	39.20 ± 1.29 ± 0.65	0.65	0.05	0.30
10	<i>Lakkavalli</i>					
a	Black mix pink granite	71.77 ± 0.81 ± 0.41	32.60 ± 0.57 ± 0.29	0.29	0.04	0.39
b	Andra marble	52.20 ± 0.50 ± 0.25	32.60 ± 0.57 ± 0.29	0.29	0.04	0.30
c	Rajasthan marble	41.32 ± 0.81 ± 0.41	32.60 ± 0.57 ± 0.29	0.29	0.04	0.24
d	Red-oxide	45.67 ± 0.51 ± 0.26	32.60 ± 0.57 ± 0.29	0.29	0.04	0.26
11	<i>Kuvempu nagara</i>					
a	Kadapa Tiles	43.50 ± 0.81 ± 0.41	33.93 ± 0.57 ± 0.29	0.29	0.04	0.25
b	Red-oxide	45.67 ± 0.9 ± 0.45	33.93 ± 0.57 ± 0.29	0.29	0.04	0.26
c	Cement	47.85 ± 1.29 ± 0.65	33.93 ± 0.57 ± 0.29	0.29	0.04	0.27
d	Gray granite	73.95 ± 0.57 ± 0.29	33.93 ± 0.57 ± 0.29	0.29	0.04	0.40
12	<i>Tavaraghatta</i>					
a	Cement	50.03 ± 0.57 ± 0.29	30.45 ± 0.57 ± 0.29	0.29	0.04	0.29
b	Red-oxide	47.85 ± 0.81 ± 0.41	30.45 ± 0.57 ± 0.29	0.29	0.04	0.27
c	Kadapa	43.50 ± 0.50 ± 0.25	30.45 ± 0.57 ± 0.29	0.29	0.04	0.25
13	<i>Malenahalli</i>					
a	Cement	50.02 ± 0.50 ± 0.25	33.06 ± 0.57 ± 0.29	0.29	0.04	0.29
b	Bare	34.80 ± 0.57 ± 0.29	33.06 ± 0.57 ± 0.29	0.29	0.04	0.21
14	<i>Gonibedu</i>					
a	Cement	50.03 ± 0.50 ± 0.25	29.58 ± 0.4 ± 0.20	0.20	0.04	0.29
b	Bare	36.97 ± 1.00 ± 0.50	29.58 ± 0.4 ± 0.20	0.20	0.04	0.22
15	<i>Junction</i>					
a	Black granite	73.95 ± 1.29 ± 0.65	33.06 ± 0.75 ± 0.38	0.38	0.04	0.40
b	Red-oxide	47.85 ± 0.81 ± 0.41	33.06 ± 0.75 ± 0.38	0.38	0.04	0.27
c	Bare	34.80 ± 1.29 ± 0.65	33.06 ± 0.75 ± 0.38	0.38	0.04	0.21

Table 4 Average measured ambient Gamma exposure rate, absorbed dose, and equivalent effective dose rate of the study area (Zone-II)

S. no	Zones of locations	Absorbed dose D ($\mu\text{C Gy h}^{-1}$)			Annual effective dose E (mSv y^{-1})					
		Indoor GAD \pm SD \pm RUN	Outdoor soil GAD \pm SD \pm RUN	Outdoor interlock GAD \pm SD \pm RUN	E_{in}	E_{out} soil	E_{out} Interlocks	E_{out} Tar Road	E_{total}	Total of all samples
1	Sports Ground Near Ceramic Tiles	43.50 \pm 0.81 \pm 0.41	41.32 \pm 0.57 \pm 0.29	50.02 \pm 0.5 \pm 0.25	0.21	0.05	0.24	0.08	0.26	0.59
2	BGS College Ceramic Tiles	47.85 \pm 1.29 \pm 0.65	30.45 \pm 0.5 \pm 0.25	60.90 \pm 0.50 \pm 0.25	0.23	0.07	0.29	0.08	0.27	0.65
3	Chemical Science Block Ceramic Tiles	52.20 \pm 0.50 \pm 0.25	39.15 \pm 0.57 \pm 0.29	56.55 \pm 0.57 \pm 0.29	0.25	0.04	0.27	0.08	0.30	0.66
4	Ladies Hostel Ceramic Tiles	58.72 \pm 0.95 \pm 0.48	41.76 \pm 0.81 \pm 0.41	58.72 \pm 0.50 \pm 0.25	0.28	0.05	0.28	0.08	0.34	0.71
5	Guest house Ceramic Tiles	50.02 \pm 0.50 \pm 0.25	40.02 \pm 0.57 \pm 0.29	63.07 \pm 1.20 \pm 0.65	0.24	0.05	0.30	0.08	0.29	0.68
6	Shankaramata Temple									
a	(a)Rock cave	8.70 \pm 0.50 \pm 0.25	26.10 \pm 0.4 \pm 0.20	58.72 \pm 0.50 \pm 0.25	0.04	0.03	0.29	0.08	0.07	0.44
b	(b)Ganesh Temple pink granite	78.30 \pm 0.81 \pm 0.41	52.20 \pm 1.29 \pm 0.65	58.72 \pm 0.50 \pm 0.25	0.38	0.06	0.28	0.08	0.45	0.82
7	Social-Science Block ceramic tiles	52.20 \pm 0.50 \pm 0.25	34.8 \pm 1.29 \pm 0.65	50.02 \pm 0.89 \pm 0.45	0.25	0.04	0.24	0.09	0.30	0.63
8	Prasaranga vitrified	45.67 \pm 0.95 \pm 0.48	30.45 \pm 0.5 \pm 0.25	50.02 \pm 0.89 \pm 0.45	0.22	0.03	0.24	0.08	0.26	0.59
9	Bio Science Block	56.55 \pm 0.5 \pm 0.25	32.19 \pm 0.5 \pm 0.25	50.02 \pm 0.89 \pm 0.45	0.27	0.03	0.24	0.09	0.31	0.65
10	MLJB Library Science Ceramic	52.2 \pm 0.81 \pm 0.41	26.10 \pm 0.4 \pm 0.20	65.25 \pm 0.57 \pm 0.29	0.25	0.03	0.32	0.09	0.29	0.69
11	Computer-Science Block	54.37 \pm 0.95 \pm 0.48	30.45 \pm 1.29 \pm 0.65	65.25 \pm 0.57 \pm 0.29	0.26	0.03	0.32	0.08	0.30	0.70
12	Library block white granite marble	56.55 \pm 0.5 \pm 0.25	28.27 \pm 0.5 \pm 0.25	65.25 \pm 0.57 \pm 0.29	0.27	0.03	0.32	0.08	0.31	0.71
13	Boys Hostel Ceramic Tiles	52.20 \pm 0.5 \pm 0.25	32.19 \pm 0.57 \pm 0.29	56.55 \pm 0.57 \pm 0.29	0.25	0.03	0.27	0.06	0.29	0.64
14	MBA Department Block Ceramic Tiles	47.85 \pm 1.29 \pm 0.65	31.32 \pm 0.75 \pm 0.38	54.37 \pm 1.25 \pm 0.63	0.23	0.03	0.26	0.08	0.27	0.62
15	Administrative Block									
a	(a) Pink Granite	97.87 \pm 0.95 \pm 0.48	40.45 \pm 1.29 \pm 0.65	63.07 \pm 1.25 \pm 0.63	0.48	0.05	0.30	0.09	0.53	0.93
b	(b) White Gray Granite	82.65 \pm 0.50 \pm 0.25	40.45 \pm 1.29 \pm 0.65	63.07 \pm 1.25 \pm 0.63	0.40	0.04	0.30	0.09	0.45	0.853
16	Distance Education Block Black mix Pink granite	67.42 \pm 0.50 \pm 0.25	40.45 \pm 1.29 \pm 0.65	52.20 \pm 0.81 \pm 0.41	0.33	0.04	0.30	0.08	0.38	0.77
17	Basava Bhavana Black & Graygranite	69.60 \pm 0.57 \pm 0.29	40.45 \pm 1.29 \pm 0.65	52.20 \pm 0.81 \pm 0.41	0.34	0.05	0.25	0.08	0.39	0.73
18	Nudi Loka Gray granite	67.4 \pm 0.95 \pm 0.48	28.27 \pm 0.95 \pm 0.48	65.25 \pm 0.57 \pm 0.29	0.33	0.03	0.32	0.10	0.36	0.78
19	Indoor Games Wooden base	30.45 \pm 0.50 \pm 0.25	39.15 \pm 0.57 \pm 0.29	65.25 \pm 0.57 \pm 0.29	0.15	0.04	0.32	0.08	0.19	0.60

Table 5 Average measured ambient Gamma exposure rate, absorbed dose, and equivalent effective dose rate of the study area (Zone-III)

S. nos	Zones of locations	Absorbed dose $D(\text{nGy h}^{-1})$		Annual effective dose $E (\text{mSv y}^{-1})$		
		Indoor $GAD \pm SD \pm RUN$	Outdoor $GAD \pm SD \pm RUN$	E_{in}	E_{out}	Total
ZONE-III						
<i>Teachers quarters</i>						
1	(a) Vitrified	45.67 $\pm 0.95 \pm 0.48$	23.92 $\pm 0.50 \pm 0.25$	0.22	0.03	0.25
	(b) Ceramic	52.20 $\pm 0.81 \pm 0.41$	23.92 $\pm 0.50 \pm 0.25$	0.26	0.03	0.29
2	Teachers quarters sports ground near	52.20 $\pm 0.81 \pm 0.41$	8.70 $\pm 0.80 \pm 0.41$	0.26	0.01	0.27
Total average measured ambient Gamma exposure rate, absorbed dose, and equivalent effective dose rate of the study area (Zone-I, Zone-II and Zone-III)						
	MAX	97.87 $\pm 1.29 \pm 0.65$	52.20 $\pm 1.50 \pm 0.75$	0.48	0.06	0.53
	MIN	8.70 $\pm 0.50 \pm 0.25$	8.70 $\pm 0.40 \pm 0.20$	0.05	0.01	0.08
	AVERAGE	42.80 $\pm 0.80 \pm 0.37$	21.34 $\pm 0.80 \pm 0.40$	0.22	0.03	0.25
	GM	33.70 $\pm 0.70 \pm 0.35$	17.3 $\pm 0.74 \pm 0.36$	0.17	0.02	0.19
	SD	23.50 $\pm 0.24 \pm 0.12$	13.5 $\pm 0.38 \pm 0.20$	0.12	0.02	0.14
	RUN	3.86 $\pm 0.03 \pm 0.20$	2.21 $\pm 0.05 \pm 0.27$	0.19	0.03	0.02
	SU	48.29 $\pm 0.39 \pm 0.65$	25.35 $\pm 0.55 \pm 0.75$	0.21	0.02	0.22

AV average, GM geometric mean, SD standard deviation, RUN random uncertainty, SU standard uncertainty, GAD gamma absorbed dose

The bold representation in this tables are the minimum, maximum, average and uncertainty values that are given at the end of each table

outdoor area is covered by interlocks and tar road. Here the average values of outdoor GAD and AED rates from the interlocks and tar road of the outside of all the buildings of the university campus compared to outdoor soil locations are given in the table-3.0. The data shows the GAD rate and AED rate all the interlocks and tar road of the all locations is higher than the indoor GADR of locations such as Sports ground near, BGS College, Guest house, Prasara, MLIB, Computer science, Library block and MBA blocks. This shows that the man made materials i.e., interlocks and tar road material are responsible for enhanced outdoor gamma radiation levels.

The measured Outdoor GAD and AED rates are higher than the indoor GAD and AED for interlocks in the locations of zone-II (Tables 3, 4, 5) such as BGS College, Guest house, MLIB, Computer Science block and Library Science block. Because the interlocks of the buildings in those locations are made up of M-sand and since M-sand is produced by Gray granite rocks, these rocks contain higher activity of radionuclides (^{226}Ra , ^{232}Th , and ^{40}K) [45]. Which enhance and in turn influence for the higher concentration of outdoor GAD. In the remaining locations of Zone II (Tables 3, 4, 5) interlocks are made up of local sand, which shows slightly lesser value compared to interlocks made-up of M-sand. The GAD and AED rates of single layer tar road are found to be highest and the Shankaraghatta state highway and Nudi Loka/Kannada department road is also shown highest gamma value for outdoor. This may be due to the less tar

content present in it. In all other locations the tar road consists of double thick layer of tar, which serves as shielding may be due to this less GAD value is observed. The ambient GAD and AED for cement road is $52.2 \pm 0.5 \text{ nGy h}^{-1}$ and $0.3 \pm 0.5 \text{ mSv y}^{-1}$ when compared to tar road and is found to be $67.4 \pm 0.5 \text{ nGy h}^{-1}$ and 0.3 mSv y^{-1} . Hence the material used for the tar road construction and the tar content in it will decide the GAD and AED rate. The average indoor measured GAD rate is as shown in Table 3. The indoor GAD and AED rate is mainly depends on the type of the building materials used for construction, local geology, types of buildings and ventilation conditions [49], the indoor GAD and AED rate are higher than the outdoor in all locations of these zones except indoor sports building, Shankaramata Cave and University Quarters. Because the entire university quarters building area is attributed by Quartz, chlorite schist and orthoquartzite. The flooring of the sports building is covered with the wooden materials, which containing lower activity of radionuclides and shielding the gamma radiations emitted from the ground. The higher values of GAD rate were observed in granites flooring at all locations of all this regions, the lower activity were observed in wooden and marble floorings of dwellings of the all the locations.

The values of indoor gamma dose rate of the entire study area varies from $3.8 \pm 0.1 \text{ nGy h}^{-1}$, to $97.9 \pm 1.3 \text{ nGy h}^{-1}$, with a mean value of 33.6 nGy h^{-1} and the average values of entire indoor GAD rate is found to be 42.8 ± 0.8 , this is less than the world average of 84 nGy h^{-1} , and the outdoor

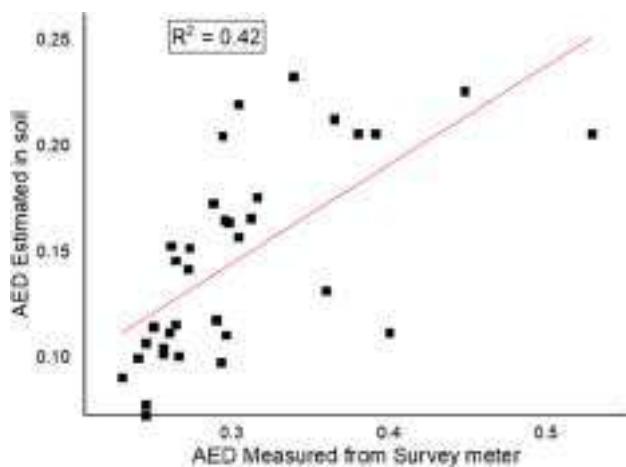


Fig. 6 a Correlation between measured AED and estimated AED from the soil

gamma dose rate values of the entire study area varies from $5.7 \pm 0.4 \text{ nGy h}^{-1}$, to $52.2 \pm 1.5 \text{ nGy h}^{-1}$, with the mean value of 17.3 nGy h^{-1} , and with an average value of 21.3 ± 0.8 which is less than the outdoor world average values outdoor gamma absorbed dose rates the world average value of 59 nGy h^{-1} , respectively [25]. The standard deviation, uncertainty and standard uncertainty in measurement of using Bayesian statistics for gamma radiation levels in indoor and outdoor atmosphere is as shown in Tables 3, 4, 5. The estimated data shows confidence level of 95.45% and with the help of ‘*T*’ table we found the coverage factor $k=2$.

Malanca et al. [50] studied the correlation between measured and estimated GAD to observed significant positive correlation between the measured and estimated GAD is not observed in general. Alencar and Freitas they have given reason that; the non-existence of correlation is due to the treatment of the samples before gamma spectrometry-factors such as, humidity; compactness degree and density in situ are different for dried samples [51]. On the flip side, they have also reported a significant positive correlation with the high correlation coefficient value between measured and estimated gamma dose rate. In order to know the correlation coefficient between measured and calculated annual effective dose due to radionuclides in the soil samples. We have performed the correlation studies and plotted a graph between AED as directly obtained from survey meter and the estimated AED from soils as shown in Fig. 6b.

Hazard indices

To compare the specific activity of radionuclides (^{226}Ra , ^{232}Th , ^{40}K) with the use of standard index parameter called Radium equivalent activity, which signifies radiation risk assessment associated with them. In the entire zones

of soil’s radium equivalent varies from 26.80 Bq kg^{-1} to 83.50 Bq kg^{-1} with a mean value of 49.70 Bq kg^{-1} . Similarly for building materials the values varies from 37.2 to 551.5 Bq kg^{-1} with a mean value of $106.22 \text{ Bq kg}^{-1}$. All the values are found to be fall within a safe limit of the world average permissible limit for radium equivalent activity is 370 Bq kg^{-1} [24].

The radiological hazard indices of the soil and building materials are given in Table 6. The calculated Gamma Index (I_γ) values for soil of the first zone ranged from 0.1 to 0.17 with a mean value of 0.13 and 0.05 to 0.08 with a mean value 0.06 for second zone and for the third zone 0.040. The Gamma Index value for the entire study area of all zone varies from 0.04 to 0.17 with a mean value of 0.09. Similarly, for building materials, the range is 0.13–2 with a mean of 0.38. According to the European Commission of Radiation Protection studies, the mean value of I_γ must be less than 1 to maintain the radiation risk assessment inconsequential to the general population. The mean I_γ values of the soil and building materials are much below the criteria limit of unity (1 mSv y^{-1}); the mean I_γ value of the area’s building materials was found to be within the safe level, posing no substantial radiation hazard to the population living in and around the study area. The estimated average values of Internal and External hazard index (H_{in} and H_{ex}) in soil samples of the entire zone are 0.14, 0.17 respectively. For building material the average values of H_{in} and H_{ex} is 0.13, 0.10 respectively. Since these values found to be < 1 (Table 7) and are in safe limit, hence in according to the report of Radiation Protection [25]. The health hazards due to these soil samples are insignificant (ECRP-1999) [27]. According to the UNSCEAR-2000 [24] report to estimate the dose received by the different body organs such as active bone marrow, Gonads and bone surface cells. The Annual Gonadal Dose Equivalent (AGDE) value of soil of entire study area found to vary from 0.09 to 0.27 mSv y^{-1} with a mean value of 0.160 mSv y^{-1} , which is less than the global average value of 0.30 mSv y^{-1} and similarly for building materials AGDE values varies from 0.12 to 1.8 mSv y^{-1} with a mean value of 0.33 mSv y^{-1} which is slightly higher than the global average value of 0.30 mSv y^{-1} . The calculated ELCR from annual effective dose equivalent varies from 0.3 to 0.9 with an average value of 0.6 these values higher than the global average value of 0.29×10^{-3} [47].

The standard deviation, uncertainty and standard uncertainty in measurement of hazard indices activity of radionuclides (^{226}Ra , ^{232}Th and ^{40}K) using Bayesian statistics for gamma radiation levels in soil and building materials is as shown in Tables 6 and 7. The estimated data shows confidence level of 95.45% and with the help of ‘*T*’ table we found the coverage factor $k=2$.

The correlation between the radionuclides of building material samples ^{226}Ra , ^{232}Th , ^{40}K with radium equivalent is

Table 6 Measured radiological hazard indices in soil sample of the Shankaraghatta environment

S. nos	Locations	Activity of radionuclides (Bq kg ⁻¹)			Ra _{eq} (Bq kg ⁻¹)	Hazard indices		Alpha index (I _α)	Gamma index (I _γ)	AGDE (mSv y ⁻¹)	ELCR
		²²⁶ Ra	²³² Th	⁴⁰ K		Hex	Hin				
ZONE-I											
1	Shankaraghatta	9.53 ± 0.50 ± 0.25	15.26 ± 2.0 ± 1.00	70.15 ± 2.50 ± 1.25	36.34	0.10	0.12	0.05	0.13	0.11	0.40
2	Tipperudrappa Layout	10.51 ± 2.50 ± 1.25	17.21 ± 2.5 ± 1.25	80.37 ± 2.00 ± 1.00	40.97	0.10	0.14	0.05	0.15	0.13	0.45
3	Kudremukh Layout	11.24 ± 1.6 ± 0.80	16.33 ± 1. ± 0.85	100.27 ± 3.00 ± 1.50	41.58	0.10	0.14	0.06	0.15	0.13	0.46
4	Shanthi Nagara	10.1 ± 1.25 ± 0.64	14.27 ± 0.7 ± 0.75	90.42 ± 2.50 ± 1.25	36.95	0.10	0.13	0.05	0.13	0.12	0.41
5	BR Project	8.25 ± 0.50 ± 0.25	12.24 ± 0.6 ± 0.35	50.16 ± 1.50 ± 0.75	29.01	0.08	0.10	0.04	0.10	0.10	0.32
6	Near Bhadra Dam	7.54 ± 0.81 ± 0.40	10.49 ± 3.5 ± 0.3	65.21 ± 1.80 ± 0.90	26.80	0.07	0.09	0.04	0.10	0.09	0.30
7	Singanamane	12.5 ± 1.57 ± 0.80	13.46 ± 2.1 ± 1.75	110.37 ± 2.60 ± 1.30	47.64	0.13	0.16	0.06	0.17	0.15	0.53
8	Fishery and Hand Post	11.52 ± 1.75 ± 0.87	15.52 ± 2.4 ± 1.05	95.79 ± 2.00 ± 1.00	37.40	0.10	0.13	0.06	0.14	0.12	0.42
9	River turn Lodge	70.12 ± 0.57 ± 0.28	18.34 ± 2.4 ± 1.20	86.47 ± 1.50 ± 0.75	35.80	0.10	0.12	0.04	0.13	0.11	0.40
10	Lakkavalli	08.5 ± 0.57 ± 0.40	15.14 ± 1.4 ± 1.20	80.42 ± 1.70 ± 0.87	40.40	0.10	0.13	0.04	0.15	0.13	0.44
11	Kuvempu Nagara	10.34 ± 1.50 ± 0.75	14.25 ± 1.3 ± 0.70	130.25 ± 2.80 ± 1.4	41.50	0.10	0.14	0.05	0.15	0.13	0.47
12	Tavaraghatta	10.52 ± 1.5 ± 0.75	11.33 ± 1.0 ± 0.65	120.46 ± 2.50 ± 1.25	39.80	0.10	0.14	0.05	0.15	0.13	0.45
13	Malenahalli	09.15 ± 0.5 ± 0.25	13.32 ± 1.5 ± 0.50	98.45 ± 3.50 ± 1.75	32.30	0.09	0.11	0.05	0.12	0.10	0.36
14	Gonibeedu	11.47 ± 1.57 ± 0.80	14.27 ± 2.3 ± 0.75	110.26 ± 4.50 ± 2.25	38.06	0.10	0.13	0.05	0.14	0.12	0.43
15	Junction	12.5 ± 1.80 ± 0.90	19.34 ± 1.7 ± 1.15	125.09 ± 4.00 ± 2.00	42.15	0.11	0.15	0.06	0.15	0.14	0.48
ZONE-II											
S. nos	Locations	Activity of radionuclides (Bq kg ⁻¹)			Ra _{eq} (Bq kg ⁻¹)	Hazard indices		Alpha index (I _α)	Gamma index (I _γ)	AGDE (mSv y ⁻¹)	ELCR
		²²⁶ Ra	²³² Th	⁴⁰ K		Hex	Hin				
1	Sports ground	12.25 ± 2.10 ± 1.05	17.52 ± 3.00 ± 1.50	185.53 ± 3.60 ± 1.8	51.30	0.14	0.17	0.19	0.06	0.17	0.58
2	BGS College	11.52 ± 2.00 ± 1.00	16.54 ± 2.60 ± 1.30	189.25 ± 3.50 ± 1.75	49.70	0.13	0.17	0.18	0.06	0.16	0.57
3	Chemical Science Block	14.24 ± 2.50 ± 1.25	35.27 ± 2.10 ± 1.05	200.00 ± 4.50 ± 2.25	79.50	0.21	0.25	0.29	0.07	0.25	0.88
4	Ladies Hostel	12.5 ± 1.74 ± 0.85	36.25 ± 2.20 ± 1.10	260.27 ± 4.20 ± 2.1	83.50	0.23	0.26	0.31	0.06	0.27	0.93
5	Guest House	14.12 ± 2.50 ± 1.25	30.15 ± 2.40 ± 1.20	215.11 ± 4.60 ± 2.3	73.50	0.20	0.24	0.27	0.07	0.24	0.82
6	Shankara mata Temple	14.52 ± 2.60 ± 1.30	35.45 ± 2.50 ± 1.25	220.25 ± 4.50 ± 2.25	81.50	0.22	0.26	0.30	0.07	0.26	0.90
7	Social Science Block	13.33 ± 2.00 ± 1.00	20.22 ± 2.30 ± 1.15	210.30 ± 3.60 ± 1.8	57.80	0.16	0.19	0.21	0.07	0.19	0.66
8	Prasaranga	12.50 ± 1.80 ± 0.90	18.25 ± 2.00 ± 1.00	200.15 ± 3.50 ± 1.75	53.60	0.14	0.18	0.20	0.06	0.18	0.61
9	Bio Science Block	13.50 ± 2.50 ± 1.25	25.15 ± 3.20 ± 1.60	180.10 ± 3.00 ± 1.50	63.10	0.17	0.21	0.23	0.07	0.20	0.70
10	Library Science Block	12.45 ± 1.90 ± 0.95	22.24 ± 3.00 ± 1.50	225.20 ± 3.40 ± 1.70	60.80	0.16	0.20	0.23	0.06	0.20	0.70
11	Computer Science Block	11.48 ± 1.50 ± 0.75	18.32 ± 2.60 ± 1.30	235.50 ± 3.50 ± 1.75	54.80	0.15	0.18	0.20	0.06	0.18	0.63
12	Mlib	11.53 ± 1.60 ± 0.80	19.38 ± 2.50 ± 1.25	250.24 ± 3.00 ± 1.50	57.90	0.16	0.19	0.22	0.06	0.19	0.67
13	Boys Hostel	10.52 ± 0.80 ± 0.40	20.42 ± 2.00 ± 1.00	240.25 ± 3.50 ± 1.75	57.60	0.16	0.18	0.22	0.05	0.19	0.66

Table 6 (continued)

S. nos	Locations	Activity of radionuclides (Bq kg ⁻¹)				R _{a,eq} (Bq kg ⁻¹)	Hazard indices	Alpha index	Gamma index (I _γ)	AGDE (mSv y ⁻¹)	ELCR	
		²²⁶ Ra		²³² Th								⁴⁰ K
		Activity ± SD ± RUN	Activity ± SD ± RUN	Activity ± SD ± RUN	Activity ± SD ± RUN							
14	Commerce & MBA Block	9.54 ± 0.50 ± 0.25	18.17 ± 2.50 ± 1.25	230.15 ± 4.10 ± 2.05	53.00	0.14	0.17	0.12	0.05	0.18	0.61	
15	Administrative Block	15.25 ± 2.40 ± 1.20	27.12 ± 1.60 ± 0.8	250.49 ± 4.50 ± 2.25	71.32	0.19	0.23	0.26	0.08	0.23	0.80	
16	Distance Education	15.25 ± 2.40 ± 1.20	27.12 ± 1.60 ± 0.80	250.49 ± 4.50 ± 2.25	72.90	0.20	0.24	0.27	0.08	0.24	0.82	
17	Basava Bhavana	15.25 ± 2.40 ± 1.20	27.12 ± 1.60 ± 0.80	250.49 ± 4.50 ± 2.25	72.90	0.20	0.24	0.27	0.08	0.24	0.82	
18	Nudi Loka	14.54 ± 2.00 ± 1.00	30.15 ± 2.10 ± 1.05	240.30 ± 4.00 ± 2.00	75.90	0.20	0.24	0.28	0.07	0.25	0.85	
ZONE-III												
19	Teachers quarters	06.52 ± 0.40 ± 0.20	10.49 ± 0.60 ± 0.40	50.16 ± 1.50 ± 0.75	35.21	0.10	0.10	0.01	0.04	0.12	0.40	
	MAX	15.25 ± 2.60 ± 1.30	36.25 ± 3.50 ± 1.60	260.27 ± 4.60 ± 2.30	83.50	0.23	0.30	0.31	0.17	0.27	0.93	
	MIN	6.52 ± 0.40 ± 0.20	10.49 ± 0.60 ± 0.40	50.16 ± 1.50 ± 1.50	26.80	0.07	0.02	0.01	0.04	0.09	0.03	
	AVERAGE	11.25 ± 1.59 ± 0.94	19.69 ± 2.04 ± 1.12	163.76 ± 3.27 ± 1.92	52.61	0.14	0.14	0.15	0.10	0.17	0.59	
	GM	10.98 ± 1.39 ± 0.84	18.54 ± 1.90 ± 1.08	147.95 ± 3.11 ± 1.90	50.14	0.13	0.11	0.11	0.09	0.16	0.56	
	SD	2.39 ± 0.70 ± 0.34	7.23 ± 0.69 ± 0.29	68.17 ± 0.96 ± 0.29	16.46	0.05	0.07	0.10	0.04	0.05	0.18	
	RUN	0.41 ± 0.12 ± 0.17	1.24 ± 0.12 ± 0.14	11.69 ± 0.16 ± 0.14	2.82	0.01	0.01	0.02	0.01	0.01	0.03	
	SU	11.99 ± 1.1 ± 0.55	12.88 ± 1.45 ± 0.60	105.05 ± 1.55 ± 0.40	28.35	0.08	0.14	0.15	0.06	0.09	0.45	

AV average, GM geometric mean, SD standard deviation, RUN random uncertainty, SU standard uncertainty

The bold representation in this tables are the minimum, maximum, average and uncertainty values that are given at the end of each table

Table 7 Radiological hazard indices in building material sample of the Shankaraghatta environment

S. nos	Locations	Activity of radionuclides (Bq kg ⁻¹)				Ra _{eq} (Bq kg ⁻¹)	Hazard indices	Alpha Index	Gamma Index (I _γ)	AGDE (mSv y ⁻¹)	ELCR	
		²²⁶ Ra		²³² Th								⁴⁰ K
		Activity ± SD ± RUN	Activity ± SD ± RUN	Activity ± SD ± RUN	Activity ± SD ± RUN							
1	Pink granite	150.42 ± 4.00 ± 2.00	200.25 ± 4.0 ± 2.00	1500.50 ± 10.00 ± 5.00	551.50	1.50	1.90	0.80	2.00	1.80	0.01	
2	Black granite	35.50 ± 2.00 ± 1.00	40.15 ± 3.50 ± 1.75	550.45 ± 8.00 ± 4.00	134.60	0.40	0.50	0.18	0.5	0.50	0.003	
3	Gray granite	95.12 ± 3.00 ± 1.5	90.35 ± 4.50 ± 2.25	1350.27 ± 12.00 ± 6.00	327.70	0.90	1.10	0.48	1.22	1.10	0.01	
4	Black mix grey	65.25 ± 2.50 ± 1.25	105.35 ± 3.0 ± 1.50	1010.25 ± 6.20 ± 3.12	293.40	0.80	1.00	0.33	1.08	1.00	0.01	
5	Maple red	53.15 ± 2.00 ± 1.00	79.92 ± 2.80 ± 1.40	1200.24 ± 14.5 ± 7.25	259.70	0.70	0.80	0.27	0.98	0.90	0.01	
6	Rajasthan marble	14.2 ± 1.50 ± 0.75	25.15 ± 2.00 ± 1.00	60.35 ± 4.00 ± 2.00	54.40	0.20	0.20	0.07	0.19	0.20	0.001	
7	Andra marble kadapa	12.25 ± 1.60 ± 0.80	20.25 ± 1.80 ± 0.90	50.20 ± 3.00 ± 1.50	44.50	0.10	0.20	0.06	0.16	0.10	0.001	
8	Ceramic tiles	150.30 ± 4.0 ± 2.00	175.17 ± 4.00 ± 2.00	390.08 ± 9.00 ± 4.50	430.30	1.20	1.60	0.8	1.50	1.30	0.01	
9	Vitrified tiles	80.45 ± 3.50 ± 1.75	135.45 ± 3.00 ± 2.00	450.11 ± 13.00 ± 6.50	307.70	0.80	1.10	0.4	1.09	1.00	0.01	
10	Mosaic TILES	38.45 ± 1.60 ± 0.80	42.26 ± 2.00 ± 1.50	355.12 ± 3.80 ± 1.90	126.60	0.30	0.40	0.20	0.46	0.40	0.003	
11	Sand-1	11.38 ± 1.40 ± 0.70	18.15 ± 1.60 ± 1.00	70.5 ± 5.00 ± 2.50	42.10	0.10	0.10	0.06	0.15	0.10	0.001	
12	Sand-2	21.42 ± 1.20 ± 0.64	41.25 ± 1.80 ± 0.8	365.74 ± 3.20 ± 1.60	46.90	0.30	0.40	0.10	0.40	0.40	0.002	
13	Penna cement	15.52 ± 0.50 ± 0.25	19.52 ± 1.20 ± 0.87	45.12 ± 2.50 ± 1.25	50.80	0.10	0.20	0.08	0.16	0.10	0.001	
14	Zuari cement	18.22 ± 0.30 ± 0.15	20.08 ± 0.20 ± 0.64	55.50 ± 2.00 ± 1.00	40.50	0.10	0.20	0.10	0.18	0.20	0.001	
15	Ultratech cement	8.17 ± 0.40 ± 0.20	19.05 ± 0.90 ± 0.43	67.32 ± 5.50 ± 2.75	59.10	0.10	0.10	0.04	0.14	0.10	0.001	
16	Brick	15.07 ± 1.80 ± 0.87	30.15 ± 2.50 ± 1.25	100.15 ± 4.00 ± 2.00	143.50	0.20	0.20	0.10	0.23	0.20	0.001	
17	Cement bricks	40.15 ± 1.800.87	52.2 ± 1.50 ± 0.75	376.18 ± 4.50 ± 2.25	50.80	0.40	0.50	0.20	0.52	0.50	0.003	
	MAX	150.42 ± 4.00 ± 2.00	200.25 ± 4.50 ± 2.25	1500.50 ± 14.5 ± 7.25	551.50	1.50	1.90	0.80	2.00	1.80	0.01	
	MIN	8.17 ± 0.30 ± 0.15	18.15 ± 0.20 ± 0.43	45.12 ± 2.00 ± 1.00	40.50	0.10	0.10	0.04	0.14	0.10	0.001	
	AV	48.32 ± 1.90 ± 0.97	62.90 ± 2.40 ± 1.30	470.30 ± 6.50 ± 3.24	174.30	0.50	0.60	0.24	0.64	0.60	0.004	
	GM	32.20 ± 1.6 ± 0.79	46.90 ± 2.00 ± 1.18	244.70 ± 5.50 ± 2.74	116.40	0.30	0.40	0.16	0.44	0.40	0.002	
	SD	39.05 ± 1.0 ± 0.57	47.30 ± 1.00 ± 0.55	427.10 ± 4.00 ± 1.95	158.50	0.40	0.50	0.23	0.60	0.50	0.003	
	RUN	6.69 ± 0.17 ± 0.10	8.11 ± 0.19 ± 0.10	73.25 ± 0.69 ± 0.33	27.18	0.07	0.09	0.04	0.10	0.09	0.00	
	SU	71.12 ± 1.85 ± 2.00	91.05 ± 2.15 ± 2.00	727.69 ± 5.00 ± 3.12	255.50	0.07	0.90	0.38	0.93	0.85	0.05	

AV average, GM geometric mean, SD standard deviation, RUN random uncertainty, SU standard uncertainty

The bold representation in this tables are the minimum, maximum, average and uncertainty values that are given at the end of each table

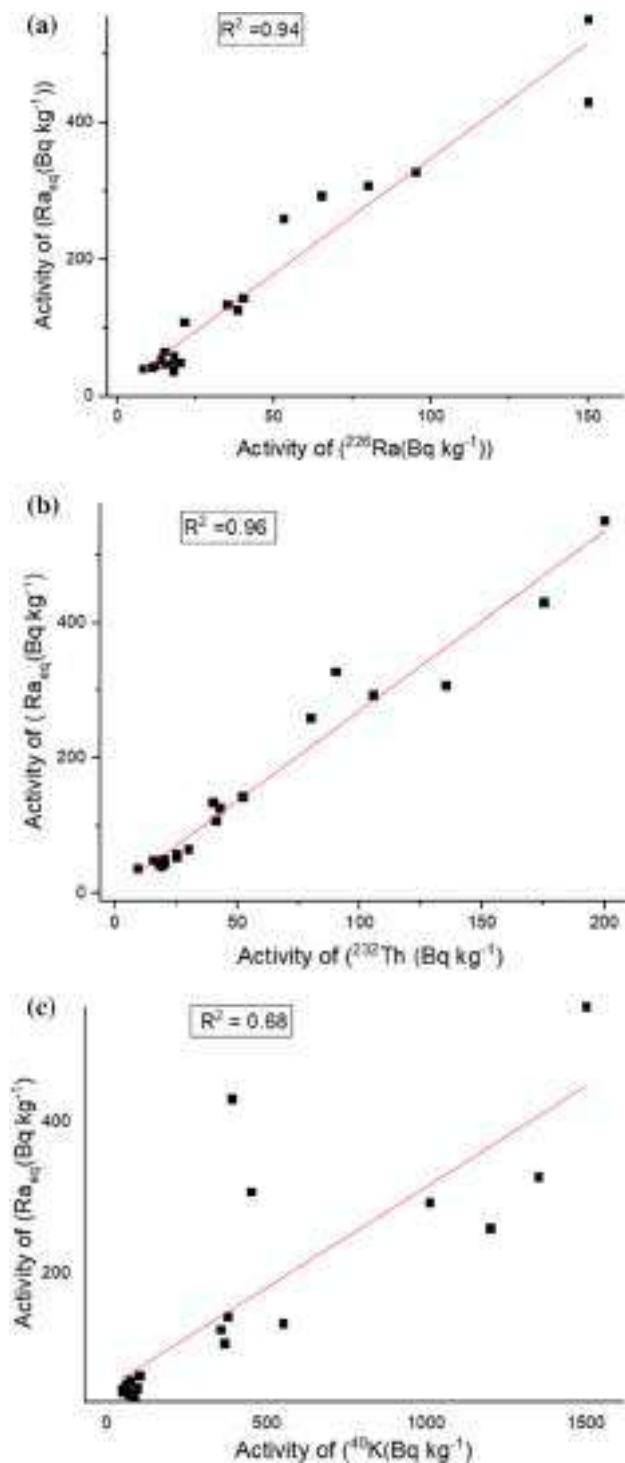


Fig. 7 **a** Correlation between ^{226}Ra and Ra_{eq} activity of building material sample, **b** Correlation between ^{232}Th and Ra_{eq} activity of building material sample, **c** correlation between ^{40}K and Ra_{eq} activity of building material sample

shown in Fig. 7a–c. It shows a linear and strong correlation coefficient of $R^2 = 0.94, 0.96$ and 0.68 respectively.

Conclusion

The activity concentration of radionuclides ^{226}Ra , ^{232}Th , ^{40}K in the soils of the study area was inspected using NaI(Tl) Gamma Ray Spectrometry is found lower than the global average values [25]. The average values of activity concentration among the radionuclides in soil and building materials follows the trend $^{40}\text{K} > ^{232}\text{Th} > ^{226}\text{Ra}$. The permissible world average value for absorbed dose rate is 55 nGy h^{-1} [24], and the permissible world average value of annual effective dose is 1 mSv y^{-1} [24]. The total GAD and AED rates of the study area to the public are lower than the global average values as recommended by international Commission on Radiological Protection [47]. The values of radiation risk assessment parameters such as Alpha Index, Gamma Index External Hazard Index, and Internal Hazard Index, all these come within the safe limit. Calculated average values of all the hazard indices of soil and building material samples are in the safer limit and will not cause health risk to the public of the area. The man made materials i.e., interlocks materials used around the building for decorative purpose, it will enhance the gamma radiation levels. The overall estimated data shows confidence level of 95.45% with coverage factor $k = 2$ for soil and building material samples. The forest influences in reducing the gamma radiation levels as the maximum area is covered by humous over top of the soil which serves as natural shielding. The activity of radionuclides in indoor gamma radiation is mostly influenced by soil type and construction materials.

References

1. Abbasi A et al (2020) Radiation hazards and natural radioactivity levels in surface soil samples from dwelling areas of North Cyprus. *J Radioanal Nucl Chem* 324(1):203–210. <https://doi.org/10.1007/s10967-020-07069-w>
2. UNSCEAR, Sérbia (2000) United Nations Scientific Committee on the Effects of Atomic Radiation. Sources and effects of ionizing radiation 2
3. UNSCEAR United Nations Scientific Committee on the Effects of Atomic Radiation on 10 September 2020.
4. Abbasi A, Mirekhtiary SF (2020) Radiological impacts in the high-level natural radiation exposure area residents in the Ramsar, Iran. *Eur Phys J Plus* 135(3):1–11. <https://doi.org/10.1140/epjp/s13360-020-00306-x>
5. Suresh S et al (2022) Estimation of natural radioactivity and assessment of radiation hazard indices in soil samples of Uttara Kannada district, Karnataka India. *J Radioanal Nucl Chem*. <https://doi.org/10.1007/s10967-021-08145-5>
6. Tawfic AF et al (2021) Natural radioactivity levels and radiological implications in the high natural radiation area of Wadi El Reddah, Egypt. *J Radioanal Nucl Chem* 327(2):643–652. <https://doi.org/10.1007/s10967-020-07554-2>
7. Sannappa J et al (2003) Study of background radiation dose in Mysore city, Karnataka State, India. *Radiat Meas* 37(1):55–65

8. Ziajahromi S, Khanizadeh M, Nejadkoorki F (2015) Using the RESRAD code to assess human exposure risk to ^{226}Ra , ^{232}Th , and ^{40}K in soil. *Hum Ecol Risk Assess Int J* 21(1):250–264. <https://doi.org/10.1080/10807039.2014.909194>
9. Flodin U et al (1990) Acute myeloid leukaemia and background radiation in an expanded case-referent study. *Arch Environ Health Int J* 45(6):364–366. <https://doi.org/10.1080/00039896.1990.10118756>
10. Ron E (1998) Ionizing radiation and cancer risk: evidence from epidemiology. *Radiat Res* 150(5):S30–S41. <https://doi.org/10.2307/3579806>
11. Ujjinappa BS et al (2021) Natural ambient gamma radiation levels, distribution of radionuclides, and evaluation of radiological hazards around Bellary thermal power plant, India. *Environ Earth Sci* 80(1):1–13
12. Navas A, Soto J, Machin J (2002) ^{238}U , ^{226}Ra , ^{210}Pb , ^{232}Th and ^{40}K activities in soil profiles of the Flysch sector (Central Spanish Pyrenees). *Appl Radiat Isot* 57(4):579–589. [https://doi.org/10.1016/S0969-8043\(02\)00131-8](https://doi.org/10.1016/S0969-8043(02)00131-8)
13. Suresh S et al (2020) Measurement of radon concentration in drinking water and natural radioactivity in soil and their radiological hazards. *J Radiat Res Appl Sci* 13(1):12–26. <https://doi.org/10.1080/16878507.2019.1693175>
14. Srinivasa E et al (2022) Natural radioactivity levels and associated radiation hazards in soil samples of Chikkamagaluru district, Karnataka, India. *J Radioanal Nucl Chem.* <https://doi.org/10.1007/s10967-021-08133-9>
15. Government of India Ministry of Water Resources (2007) Central Ground Water Board. Ground Water Information Booklet Shimoga District, Karnataka
16. Volchok HL, de Planque G (1983) EML procedures manual 26th edition. United States: N. p. Web
17. Sannappa J, Ningappa C, Narasimha KN (2010) Natural radioactivity levels in granite regions of Karnataka State. <http://nopr.niscair.res.in/handle/123456789/10487>
18. Ramasamy V, Murugesan S, Mullainathan S (2004) Gamma ray spectrometric analysis of primeval radionuclides in sediments of Cauvery River in Tamilnadu, India. *Ecologica* 2:83
19. Ahmed N, El-Arabi AGM (2005) Natural radioactivity in farm soil and phosphate fertilizer and its environmental implications in Qena governorate Upper Egypt. *J Environ Radioact* 84(1):51–64. <https://doi.org/10.1016/j.jenvrad.2005.04.007>
20. Aslam M et al (2002) Radiological significance of Pakistani marble used for construction of dwellings. *J Radioanal Nucl Chem* 253(3):483–487. <https://doi.org/10.1023/a:1020438007471>
21. Yousef MI, Abu El-Ela A, Yousef HA (2007) Natural radioactivity levels in surface soil of Kitchener Drain in the Nile Delta of Egypt. *J Nucl Radiat Phys* 2(1):61–68
22. IAEA/RCA (1989) Regional workshop on Environmental sampling and measurement of radioactivity for monitoring purposes. Health Phys. Division, BARC, Kalpakkam, India, pp 85–95
23. Nambi KSV et al (1987) Country-wide environmental radiation monitoring using thermoluminescence dosimeters. *Radiat Prot Dosimetry* 18(1):31–38
24. UNSCEAR (2000) Sources and effects of ionizing radiation. United Nations Scientific Committee on the Effects of Atomic Radiation Report to the General Assembly, with scientific annexes
25. UNSCEAR (2008) United Nations Scientific Committee on the effect of Atomic Radiation. 2008 report on the Sources and Effects of Ionizing Radiation. Report to the General Assembly with Scientific Annexes. United Nations, New York
26. Beretka J, Mathew PJ (1985) Natural radioactivity of Australian building materials, industrial wastes and by-products. *Health Phys* 48:87–95
27. European Commission (1999) Radiation Protection 112, Radiological Protection Principles Concerning the Natural Radioactivity of Building Materials. European Commission
28. Rao DD (2018) Use of hazard index parameters for assessment of radioactivity in soil: a view for change. *Radiat Protect Environ* 41(2):59
29. Righi S, Bruzzi L (2006) Natural radioactivity and radon exhalation in building materials used in Italian dwellings. *J Environ Radioact* 88(2):158–170. <https://doi.org/10.1016/j.jenvrad.2006.01.009>
30. Fares S, Hassan AK, El-Saeedy HI (2017) Environmental Characterization and Natural Radioactivity Influential on the Mountains of the Red Sea Coast, Egypt. *ChemXpress* 10(1):119
31. Iqbal M, Tufail M, Mirza M (2000) Measurement of natural radioactivity in marble found in Pakistan using a NaI (TI) gamma-ray spectrometer. *J Environ Radioact* 51:255–265
32. Beck HL, DeCampo J, Gogolak C (1972) In Situ Ge(Li) And NaI(Tl) Gamma-Ray Spectrometry. United States: N. p., Web
33. Ugbede FO, Echeweozo EO (2017) Estimation of annual effective dose and excess lifetime cancer risk from background ionizing radiation levels within and around quarry site in Okpoto–Ezillo, Ebonyi State, Nigeria. *The land* 7:12
34. ICRP protection 103 (2007) Ann.ICRP 37(2–4)-F. The Recommendations of the International Commission on Radiological Protection
35. Taskin H et al (2009) Radionuclide concentrations in soil and lifetime cancer risk due to gamma radioactivity in Kirklareli, Turkey. *J Environ Radioact.* <https://doi.org/10.1016/j.jenvrad.2008.10.012>
36. Ningappa C, Sannappa J, Karunakara N (2008) Study on radionuclides in granite quarries of Bangalore rural district, Karnataka, India. *Radiat Protect Dosim* 131(4):495–502. <https://doi.org/10.1093/rpd/ncn203>
37. Obasi I et al (2020) In situ measurement of radionuclide concentrations (^{238}U , ^{40}K , ^{232}Th) in middle Cretaceous rocks in Abakaliki-Ishiagu areas, southeastern Nigeria. *Arab J Geosci* 13:1–9. <https://doi.org/10.1007/s12517-020-05360-4>
38. Fakeha A (2012) Activity concentrations of natural radionuclides in sedimentary rocks from North of Arabian Shield (Hail), Saudi Arabia. *Life Sci J* 9:4
39. Srilatha MC, Rangaswamy DR, Sannappa J (2015) Measurement of natural radioactivity and radiation hazard assessment in the soil samples of Ramanagara and Tumkur districts, Karnataka-India. *J Radioanal Nucl Chem* 303:993–1003. <https://doi.org/10.1007/s10967-014-3584-1>
40. Hameed PS et al (2014) Measurement of gamma radiation from rocks used as building material in Tiruchirappalli district, Tamil Nadu, India. *J Radioanal Nucl Chem* 300(3):1081–1088. <https://doi.org/10.1007/s10967-014-3033-1>
41. Nace T (2016) Why granite colours range from white to black. *Forbes* (June 5, 2016)
42. Chandrashekara MS, Veda SM, Paramesh L (2012) Studies on radiation dose due to radioactive elements present in ground water and soil samples around Mysore city, India. *Radiat Prot Dosimetry* 149(3):315–320
43. Alkhomashi N, Almasoud FI, Alhorayess O, Alajayan TM, Alamah AS, Alssalim YA, Ababneh ZQ (2017) Assessment of radioactivity and trace elements of cement produced in Saudi Arabia. *Environ Earth Sci* 76:280. <https://doi.org/10.1007/s12665-017-6605-x>
44. Abbasi A (2017) Modeling of lung cancer risk due to radon exhalation of granite stone in dwelling houses. *J Cancer Res Ther* 13(2):208. <https://doi.org/10.4103/0973-1482.204851>
45. Abbasi A (2013) Calculation of gamma radiation dose rate and radon concentration due to granites used as building materials in Iran. *Radiat Prot Dosimetry* 155(3):335–342. <https://doi.org/10.1093/rpd/nct003>
46. United Nations Scientific Committee on the Effects of Atomic Radiation. Sources and Effects of Ionizing Radiation, United Nations Scientific Committee on the Effects of Atomic Radiation

- (UNSCEAR) 1993 Report: Report to the General Assembly, with Scientific Annexes. United Nations, 1993
47. International Commission on Radiological Protection (ICRP) 1990 Recommendations of Radiological Protection. ICR Publication 60, Pergamon Press, Oxford
 48. Johnson SS (1990) Natural Radiation; Heavy-mineral studies—Virginia Inner Continental Shelf, edited by C.R. Berquist, Jr
 49. Ghosh D et al (2008) Assessment of alpha activity of building materials commonly used in West Bengal, India. *J Environ Radioact* 99(2):316–321
 50. Malanca A, Pessina V, Dallara G (1993) Radionuclide content of building materials and gamma ray dose rates in dwellings of Rio Grande Do Norte, Brazil. *Radiat Prot Dosimetry* 48(2):199–203
 51. Alencar AS, Freitas AC (2005) Reference levels of natural radioactivity for the beach sands in a Brazilian south eastern coastal region. *Radiat Meas* 40(1):76–83. <https://doi.org/10.1016/j.radmeas.2004.08.003>

Publisher's Note Springer Nature remains neutral with regard to jurisdictional claims in published maps and institutional affiliations.

A simple uric acid assay by using 3-hydroxytyramine as a chromogenic colorimetric sensor in human serum samples: Density functional theory supported mechanistic approach

Honnur Krishna¹ | Avinash Krishnegowda² | Shivakumar Anantharaman³ | Kumar Shrestha Ashwinee⁴ | A Edalli Vijayalakshmi¹

¹Department of Chemistry, S. D. V. S. Sangh's S. S. Arts College and T. P. Science Institute, Belagavi, India

²Department of Chemistry, ATME College of Engineering, Mysore, India

³Department of Chemistry, St. Philomena's College, PG centre, Mysore, India

⁴Department of Pharmacy, Kathmandu University, Kathmandu, Nepal

Correspondence

Honnur Krishna, Department of Chemistry, S. D. V. S. Sangh's, S. S. Arts College and T. P. Science Institute, Sankeshwar, (Affiliated to) Rani Channamma University, Belagavi 591313, Karnataka, India.
Email: krishnachem08@gmail.com

Shivakumar Anantharaman, Department of Chemistry, St. Philomena's College, PG centre, Mysore 570 006, India.
Email: shivakem77@gmail.com

Funding information

University of Mysore

Abstract

A simple, fast, sensitive, convenient, and economical accurate enzymatic colorimetric sensor is developed for the quantification of the clinically important biomarker uric acid (UA) in human serum samples. The method is based on the quantification of UA using 3-hydroxytyramine (3-HT) as a chromogenic substrate by using peroxidase (POD) and uricase (UOx). UOx catalyzes the oxidation of UA where H_2O_2 is generated in-situ to produce allantoin and CO_2 . The POD in oxidative coupling of peroxide in presence of 3-HT, forms an intense orange-colored product with $\lambda_{max} = 500$ nm. The reaction was carried out in a citric acid-tripotassium-citrate buffer (12.5 mM) of pH = 6.8 at room temperature. Computational calculations were done by Gaussian-16 employing the B3LYP functional basis set. The standard curve for UA was found to be linear between 12.3–297.3 and 3.07–396.5 μ M by rate and fixed time method, respectively. The LOD and LOQ for UA were 1.5 and 2.9 μ M, respectively. Within-day and day-to-day precision was 1.50–3.07 and 3.10–4.16% ($n = 7$), respectively. The accuracy ranges for UA concentrations of 24.7, 198 and 297.3 μ M were 87%–101.50%, 90%–105%, and 89%–107%, respectively. The UA recovery range by the proposed method was 98.00%–100.47% with a mean recovery of 99.5% and has a good correlation coefficient of 0.981 with the standard method.

KEYWORDS

clinical biomarker, enzymatic, oxidative coupling, serum analysis, uric acid

Abbreviations: 3-HT, 3-hydroxytyramine; 4-AAP, 4-aminoantipyrine; CV, coefficient of variations; CV, cyclic voltammetry; DFT, density functional theory; DPV, differential pulse voltammetry; ESP, electrostatic potential; EU, enzyme unit; LOD, limits of detection; LOQ, limits of quantification; NBO, natural bond order analysis; POD, peroxidase; UA, uric acid; UOx, uricase.

1 | INTRODUCTION

Uric acid (UA), a simple biochemical final breakdown product of purine nucleoside metabolism. It is degraded in most mammals by the hepatic enzyme, Urate oxidase (Uricase-UOx) to allantoin, which is freely excreted in the urine.^[1] It is known that UA is produced by high

purine foods, which tend to accumulate in the body, due to the low solubility, which results in high UA levels. The standard concentration of UA in the human serum reference range is from 0.24 to 0.52 mM (Male: 3.4–7.0 mg/dl and Female: 2.4–6.0 mg/dl).^[11,21] The standard concentration of UA in human urine is 1.4–4.4 mM. When the higher abnormal concentration of UA in the blood fluid is greater than 7 mg/dl, then the body fluid becomes acidic, which affects the normal function of the cellular system. The increase in the UA level causes hyperuricemia that causes crystals of UA or urate deposition in the joints resulting in the gout condition, which is a form of arthritis and also forming hypertension, Lesch-Nyhan syndrome.^[3] When the crystals settle in the kidney, that results in some of the serious issues, like renal diseases,^[4] cardiovascular diseases, and so forth, concerning the purine metabolism. One of the studies suggests that UA may increase dopamine levels in the brain.^[15] Furthermore, some of the experimental studies revealed that an elevated UA can induce small vessel disease in the kidney that can alter auto-regulation, which is more common in subjects with vascular dementia^[6,7] and stroke.^[8–10] Therefore, it has practical significance for clinical approaches. Also, UA is known to function as an antioxidant. Some of the reports have shown that UA could react with a wide variety of oxidants, such as peroxynitrite, superoxide, and hydroxyl radical,^[11,12] and could also be shown to protect cells from oxidant injury.^[13] Therefore, it is very important to monitor the concentration of UA in the biological fluids.

Various analytical techniques, such as electrochemical cyclic voltammetry (CV),^[14] differential pulse voltammetry (DPV),^[15] capillary electrophoresis with electrochemical detection,^[16] non-invasive non-enzymatic electrochemical sensors,^[17] fluorescence,^[18] chemiluminescence,^[19] chromatographic methods,^[20] liquid chromatography and tandem mass spectrometry using urate anion as internal standard,^[21] UOx free colorimetric sensor,^[22] microfluidic paper-based colorimetric device,^[23] and flow injection analysis using dithiothreitol,^[24] have been used to detect the quantification of UA in different sources including human serum samples.

Unfortunately, in the case of electrochemical techniques, other electro-active compounds that coexist in body fluids, such as ascorbic acid and dopamine, will critically interfere with the UA sensing system. Glucose, a strong reducing agent, could also interfere with the results of the electrochemical method and other bioactive molecules that are present in the blood or urine samples. The spectrofluorescence method is ultrasensitive, but the reagents used are highly photosensitive, and the instrument used is expensive. Furthermore, the chromatographic column requires extensive use of extremely pure

solvents, time consuming and high pressure and temperature should be maintained throughout the experimental procedures, and also requires highly skilled labor, which restricts the use of this method.

Some of the analytical reagents based on spectrophotometric or colorimetric methods such as 3,5-Dichloro-2-hydroxy benzenesulfonic Acid/4-Aminophenazone (4-AAP) (DHBS-4-AAP),^[25] *p*-hydroxybenzoate and 4-AAP,^[26] 2,4,6-tribromophenol & 4-AAP,^[27] tetrazolium salt,^[28] silver composite nanobelts^[29] have also been used for the quantification of UA. Some of the drawbacks for the UA determination that are reported in the literature include spectrophotometer: DHBS-4-AAP is that incubation period of 15 min, interference from bilirubin up to 170 $\mu\text{mol/L}$ was eliminated by use of ferrocyanide, through which the peroxidase (POD)-H₂O₂ oxidation to ferricyanide, seems to increase the specificity of the color reaction and ascorbate oxidase is used to eliminate ascorbic acid interference especially in urine analysis, which are some of the demerits of the method^[25]; *p*-hydroxybenzoate and 4-AAP, bilirubin at moderate conditions will interfere strongly and also use of K₂Cr₂O₇ reagent for the elimination of interference caused by 17 U/L of Catalase^[26]; 2,4,6-tribromophenol & 4-AAP, this method uses a large volume of serum sample (1.0 ml) and deproteinization of serum sample using acetic acid, assay procedure takes around 45 min for extraction of the colored product by using *n*-butyl acetate which is time consuming process and suffer serious interference from ascorbic acid and bilirubin^[27]; tetrazolium salt, the main drawback of the method is that, it uses three enzyme system such as Catalase, UOx, and formaldehyde dehydrogenase and also ascorbate oxidase is used to eliminate ascorbic acid interference resulting in high cost of the experimental procedure^[28]; UV method using alkaline ferricyanide suffer from background interference caused by the serum proteins.^[30]

Nano-technological approaches have also been utilized to detect the UA concentration, either by using the POD mimic or as a non-enzymatic sensor assay.^[17,22,31,32] However, most of the nanotechnology methods, which involve the top-down or bottom up approach for instance, they are of high cost, such as arc furnace, nanolithography techniques or hydrothermal method which require high temperature, power consumptions, suffer from defects in nanoparticles (NPs) surface, not reproducible in most of the cases, that is, synthesizing the same size NPs or maintaining the uniform size distribution and the technique involve multiple steps in the preparation and purification of these NPs. Some of the quantum dots-based NPs are derived from heavy metals, such as Hg, Cd, Pd, and so forth, which are highly toxic not only for the environmental ecosystem but also for the



biological system. Therefore, the need for the development of a simple, rapid, economical, and most convenient and affordable analytical method for the determination of UA is in great demand to continuously monitor the UA in real time analysis.

In this perspective, spectrophotometric method is the most simple convenient analytical technique and available in most of the clinical laboratory and is highly accurate and sensitive method.^{12,51} In some of the spectrophotometric methods, even though it looks simple at the outside but most of the techniques are either time consuming process or involves multiple steps of pre-concentration steps before the analysis. Therefore, in clinical medical pathology and daily monitoring of the UA, the most convenient, low cost, simple, rapid, and novel sensors are need of the hour for real time analysis.

In this work, we have described a newly developed Spectrophotometric method for the quantification of UA, which is simple, reliable, economical and rapid (within 5 min) enzymatic based assay in the physiological sample that is human serum samples. This paper describes the first example of using 3-HT as the chromogenic single reagent for the development of UA assay. Furthermore, we have studied the DFT-based quantum mechanical approach toward understanding the insights of the chemical mechanism of formation of the colored product.

2 | EXPERIMENTAL METHODS

2.1 | Instrumentation, chemical reagents and their preparation

3-Hydroxytyramine (98%) was purchased from SD Fine-Chem Ltd., Mumbai. 3-HT (78.33 mM) was prepared by dissolving the required quantity in water. The solution was kept under refrigeration for effective maintenance of molarity. For the assay, a freshly prepared solution was used to get better results.

Stock solution of citric acid—Tripotassium citrate buffer (pH 6.8, 500 mM)—was prepared by dissolving 5.253 g of citric acid monohydrate in 50 ml and 8.560 g of tripotassium citrate in 50 ml of distilled water. The above stock solution of 0.5 M was diluted to eight times to get 62.5 mM. From this 0.6 ml of buffer solution was used for the assay.

UA (98%) was obtained from SD Fine-Chem Ltd., Mumbai and a stock solution (5.948 mM or 1,000 ppm) was prepared by using the procedure as reported by R. C. Trivedi et al., with slight modification.^{12,51} Li_2CO_3 of 60 mg were dissolved in 20 ml of distilled water at 60°C. While still hot, this solution was filtered through Whatman No. 1 paper and exactly 100 mg of UA was dissolved

in the hot filtrate. After cooling to room temperature, the solution was diluted with distilled water to 100 ml in a volumetric flask. Dilutions of this stock UA standard were used as and when required. The stock solution was stable for at least 1 month when stored at 4°C. Standards.

Lyophilized UOx enzyme 12 units/mg from *Bacillus fastidious* was purchased from Sigma Aldrich Chemicals Pvt. Ltd., Bangalore, India. A stock solution of (12 units/mg) was prepared by dissolving the whole lyophilized enzyme in 5 ml of distilled water. Further dilution with double distilled water was made as and when required, freshly. POD (100 units/mg) was purchased from Himedia Laboratories, Mumbai, India. The stock solution was prepared by dissolving 2 mg of POD in 10 ml of 100 mM potassium dihydrogen phosphate/sodium hydroxide buffer with a pH 6.0. It was used as a standard stock solution. Further dilution with the same buffer was made freshly as and when required. All the above solutions were kept under refrigeration for effective maintenance of molarity. A freshly prepared solution was always used for the assay procedures.

All the chemicals used in the assay were of analytical grade, and double distilled water was used throughout the assay procedure unless otherwise stated.

A Jasco model UVIDEK-610 ultraviolet-visible (UV-Vis) spectrophotometer (Tokyo, Japan) with 1.0-cm matched cells was used for all the absorbance measurements. A water bath shaker (NSW 133, New Delhi, India) was used to maintain a constant temperature for color development. All pH measurements and adjustments were done by a digital pH meter (model EQ-614, Equiptronics, Mumbai, India). Micropipettes used in the enzymatic UA assay were from Bohit Proline, Finland. Serum samples were centrifuged using Remi R-24 (Mumbai, India) research centrifuge having 17,300 rpm and 27,440 "g" RCF. Remi cyclomixer was used throughout the experimental performance for uniform mixing of the reagent solution in the control as well as in the sample reaction mixture effectively in the test vials before recording the absorbance.

2.1.1 | Human serum sample collection and preparation for uric acid determination

Human blood samples collected from a local hospital and also from a clinical laboratory were preserved at -20°C for use. Blood samples were collected in heparinized tubes and centrifuged. The accuracy of the proposed method was assessed by comparing the results obtained with a reported UA assay method.^{12,51}

Necessary permission was obtained from the Institutional Human Ethical Committee (IHEC-UOM No.22/

Ph.D/2008-09) of the University of Mysore for the use of human blood samples in the experiment. The patients were well informed, and their consents were obtained before collecting the blood samples.

2.2 | Standardization of the reaction conditions

Optimizing the reaction conditions and different mediums of sets of reactants were varied to yield highly stabilized colored products with maximum absorbance in the experimental samples and minimum color formation in the blank in a final 3 ml volume of test vials.

The dual enzymatic system is standardized kinetically in such a way that the sample should show maximum absorbance and also have the rate increased twice as with the increase in concentration of the enzymatic solution in the reaction medium. This progress of the reaction is monitored kinetically as a function of time. Initial rates of the reactions were calculated using the slopes from the time-absorbance response curves in terms of 5 min over an interval of 1 min.

First, the POD enzyme concentration was standardized, followed by the UOx enzyme concentration in the consequent steps. The suitable volume of the reagent and 100 μ l concentrations of POD (9.46 nM) and UOx (0.18 U/mg) are required, respectively, for the maximum development of color and fixed for the rest of the assays. In all the above cases, the reaction medium and the experimental conditions were varied for high absorbance and maximum stability of colored product. Different concentrations and volumes of varying concentrations of the reactants were added to the test vials, and their optical densities were measured carefully.

2.3 | General assay procedures

2.3.1 | Determination of hydrogen peroxide

The reaction mixture containing H_2O_2 concentrations in the range of 128–6,400 μ M was used for its quantification by using the kinetic method. Reagent concentrations of 2.611 μ M 3-HT, 9.46 nM POD in 12.5 mM citric acid–tripotassium-citrate buffer of pH 6.8 at room temperature was mixed with different H_2O_2 concentrations. The absorbance was measured for up to 5 min at an interval of 1 min for different H_2O_2 concentrations. Then the graph of absorbance as a function of time would give a regression equation having a slope value equivalent to the rate of the assay.

2.4 | Determination of UA

2.4.1 | Standard assay method

The UA sensing assay was carried out by adding 100 μ l of varying concentrations of UA (9.21–1,189.5 μ M) to a reaction mixture containing 100 μ l of 3-HT (78.330 mM), 100 μ l of POD (9.46 nM), 100 μ l of UOx (0.18 U/mg) and 600 μ l of citric acid–tripotassium citrate buffer (12.5 mM, pH 6.8). The final volume of the solution was made up to 3 ml using distilled water. The reaction mixture was incubated for 5 min at room temperature ($26 \pm 3^\circ\text{C}$) and color intensity was measured at 500 nm. A reaction mixture without the addition of UA served as the control.

For analyzing the blood samples, 30 μ l of the serum sample was considered for the UA quantification and statistically compared with the reported method.

2.4.2 | Unit of enzyme (EU)

One unit of POD activity is defined as that amount of enzyme, which utilizes 1 μ M of H_2O_2 in the oxidative formation of protonated form of quinone from 1 μ M of 3-HT to give orange colored product per min under standard assay conditions.^[33]

One unit of UOx is defined as that amount of enzyme activity, which is required to oxidize 1 μ M of UA to generate allantoin and 1 μ M H_2O_2 per min under standard assay conditions.^[34]

2.5 | Electron density mapping of 3-HT supporting enzyme catalyzed for UA sensing methodology

2.5.1 | Software and instrumentation

Computational calculations were done by Gaussian 16^[35] employing B3LYP functional involving dispersion correction with 6-311++G (d,p) basis set to achieve an optimized geometry. Cations and anions were analyzed by unrestricted formalism. Avogadro^[36] and Gausssum^[37] were used as virtual interfaces. Solvent effects on the optimized structure were investigated with a self-consistent reaction field by the polarized continuum method. The optimized structures were checked for any imaginary frequencies. Theoretical calculations were done on the molecular systems that include single point energies, IR, and UV-Vis data for visualization. The adiabatic excitation energies were computed using TD DFT calculations. Natural charges and the gradient pattern in the electron density calculations were computed for 3-HT and the



final quinone using NBO and ESP DFT codes. Fukui functions and dual descriptors are calculated without changing the geometrical structure of the molecule from neutral to anion/cation species.

2.5.2 | Mathematical relevance of DFT: A theoretical viewpoint

Global hardness has been identified as a derivative of the electronic potential with reference to the number of electrons.^[38] The electrophilicity index (ω) can be defined as the stabilization energy when the atoms or molecules in their ground states acquire additional electronic charge from the environment. In the DFT framework, as defined by Parr and his research group^[39] as the summation of electronegativity and chemical potential can be mathematically expressed as

$$\chi + \mu = 0$$

Chemical potential (μ) refers to the intrinsic acidic or basic strength,^[40] and it is identified as the opposite of the electronegativity (χ), defined as the derivative of the electronic energy with reference to the number of electrons at a constant external potential.

The energy change (ΔE) due to the transfer of electron should satisfy the below equation,

$$\Delta E = \mu \Delta N + \frac{1}{2} \eta \Delta N^2$$

where " μ " and " η " are the chemical potential and chemical hardness as first derivative and second derivative defined respectively, and N represents number of electrons as

$$\mu = \left(\frac{\partial E}{\partial N} \right)_{v(r)} \text{ and } \eta = \left(\frac{\partial}{\partial N} \left(\frac{\partial}{\partial N} \right) \right)_{v(r)}$$

where, $v(r)$ is the external potential of the electrophile. The complementary term softness is defined as inverse of hardness

$$S = \left(\frac{1}{\eta} \right)$$

As per the HSAB concept, defined hard acids prefer to combine with hard bases and soft acids prefer to bind soft bases.^[41]

Global hardness is commonly approximated as

$$\eta = \frac{1}{\epsilon_L - \epsilon_H}$$

Where ϵ_L and ϵ_H corresponds to the Kohn-Sham one electron^[42] Eigen values of lowest and highest occupied molecular orbital (LUMO and HOMO) orbitals.

Furthermore, local softness allows the reactivity of the molecule on an atom to atom basis which are defined mathematically as

$s_k^+ (r) = S f_k^+ (r)$ and $s_k^- = S f_k^- (r)$; k refers to the k th atom in the molecular system.

Local softness (s) are used for intermolecular comparison whereas, global softness (S) refers to the molecule system as a whole.

Working equations for the chemical potential (μ) and hardness (η) by self-consistent field (SCF) and HOMO/LUMO are equated as

$$\mu = - \left(\frac{1}{2} \right) (IP + EA) = - \left(\frac{1}{2} \right) (\epsilon_L - \epsilon_H)$$

$$\eta = (IP - EA) = (\epsilon_L - \epsilon_H)$$

where IP and EA are vertical ionization potential and electron affinity, respectively.

Thus the μ and η , can be also be mathematically manipulated as for a system of " N " electrons at a constant external potential^[43] as,

$$E_k = \left[\left(E_{v(r)}^{N-1} - E_{v(r)}^N \right) - \left(E_{v(r)}^N - E_{v(r)}^{N+1} \right) \right] = IP - EA$$

Furthermore, electrophilicity based on electronegativity and global hardness can be defined as,

$$\zeta^+ = \frac{\mu^2}{2\eta}$$

3 | HARDNESS AND SOFTNESS BASED ON FUKUI FUNCTIONS

The discontinuity of the electron density from either side of the derivative with reference to the N number of electrons by finite difference leads to three types of Fukui functions namely, positive, negative and neutral ($f_k^{\pm,0}$) for charged or radical attack. The positive and negative Fukui functions refer to the variation in the electron density caused by the removal and addition of one electron to the neutral system, and the neutral Fukui function to

the average of the positive and negative Fukui functions. The quantitative and qualitative values of the Fukui function can be interpreted as: large f^+ indicates the molecule accepts electrons, and large f^- indicates the molecule donates electrons. The Fukui functions based on the finite differences method can be defined as,

$$f^+(r) = \left(\frac{\Delta\mu^+}{\Delta v(r)} \right)_N = - \left(\frac{\Delta A}{\Delta v(r)} \right)_N = \left(\frac{\Delta\rho(r)}{\Delta v(r)} \right)^+$$

$$f^-(r) = \left(\frac{\Delta\mu^-}{\Delta v(r)} \right)_N = - \left(\frac{\Delta I}{\Delta v(r)} \right)_N = \left(\frac{\Delta\rho(r)}{\Delta v(r)} \right)^-$$

$$f^0 = \left(\frac{1}{2} \right) (f^+(r) + f^-(r))$$

where A and I refers to the electron affinity and ionization potential. At point, $f^0(r)$, $f^+(r)$ and $f^-(r)$ are the measure of reactivity toward radical, nucleophilic, and electrophilic, respectively.

Furthermore, some of the researchers define a new index called dual descriptor for both electrophilic and nucleophilic attacks. The dual descriptor can be defined as the chemical hardness to external potential changes or the change in the Fukui function at each point when the total number of electrons is changed

$$\Delta f(r) = \left(\frac{\delta\eta}{\delta v(r)} \right)_N = \left(\frac{\delta f(r)}{\delta N} \right)_{v(r)}$$

Since the Fukui function is normalized, the normalization condition for $\Delta f(r)$ is

$$\frac{\delta}{\delta N} \int f(r) dr = 0$$

$$\int \Delta f(r) dr = 0$$

Hence the nucleophilic/electrophilic behavior of the molecule can be characterized through the sign and amplitude of the function $\Delta f(r)$. When $\Delta f(r) > 0$ then the point r is favored for nucleophilic attack, whereas $\Delta f(r) < 0$ is the point favored for an electrophilic attack.^[44]

Dual descriptor values, $\Delta f(r)$ values, that is, the difference of electron density on the LUMO and that on the HOMO used to study the electron density pattern on the atoms associated with the molecule. It was observed from the worked out calculations that $\Delta f(r) < 0$ for O₁₁, O₁₀, N₉, C₆, C₅, C₃, C₂ indicating the electron rich positions. The relative electron density gradient pattern and amplitude have been evaluated. The red position and blue on the surface

gradient pattern indicate the higher and less electron denser positions, indicating the phenolic oxygen is more prone to reduction compared to N₉ of 3-HT.

3.1 | Kinetic or catalytic parameters

3.1.1 | Kinetic or rate method

Kinetic or rate method involves the measurement of the absorbance of the sample solution against the reagent blank with time for the first 5 min with an interval of 1 min and by plotting a graph of time versus absorbance.

3.1.2 | Fixed time method

Fixed time method involves the measurement of the absorbance of the sample solution for incubating the reaction mixture for the specified period of time as against the reagent blank (5 min).

3.1.3 | Maximum velocity of the reaction (V_{max})

V_{max} is a numerical constant representing the maximum velocity obtained when the enzyme E exists completely in the form of ES [$V_{max} = K(E_{total})$]. For any catalytic reaction V_{max} is obtained when the entire enzyme gets bound in the ES complex or otherwise when the solution containing the enzyme becomes saturated with the substrate in a reaction.

3.1.4 | Catalytic constant (k_{cat})

Catalytic constant is defined as the maximum number of molecules of substrate that an enzyme can convert into product per catalytic site per unit time, or simply it is defined as the number of substrate molecules handled by one active site per second and is calculated as

$$k_{cat} = V_{max} / [E]$$

3.1.5 | Catalytic efficiency (K_{eff})

The efficiency of an enzyme is expressed in terms of k_{cat}/K_m . This is also called the specificity constant and incorporates the rate constants for all steps in the reaction. Because the specificity constant reflects both affinity and catalytic ability, it is useful for comparing different



enzymes against each other or the same enzyme with different substrates.^[45] The efficiency of enzyme catalysis differs, but most enzymes can enhance the rate of an uncatalyzed reaction by a factor of 10^5 – 10^{14} . It can also be calculated as

$$K_{eff} = 1/\text{Slope} \times [E]$$

where, Slope is obtained by using Lineweaver–Burk plot rate versus concentration of substrate at saturated concentration of substrate.

3.1.6 | Catalytic power (K_{pow})

The catalytic power of enzymes has long been attributed to specific interactions with substrates in the transition state.^[46] It depends upon the decrease of the energy difference between the ground state and the transition state, and this process has been attributed to the tighter binding of the transition-state structure relative to the substrate.^[47]

The catalytic power is the ratio of two constants, the catalytic constant to Michaelis–Menten constant, expressed in terms of min^{-1} . It can be evaluated as:

$$K_{pow} = V_{max}/K_m$$

3.1.7 | Specificity constant (k_{cat}/K_m)

The specificity constant gives a direct measure of the catalytic efficiency at substrate concentrations that are significantly below the saturating levels. It is also an apparent constant value with a simple ratio of the catalytic constant to the Michaelis–Menten constant ($\text{min}^{-1} \text{mM}^{-1}$).

4 | RESULTS AND DISCUSSION

4.1 | Absorption spectrum for H_2O_2

Initially, the reaction condition is optimized before the optimization of the UOx enzyme, and recorded the absorption spectrum for H_2O_2 , which is a plot of absorbance as a function of wavelength. The spectrum is recorded after incubating the reaction mixture for 5 min at 30°C between 400 and 600 nm against the corresponding reagent blank at varying 76, 102, and 204 μM concentrations of H_2O_2 . It was found that the maximum absorption wavelength is equal to 500 nm (Figure S1A). The inset figure shows the colored photograph of the corresponding reagent blank and sample solution at varying

concentrations of H_2O_2 (76, 102, and 204 μM) respectively. The coefficient of variation (CV) was 3.2% for 60 μM H_2O_2 .

4.2 | Optimized reagents conditions

The reaction medium and conditions were varied to obtain the high absorbance and stability of the colored product. Different volumes of the reagents (100, 200, 400 and 800 μl), pH of the buffer solutions, and varying concentrations in suitable medium were added to the test vials, and the absorbance was measured, maintaining the final 3 ml of the reaction volume uniformly throughout the experiments.

4.2.1 | Calibration curves of the substrate parameters

The experimental assay conditions were as described in the general procedure. The linearity of the H_2O_2 curve is as shown in Figure S1B. The concentration of substrate and enzyme is selected after the calibration curves are obtained in order to get the maximum optical density and a stable colored product.

After the optimization of the concentration of H_2O_2 , the concentration of POD was optimized. To explore the effect of POD on the rate of the reaction, the increase in the absorbance of colored products was monitored at 500 nm by UV–Vis spectrophotometer for varying concentrations of POD by rate method (Figure S2A). The linear ranges for the determination of POD were found to be 0.59–18.92 and 0.443–9.46 nM by the kinetic and fixed time methods, respectively. The results are as shown in Figure S2B. Followed by the standardization of POD, the concentration of UOx was explored for the maximum color development in the sample solution. The relative time-absorbance plot is as shown in Figure S3A for different concentrations of UOx. The results reveal that the linearity for the UOx was from 0.022 to 0.18 units/mg, and with any further increase in the concentration of UOx, the rate remained constant Figure S3B. Later, using the POD assay and coupling with the UOx enzyme catalyzed reaction, the sensing curve for UA was measured based on varying concentrations of UA between 0.012 and 0.298 mM Figure 1a. The results show that the linearity range was 12.3–297.3 and 3.07–396.5 μM by rate method and fixed time method, respectively, as shown in Figure 1b. The apparent molar absorptivity for UA was $0.1003 \times 10^4 \text{M}^{-1} \text{cm}^{-1}$ and the determination of 250 μM UA has a CV of 2.87 ($n = 6$). The limits of detection (LOD) and quantification (LOQ) for UA were 1.5 and 2.9 μM , respectively by fixed time method.

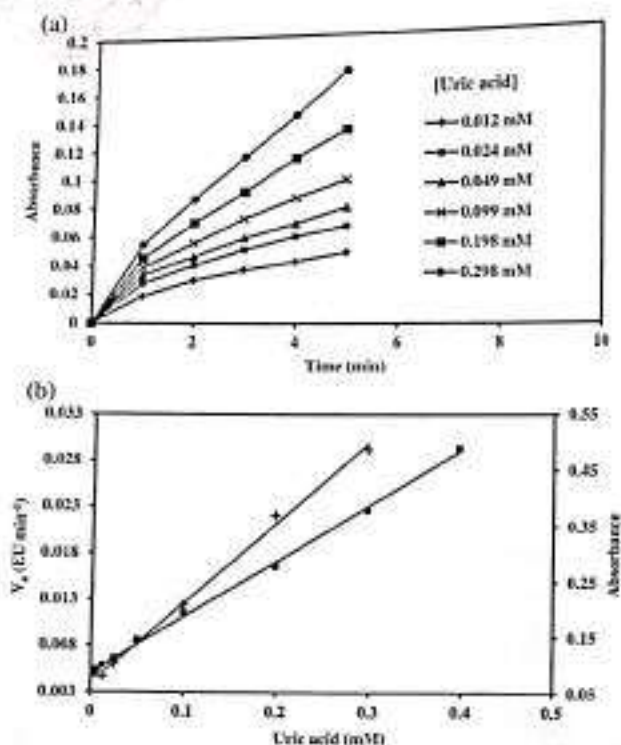


FIGURE 1 (a) The increase in the absorbance of reactive colored products was monitored at 500 nm by UV-Vis spectrophotometer for varying concentrations of uric acid by rate method. (b) Calibration graph for the quantification of uric acid by the rate (+) and fixed time (■) methods.

4.2.2 | Analytical method validation

For any method to be adopted as a standard method, it should be thoroughly validated for its analytical parameters. To explore the superiority of the present method, various analytical parameters such as accuracy, precision (day-to-day and intra-day precision), linearity range (calibration curve), LOD, LOQ, sensitivity and selectivity, interference tests, and applications have been tested both by kinetic analysis and by standard addition method wherever necessary. In addition to testing the suitability of the method, it was performed in the serum sample analysis. The mechanisms of the formation of colored products have been studied using DFT based quantum chemical calculations. The following are the methods of validation steps performed to test the suitability of the method for the assay of UA in serum samples.

4.2.3 | Precision and accuracy studies

Precision and accuracy of the method were determined by analyzing solutions containing known amounts of UA

using the following method with a slight modification.^{16c} The concentrations of the UA selected for the precision and accuracy experiments were from within the calibration graph. Three different concentrations were selected from the linearity graph, for instance, low, median, and high concentration values. The results showed that within-day precision was 1.50%–3.07% ($n = 7$) and day-to-day precision was 3.10%–4.16% ($n = 7$). The accuracy ranges for UA having concentrations of 24.7, 198, and 297.3 μM were 87.00%–101.50%, 90.00%–105.00%, and 89.00%–107.00%, respectively. The within-day and day-to-day precisions of the method gave a very low standard deviation (SD) and CV, indicating high precision and reproducibility of the method. The accuracy value was also high. Results are presented in Table 1.

4.2.4 | The effect of 3-HT on the color development

The influence of the 3-HT reagent on the reaction was studied by kinetic method varying its concentration (0.6527–10.444 mM), volume (100, 200, 400, and 800 μl), and the effect of order of addition was also carried out simultaneously. The rate of the reaction is directly proportional to the formation of the colored product, which is obtained by the plot of absorbance as a function of time with an increment of 1 min up to 5th min. The volume of 3-HT was optimized in such a way to get an intense color in the experimental sample solution with respect to minimal color formation in the blank solution. 3-HT (78.33 mM) was prepared by dissolving the required quantity in water. Different concentrations of 3-HT were varied, starting from 0.6527 to 10.444 mM. From Figure S4, it shows that there is a linear increase in the rate of the reaction with the increase in the concentration of the 3-HT till and further increase shows unaltered in the rate of reaction. A 100 μl , of 78.33 mM concentration of 3-HT before the addition of other substrates appears to provide the required stability and the maximum optical density of the reaction product. Therefore, the concentration of 2.611 μM of 3-HT was found to be sufficient for the maximum development of color and fixed for the rest of the assay performance.

4.2.5 | pH effect on the reaction condition

To obtain the stable, water soluble, and maximum development of the colored product, we studied the pH effect on the catalysis of the 3-HT in the presence of enzyme and substrate molecules in both acidic and basic buffer solutions. The assay was performed in various kinds of



TABLE 1 Within day and day-to-day precision and % of accuracy range.

Within day precision*				Accuracy range %	Day-to-day precision*				Accuracy range %
Uric acid (μM)	SD	CV	n	---	Uric acid (μM)	SD	CV	n	---
Low conc. (24.7)	0.00248	2.22	7	89.10–94.14	Low conc. (24.7)	0.00346	3.10	7	87.36–101.59
Medium conc. (198)	0.00427	1.50	7	95.48–105.00	Medium conc. (198)	0.00613	3.24	7	90.12–102.00
High conc. (297.3)	0.0116	3.07	7	92.56–107.00	High conc. (297.3)	0.01591	4.16	7	89.16–103.96

Abbreviations: CV, Coefficient of variation; n, number of runs; SD, Standard deviation.

*Duplicate measurement.

buffer systems varying from acidic pH to basic pH (3.0–10.5), and its concentration was varied from 0.1 to 2.0 M. The following are the lists of buffer solutions used for the assay development. A combination of acetic acid and sodium acetate buffer (pH 3.5–5.6), citric acid and sodium citrate buffer (pH 4.5–6.5), sodium hydrogen phosphate and sodium dihydrogen phosphate (pH 7.0–10.5), sodium hydroxide and potassium hydrogen phosphate buffer (pH 7.0–10) and tris buffer (pH 9.8) were used for the assay. Highest activity was observed in citric acid/tris potassium citrate buffer of pH 6.8 and it was selected for the further assay. Also, increases in the concentration of the buffer showed no effect on the rate of reaction. Whereas a decrease in the concentration of buffer from 500 to 62.5 mM, results in an increase in the reaction rate, and a further decrease in the buffer concentration has no effect on the rate of reaction and results in an increase in the reagent blank color. By considering the color stability and the maximum absorbance, the reaction was found to be suitable in citric acid-tripotassium-citrate buffer (12.5 mM) of pH 6.8 at room temperature. A detailed discussion about the buffer study has been provided at the end of the Supplementary Information (Tables S4 and S5).

4.2.6 | Temperature effect on the UA assay

To gain further insight into the effect of temperature on the enzyme activity for the maximum color development of the reaction product, was investigated by incubating the reaction mixture for a period of 5 min using the standard assay conditions for the concentrations of the reagents except varying the temperature of the reaction system. The activity of the enzyme in terms of percentage as a function of temperature with an increment of 5°C is plotted, and the results have been shown in Figure S5. A careful analysis of the temperature effect in the range between 5 and 45°C was selected for the study. It was found that there was a significant increase in the enzyme activity linearly in response to temperature from 10 to 25°C and remained unaltered until it reached 32°C,

TABLE 2 Tolerance ratios for the measurement of UA.

Interferants	Tolerance ratio*
Bilirubin	0.095
Ascorbic acid	0.098
Nitrite	0.1120
Iron (II)	0.1560
Iron (III), Mo (VI)	0.250
L-cystine	1.64
Copper (II)	3.58
F ⁻ , L-cysteine, L-leucine, L-tryptophan, L-tyrosine, urea	5.48
Magnesium (II), chloride, calcium (II), lactose, maltose	10.00
EDTA, citric acid, mannose, L-histidine,	16.00
DL-methionine, glucose, DL-threonine	22.00
Creatinine, Isoleucine, fructose, Potassium (I)	28.00
Nitrate, L-serine, D-asparagine	42.00
D-galactose, sucrose	96.00
Carbonate, sodium, oxalic acid, sulfate,	150.00
Glycine, ammonium	300.00
Acetone	356.00

Note: Tolerance ratio corresponds to the ratio of limit of interferants concentration to that of concentration of UA used.

*Tolerance ratios for the measurement of 198 μM UA.

thereafter decreasing in activity of the enzyme with the further increase in temperature. Therefore, these observations suggest that $26 \pm 3^\circ\text{C}$ is more suitable as the optimum room temperature for further working assay conditions.

4.2.7 | Interference studies

Interference by any common blood constituents in the quantification of UA was studied at a UA concentration of 198 μM . The concentrations of interferants as well as their tolerance limits are summarized in Table 2. Results

TABLE 3 Determination of UA in human serum samples by standard addition method.

Serum samples	UA (μM)		Added (μM)	Found* by proposed method (μM)	Recovery (%)	CV
	Proposed method	Reference method ^b				
1	145.92	149.08	24.7	168.93	98.84	1.58
2	168.80	172.20	49.5	219.10	100.47	2.26
3	243.2	240.24	12.3	254.62	99.63	1.86
4	185.14	186.22	99.5	282.12	98.63	3.02
5	345.51	341.10	12.3	358.60	100.22	1.52
6	321.62	318.30	24.7	343.80	99.21	2.78

*Mean of three replicate measurements; CV: coefficient of variation.

^bThe samples were also analyzed in the laboratory by the reference method.^[21]

revealed that most of the common ions present in serum samples exhibited negligible interference effects on the determination of UA, and the proposed method is highly selective and specific for UA measurement.

Interestingly, some of the common organic compounds, carbohydrate derivatives, acted as strong reducing agents along with the non-metals, such as nitrates or other functional compounds, and did not exhibit significant interference even when present at higher concentrations with the UA assay system, demonstrating the selectivity. Even some of the common biomolecules, such as creatinine, urea, and so forth, and some of the amino acids, such as glycine, L-serine, D-asparagine, Isoleucine, and so forth, which is present in the blood do not show much interference with the present assay. Furthermore, these experiments confirmed that the method is highly sensitive to the UA only.

4.2.8 | Standard addition method and Bland–Altman plot comparison

To explore the suitability of the proposed method, the standard addition method or the recovery tests were performed. The six different serum samples were considered from the healthy volunteers after their consent, and each sample is spiked with known concentrations of UA based on the linearity graph of the assay. The UA levels recovered by the proposed method were compared with the results obtained by the reported assay method, and the results are shown in Table 3. The UA recovery range by the proposed method was 87%–107% with a mean recovery of 96.87% demonstrates the high accuracy and minimum interference from the foreign species present in the blood samples, which are very crucial analytical steps for the newly developed method.

A Bland–Altman plot was proposed for the UA assay, which was performed by plotting a graph of the present

method and comparing the results with those obtained with the reported UA assay.^[23] From the regression equation, a correlation coefficient of 0.998 was achieved between the proposed method and the reported method. These results indicate that the proposed method is on par with the reference method. Results are shown in Figure S6.

4.2.9 | Kinetic studies

To understand and evaluate the selectivity and specificity of the substrate and enzyme catalytic site with the reagent co-substrate, the kinetic experiments were performed under the same assay conditions. From the results of the Michaelis–Menten catalysis equation, it can be observed that the lower value of K_m toward the substrates signifies not only that there is maximum interaction but also is highly selective between the catalytic active site of the enzyme and the substrate molecules.

Further, the results reveal that the ability of the 3-HT as a co-substrate molecule to increase the color response of the reaction product is very high, further suggesting that there is a strong interaction between the enzyme and the substrate molecules in the presence of the 3-HT reagent.

4.2.10 | Evaluation of kinetic constants for the measurement of catalytic parameters

The Lineweaver–Burk plot,^[49] for the catalytic reaction of H_2O_2 in the presence of POD is shown in Figure S7 and its linear regression equation having correlation coefficient of 0.996 was found to be $\frac{1}{v_0} = 3193 \left(\frac{1}{[C_{H_2O_2}]} \right) + 31.03$. The Lineweaver–Burk plot for UA in the presence of UOx is shown in Figure S8 and its linear regression equation was found to be $\frac{1}{v_0} = 5.960 \left(\frac{1}{[C_{UOx}]} \right) + 15.52$ having

correlation coefficient of 0.995. Data of kinetic constants for the Lineweaver-Burk plot of POD by the proposed method are the following: Michealis-Menten constant (K_m) is 102.90×10^{-6} M, and maximum velocity (V_{max}) is $0.0322 \times 10^{-6} \text{ M}^{-1} \text{ min}^{-1}$, the catalytic constant (K_{cat}) is 6.80 min^{-1} and the specificity constant $\left[\frac{K_{cat}}{K_m}\right]$ is $0.0660 \times 10^6 \text{ M}^{-1} \text{ min}^{-1}$. The catalytic efficiency and catalytic power at 4.73 nM POD concentration were found to be $0.066 \times 10^6 \text{ M}^{-1} \text{ min}^{-1}$ and $3.12 \times 10^{-4} \text{ min}^{-1}$, respectively.

The Michaelis-Menten constant for the UA substrate using UOx by the proposed method was found to be $K_m = 0.384 \text{ mM}$ and $V_{max} = 0.0644 \text{ (mM)} \text{ min}^{-1}$. Lower K_m value of 3-HT system indicates that there is more interaction between active sites of substrate and cosubstrate (3-HT) with the binding site of UOx/POD system. The catalytic efficiency and catalytic power of the proposed method are $K_{eff} = 1.864 \text{ (mM)}^{-1} \text{ EU min}^{-1}$ and $K_{pot} = 0.1677 \text{ min}^{-1}$. The catalytic constant (K_{cat}) and specificity constant $\left[\frac{K_{cat}}{K_m}\right]$ at saturated concentration of the co-substrates were $0.715 \text{ (mM)} \text{ min}^{-1} \text{ (EU)}^{-1}$ and $1.8619 \text{ (EU)}^{-1} \text{ min}^{-1}$ by the proposed assay.

4.3 | DFT based computational investigation

4.3.1 | UV-Vis spectrum: a theoretical description for practical data

Quantum mechanical calculations were carried out to study the electronic properties of the final quinone product. The TD-DFT calculations were performed using the B3LYP/6-311++G(d,p) basis set for five low-lying excited states in investigating the UV-Vis absorption spectra of the quinone product. The theoretical results involving the excitation energies, oscillator strengths, and wavelength, were worked out and compared with the experimental wavelengths. The electronic absorption spectrum was found at 500 nm, the quantum mechanical calculation performed predicted bands at 482.66, 434.30, and 259.36 nm with corresponding oscillatory strengths of 0.0031, 0.0307, and 0.1774. The absorption maximums at 434.30 and 259.36 nm to two different $n \rightarrow \pi^*$ and $\pi \rightarrow \pi^*$ transitions, respectively. The presence of citric acid buffer stabilizes the excited LUMO state due to the hydrogen bonding to an extent of 0.3720 eV. The theoretical absorption spectrum for the quinone product is as shown in Figure 2. Table S1 summarizes the calculated and experimental absorption maximum.

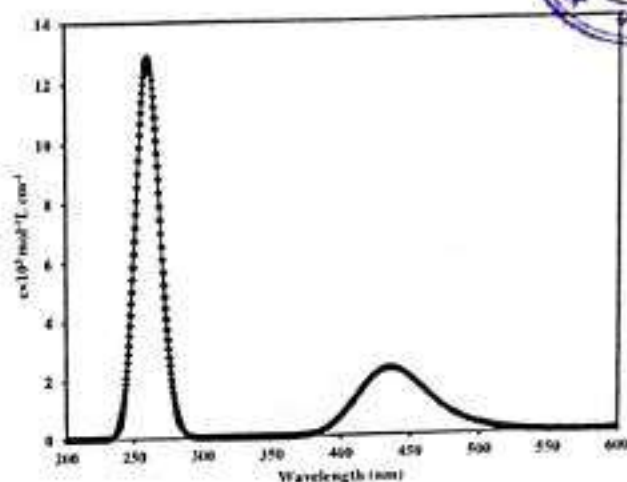


FIGURE 2 Simulated absorption spectra of the final quinone product in aqueous phase.

TABLE 4 Quantum mechanical parameters of 3-HT and final product.

	3-HT	Final quinone product
HOMO (eV) (E_h)	-6.043	-6.978
LUMO (eV) (E_l)	-0.447	-3.874
$\Delta E = E_l - E_h$	5.596	3.104
Ionization energy (I)	0.2203	0.258
Electron affinity (A)	0.027	0.145
Electronegativity (μ)	-0.12365	-0.2015
global hardness (η)	0.1933	0.113
global softness (S)	5.173	8.849
Electrophilicity (ω)	0.0395	0.1796

Furthermore, the ionization energy, electron affinity, electronegativity, global hardness/softness, and electrophilicity calculated for both the 3-HT and final quinone product are provided in Table 4. The molecular electrostatic potential on various atoms displaying red and blue gradient patterns are indicated in Figure 3. Dual descriptor values, $\Delta f(r)$ values, that is, the difference between the electron density on the LUMO and that on the HOMO, used to study the electron density pattern on the atoms associated with the molecule. It was observed from the worked out calculations that $\Delta f(r) < 0$ for O₁₁, O₁₀, N₉, C₆, C₅, C₃, C₂ indicating the electron rich positions. The relative electron density gradient pattern and amplitude has been evaluated Table S2. The red position and blue on the surface gradient pattern indicate the higher and less electron denser positions, indicating the phenolic oxygen is more prone to reduction compared to N₉ of 3-HT.

4.3.2 | The principle of the colorimetric sensor for UA sensing system

It is a well known enzymatic reaction that in the first step of the Scheme 1, the enzyme UOx catalyzes the oxidation of UA in presence of dissolved oxygen and water to produce allantoin, CO_2 , along with the formation of H_2O_2 .^[50] Later, the generated H_2O_2 in situ reacts with POD, which is acting as an oxidizing agent for the oxidation of dopamine or 3-IT in the oxidative coupling of peroxide. In the experimental condition, 3-IT loses one electron and one proton upon enzymatic oxidation at the active sites of *o*-position to the hydroxyl group of 3-IT. This results in the formation of an orange colored quinone form of chromophore having maximum absorption peak in the red region at 500 nm.^[51,52]

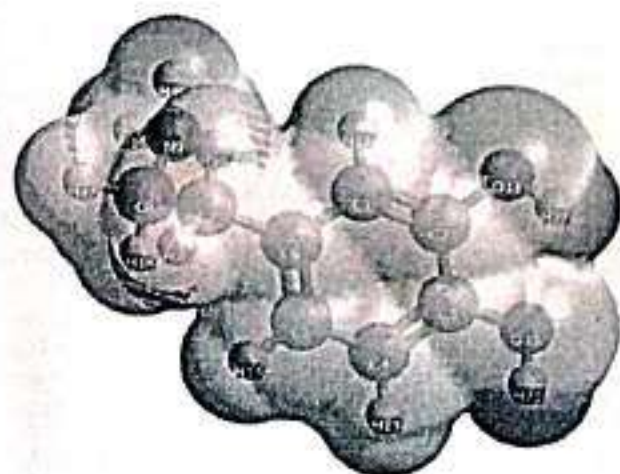
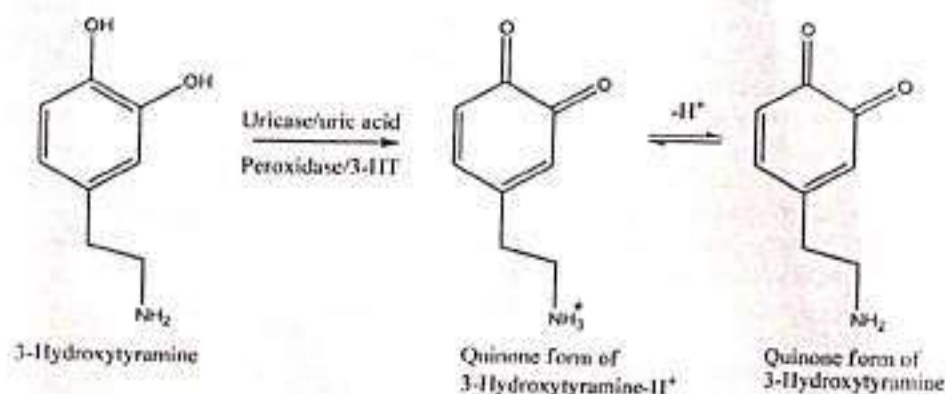


FIGURE 3 Molecular electrostatic potential on various atomic groups of 3-IT. Relative electron density on various one to one position atoms are shown in red and blue color referring to high and low denser positions.



SCHEME 1 Proposed biochemical reaction pathway for the formation of orange-colored product of quinone form of 3-IT involving POD, UOx, in the presence of UA.

Further, to gain insight into the biochemical reaction mechanism, we attempted to study the bi-enzymatic reaction system with DFT-based quantum chemical calculations. From the results of DFT studies, it is observed that the chemical molecule formed is the quinone form of 3-IT, which is an orange-colored product involving POD and UOx in the presence of UA. The final product is formed via the reactive cation intermediate, which is in equilibrium.

The merits and demerits of some of the various analytical methods of techniques in comparison with the reported method have been discussed as shown in Table S3. By considering these facts, it is observed that the present method is the most suitable for the analysis of serum UA. Further, from the linearity range of the proposed UA assay, it is found to be consistent from day to day, owing to not only the excellent stability of the reagents but also the resulting coloring product. The low values of CV signify the high accuracy and reproducible measurement of the UA with a lesser error percentage. The lower values for limit of detection and limit of quantification for UA show that the developed method is highly sensitive.

4.3.3 | Application of UA assay to human serum samples

To determine the efficacy of the naked eye sensing enzymatic system, it has been tested in the physiological near pH condition using real human serum samples. The recovery data has been shown in Table 3. It is observed that the sensing method shows a high accuracy range attributing to minimum interference from the foreign species present in the real sample system. To gain the superior functionality of the sensing method, it is compared with the standard kit method. From the results obtained, it can be seen that it is well correlated with the



standard kit method, having a value of 0.998 for the regression coefficient equation, suggesting that the present method is in good agreement with the standard reported method. Further, to ascertain its selective and specific interaction with the UA, kinetic studies have been performed. The results show that the enzymatic reaction system is highly selective and specific for the substrate with a high catalytic rate.

5 | CONCLUSIONS

In summary, the present work possesses multiple advantages when compared to the existing colorimetric sensors discussed. The method is simple, rapid with the naked eye detection technique qualitatively and gives excellent recovery results with minimum interferants from the foreign species at a near neutral pH. Moreover, to check the suitability of the assay, it has been executed with most of the commonly associated organic compounds and inorganic elements in the real blood samples. There is no significant interference from most of the commonly present biomolecules or ions in the serum samples, which signifies the sensitivity and selectivity of the method. Interestingly, the assay has been performed in human serum samples directly, without any pre-concentration steps, which is an added advantage to the proposed sensing method. It also depicts its uniqueness in the analytical performance signal when compared to other reported methods, which lack the interference studies in detail with respect to foreign excipients. Furthermore, the accuracy study and the recovery study reveal that the method is highly accurate and highly selective for UA only. The electronic properties investigated by the DFT results depict that there is good agreement for the color formation of the final quinone product from the 3-HT as the co-substrate. This is the first report that utilizes the DFT based quantum mechanical calculations supported by the dual descriptors for the colored product exploration. In addition to this, kinetic studies were conducted to assess the catalytic activity of the substrate and co-substrate with the enzymatic system, suggesting that the 3-HT can have high affinity and high catalytic efficiency. Further, the naked eye detection of UA explains the simplicity of the assay qualitatively. The low cost of the method and its simplified procedure are an added advantage for its implementation in high throughput assays such as micro-titer plate readers for a very large number of sample analyses.

ACKNOWLEDGMENTS

One of the authors, Honnur Krishna would like to thank University of Mysore, Mysore, Karnataka, India (SC/ST

special cell) for financial support for the research work and for providing the research laboratory facilities. Further, HK appreciates the laboratory support rendered by the SSTP College, Sankeshwar. Also the K.R. Hospital, Mysore, Karnataka, India is acknowledged for providing the blood samples. This work is dedicated to late Dr. P. Nagaraja, Professor of Analytical Chemistry, Department of Studies in Chemistry, University of Mysore, Mysore.

ORCID

Honnur Krishna © <https://orcid.org/0000-0001-6963-8860>

REFERENCES

- [1] R. J. Johnson, D.-H. Kang, D. Feig, S. Kivlighn, J. Kanellis, S. Watanabe, K. R. Tuttle, B. Rodriguez-Iturbe, J. Herrera-Acosta, M. Mazzali, *Hypertension* 2003, 41(6), 1183.
- [2] R. J. Johnson, M. A. Lanasa, E. A. Gaucher, *Semin. Nephrol* 2011, 31(5), 394.
- [3] A. Leiba, S. Vinker, D. Dinour, E. J. Holtzman, M. Shani, *J. Am. Soc. Hypertens* 2015, 9(8), 600.
- [4] D.-H. Kang, T. Nakagawa, L. Feng, S. Watanabe, L. Han, M. Mazzali, L. Truong, R. Harris, R. J. Johnson, *J. Am. Soc. Nephrol* 2002, 13(12), 2888.
- [5] S. Guerreiro, A. Ponceau, D. Toulorge, E. Martin, D. Alvarez-Fischer, E. C. Hirsch, P. P. Michel, *J. Neurochem* 2009, 109(4), 1118.
- [6] D. J. Schretlen, A. B. Inscore, H. Jinnah, V. Rao, B. Gordon, G. D. Pearson, *Neuropsychology* 2007, 21(1), 136.
- [7] D. Schretlen, A. Inscore, T. Vannorsdall, M. Kraut, G. Pearson, B. Gordon, H. Jinnah, *Neurology* 2007, 69(14), 1418.
- [8] G. Seghieri, D. Moruzzo, S. Fascetti, C. Bambini, R. Anichini, A. de Bellis, L. Alvisi, F. Francini, *Diabetes Care* 2002, 25(5), 1095.
- [9] A. M. Strasak, C. C. Kelleher, L. J. Brant, K. Rapp, E. Ruttman, H. Concini, G. Diem, K. P. Pfeiffer, H. Ulmer, Vhm, P.S. Group, *Int. J. Cardiol* 2008, 125(2), 212.
- [10] C. J. Weir, S. W. Muir, M. R. Walters, K. R. Lees, *Stroke* 2003, 34(8), 1951.
- [11] B. N. Ames, R. Cathcart, E. Schwiers, P. Hochstein, *Proc. Natl. Acad. Sci* 1981, 78(11), 6858.
- [12] B. Becker, N. Reinholz, B. Leipert, P. Ruschke, B. Fermanetter, E. Gerlach, *Chest* 1991, 100(3), 176 S.
- [13] N. Kuzkaya, N. Weissmann, D. G. Harrison, S. Dikalov, *Biochem. Pharmacol* 2005, 70(3), 343.
- [14] S. Jain, S. Verma, S. P. Singh, S. N. Sharma, *Biosens. Bioelectron* 2019, 127, 135.
- [15] M. Shahbakhsh, H. Saravani, Z. Hashemzadei, S. Narouie, *Microchim. Acta* 2020, 187(7), 411.
- [16] G. Chen, Q. Chu, L. Zhang, J. Ye, *Anal. Chim. Acta* 2002, 457(2), 225.
- [17] R. Sha, N. Vishnu, S. Badhulika, *Sensors Actuators B Chem* 2019, 279, 53.
- [18] L.-J. Han, Y.-J. Kong, X.-M. Zhang, G.-Z. Hou, H.-C. Chen, H.-G. Zheng, *J. Mater. Chem. C* 2021, 9(18), 6051.
- [19] M. Saqib, L. Qi, P. Hui, A. Nsabimana, M. I. Halawa, W. Zhang, G. Xu, *Biosens. Bioelectron* 2018, 99, 519.

- [20] J. Zhao, *Biomed. Chromatogr.* **2015**, *29*(3), 410.
- [21] K. M. Kim, G. N. Henderson, X. Ouyang, R. F. Frye, Y. Y. Sautin, D. I. Feig, R. J. Johnson, *J. Chromatogr. B* **2009**, *877*(22), 2032.
- [22] Y. He, F. Qi, X. Niu, W. Zhang, X. Zhang, J. Pan, *Anal. Chim. Acta* **2018**, *1027*, 113.
- [23] F. Farshchi, A. Saadatf, M. Hasanzadeh, F. Seidi, *RSC Adv.* **2021**, *11*(44), 27298.
- [24] Y. Hasebe, K. Nawa, S. Ujita, S. Uchiyama, *Analyst* **1998**, *123*, 1775.
- [25] P. Fossati, L. Prencipe, G. Berti, *Clin. Chem.* **1980**, *26*(2), 227.
- [26] R. C. Trivedi, L. Rebar, E. Berta, L. Stong, *Clin. Chem.* **1978**, *24*(11), 1908.
- [27] P. Kabasakalian, S. Kalliney, A. Westcott, *Clin. Chem.* **1973**, *19*(5), 522.
- [28] Y. Kayamori, Y. Katayama, T. Matsuyama, T. Urata, *Clin. Biochem.* **1997**, *30*(8), 595.
- [29] L. Sun, H. Shen, L. Zheng, P. Gao, Z. Xiang, *J. Electron. Mater.* **2021**, *50*(7), 3907.
- [30] L. G. Morin, *Clin. Chem.* **1974**, *20*(1), 51.
- [31] P. Zhang, X. Wu, H. Xue, Y. Wang, X. Luo, L. Wang, *Anal. Chim. Acta* **2022**, *1212*, 339911.
- [32] F. Li, T. He, S. Wu, Z. Peng, P. Qiu, X. Tang, *Microchem. J.* **2021**, *164*, 105987.
- [33] Q. Huang, W. J. Weber, *Environ. Sci. Technol.* **2005**, *39*(16), 6029.
- [34] K. Phaugat, M. Bhambi, C. S. P. Renu, *J. Mol. Catal. B Enzym.* **2010**, *62*(1), 27.
- [35] M.J. Frisch, G.W. Trucks, H.B. Schlegel, G.E. Scuseria, M.A. Robb, J.R. Cheeseman, G. Scalmani, V. Barone, G.A. Petersson, H. Nakatsuji, X. Li, M. Caricato, A.V. Marenich, J. Bloino, B.G. Janesko, R. Gomperts, B. Mennucci, H.P. Hratchian, J.V. Ortiz, A.P. Izmaylov, J.L. Sonnenberg, Williams, F. Ding, F. Lipparini, F. Egidi, J. Goings, B. Peng, A. Petrone, T. Henderson, D. Ranasinghe, V.G. Zakrzewski, J. Gao, N. Rega, G. Zheng, W. Liang, M. Hada, M. Ehara, K. Toyota, R. Fukuda, J. Hasegawa, M. Ishida, T. Nakajima, Y. Honda, O. Kitao, H. Nakai, T. Vreven, K. Throssell, J.A. Montgomery Jr., J.E. Peralta, F. Ogliaro, M.J. Bearpark, J.J. Heyd, E.N. Brothers, K.N. Kudin, V.N. Staroverov, T.A. Keith, R. Kobayashi, J. Normand, K. Raghavachari, A.P. Rendell, J.C. Burant, S.S. Iyengar, J. Tomasi, M. Cossi, J.M. Millam, M. Klene, C. Adamo, R. Cammi, J.W. Ochterski, R.L. Martin, K. Morokuma, O. Farkas, J.B. Foresman, D.J. Fox, *Gaussian 16 Rev. C.01*, Wallingford, CT, **2016**.
- [36] M. D. Hanwell, D. E. Curtis, D. C. Lonie, T. Vandermeersch, E. Zurek, G. R. Hutchison, *J. Cheminf.* **2012**, *4*(1), 17.
- [37] N. M. O'boyle, A. L. Tenderholt, K. M. Langner, *J. Comput. Chem.* **2008**, *29*(5), 839.
- [38] J. Sánchez-Márquez, D. Zorrilla, A. Sánchez-Coronilla, D. M. de los Santos, J. Navas, C. Fernández-Lorenzo, R. Alcántara, J. Martín-Calleja, *J. Mol. Model.* **2014**, *20*(11), 1.
- [39] R. G. Parr, R. A. Donnelly, M. Levy, W. E. Palke, *J. Chem. Phys.* **1978**, *68*(8), 3801.
- [40] P. W. Ayers, R. G. Parr, R. G. Pearson, *J. Chem. Phys.* **2006**, *124*(19), 194107.
- [41] R. G. Parr, R. G. Pearson, *J. Am. Chem. Soc.* **1983**, *105*(26), 7512.
- [42] W. Kohn, L. J. Sham, *Phys. Rev.* **1965**, *140*(4A), A1133.
- [43] A. J. Cohen, P. Mori-Sánchez, W. Yang, *Phys. Rev. B* **2008**, *77*(11), 115123.
- [44] C. Morell, A. Grand, A. Toro-Labbé, *Chem. Phys. Lett.* **2006**, *425*(4), 342.
- [45] R. Eisenthal, M. J. Danson, D. W. Hough, *Trends Biotechnol.* **2007**, *25*(6), 247.
- [46] M. Harel, D. M. Quinn, H. K. Nair, I. Silman, J. L. Sussman, *J. Am. Chem. Soc.* **1996**, *118*(10), 2340.
- [47] B. Ma, S. Kumar, C.-J. Tsai, Z. Hu, R. Nussinov, *J. Theor. Biol.* **2000**, *203*(4), 383.
- [48] I. Taverniers, M. De Loose, E. Van Bockstaele, *TrAC Trends Anal. Chem.* **2004**, *23*(8), 535.
- [49] H. Lineweaver, D. Burk, *J. Am. Chem. Soc.* **1934**, *56*(3), 658.
- [50] N. Modrić, A. E. Derome, S. J. H. Ashcroft, M. Poje, *Tetrahedron Lett.* **1992**, *33*(44), 6691.
- [51] A. Napolitano, O. Crescenzi, A. Pezzella, G. Prota, *J. Med. Chem.* **1995**, *38*(6), 917.
- [52] B. S. Karon, T. M. Daly, M. G. Scott, *Clin. Chem.* **1998**, *44*(1), 155.

AUTHOR BIOGRAPHIES



Honnur Krishna received his PhD degree in enzyme assays from University of Mysore, Mysore in 2014. He is currently working as an Assistant Professor of Chemistry, in SDVS Sangh's, S. S. Arts College and T. P. Science Institute, Sankeshwar affiliated to Ram

Channamma University, Belagavi, India. His research focuses on analytical method development and its validation for the clinically important biomarkers and environmental analytes. He is also interested in DFT studies for prediction of chemical reactions insight through computational chemical approach; nano technological applications and its sensing applications.



Avinash Krishnegowda earned his PhD from University of Mysore, Mysore in 2013. He is currently working as an Assistant Professor of Chemistry, Department of Chemistry, ATME College of Engineering, Mysore - 570 028, India. His research

interest includes analytical chemistry and nanotechnology for sensing applications.



Shivakumar Anantharaman, earned his Ph.D. from the University of Mysore in 2011. For three years, he served as an Assistant Professor at the Regional Institute of Education in Mysore. He joined the PG department of chemistry, St. Philomena's College in 2013 as an



assistant professor and has since been promoted to associate professor. His areas of interest in research include computational chemistry, nanozymes, and analytical chemistry and biochemistry.



Kumar Shrestha Ashwinee earned his PhD from University of Mysore, Mysore in 2013. He is currently working as an Assistant Professor of Pharmacy, Department of Pharmacy, Kathmandu University, Kathmandu, Nepal. His research interest includes analytical chemistry and pharmacokinetic studies.



A Edalli Vijayalakshmi received her PhD degree in Biodegradation and bio-remediations using enzymes, from Karnatak University, Dharwad. She is currently works as an Assistant Professor of Chemistry, in SDVS Sangh's, S. S. Arts College and T. P.

Science Institute, at Sankeshwar affiliated to Channamma University, Belagavi, India. Her research focuses on environmental bio-remediation studies and method development based on enzyme assays. She is also interested in nano technological and its sensing applications.

SUPPORTING INFORMATION

Additional supporting information can be found online in the Supporting Information section at the end of this article.

How to cite this article: H. Krishna, A. Krishnegowda, S. Anantharaman, K. S. Ashwinee, A. E. Vijayalakshmi, *J. Chin. Chem. Soc.* **2023**, *1*. <https://doi.org/10.1002/jccs.202200513>



Electrostatic potential mapping of ascorbic acid and dimethoxyaniline for the antioxidant evaluation capacity

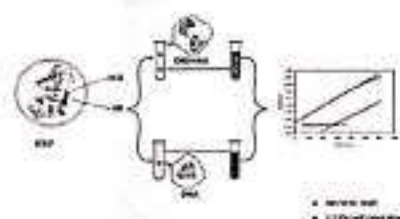
 Shivakumar Anantharaman¹  · Honnur Krishna² · Rajesh Biligere Muddegowda³

 Received: 9 July 2022 / Accepted: 26 May 2023
 © Springer-Verlag GmbH Austria, part of Springer Nature 2023

Abstract

We have here presented an extended theoretical and experimental study of hydroxyl radical (HR) trapping assay by ascorbic acid (AA), 2,4-Dimethoxyaniline (DMA) in the presence of hydrogen peroxide and horseradish peroxidase (HRP) produces an imine form of 2,4-DMA (DMA*), a violet colored product with an UV-Vis absorption maximum at 540 nm. The formation of the violet colored product was inhibited by the addition of AA. Fukui functions and dual descriptor enumerating the local and global electron densities of the atoms on the DMA, AA, and HR systems were calculated. The preferential electron density pattern on DMA, AA, and HR was assessed by left and right Fukui functionals at constant external potential. Highest occupied molecular orbital–lowest unoccupied molecular orbital (HOMO–LUMO) gap for DMA and AA were found to be 8.834 and 10.908 eV, respectively, and singly occupied molecular orbital–highest occupied molecular orbital (SOMO–HOMO) gap for HR was 16.872 eV. The global softness for DMA, HR, and AA was 12.99, 6.10, and 11.70, respectively. The electronic transitions (n to π^* and π to π^*) of the proposed colored product were simulated by time dependent-density functional theory (TD-DFT) calculation with its correlation with the practical UV-Vis data. Natural bond order analysis (NBO) and electrostatic potential (ESP) providing theoretical information on the relative electron density over the atomic position of AA and DMA were presented. This article can provide a unique way of understanding the position of HR radical attack on AA and DMA.

Graphical abstract



Keywords Density functional theory · Colorimetric inhibition assay · Hydroxyl radical antioxidant capacity assay · HOMO · SOMO–LUMO · UV-Vis simulation · Isosurface · Fukui functions

✉ Shivakumar Anantharaman
shivakem77@gmail.com

✉ Honnur Krishna
krishnachem08@gmail.com

¹ PG Studies and Research Centre in Chemistry (A Recognized Research Centre of University of Mysore), St. Philomena's College, Bangalore-Mysore Road, Bannimantap, Mysore 570015, India

² Department of Chemistry, S. D. V. S. Sangh's, S. S. Arts College and T. P. Science Institute, Sankeshwar, Belagavi 591313, Karnataka, India

³ Department of Physics, RV College of Engineering, Bengaluru 560059, Karnataka, India

Introduction

Free radicals are highly unstable species having an unpaired electron in the outermost shell, seeking stability through pairing with biological systems [1]. One of the contributions for its instability is lack of octet configuration. Reactive oxygen and reactive nitrogen species have characteristic properties such as short life time, generation of intermediate reactive species that in turn kill the immediate cell adjacent to its generation [2]. Hence, the instability of these species is a serious threat to the nearby cells which are implied in aging and more than 100 diseases that includes heart disease, diabetes, cancer, and neurodegenerative diseases. The main cause of these diseases are attributed to the damaging of crucial biomolecules such as DNA, RNA, lipids, proteins, polyunsaturated fatty acids, carbohydrates, and so on [3].

Antioxidants can be classified as primary, secondary, endogenous, exogenous, enzymatic, and non-enzymatic. Generally antioxidants are the molecules that contain hydroxyl groups which might be phenolic or non-phenolic in nature that includes ascorbic acid (AA), tocopherols, polyphenols, flavonoids, and so on [4].

AA has been widely studied due to its biological importance, which is a well-known radical scavenger and an antioxidant in the living systems. Apart from usual activity as a reducing agent of free radical species, it can also act as a cofactor in the enzymatic biosynthesis of collagen, catecholamine, carnitine, and peptide neurohormones [5]. Under *in vitro* electrochemical oxidation, AA normally loses one electron, but two electron oxidation can also be observed. AA is also involved in the oxidation of low density lipoprotein and is used as biochemical marker of oxidative stress in clinical investigations [6]. Due to their numerous health advantages, including anti-aging and anti-inflammatory properties, AA have emerged as scientifically intriguing substances. Dehydroascorbic acid has been used as a biochemical marker of oxidative stress in clinical investigations and also vitamin C is used as a dietary supplement. Hence, assay of AA plays a pivotal role in the food technology, health sector, microbiology and such others [7].

An antioxidant assay are characterized by two different terms namely, antioxidant activity and antioxidant capacity. First, the antioxidant activity corresponds to the rate constant trapping of single antioxidant against the given free radical. Second term is the antioxidant capacity that corresponds to the total molar concentration of the free radicals that scavenges against the test sample which is dependent on the presence of variety of antioxidants in the mixture [8]. An assay can include direct and indirect methodology, direct method relies on its tendency of the free

radical to reduce or oxidize the reaction probe and indirect method adopts the inhibitory capacity of the antioxidants for the formation of the products.

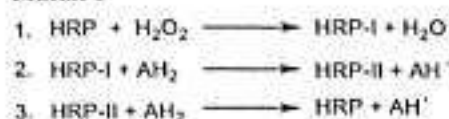
Based on the nature of the mechanism, it can be broadly classified into electron transfer (ET) and hydrogen atom transfer (HAT) reactions. Different types of antioxidant assay include online extraction of high-performance liquid chromatography—ferric reducing antioxidant parameter [9], copper reducing antioxidant capacity—thin layer chromatography [10], 2,2'-azinobis (3-ethylbenzothiazoline-6-sulfonic acid) by advanced statistical methods [11], 2,2-diphenyl-1-picrylhydrazyl [12], fluorescence—cetric reducing antioxidant capacity [13], crocin bleaching assay [14], luminol enhanced chemiluminescence-flow injection analysis [15], β -phycoerythrin-fluorescence system [16], lipid peroxide generation [17], hydroxyl radical averting capacity [18], oxygen radical absorbance capacity assays [19], total radical antioxidant parameter [20], Folin-Ciocalteu reagent assays [21], Trolox equivalent antioxidant capacity assays [22], and such others. In general AA, an antioxidant substance can reduce the metal or organic system either by ET or HAT mechanism, providing the signal response either by positively or negatively in the graphical representation.

The proposed antioxidant assay relies on the formation of oxidized colored product of dimethoxyaniline (DMA) by horseradish peroxidase (HRP) involving hydrogen peroxide as a substrate, which is inhibited by AA. HRP are heme proteins that contain iron(II) protoporphyrin (ferriprotoporphyrin) as prosthetic group with molecular weight ranging between 30 and 150 kDa. HRP can react with reactive oxygen species like superoxide radical and its protonated form, hydrogen peroxide, and hydroxyl radical (HR) [20, 21]. In the absence of the reducing substrates like phenols, amines, the HRP during the cycle releases protonated superoxide and other reactive oxygen species [23–25].

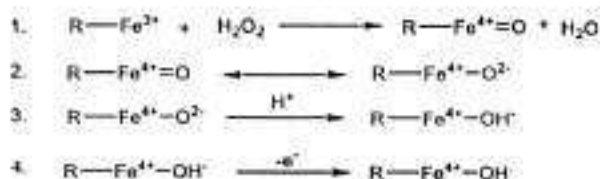
HRP catalyzes the oxidation of wide variety of substrates using hydrogen peroxide or other peroxides as a primary substrates [26]. The HRP catalytic cycle involves the formation of two distinct intermediates namely HRP-I and HRP-II on its reaction with hydrogen peroxide and organic co-substrate. In the initial stage, the native ferric enzyme is oxidized by hydrogen peroxide form an unstable intermediate called HRP-I, which has a heme structure $\text{Fe}^{\text{IV}}=\text{O}$ -porphyrin π -cation radical and consequently reduction of peroxide to water takes place. Then HRP-I oxidizes an electron donor substrate (AH_2) to give HRP-II (protonated form of HRP-I), releasing a free radical. HRP-II gets further reduced by second substrate molecule, generating the ferric state producing free radical, summarized in Scheme 1.

Another mechanism as suggested by Svistunenko et al. [27], the heme group gets oxidized with the formation of oxoferryl heme and free radical located on the π -system of the heme. The radical is then transferred to an amino acid

Scheme 1



Scheme 2



counter part of the enzyme which further undergoes transformation resulting in the formation of HR (Scheme 2).

HR system, highly reactive oxygen species due to its short of octet configuration, tries to attain the stability by abstracting hydrogen atom from either AA or 2,4-dimethoxyaniline (DMA). Thus, AA and DMA act as an HRP radical scavenger.

There are three possible plausible routes by which the amine DMA interacts with HR to produce DMA[•]. A violet color product (step I) then yields the final dimeric product (step II) (Scheme 3). The principle utilized in the AA assay is graphically depicted in Fig. 1. The relatively more reducing property of AA compared to DMA emphasizes the decrease in intensity of violet color product, which asserts

the induction period of the reaction in the presence of AA (Fig. 1).

- (a) Step I
- (b) HR abstracts an electron from DMA to form a DMA cationic intermediate. Further, cationic intermediate loses a proton resulting in the formation of imine form of 2,4-DMA (DMA[•]) (Scheme 3a and 3b).
- (c) By proton coupled electron transfer (PCET) mechanism, DMA loses proton and electron in subsequent steps ultimately leading to DMA[•] (Scheme 3c and d).
- (d) HR interacts with DMA and knocks out atomic hydrogen and forms DMA[•] (Scheme 3e).
- (e) Step II

Dimerization takes place by radical cation intermediate and DMA[•] resulting in the radical adduct formation (RAF) product (Scheme 3f, g, and h).

Mechanism shown in Scheme 3 addresses the formation of stable DMA radical and its dimerization.

Our earlier research article [8] claims the number of active sites for hydroxyl group attack has a strong influence on the radical scavenging activity. The DMA has a number of active sites for the attack of HR, released by the reaction of HRP with substrate hydrogen peroxide. This study will give distinct idea about place of attack of the HR on DMA.

AA and DMA are antioxidant substances that have a preferential electron density over the soft oxygen and nitrogen atoms, respectively, where exact reducing positions can be established by density functional theory (DFT). DFT

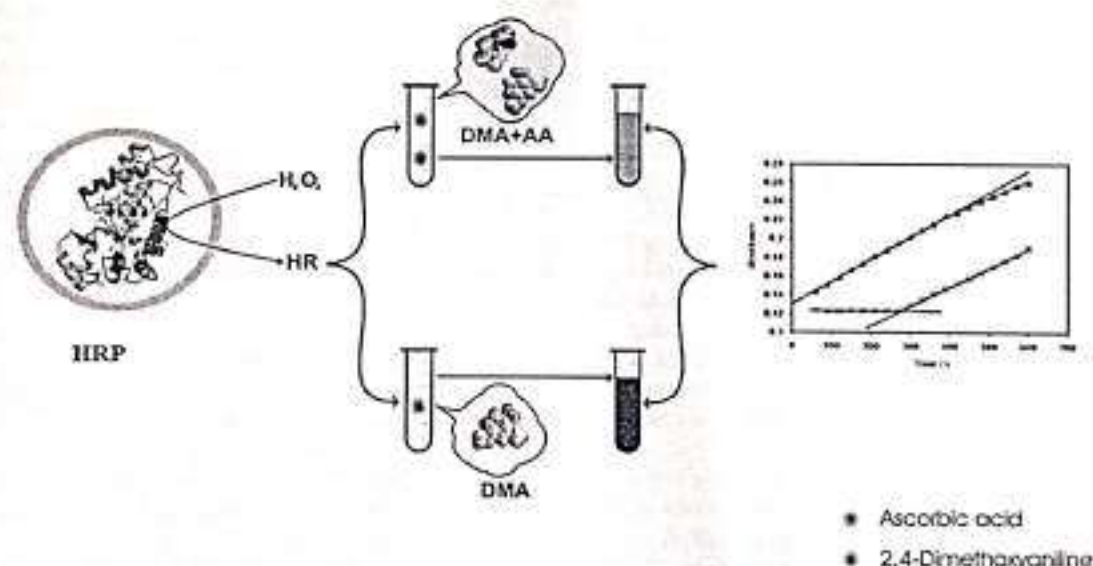
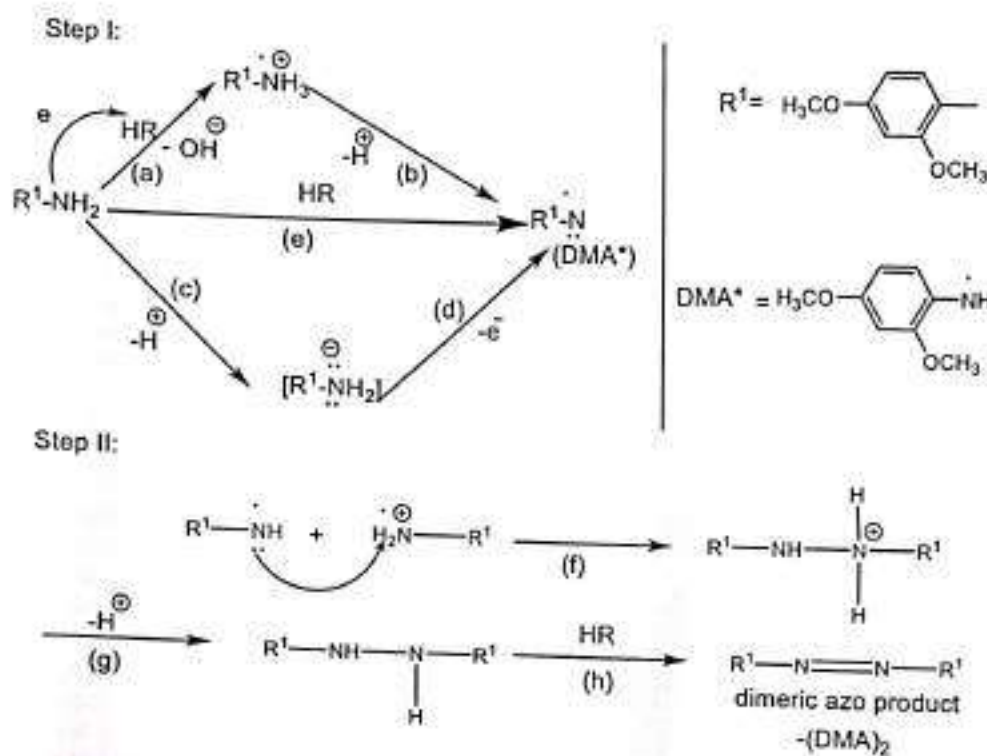


Fig. 1 Principle of the DMA/HRP/AA antioxidant assay



Scheme 3



provides a powerful theoretical framework for the study of both chemical reactivity and selectivity. From the DFT equations, many concepts are widely used by experimental chemists which have both mathematical and physical meaning. Indeed, concepts such as electronic chemical potential, which characterizes the escaping tendency of electrons and global hardness (representing the resistance to charge transfer), have proven to be successful in the rationalization of chemical processes [28].

Several research groups have studied AA by DFT calculations in the vibrational IR band assignment [29], studying the reaction process with HR in aqueous phase [30, 31], discussing the nature of free radical product of its reaction involving HR by frontier orbital approach [32], Mulliken charge distribution, and molecular electrostatic potential in defining the activity of the molecule [33], designing the scheme of mechanism for its reaction with reactive oxygen species [34], nano C_{16} cluster as its carrier [35] and the reaction enthalpies mechanism related to radical scavenging property [36].

This research article gives an idea about the attack of HR on AA and DMA, which is an attempt in studying the abstraction of hydrogen using Fukui function, bond dissociation energy (BDE), and bond dissociation enthalpy (BDH). The HR initiated colored product is inhibited by AA. The theoretical justification of hydrogen abstraction from AA

and DMA is provided. The article is emphasized on the electron density over the AA, and DMA by atomic Fukui functions involving right and left derivatives of electron density with respect to constant chemical potential under frozen molecular conditions. The theoretical spectral simulations were correlated with experimental UV-Vis generated data. This proposed assay is an indirect quantification of AA based on induction period developed by addition of AA for HRP initiated reaction. The present research article involving AA, DMA and HRP is further extension of the research work carried earlier [37] by our group. The research article has two parts, first dealing with the development of analytical assays for antioxidant activity, and second the theoretical path discussions by quantum mechanical studies.

Results and discussion

DMA-HRP-AA assay protocol

Three cm^3 of the reaction mixture containing 2233 μM DMA, 0.756 nM HRP and 82.88 μM H_2O_2 in 100 mM potassium dihydrogen orthophosphate/sodium hydroxide buffer of pH 6.0 was taken. For the evaluation of the linear calibration graph, 100 mm^3 of varying concentrations of AA were considered, so that the final concentration in 3

cm^3 of the solutions ranged between 11.9 and 37.8 μM . The absorbance of the violet colored imine form of 2,4-dimethoxyaniline (DMA*) product was recorded continuously for 600 s at 540 nm with 30 s intervals. The absorbance of the control and test solution was recorded with reference to distilled water. The induction period of test solution containing 37.8 μM of AA, and control without AA recorded by the plot of absorbance vs. time (in s) is shown in Fig. 2. The plot of concentration vs. induction period was used for the evaluation of linearity in the calibration graph as shown in Fig. 3.

Addition of AA to the reaction mixture inhibits the formation of free radical, thus initiating the induction time during course of the reaction. Increase in the time lag with increase in the concentration of AA substantiates the inhibition kinetics.

Optimization of the reaction condition

For establishing the optimized concentration of H_2O_2 in terms of induction period, 3 cm^3 of the reaction mixture containing 2233 μM DMA and 0.756 nM HRP at varying concentrations of AA and H_2O_2 were taken. The H_2O_2 concentrations that were used in the optimization procedure ranged between 20 and 663.04 μM with varying AA concentrations of 45.42, 75.7 and 189.23 μM . From Fig. 1S, it can be seen that the induction period varies linearly between 20 and 82.88 μM , beyond which it gets saturated due to the enzymatic reaction. Hence, a final concentration of 82.88 μM of H_2O_2 was selected for further assay procedure.

As the proposed assay procedure is based on release of HR by HRP, the optimized pH/temperature that was recorded for our earlier work [37] is selected as a reference. The optimized pH that was selected under the optimized

Fig. 2 Evaluation of the induction period for 2233 μM DMA, 0.756 nM HRP, and 82.88 μM H_2O_2 in 100 mM potassium dihydrogen orthophosphate/sodium hydroxide buffer containing 37.8 μM AA in a total 3 cm^3 of the reaction mixture. The control (Δ) and sample (\times) readings were recorded against the distilled water

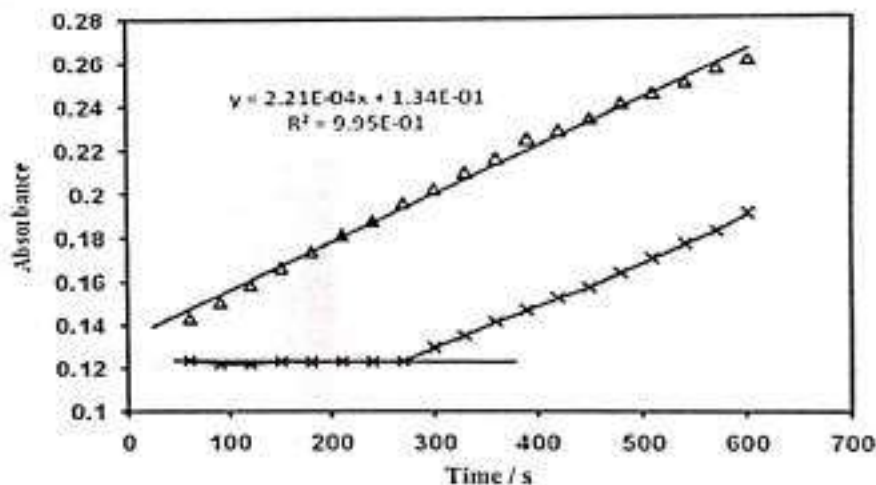
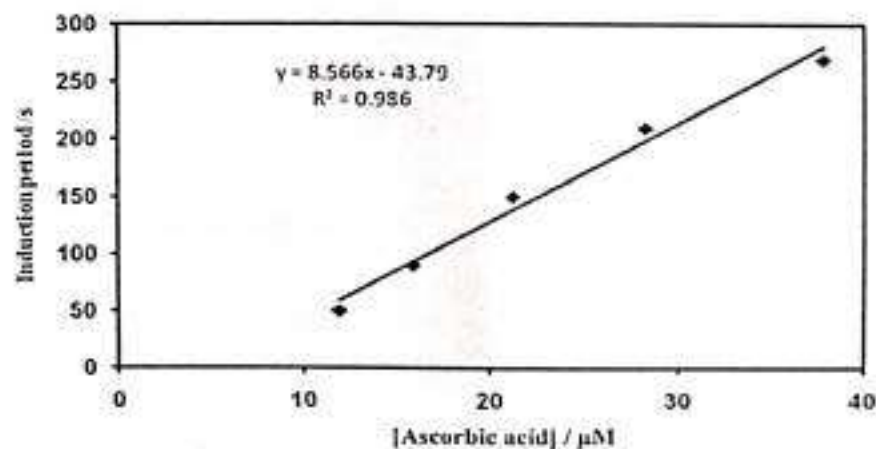


Fig. 3 Calibration graph for determination of AA containing 2233 μM DMA, 0.756 nM HRP and 82.88 μM H_2O_2 in 100 mM potassium dihydrogen orthophosphate / sodium hydroxide buffer of pH 6.0 in a total 3 cm^3 of the reaction mixture containing in the range between 11.9 and 37.8 μM of AA





concentrations of the DMA, HRP, and H_2O_2 is 6.0. The effect of temperature was studied in the range 0–80 °C and it was found that the sensitivity remains stable in the range 20 to 30 °C. Hence, 25 °C is selected during the assay procedure.

Physical fitting models for calibration and optimization

The dependent variables that were selected includes different concentrations of H_2O_2 , AA and the induction period responses for all ten experimental runs are summarized in Table 1. This model was validated, where the significant Z (deviation of a data point from the mean, relative to one standard deviation) at 95% confidence values less than 1.96 were accepted. During the model selection, the best fitted models for the induction period were linear and logarithmic based and the regression value, R^2 closer to 1. The RSD, a measure of the reproducibility of the model having less than 3.0% and the R^2 values close to 1, indicates a good relationship between the experimental data and those of the fitted models. The R^2 values well within the acceptable limit ≥ 0.91 indicate the experimental data fitted well with linear and logarithmic equations. The final equation indicating the actual slope and intercept is shown in Table 1. Positive values represent the effect of concentration on optimization, whereas negative values represent an inverse relationship between the concentration factor and the induction period. The slope of the graph indicates its nature, i.e., change in the induction period with reference concentration. The percentage error associated in the determination of AA lies in the range 0.5 to 1.0.

Spectral characteristics

An intense violet colored product, DMA*, was scanned in the wavelength range from 400 to 800 nm against the control. The absorption spectrum has dual maximum one at 540 nm and another at 600 nm, attributed to π to π^* and n to π^* transitions, respectively [38]. The experimental observation was made at 540 nm due to its high molar absorptivity ($0.718 \text{ mM}^{-1} \text{ cm}^{-1}$) as reported earlier [37]. The control has

negligible absorptions in the entire range. The absorption spectrum of the violet colored product is as shown in Fig. 4.

Reaction mechanism

AA is a good scavenger of superoxide radical anion, hydrogen peroxide, HR and singlet oxygen. Oxidation of AA produces two moles of electron along with quinone analog. But, some researchers claim that single electron change through the formation of uni-radical conjugated by carbonyl group stabilized by resonance [39]. The formation of dehydroascorbic acid is greatly expected as the single electron change involving the specific removal of targeted hydrogen which is kinetically forbidden process [8]. Scheme 4 depicts two different routes (Scheme 4a and b) of formation of dehydroascorbic acid molecule.

AA inhibition mechanism of DMA

HR scavenging assay was measured based on the relative competitive inhibition in the formation of colored product. AA is a strong scavenger of HR with formation constant $K_f = 1.8 \times 10^8 \text{ dm}^3 \text{ mol}^{-1} \text{ s}^{-1}$ [40], compared to DMA due to its high inhibition rate which initiates a time lag in the formation of the colored product. It was observed that there was time lag in the formation of the product which increases as the concentration of AA increased proportionately. The contributing competitive reaction is as shown below (Scheme 5).

According to above competitive reaction described, the following relation can be established [41].

$$\frac{A_0}{A} = 1 + \frac{k_i[\text{AA}]}{k_0[\text{DMA}]} \quad (1)$$

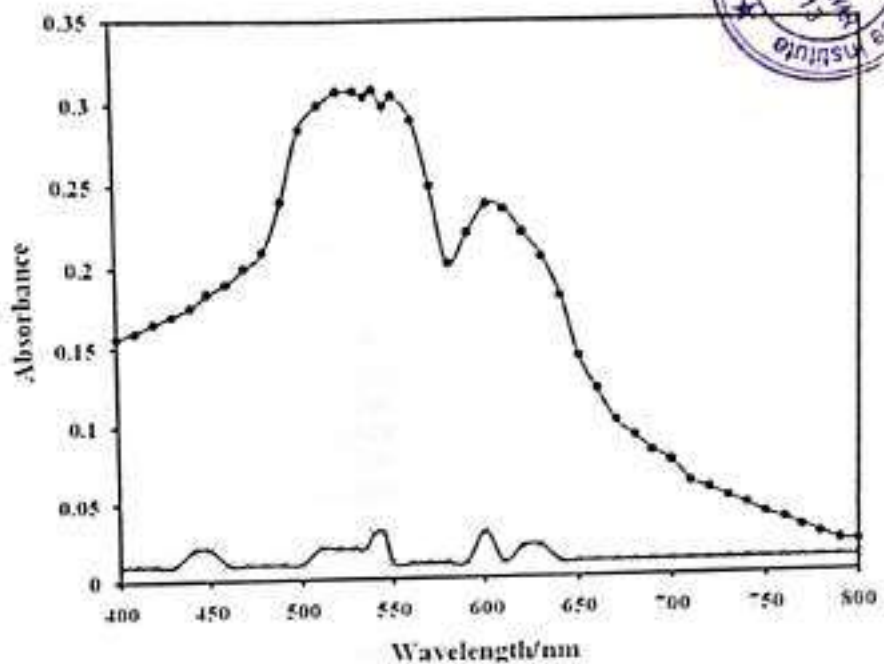
where A_0 and A are the absorbance of corresponding control and samples for fixed concentration of DMA and various concentrations of AA at a constant time, t . k_i and k_0 are AA inhibited and blank rate constant, respectively.

The inhibition kinetics as per the above Eq. (1) is as shown in Fig. 2S. The formation of HR initiated colored product is as shown below (Scheme 6).

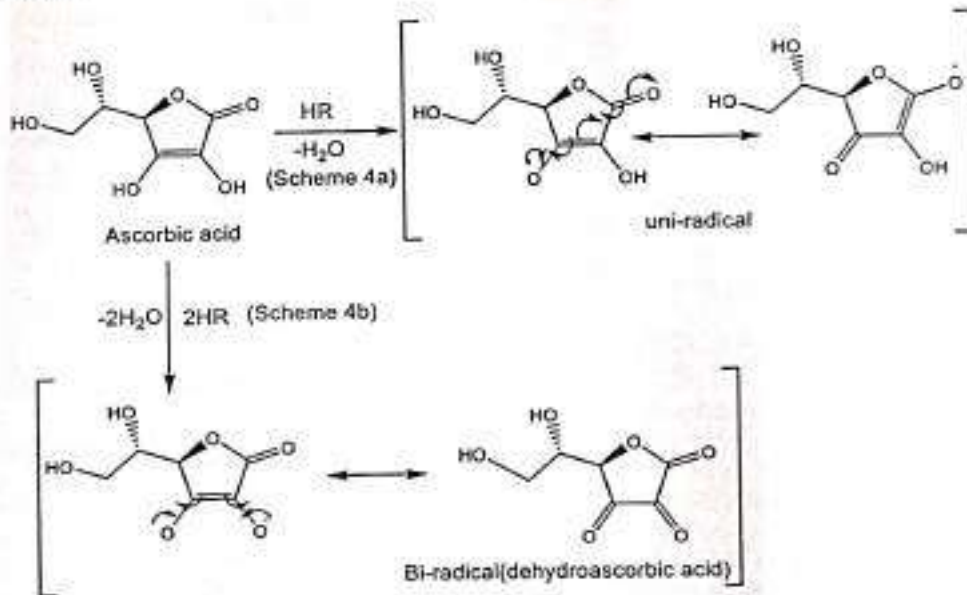
Table 1 Predicted response models and statistical parameters obtained

Figure No	Type of the model	Two dimensional plot	Equation model for y	R^2	CV/%	Error/%
02	Linear	Time versus absorbance	$2.21 \times 10^{-4}x + 1.34 \times 10^{-1}$	0.995	1.0–2.0	–
03	Linear	Induction period versus [AA]	$8.566x - 43.79$	0.986	1.3–2.2	0.5–1.0
Supplementary 1S	Logarithmic	Induction period versus [H_2O_2] during optimization	$-187 \ln x + 1514$ $-132 \ln x + 1005$	0.987 0.976	0.5–1.0	–
Supplementary 2S	Linear	Signal ratio versus [AA]/[DMA]	$-127 \ln x + 871.7$ $27.08x + 1$	0.942 0.919	1.5–3.0	–

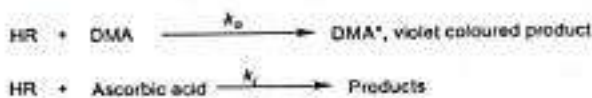
Fig. 4 Absorption spectra of the intense violet colored DMA* were recorded for a 3 cm² of the reaction mixture containing 2263 μM DMA, 0.757 nM HRP, and 330 μM H₂O₂ in a 100 mM potassium dihydrogen orthophosphate/sodium hydroxide buffer of pH 6.0 at 25 °C (•) after incubating for a period of 10 min against the control (×) without H₂O₂



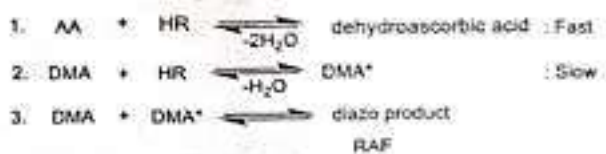
Scheme 4



Scheme 5



Scheme 6



BDE and BDH of AA and DMA

BDE is the energy required to break a bond between two atomic positions of a molecular system with each atom gaining one electron. The enthalpy (H) of the system is equal to the sum of internal energy and product of pressure and volume. The BDE and BDH values are indication of the molecular system reacting by HAT mechanism. The AA acts as an antioxidant which depends upon the removal of hydrogen atom of the hydroxyl group attached to the lactone ring with subsequent formation of dehydroascorbic acid [42]. The removal of hydrogen by HR depends on the BDE and BDH of different hydrogen atoms attached to the AA molecule. The pictorial representations of the AA and DMA along with the local atomic positions are labeled in Fig. 5. The BDE and BDH have been calculated by the below relation:

$$\text{BDE} = E(\text{Dehydroascorbic acid}) + nE(\text{Hydrogen atom}) - E(\text{Ascorbic acid}) \quad (2)$$

$$\text{BDH} = H(\text{Dehydroascorbic acid}) + nH(\text{Hydrogen atom}) - H(\text{Ascorbic acid}) \quad (3)$$

where n refers to the number of hydrogen atom eliminated from the parent molecular system and E represents electronic energy.

The least values of the BDE (Table 2) of AA have been calculated for H_{17} and H_{19} atom, thereby implying easy removal of H_{17} and H_{19} hydrogen atom from AA by HR radical. The calculated BDE is of the increasing order $H_{17} = H_{19}$, H_{20} , H_{13} , $H_{9/10}$, H_{14} , H_{11} . The effective transfer of electron over O_{18} and O_{16} contributes to highest BDE of H_{17} and H_{19} . The HR can attack H_{17} and H_{19} (Fig. 5) which can subsequently result in the formation of dehydroascorbic acid. The formation of dehydroascorbic acid by losing H_{17} and H_{19} in AA is a favourable condition due to the more electron density at the O_{16} and O_{18} , justified by Fukui functions. The ΔH of the AA system follows the sequential decreasing order H_{17} , H_{19} , H_{13} , H_{20} , H_{14} , $H_{9/10}$, H_{11} .

Table 2 BDE and BDH of AA in aqueous environment

Hydrogen atom position	AA (aqueous)/kJ mol ⁻¹			Discrepancy
	Proposed method	Reported method [6]/[44]		
	BDE	BDH	BDH	BDH
17	318	288	316	28
19	318	288	334/326	46/38
20	373	340	336	06
13	417	386	-	-
9/10	425	391	-	-
14	459	427	435	08
11	465	427	430	03

The antioxidant tendency of DMA also depends on the formation of hydroxylated products at different aryl positions, as shown in Fig. 5. The BDE at different position of the potential binding sites was calculated based on the placement of hydroxyl group and oxygen radical on DMA. The BDE and ΔH of DMA have been calculated by the relation,

$$\text{BDE} = E(\text{Oxygenated DMA}) + E(\text{Hydrogen atom}) - E(\text{DMA-OH}) \quad (4)$$

$$\text{BDH} = H(\text{Oxygenated DMA}) + H(\text{Hydrogen atom}) - H(\text{DMA-OH}) \quad (5)$$

for both aqueous and gas condition.

The optimized structures that have been chosen for the study of free radical assay viz., DMA, AA and (DMA)₂ are as shown in Figs. 3S and 5.

The BDE (Table 3) of DMA for gaseous and aqueous system follows an decreasing order $H_{15}/H_{16}/H_{17}$, $H_{11}/H_{12}/H_{13}$, H_{20} , H_{19} , H_{18} and H_{20} , $H_{11}/H_{12}/H_{13}$, $H_{15}/H_{16}/H_{17}$, H_{18} , H_{19} , respectively. The BDH for gaseous and aqueous system follows decreasing order as H_{18} , H_{19} , H_{20} , $H_{15}/H_{16}/H_{17}$, $H_{11}/H_{12}/H_{13}$ and H_{19} , H_{18} , H_{20} , $H_{15}/H_{16}/H_{17}$, $H_{11}/H_{12}/H_{13}$, respectively.

Fig. 5 Optimized molecular structures of AA (left) and DMA (right) in ground states

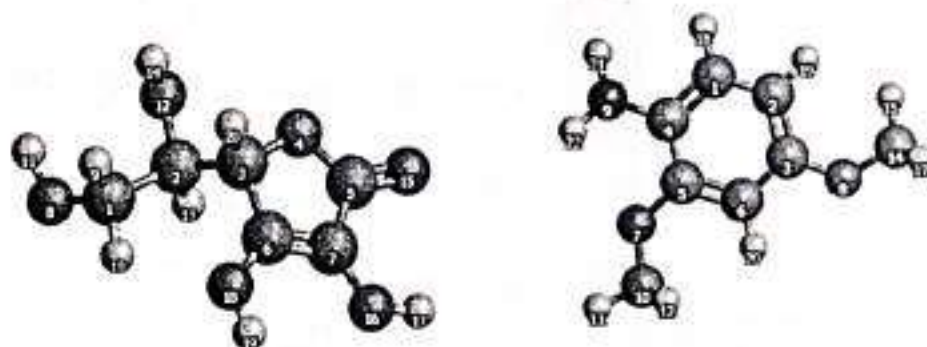


Table 3 BDE and BDH of DMA in gaseous and aqueous environment

Hydrogen atom position	DMA/kJ mol ⁻¹			
	Gaseous		Aqueous	
	BDE	BDH	BDE	BDH
11,12,13	412	378	305	263
15,16,17	428	391	302	266
19	323	295	263	234
18	307	278	273	243
20	333	305	336	306

The structural factors that stabilize the oxygenated DMA and destabilize the hydroxyl DMA reduce BDE. The effective transfer of the electron density from the hydroxyl group to the phenyl ring takes place at a maximum extent in the case of methoxy group (H₁₂/H₁₆/H₁₇) and H₂₀ which contributes to the highest BDE in gaseous and aqueous media, respectively. The reason for the lowest BDE in the gaseous medium for H₁₈ is due to the orbital interaction between the hydroxyl oxygen and amine hydrogens. The orbital interaction stabilizes the resulting radical, hence contributes for less BDE in gaseous medium. The polarizing factors contribute to the highest BDE of H₂₀ and least for H₁₉ in aqueous medium. H₂₀ in the aqueous environment assists the stabilizing of π -electron density, thus leading to increase in the BDE [43].

The BDH is calculated in aqueous phase for the possible radicals of AA structures that lies in the range between 288 and 427 kJ/mol (Table 2). These values as reported by Štellerová et al. [6] lies between 316 and 435 kJ/mol. The homolytic dissociation of hydroxyl groups located on C₁ (H₁₁) and C₂ (H₁₄) is less preferable path due to its high BDH. The discrepancy in the BDH values between proposed method and reported method lies between 3 and 46 kJ/mol. The probable discrepancy is due to the stable AA structure that was selected during the studies which lacks hydrogen bond. The energetically preferred position for the removal of hydrogen in the formation of dehydrogenated AA is H₁₇ and H₁₉.

Similarly, BDH for the formation of hydroxylated DMA product (Table 3) in gaseous and aqueous phase follows an increasing order H₁₈, H₁₉, H₂₀, H_{11/12/13}, H_{15/16/17} and H₁₉, H₁₈, H_{11/12/13}, H_{15/16/17}, H₂₀, respectively. The BDE and BDH of DMA and AA are tabulated in Tables 2 and 3.

Fukui functions and dual descriptors for DMA and HR

AA reacts with HR by a free radical mechanism resulting in dehydroascorbic acid. The quantifiable value in terms of the local softness of an atom can be demonstrated by the Fukui functional value and dual descriptor. The radical descriptors, $f_k^+(r_k^0)$, and dual descriptor $\Delta f(r)$ for hydrogen atom over the DMA and AA allow us to characterize the HR radical attacking position. The decreasing order for AA radical descriptor is H₂₀, H₁₉, H₁₇, H₁₃, H₉, H₁₄, H₁₁, H₁₀ and dual descriptor as H₁₉, H₁₇, H₁₁, H₁₄, H₂₀, H₁₀, H₁₃, H₉. The hydrogens that is susceptible for the attack by HR are H₁₉, H₂₀, H₁₇. The decreasing order of radical descriptor for oxygen atoms over the AA is O₁₅, O₁₈, O₁₆, O₄, O₁₂, O₈. The O₁₈, O₁₆ are more exposed to the HR attack due to the available H₁₉ and H₂₀. Also it is noticed that the more negative dual descriptor over O₁₆ and O₁₈ enumerates the attack of HR.

Similarly, radical descriptor for DMA follows decreasing order as H₁₈, H₂₀, H₁₂, H₁₉, H₂₃, H₂₂, H₁₇, H₁₁, H₁₃, H₁₆, H₁₅ and dual descriptor as H₁₂, H₂₀, H₁₈, H₁₉, H₁₇, H₂₁, H₁₃, H₂₂, H₁₁, H₁₆, H₁₅. The aryl hydrogens such as H₁₈, H₂₀, H₁₉ overrule the formation of the benzene radical as aryl compounds are stable. The electron density over the H₂₁ and H₂₂ more susceptible for homolytic cleavage as $\Delta f(r)$ of N₉ is less than zero.

The summative softness of the AA oxygen (O₁₆ and O₁₈) to that of DMA nitrogen (N₉) is found to be greater, thus inferring better reducing capacity of AA compared to DMA.

The Fukui functions and dual descriptors are marked in the bold form for clear cut identification of the density marker on one to one atom in the molecule (Table 4).

Frontier molecular orbital concept in explanation of hard-soft acid base concept

Frontier orbital energy gap, that is the difference between the HOMO/SOMO and LUMO energies, shows the interaction of the molecule with other species. Frontier orbital energy difference helps to differentiate between the chemical reactivity of the molecules. HOMO or SOMO values are -7.729, -9.722, and -15.393 eV for DMA, AA, and HR, respectively, and corresponding LUMO values are 1.105, 1.186, and 1.479 eV. The corresponding HOMO or SOMO-LUMO differences for DMA, AA, and HR are 8.834, 10.908, and 16.872 eV as tabulated in Table 5. These tabulated values were calculated from the energies (Supplementary information, Fukui functions) of frontier molecular orbitals.

A hard molecule has a large SOMO/HOMO-LUMO gap and a soft molecule has a small SOMO/HOMO-LUMO gap. Among these, HR is hard, AA is intermediate, and DMA is

Table 4 Fukui functions of DMA, AA, HR

Atom by atom position	f_k^0	S_k^0	$\Delta f(0)$
DMA			
C-1	0.0491	0.3030	-0.0391
C-2	0.0498	0.3068	-0.0512
C-3	0.0790	0.4868	-0.0983
C-4	0.1018	0.6272	-0.1628
C-5	0.0420	0.2593	-0.0355
O-7	0.0229	0.1412	0.0096
O-8	0.0174	0.1073	-0.0204
N-9	0.0241	0.1487	-0.0330
C-10	0.0934	0.5755	-0.1708
C-14	0.0019	0.0120	0.0153
H-11	-0.0040	-0.0252	0.0130
H-12	0.0207	0.1280	0.0175
H-13	0.0746	0.4598	0.1275
H-15	0.0203	0.1254	0.0190
H-16	0.0162	0.1001	0.0089
H-17	0.0196	0.1209	0.0115
H-18	0.0462	0.2847	0.0687
H-19	0.0817	0.5034	0.0948
H-20	0.0654	0.4029	0.0724
H-21	0.0757	0.4667	0.1003
H-22	0.0550	0.3389	0.0339
	0.0467	0.2880	0.0186
AA			
C-1	-0.0015	-0.0075	0.0326
C-2	0.0090	0.0451	0.1604
C-3	-0.0372	-0.1857	0.1259
O-4	0.0271	0.1352	-0.5970
C-5	0.1462	0.7284	1.4010
C-6	0.3149	1.5685	0.5400
C-7	0.1157	0.5764	-0.3686
O-8	0.0041	0.0208	-0.7814
H-9	0.0045	0.0227	0.1376
H-10	0.0005	0.0024	0.1739
H-11	0.0012	0.0062	0.4753
O-12	0.0077	0.0386	-0.7839
H-13	0.0066	0.0330	0.1676
H-14	0.0028	0.0144	0.4730
O-15	0.1691	0.8424	-0.7052
O-16	0.0814	0.4058	-0.8701
H-17	0.9097	0.0485	0.4957
O-18	0.0842	0.4197	-0.8036
H-19	0.0113	0.0563	0.5066
H-20	0.0419	0.2090	0.2200
HR			
H-1	0.0527	0.1679	-0.0589
O-2	0.9472	3.0121	0.0589

1. Calculations were performed as per the mathematical section based on FUKUI FUNCTIONS, discussed in supplementary information

2. Fukui function, local softness and dual descriptor refer to the partial derivative of the electron density with reference to the electron number ($N-1, N, N+1$) in a specific molecular system [44] i.e., $\left(\frac{\partial \rho}{\partial N}\right)_{r(1)}$

Table 4 (continued)

Significance of bold refers to the Fukui functions and dual descriptor of the targetted atoms in AA, DMA and HR

Table 5 Quantum mechanical parameters of HR, DMA, and AA

	DMA ^b	HR ^a	AA ^b
SOMO/HOMO (E_e)/eV	-7.729	-15.393	-9.722
LUMO (E_e)/eV	1.105	1.479	1.186
$\Delta E = E_e - E_g$ /eV	8.834	16.872	10.908
Electronegativity μ /eV	-3.312	-7.057	-4.268
Global hardness η /eV	4.417	8.536	5.454
Global softness S /eV ⁻¹	0.226	0.117	0.183
Electrophilicity ζ /eV	1.24	2.91	1.66
$\frac{\sigma^+}{\sigma^-}$	25.02	16.48	20.60
Reactivity toward HR radical	Less reactive	-	Highly reactive

All the calculations are done for the optimized molecular system under aqueous condition

^aOccupied molecular orbital corresponds to SOMO

^bOccupied molecular orbital corresponds to HOMO

$\frac{\sigma^+}{\sigma^-}$ refers to the ratio of propensity to accept and donate electron as per Eq. (8), supplementary information

soft. Hence, DMA will have a tendency to change electron density more easily than that of AA on interacting with HR. Hard reactant, where electron density is hard to change relies on the electrostatic effects. Soft molecules, with a small Frontier molecular orbital gap, will have their electron density more easily polarized than a hard molecule [45]. Hence, DMA is more polarizable than that of HR and AA.

Hard acids prefer to react with hard bases, and soft acids prefer soft bases. Hardness claims HR kinetically reacting faster with AA and slower with DMA [46]. This enumerates the induction period developed during the course of the reaction in the presence of HRP enzyme, which is consistent with the description provided by Gazquez [47]. Figure. 6 illustrates the isosurface pattern of one to one atom of AA and DMA.

Ultraviolet-visible spectral simulation of product

The simulated absorption wavelengths were found to be 214, 232 and 233 nm for DMA; 234, 276, and 383 nm for DMA*; and 215, 300, and 374 nm for its coupled diazo (DMA)₂ product in aqueous phase. The three excited states of all the three species are as tabulated in Table 6. The UV-Vis simulated spectra generated for DMA* and (DMA)₂ by Gausssum are as shown in Fig. 7. The theoretical calculation performed does not consider stabilization of the excited/ground state. The phosphate buffer used in the enzymatic

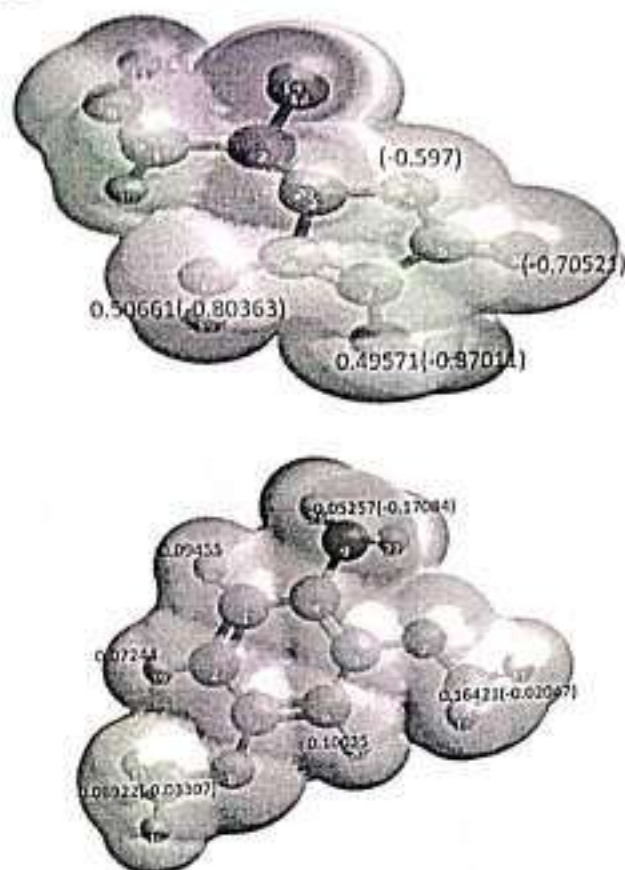


Fig. 6 Molecular isosurface (set at ± 0.0769) on various atomic groups of AA (top) and DMA (bottom). Relative electron density on various one to one position atoms is shown in red (negative isosurface) and blue (positive isosurface) color referring to high and low denser positions for HR attack, respectively. The cumulative Fukui functions of hydrogen and hetero atoms are illustrated with $\Delta f(r)$ values of hetero atoms in the brackets

Table 6 Theoretical absorption wavelengths for three excited states, its oscillator strengths, different forms of DMA

Molecular system	Excited states/nm	Oscillator strength
DMA	215	0.0328
	232	0.0049
	233	0.1578
DMA*	234	0.1374
	276	0.0182
	383	0.0037
	(DMA) ₂	215
	300	1.0013
	374	0.0000

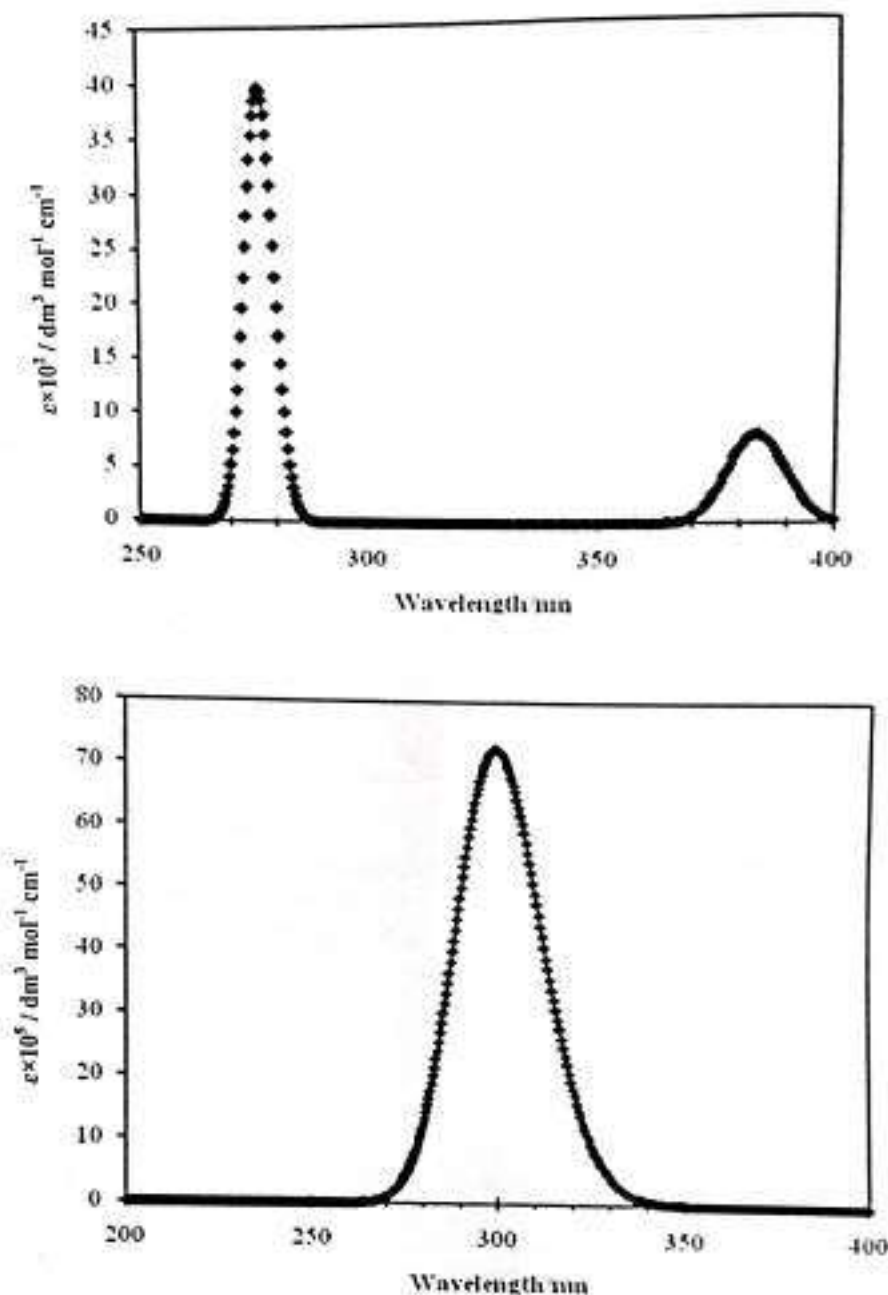
reaction stabilizes the excited state involving bathochromic shift of the absorption maximum. Furthermore, the dual peaks presence in the practically measured absorption maximum confirms the radical nature of DMA* product. Whereas, theoretical absorption maximum of dimeric azo product at 300 nm has no extra sister peak. Hence, the only product during the reaction of DMA with HRP in the presence of H₂O₂ is DMA*.

Conclusion

An antioxidant inhibition assay involving HRP as an HR generator has been proposed involving DMA as an enzymatic co-substrate. The method is based on the inhibition on the formation of the colored product in the presence of AA. The induction period increases with increase in the AA concentration. The linearity of the antioxidant as AA equivalents is found to be in the range between 11.9 and 37.8 μ M, ESP at different positions of the associated atoms are generated by Avogadro visual interface. UV-Vis absorption excitation energies are generated for different possible molecular systems such as DMA* and (DMA)₂ which are further correlated with the experimental absorption maximum and it was found that the DMA* is the only product that is formed during the reaction of DMA with hydrogen peroxide in the presence of HRP. The formation of dehydroascorbic acid was theoretically confirmed by studies involving Fukui function, BDE, and BDH. The isosurface at various atomic positions by intense red color indicates the nucleophilic nature of DMA and AA. The BDE and BDH of AA and DMA evaluated by homolytic breakage at specific local atomic position confirm the formation of expected product as predicted practically. The relative electron density at various positions as quantified by Fukui function gives us the targeted point of attack in AA and DMA. The bridging gap in the inhibitory studies was narrowed by the energy correlation of HOMO-LUMO gap among the HR, DMA, and AA. The molecular ESP and NBO analysis provides the chemistry of DMA and AA for its reducing capacity. Thus, providing a practical data with substantial theoretical proof can enlarge ideas in correlating and expanding our visualization in observation of antioxidant inhibition mechanism. Furthermore, these quantum mechanical calculations in justifying reaction pathways involving AA can enhance our vision in exact point of HR attack.



Fig. 7 Simulated absorption spectra of a DMA⁺ (top) and b (DMA)₂ (bottom) in aqueous phase with gaussian width 3000 cm⁻¹. No intense absorption was observed beyond this mentioned range



Experimental

All the chemicals used in the assay were of analytical grade. DMA, HRP (E.C. 1.11.1.7, 100 units/mg), AA were purchased from Himedia laboratories (Mumbai, India). Double distilled water was used throughout the experiment. DMA (100 mM) was prepared initially by dissolving 0.150 g using 1000 mm³ of alcohol, and finally by water to a total volume of 10 cm³. Freshly prepared 100 mM H₂O₂ was used throughout the experiment. Further dilutions of H₂O₂ were prepared as per the need of the experiment. Two nM of HRP

was dissolved in 10 cm³ of 0.1 M phosphate buffer of pH 6.0.

Computational and software details

Computational simulations were carried out with the Gaussian16 program [48] employing B3LYP-D3(BJ) functional with 6-311++G(d,p) basis set to achieve an optimized geometry (Tables 1S, 2S, 3S, and 4S). The completely filled molecular systems and unpaired molecular systems (such

as radicals, cations, and anions) calculations were carried out by restricted and unrestricted Kohn–Sham formalism, respectively. S^2 error associated with dehydrogenated and oxygenated free radicals of AA and DMA, respectively, lies in the range 0.0 to 0.04% (Table 5S).

The optimization of the geometry was achieved without any geometry constraints. Avogadro [49] and GaussSum [50] were used as visual interfaces. Solvent effects on the optimized structure were investigated with self-consistent reaction field by polarized continuum method using %CRF = (Solvent = Water) DFT keyword (non-symmetric T-matrix model). Each of the structure was stabilized, optimized and checked for any imaginary frequencies and most energetically preferred conformation was selected. Frequency calculations exhibiting zero values correspond to translational and rotational character behavior of the molecules. Theoretical calculations were done on the molecular systems that include electronic energies, IR, and UV–Vis data for visualization. The adiabatic excitation energies were computed using TD-DFT calculations. NBO analysis and ESP calculations were computed for DMA, AA, HR using Pop = NBO and Pop = ESP DFT keyword. Molecular isosurface values were set at ± 0.0769 in the Avogadro software.

The BDE and BDH of different hydrogen atoms attached to DMA were calculated at 298.150 K by electronic energy using the relation $BDE = E(\text{Oxygenated DMA}) + E(\text{Hydrogen atom}) - E(\text{DMA-OH})$ and $BDH = H(\text{Oxygenated DMA}) + H(\text{Hydrogen atom}) - H(\text{DMA-OH})$. $E_{\text{hydrogen}} = -1312.8 \text{ kJ/mol}$ and $H_{\text{hydrogen}} = -1306.12 \text{ kJ/mol}$ [48] are used as the energy and enthalpy of the hydrogen atom. The interaction of HR with DMA has been studied by placing radicals at the potential binding sites of parent structure for geometrically optimized molecules. The antioxidant property of AA was initiated by knocking out hydrogen at different sites which results in the formation of dehydrogenated ascorbic acid.

Ultraviolet–visible absorption spectra of the molecules have been simulated with TD-DFT calculation using B3LYP-D3(BJ) functional and 6–311++G(d,p) basis set.

Calculations of ionization potential (IP), electron affinity (EA), electrophilicity (ξ), global hardness (η), global softness (S), electron change during either oxidation or reduction were carried out as suggested by Ser et al. [51]. IP and EA were evaluated by frozen molecular conditions for cationic and anionic molecular systems.

Fukui function and local softness were evaluated as inferred by Fuentealba research group [52]. Fukui functions were evaluated in the frozen molecular condition by left and right differentiation. The left and right correspond to differentiation of cation and anionic compartment of the DMA and AA. Experimental errors, statistical models [53], left and right derivatives were evaluated by Microsoft excel 2007 program.

Instrumentation

A SYSTRONICS model 2202 PC-based double beam UV–Vis spectrophotometer with 1.0 cm matched cells was used for all absorbance measurements and temperature was controlled using a constant temperature cell holder with a stirrer.

Supplementary Information The online version contains supplementary material available at <https://doi.org/10.1007/s00706-023-03085-0>.

Acknowledgements One of the authors Dr. Anantharaman Shivakumar (A.S.K), thanks St. Philomena's College for providing facilities to carry out this research investigation. Authors also acknowledge the support rendered by Dr. T.S. Shivalingaswamy, PG Department of Physics, Government College (Autonomous), Mandya, Karnataka, India for DFT calculation.

Data Availability All data generated or analysed during this study are included in this published article.

References

- Nagaraja P, Aradhana N, Suma A, Shivakumar A, Chamaraja NA (2014) *Anal Sci* 30:251
- Zorov DB, Juhaszova M, Sollott SJ (2014) *Physiol Rev* 94:909
- Diplock AT, Charuleux J-L, Crozier-Willi G, Kok FJ, Rice-Evans C, Roberfroid M, Stahl W, Viña-Ribes T (1998). *Br J Nutr*. <https://doi.org/10.1079/BJN19980106>
- Cai Y-J, Dai J-Q, Fang J-G, Ma L-P, Hou L-F, Yang L, Liu Z-L (2002) *Can J Physiol Pharmacol* 80:1187
- Wilson IX (2002) *FEBS Lett* 527:5
- Štellerová D, Lukeš V (2021) *Acta Chim Slovaca* 14:32
- Zehiroglu C, Ozturk Sarikaya SB (2019) *J Food Sci Technol* 56:4757
- Shivakumar A, Yogendra Kumar MS (2018) *Crit Rev Anal Chem* 48:214
- Shi S, Guo K, Tong R, Liu Y, Tong C, Peng M (2019) *Food Chem* 288:215
- Akar Z, Burnaz NA (2019) *LWT Food Sci Technol* 112:105212
- Sridhar K, Charles AL (2019) *Food Chem* 275:41
- Yeo J, Shahidi F (2019) *J Agric Food Chem* 67:7526
- Fatih K, Dilek O, Birsan O (2019) *Fresenius Environ Bull* 28:6589
- Spagnol CM, Assis RP, Brunetti IL, Isaac VLB, Salgado RN, Corrêa MA (2019) *Spectrochim Acta Part A Mol Biomol Spectrosc* 219:358
- Chládková G, Kunovská K, Chocholouš P, Poláček M, Sklenářová H (2019) *Anal Methods* 11:2531
- Vuolo MM, Lima VS, Maróstica Junior MR (2019) Phenolic compounds: structure, classification, and antioxidant power. Bioactive compounds. Elsevier, UK, p 33
- Soobrattee MA, Baharon T, Neerghen VS, Googoolye K, Aruoma OI (2008) *Toxicol In Vitro* 22:45
- Marchica A, Lorenzini G, Papini R, Bernardi R, Nali C, Pellegrini E (2019) *Sci Total Environ* 657:568
- Gunawardena H, Silva R, Ranasinghe P (2019) *BMC Res Notes* 12:809
- Villaverde P, Lajous M, MacDonald C-J, Fagherazzi G, Bonnet F, Boutron-Ruault M-C (2019) *Nutr J* 18:31
- Gao M-R, Xu Q-D, He Q, Sun Q, Zeng W-C (2019) *J Food Meas Charact* 13:1349



22. Keskin S, Şirin Y, Çakir HE, Keskin M (2019) *South African J Bot* 120:170
23. Chen S, Schopfer P (1999) *Eur J Biochem* 260:726
24. Regalado C, García-Almendárez BE, Duarte-Vázquez MA (2004) *Phytochem Rev* 3:243
25. Torres E, Bustos-Jaimes I, Le Borgne S (2003) *Appl Catal B Environ* 46:1
26. Shivakumar A, Jashmitha BG, Dhruvaraj MR (2017) *J Clin Nutr Diet* 3:1
27. Svistunenko DA (2005) *Biochim Biophys Acta - Bioenerg* 1707:127
28. Morell C, Grand A, Toro-Labbé A (2005) *J Phys Chem A* 109:205
29. Bichara LC, Landú HE, Nieto CG, Brandán SA (2010) *J Phys Chem A* 114:4997
30. Allen RN, Shukla MK, Reed D, Leszczynski J (2006) *Int J Quantum Chem* 106:2934
31. Singh G, Mohanty BP, Saini GSS (2016) *Spectrochim Acta Part A Mol Biomol Spectrosc* 155:61
32. Yamabe S, Tsuchida N, Yamazaki S, Sakaki S (2015) *Org Biomol Chem* 13:4002
33. Ahmed L, Omer R (2020) *Cunhur Sci J* 41:916
34. Tu Y-J, Njus D, Schlegel HIB (2017) *Org Biomol Chem* 15:4417
35. Ardalan T, Ardalan P, Monajjemi M (2014) *Nanotub Carbon Nanostructures* 22:687
36. Liu Y, Liu C, Li J (2020) *ACS Omega* 5:25467
37. Anantharaman S, Rangappa D, Krishna H, Nagaraja P (2010) *Enzyme Microb Technol* 47:243
38. Penner MH (2017) *Basic Principles of Spectroscopy*. In: Nielsen SS (ed) *Food Analysis*. Springer International Publishing, Cham, p 79
39. Gülçin İ (2012) *Arch Toxicol* 86:345
40. Sprinz H, Beckert D, Brede O (1998) *J Radioanal Nucl Chem* 232:39
41. Louit G, Hamedanian M, Taran F, Coffigny H, Renault JP, Pin S (2009) *Analyst* 134:250
42. Boettner GR, Jurkiewicz BA (1993) *Free Radic Biol Med* 14:49
43. Vakarelska-Popovska MH, Velkov Z (2016) *Comput Theor Chem* 1077:87
44. Warren JJ, Tronic TA, Mayer JM (2010) *Chem Rev* 110:6961
45. Pearson RG (2005) *J Chem Sci* 117:369
46. Chermette H (1999) *J Comput Chem* 20:129
47. Gazquez JL, Mendez F (1994) *J Phys Chem* 98:4591
48. Frisch MJ, Trucks GW, Schlegel HB, Scuseria GE, Robb MA, Cheeseman JR, Scalmani G, Barone V, Petersson GA, Nakatsuji H, Li X, Caricato M, Marenich AV, Bloino J, Janesko BG, Gomperts R (2016) *Gaussian 16, Revision B.01*; *GaussView 5.0*. Gaussian Inc, Wallingford, CT
49. Hanwell MD, Curtis DE, Lonie DC, Vandermeersch T, Zurek E, Hutchison GR (2012) *J Cheminform* 4:17
50. O'boyle NM, Tenderholt AL, Langner KM (2008) *J Comput Chem* 29:839
51. Ser CT, Žuvela P, Wong MW (2020) *Appl Surf Sci* 512:145612
52. Fuentetaja P, Florez E, Tiznado W (2010) *J Chem Theory Comput* 6:1470
53. Skoog DA, West DM, Holler JF, Crouch SR (2004) *Fundamentals of analytical chemistry*. Cengage Learning India Private Limited, New Delhi

Publisher's Note Springer Nature remains neutral with regard to jurisdictional claims in published maps and institutional affiliations.

Springer Nature or its licensor (e.g. a society or other partner) holds exclusive rights to this article under a publishing agreement with the author(s) or other rightsholder(s); author self-archiving of the accepted manuscript version of this article is solely governed by the terms of such publishing agreement and applicable law.



PLACEMENT OF OUTGOING STUDENTS 2022-23

SL.NO.	YEAR	NAME OF THE STUDENT PLACED	PROGRAM GRADUATED FROM	NAME OF THE EMPLOYEE	PAY PACKAGE AT APPOINTMENT
1	2022-23	LOKESH PATIL	B.Sc	INDIAN ARMY	
2	2022-23	DHEERAJ T SHRAVANE	B.Sc	INDIAN ARMY	
3	2022-23	PRATHAMESH KHADE	B.Sc	INDIAN ARMY	
4	2022-23	AKASH TODAKAR	B.Sc	INDIAN ARMY	
5	2022-23	KIRAN MASTI	B.Sc	INDIAN ARMY	
6	2022-23	RAHUL MANKALE	B.A	INDIAN ARMY	
7	2022-23	SUDARSHAN ARABALLI	B.Sc	INDIAN ARMY	
8	2022-23	SACHIN BADAOKAR	B.A	INDIAN ARMY	
9	2022-23	NVINODAKUMAR NAIK	B.Sc	INDIAN NAVY	
10	2022-23	BASAPPA KAROSHI	B.Sc	POLICE DEPT	
11	2022-23	VIJAY WAJANTRI	B.A	POLICE DEPT	
12	2022-23	SHIWETA GUNDI	B.Sc	DEPT OF POSTS	
13	2022-23	BHAGYASHREE SANGANALE	B.Sc	DEPT OF POSTS	
14	2022-23	PRIYANKA PARIT	B.Sc	DEPT OF POSTS	
15	2022-23	DHEERAJKUMAR VAJANTRI	B.Sc	FIRE BRIGADE	
16	2022-23	RAJU GUDASI	B.Sc	FIRE BRIGADE	
17	2022-23	OMKAR PATIL	B.Sc	FIRE BRIGADE	
18	2022-23	CHETAN NAIK	B.Sc	FIRE BRIGADE	
19	2022-23	MANOJ DEVARESHIPUJERI	B.Sc	FIRE BRIGADE	
20	2022-23	SNEHA CHALAWADI	B.Sc	HIGH CORT	
21	2022-23	VISHWANATH HADALAGE	B.Sc	CIPLA	
22	2022-23	SUPRITA APARAJ	B.Sc		
23	2022-23	CHANDRAKANT NAVI	B.Sc	A P I	
24	2022-23	PRAVEEN KHANADALI	B.Sc	A P I	
25	2022-23	VEENA PATIL	B.Sc	AGASTYA	
26	2022-23	VEENA MUCHANDI	B.Sc	TCSL (TATA)	

26 2022-23 SACHIN S DESAI

B.Sc

CISP


PrincipalS. S. Arts College & T. P. Science Institute
SANKESHWAR



ADMIT CARD

(TO BE ISSUED TO THE INDIAN SUCCESSFUL COMPLETION OF MED EXAM)

RMS No : 5239

IVRS Code : 1333115239 IVRS Phone No : 00025599290

1. Candidate Name : LOKESH PATHI

S/O RAJU

2. Date of Birth : 04/09/2000

3. Roll No : HANTRUBELNA26022350872

4. Date of Exam : 26/07/2023

Time : 0300 AM Place : Colachel Stadium, Pangode Mel Str

5. Branch : NOI TECHNICAL

Trivandrum

6. Identification Marks

6.1 ARM IN FRONT OF THE THE NECK LEFT SIDE

6.2 YOUTH CARD BELOW THE REGULAR ID CARD INSER ASPECT

(Signature)

(Sign of the Candidate)



**MANI SURESH A
COL
HOST DIR
ARU TRIVANDRUM**



SEAL OF ARU

REGD BY POST
MADRAS REGT CENTRE
WELLINGTON (INDIA)



04 Feb 2023

Sl. No. SN/2023/REGT/1502/M1401/20
Name: THEERJA TANALI SHIVARAM
Roll No: TANALI BALKI SHIVARAM
Age: ANNALE
Religion: HINDU
Caste: SANKI SIKKAR
Address: 95, ARUNG
City: Madurai
Pin: 625 012



CALL LETTER FOR DESPATCH: CLE 15 of 2023

REGD BY POST
MADRAS REGT CENTRE
WELLINGTON (INDIA)
25.01.2023
ADVERSE (GENERAL DUTY)
25.01.2023
Note: Candidates will be final only after receiving the
Mail of completion and after checking/verification of complete documents and fulfillment of all

22 Feb 23
MADRAS REGT CENTRE, WELLINGTON (INDIA) at the following
Address: Wellington

- (a) 100 x 100 mm size photograph
- (b) 100 x 100 mm size photograph
- (c) 100 x 100 mm size photograph
- (d) 100 x 100 mm size photograph
- (e) 100 x 100 mm size photograph
- (f) 100 x 100 mm size photograph
- (g) 100 x 100 mm size photograph
- (h) 100 x 100 mm size photograph
- (i) 100 x 100 mm size photograph
- (j) 100 x 100 mm size photograph
- (k) 100 x 100 mm size photograph
- (l) 100 x 100 mm size photograph
- (m) 100 x 100 mm size photograph
- (n) 100 x 100 mm size photograph
- (o) 100 x 100 mm size photograph
- (p) 100 x 100 mm size photograph
- (q) 100 x 100 mm size photograph
- (r) 100 x 100 mm size photograph
- (s) 100 x 100 mm size photograph
- (t) 100 x 100 mm size photograph
- (u) 100 x 100 mm size photograph
- (v) 100 x 100 mm size photograph
- (w) 100 x 100 mm size photograph
- (x) 100 x 100 mm size photograph
- (y) 100 x 100 mm size photograph
- (z) 100 x 100 mm size photograph

PASSED

INS
MAJ
ADJT
MRC

letter stands automatically nullified/canceled at the time of despatch, if any discrepancy
physical both lack of production of documents/tiding of facts.

Read By Post / By Hand

Army Recruiting Office
Fort Belgaum
PIN- 590 016

01 Feb 2023



31/15012023/CEE/Recr 4

6 BAN/BEL/AST/150123/175112

PRATHAMESH DUNDAPPA KHADE

DUNDAPPA KHADE

WAKALE Post Office ANKALE

MUKKERI District BELAGAVI (Karnataka)

Age 591313

CALL LETTER FOR DESPATCH : CEE 15 JAN 2023

To: Candidate,

You have provisionally been selected for recruitment in **Agnivisar TECHNICAL** on the basis of the CEE held on **15 Jan 2023**.

You are hereby directed to report to ARO, Belgaum for initial checking of documents on **01 Feb 2023** alongwith the following documents in original for enrolment formalities and subsequent respective training centre in **Feb 2023** :-

1. SSLC/ PUC/ Degree marks card.
2. School/ College leaving certificate of SSLC/ PUC/ Degree with your photo affixed on it. Date of entering and leaving the school/ college must be mentioned in the certificate.
3. Character certificate issued by Village Sarpanch / Head Master / Principal with your photo affixed on it (Should not be more than 02 months old).
4. Police verification certificate issued by Civil Police (SP/ Dy SP) with your photo affixed on it and round stamp of Superintendent of Police Office (Should not be more than 03 months old as on Mar 2023).
5. Permanent Residential, Domicile & Caste Certificates (duly mentioned the particular caste) issued by Tehsildar as per Karnataka Govt web site Nadakatagovt.in URL.
6. Self affidavit from Executive Magistrate / Sub Divisional Magistrate as per specimen attached by this ARO (Spelling of Self, Father & Mother should be as per 10th Marks Card & Name of Village, Taluk and District should be same as mentioned in residential certificate).
7. CERTIFICATE / STATEMENT THAT HE HAD OR HAS NOT BEEN MEMBER OF ANY POLITICAL OR POLITICAL ORGANISATION AND HAS NEVER BEEN IN CUSTODY IN JAIL & NO CRIMINAL OR JUDICIAL CASE IS PENDING AGAINST HIM IN ANY COURT OF LAWS IN INDIA / ABROAD AND THAT HE HAS NOT BEEN EVER CONVICTED FOR ANY OFFENCE UNDER THE LAW).
8. Character/ Pre-Verification certificate from Village Sarpanch as per specimen attached (copies in original). Photographs of family members required to be paste at the space provided for it. Name and Date of birth should be mentioned correctly. Complete family photograph to be also pasted on reverse side of the form. All photographs to be attested by Village Sarpanch with stamp.
9. Particulars of family members duly supported with proof of date of birth (in English) (English only) in respect of each member as per specimen attached. Name and Date of birth should be mentioned correctly.
10. NCC certificate A/B/C, if held duly signed by Commanding Officer of NCC Battalion.
11. Relationship Certificate issued by Record Office (for son of Serviceman/Ex-serviceman).
12. Unmarried certificate duly signed by Village Sarpanch.
13. Self PAN Card, Aadhar Card and Self Saving Bank Account (if any) opened in any authorised Bank.
14. Call up letter issued by ARO Belgaum.

D/0423/15032023/CEE/Result

01 Feb 2023



Roll No. BAN/BEL/AGD/150123/143804
 Name AKASH T TODAKAR
 Sex TANAJI
 Vill ANKALE Post Office : ANKALE
 Taluk BELAGAVI District : BELAGAVI (Karnataka)
 PIN Code - 591313

CALL LETTER FOR DESPATCH : CEE 15 JAN 2023

Dear Candidate,

1. You have provisionally been selected for recruitment in Agniveer GENERAL DUTY on the basis of the merit of CEE held on 15 Jan 2023.

2. You are hereby directed to report to ARO, Belgaum for initial checking of documents on 7 Feb 2023 alongwith the following documents in original for enrolment formalities and subsequent despatch to respective training centre in Feb 2023 :-

- (a) SSLC/ PUC/ Degree marks card.
- (b) School/ College leaving certificate of SSLC/ PUC/ Degree with your photo affixed on it. Date of entering and leaving the school/ college must be mentioned in the certificate.
- (c) Character certificate issued by Village Sarpanch / Head Master / Principal with your photo affixed on it (Should not be more than 02 months old).
- (d) Police verification certificate issued by Civil Police (SP/ Dy SP) with your photo affixed on it with round stamp of Superintendent of Police Office (Should not be more than 03 months old as on 01 Mar 2023).
- (e) Permanent Residential, Domicile & Caste Certificates (duly mentioned the particular caste) issued by Tehsildar as per Karnataka Govt web site [Nadprachen URI](http://Nadprachen.URI).
- (f) Self affidavit from Executive Magistrate / Sub Divisional Magistrate as per specimen provided by this ARO (Spelling of Self, Father & Mother should be as per 10th Marks Card & Spelling of Village, Taluk and District should be same as mentioned in residential certificate and A CERTIFICATE / STATEMENT THAT HE HAD OR HAS NOT BEEN MEMBER OF ANY BANNED / POLITICAL ORGANISATION AND HAS NEVER BEEN IN CUSTODY IN JAIL & NO CRIMINAL OR JUDICIAL CASE IS PENDING AGAINST HIM IN ANY COURT OF LAWS IN INDIA / ABROAD AND THAT HE HAS NOT BEEN EVER CONVICTED FOR ANY OFFENCE UNDER THE LAW).
- (g) Character/ Pre-Verification certificate from Village Sarpanch as per specimen attached (four copies in original). Photographs of family members required to be paste at the space provided for it. Name and Date of birth should be mentioned correctly. Complete family photograph to be also pasted on reverse side of the form. All photographs to be attested by Village Sarpanch with stamp.
- (h) Particulars of family members duly supported with proof of date of birth (in English/ Hindi language only) in respect of each member as per specimen attached. Name and Date of birth should be mentioned correctly.
- (i) NCC certificate A/B/C, if held duly signed by Commanding Officer of NCC Battalion.
- (k) Relationship Certificate issued by Record Office (for son of Serviceman/Ex-serviceman only).
- (l) Unmarried certificate duly signed by Village Sarpanch.
- (m) Self PAN Card, Aadhar Card and Self Saving Bank Account to be opened in any Nationalised Bank.
- (n) Call up letter issued by ARO Belgaum.



NO. 12345
DATE: 15/01/2023
BY: [Signature]

123456789
123456789
123456789
SHIRHATTI Post Office SHIRHATTI
HLEBARI District BELAGAVI (Karnataka)
- 581305

CALL LETTER FOR DESPATCH : CEE 15 JAN 2023

You have provisionally been selected for recruitment in **Agniveer TECHNICAL** on the basis of CEE held on **15 Jan 2023**

You are hereby directed to report to ARO Belgaum for initial checking of documents in **Feb 2023** alongwith the following documents in **original** for enrolment formalities and to respective training centre in **Feb 2023**

1. **SSLC/PUC Degree marks card**
2. **School/College leaving certificate of SSLC/PUC Degree with your photo affixed on it. Date of entering and leaving the school/college must be mentioned in the certificate**
3. **Character certificate issued by Village Sarpanch / Head Master / Principal with your photo affixed on it. Should not be more than 02 months old.**
4. **Police verification certificate issued by Civil Police (SF / Dy SP) with your photo affixed on it and round stamp of Superintendent of Police Office. Should not be more than 03 months old as on 15/01/2023.**
5. **Permanent Residential, Domestic & Caste Certificates (duly mentioned the particulars as required by Tehsildar as per Karnataka Govt web site Nad.karnataka.gov.in)**
6. **Self affidavit from Executive Magistrate / Sub-Divisional Magistrate as per specimen provided by the ARO. Spelling of Self, Father & Mother should be as per 10th Marks Card and Spelling of Village, Taluk and District should be same as mentioned in residential certificate. **A CERTIFICATE - STATEMENT THAT HE HAD OR HAS NOT BEEN MEMBER OF ANY UNLAWFUL / POLITICAL ORGANISATION AND HAS NEVER BEEN IN CUSTODY IN JAIL & NO CRIMINAL OR JUDICIAL CASE IS PENDING AGAINST HIM IN ANY COURT OF LAWS IN INDIA / ABROAD AND THAT HE HAS NOT BEEN EVER CONVICTED FOR ANY OFFENCE UNDER THE LAWS****
7. **Character Pre-Verification certificate from Village Sarpanch as per specimen attached (four copies in original). Photographs of family members required to be paste at the top as provided for it. Name and Date of birth should be mentioned correctly. Complete family photograph to be also pasted on reverse side of the form. All photographs to be attested by Village Sarpanch with stamp.**
8. **Particulars of family members duly supported with print of date of birth (in English in Hindi language only) in respect of each member as per specimen attached. Name and Date of birth should be mentioned correctly.**
9. **NOC certificate A/B/C if held duly signed by Commanding Officer of A. J. College & T. P. School.**
10. **Relationship Certificate issued by Return Officer if a son of Sarpanch or a son of Sarpanch.**
11. **Unclaimed certificate duly signed by Village Sarpanch**
12. **Self PAN Card, Aadhar Card and Self Saving Bank Account to be opened in any recognised Bank.**
13. **Call up letter issued by ARO Belgaum**



PAGE No. _____
Date _____

QUESTION PAPER

NAME: _____
ROLL NO: _____

CLASS: _____

INSTRUCTIONS:

1. Read the questions carefully and answer them in your own words.
2. The questions are of two types: (a) Short Answer type and (b) Long Answer type.
3. The questions are of two types: (a) Short Answer type and (b) Long Answer type.
4. The questions are of two types: (a) Short Answer type and (b) Long Answer type.
5. The questions are of two types: (a) Short Answer type and (b) Long Answer type.
6. The questions are of two types: (a) Short Answer type and (b) Long Answer type.
7. The questions are of two types: (a) Short Answer type and (b) Long Answer type.
8. The questions are of two types: (a) Short Answer type and (b) Long Answer type.
9. The questions are of two types: (a) Short Answer type and (b) Long Answer type.
10. The questions are of two types: (a) Short Answer type and (b) Long Answer type.

S. S. Arts College & T. P. School
Sankeshwar, Solapur

JL Number- ARO/BGM/23 FEB23/ARTY HYD/ 3)

(In lieu of and same as Rahdari Certificate No)



JOINING LETTER FOR AGNIVEER (GENERAL DUTY) BY OFFICE OF
ARO BELGAUM



Dear Candidate,

1. Congratulations on being shortlisted for enrolment as an Agniveer in the Recruiting Year 2022-23

2. Your personal details are as under :-

- | | |
|--|---|
| (a) Name | : SUDARSHAN ARABALLI |
| (b) Father/Guardian Name | : MARUTI |
| (c) Date of Birth | : 01-Sep-2001 |
| (d) Category/Trade | : AGNIVEER (GENERAL DUTY) SIC |
| (e) Identification Marks | : i BM JUST BELOW LT ANGLE OF MOUTH
ii BM OVER LOWER BACK 9 CM RT TO MIDLINE |
| (f) Highest Education Qualification | : 10th(SSC) |
| (g) Education Qualification for Entry/Recruitment | : 10th(SSC) |
| (h) Details of relaxation/ Lowering of Physical Standards, granted, if any (HT, WI, Chest) | : - |
| (i) Roll No | : BAN/BEL/AGD/150123/140722 |
| (k) Block/Locality | : HUKKERI |
| (l) District | : BELAGAVI |
| (m) State | : Karnataka |
| (n) Pin Code | : 591340 |
| (o) Regiment Allotted | : ARTY CENTRE, HYDERABAD |
| (p) Date of Rally Screening | : 9-Dec-2022 |

D/0423/15012023/CEE/Result

01 Feb 2023



Roll No : BAN/BEL/AGD/150123/141400

Name : SACHIN BADAJAP

S/o : RAMACHANDRA

Vill : GAVANAL Post Office : KAMATANUR

Taluk : HUKKERI District : BELAGAVI (Karnataka)

PIN Code - 581340

CALL LETTER FOR DESPATCH : CEE 15 JAN 2023

Dear Candidate,

1. You have provisionally been selected for recruitment in Agniveer GENERAL DUTY on the basis of the merit of CEE held on 15 Jan 2023.

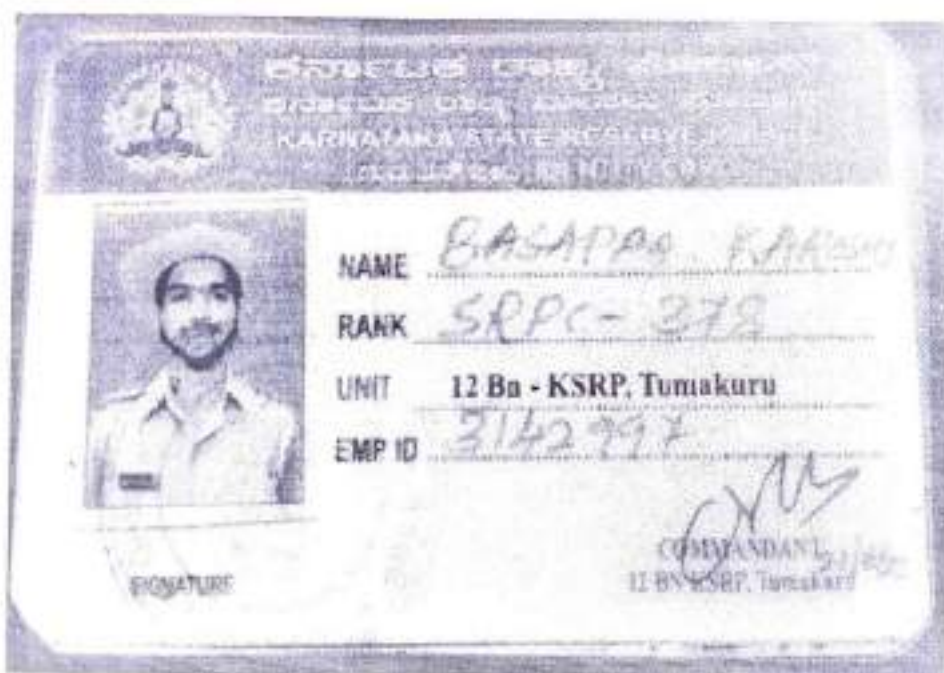
2. You are hereby directed to report to ARO, Belgaum for initial checking of documents on 01 Feb 2023 alongwith the following documents in original for enrolment formalities and subsequent despatch to respective training centre in Feb 2023 -

- (a) SSLC/ PUC/ Degree marks card.
- (b) School/ College leaving certificate of SSLC/ PUC/ Degree with your photo affixed on it. Date of entering and leaving the school/ college must be mentioned in the certificate.
- (c) Character certificate issued by Village Sarpanch / Head Master / Principal with your photo affixed on it (Should not be more than 02 months old).
- (d) Police verification certificate issued by Civil Police (SP/ Dy SP) with your photo affixed on it with round stamp of Superintendent of Police Office (Should not be more than 03 months old as on 01 Mar 2023).
- (e) Permanent Residential, Domicile & Caste Certificates (duly mentioned the particular caste) issued by Tehsildar as per Karnataka Govt web site [Nadakacheri URL](http://Nadakacheri.URL).
- (f) Self affidavit from Executive Magistrate / Sub Divisional Magistrate as per specimen provided by this ARO (Spelling of Self, Father & Mother should be as per 10th Marks Card & Spelling of Village, Taluk and District should be same as mentioned in residential certificate) and A CERTIFICATE / STATEMENT THAT HE HAD OR HAS NOT BEEN MEMBER OF ANY BANNED / POLITICAL ORGANISATION AND HAS NEVER BEEN IN CUSTODY IN JAIL & NO CRIMINAL OR JUDICIAL CASE IS PENDING AGAINST HIM IN ANY COURT OF LAWS IN INDIA / ABROAD AND THAT HE HAS NOT BEEN EVER CONVICTED FOR ANY OFFENCE UNDER THE LAW).
- (g) Character/ Pre-Verification certificate from Village Sarpanch as per specimen attached (four copies in original). Photographs of family members required to be paste at the space provided for it. Name and Date of birth should be mentioned correctly. Complete family photograph to be also pasted on reverse side of the form. All photographs to be attested by Village Sarpanch with stamp.
- (h) Particulars of family members duly supported with proof of date of birth (in English language only) in respect of each member as per specimen attached. Name and Date of birth should be mentioned correctly.
- (i) NCC certificate A/B/C, if held duly signed by Commanding Officer of NCC Battalion.
- (k) Relationship Certificate issued by Record Office (for son of Serviceman/Ex-serviceman only).



You

today at 2:21 PM





ಕರ್ನಾಟಕ ರಾಜ್ಯ ಪೊಲೀಸ್

KARNATAKA STATE POLICE

IDENTITY CARD ಗುರುತಿನ ಚೀಟಿ



NAME : VIJAY A WAJANTRI

DESIGNATION: POLICE CONSTABLE

UNIT : 10thBN, KSRP, SHIGGAVI, HAVERI

EMP NO : 4006232


COMMANDANT

10 BN KSRP SHIGGAVI
COMMANDANT

10thBN, KSRP, SHIGGAVI .581205



You

today at 2:21 PM



Commission of India
Department of Posts, India
Office of the SO - Channarayana Division Division, Channarayana

ORDERLY PROFESSIONAL ENGAGEMENT

2209W/Channarayana/2022 Date: 18/06/2022 at Channarayana No. 2145/2022

is referred to the notification No. NOTIFICATION: 17-21-2022-GOS Dated: 27/01/2022

Dr./Smt./Mr. SHWETA MAHADEV GUNDI son / daughter of
Mr. MAHADEV GUNDI whose Date of Birth is: 12/08/2002

and who belongs to EWS/SC category is hereby
engaged as GOS BPM, Kudur B.O in accord with order
Channarayana H.O/Channarayana H.O _____ on PROVISIONAL BASIS with effect from dated
18/06/2022 (W/V) in the TACA scale of 50000 (W/V) shall be paid every
month in respect of post admissible from time to time.

2. She/He/He, SHWETA MAHADEV GUNDI son/daughter of Mr.
MAHADEV GUNDI does hereby undertake that his/her engagement
as GOS BPM, Kudur B.O in accord with 7 under
Channarayana H.O/Channarayana H.O _____ shall be in the nature of a contract
to be terminated by him/her or by the undersigned by notifying the order in writing and
that his conduct and Engagement shall be governed by the department of Posts, G.O. (S) 2020
(S) (Conduct and Engagement) Rules, 2020 as amended from time to time.

3. This Provisional Engagement is subject to satisfactory verification of the prescribed
educational qualification, community certificate and other certificates, wherever prescribed. The
candidate will have to undergo satisfactory prescribed induction Training course and Practical
Training as and when issued.

4. The engagement is provisional and subject to certificate being verified through proper
channels. If the verification reveals that the date of the candidate belonging to Scheduled
Caste/Scheduled Tribe /Other backward class(es)/not belong to creamy layer/ is false or
educational certificates are not genuine or found unfit on Police Verification, neither

2023/6/18 21:26





You

Today at 2:21 PM



GOVERNMENT OF INDIA
Ministry of Communications
DEPARTMENT OF POSTS
Supdt. of Post Offices, Belagavi Division, Belagavi-590001
Tel : 0831-2431860, 2464428, 2463550

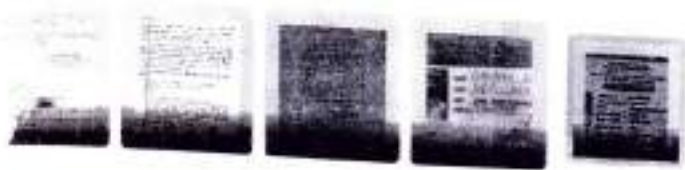
IDENTITY CARD



Valid up to : 31-12-2028
Unique Emp. ID : 50518600
Name : Bhagyashree V. Sanganele
Designation : GDS MD
Date of Birth : 07/05/2000
Blood Group : B+ ve
Date of Issue : 01/01/2023

Signature of Card Holder

Supdt. of Post Offices
Belagavi Division, Belagavi 5900-1





ORDER OF PROVISIONAL ENGAGEMENT

IP/Sagar/GDS OL/Jogfalls SO

In response to the notification No. NOTIFICATION: 17-21/2023-GDS Dated: 27.01.2023
Shri/Smt/Ms. PRIYANKA PARIT son / daughter of
Shri. RAVINDRA whose Date of Birth is 04/09/2000
and who belongs to UR category/selected against UR category is hereby
engaged as GDS ABPM, Jog Falls S.O in account with under
Jog Falls S.O/Sagar H.O on PROVISIONAL BASIS with effect from dated
23.06.2023 AN/EN in the TRCA scale of 10000. He/she shall be paid such
allowances as are admissible from time to time.

2. Shri/Smt/Ms. PRIYANKA PARIT Son/daughter of Shri
RAVINDRA should clearly understand that his/her engagement
as GDS ABPM, Jog Falls S.O in account with / under
Jog Falls S.O/Sagar H.O shall be in the nature of a contract
liable to be terminated by him/her or by the undersigned by notifying the order in writing and
that his conduct and Engagement shall be governed by the department of Posts, Gramin Dak
Sevak (Conduct and Engagement) Rules, 2020 as amended from time to time.

3. This Provisional Engagement is subject to satisfactory verification of the prescribed
educational qualification, community certificate and other certificates, wherever prescribed. The
candidate will have to undergo satisfactory prescribed Induction Training course and Practical
Training as and when issued.

4. The engagement is provisional and subject to certificates being verified through proper
channels. If the verification reveals that the claim of the candidate belonging to Scheduled
Caste/Scheduled Tribe /Other backward classes/(not belong to creamy layer)/ is false or
educational certificates are not genuine or found unfit on Police Verification, his/her

Handwritten signature

Engagement shall be terminated forthwith without assigning any further reasons and without prejudice to other criminal/legal action as may be taken under the provisions of Indian Penal Code for production of false certificate as a consequence.

5. The engagement of (Economically Weaker Sections) EWS candidates is provisional and subject to the Income and Asset certificate being verified through proper channels and if the verification reveals that the claim to belong to EWS is fake/false the Engagements will be terminated forthwith without assigning any further reasons and without prejudice to take further action as may be taken under the provisions of the Indian Penal Code for production of fake/false certificate.

6. The BPM will have to provide accommodation for Branch Post Office at Branch Office Village if the accommodation is not provided by Central Govt/State Govt/Gram Panchayat or any other local Body as per standard prescribed by Directorate order no.17-31/2016-GDS dated 25.06.2018 & 28.09.2018 (which has already been mentioned in notification NOTIFICATION: 17-21/2023-GDS Dated:27.01.2023 As per Rule 3-A(vii) of GDS (Conduct and Engagement) Rules 2020, you should take up residence in Post Office village within a month of selection but before engagement as it is mandatory to you by these Rules. Failure to reside in place of duty for GDS BPM after engagement shall be treated as violation of conditions of engagements and liable for disciplinary action under Rule-10 of GDS (Conduct and Engagement) Rules, 2020 resulting in removal/dismissal from engagement.

6.1 Failure to reside within the delivery jurisdiction of the Post Office for other categories of Gramin Dak Sevaks after engagement shall be treated as violate of conditions of engagement and liable for disciplinary action under Rule 10 of the GDS (Conduct & Engagement) Rules, 2020 requiring removal/dismissal.

ಭೃತ್ಯಾಭಿ ಮನಾ ನೇರೇಶವರಾ ಹಾಸಿ.
 ಮನಾ ನಿರೀಶವರವರ ರಮಣ
 ಕರ್ನಾಟಕ ಅಗ್ನಿ ಶಾಖಾ ಮತ್ತು ಪುಸ್ತಕ ಸೇವಾ
 ದು. 1, ಕರ್ನಾಟಕ ಮಹಾವಿದ್ಯಾಲಯ ರಸ್ತೆ,
 ಬೆಂಗಳೂರು - 560 042.



ಕರ್ನಾಟಕ ಸರ್ಕಾರ
ಕರ್ನಾಟಕ ರಾಜ್ಯ ಅಗ್ನಿಶಾಮಕ ಮತ್ತು ಪುಸ್ತಕ ಸೇವೆಗಳು

ಸಂಖ್ಯೆ:ಸಿಬ್ಬಂದಿ(7)47/ನೇಮಕಾತಿ/2019-20
 ಓ.ಬಿ.ಸಂಖ್ಯೆ:170/2022

ದಿನಾಂಕ:15-07-2022

ನೇಮಕಾತಿ ಆದೇಶ

ವಿಷಯ : ಕರ್ನಾಟಕ ರಾಜ್ಯ ಅಗ್ನಿಶಾಮಕ ಮತ್ತು ಪುಸ್ತಕ ಸೇವಾ ಇಲಾಖೆಯಲ್ಲಿ ಖಾಲಿ ಇರುವ ಅಗ್ನಿಶಾಮಕ ಹುದ್ದೆಗೆ ಅಂತ್ಯಿಯಾದ ಅಭ್ಯರ್ಥಿಗಳಿಗೆ ನೇಮಕಾತಿ ಆದೇಶ ನೀಡುವ ಬಗ್ಗೆ.

- ಉಲ್ಲೇಖ : 1. ನೇಮಕಾತಿ ಅಧಿಸೂಚನೆ ಸಂಖ್ಯೆ:ಸಿಬ್ಬಂದಿ(7)47/ನೇಮಕಾತಿ/2019-20, ದಿನಾಂಕ:18-06-2020
 2. ಎಡಿಪಿಪಿ ನೇಮಕಾತಿ ರವರ ಶಾಖಾಲಿಕ ಆಯ್ಕೆ ಪಟ್ಟಿ ಪತ್ರ ಸಂಖ್ಯೆ 24/ನೇಮಕಾತಿ-2/2019-20, ದಿನಾಂಕ:30-11-2021
 3. ಸರ್ಕಾರದ ಆದೇಶ ಸಂಖ್ಯೆ: ಎಫ್.ಡಿ.(ಎಸ್.ಪಿ.ಎಲ್)04/ಎಇಟಿ/2005, ದಿನಾಂಕ:31-03-2006
 4. ಸರ್ಕಾರದ ಆದೇಶ ಸಂಖ್ಯೆ: ಹೆಚ್.ಡಿ 158 ಎಫ್.ಎಫ್.ಪಿ 2020 ದಿನಾಂಕ:30-04-2022
 5. ಸಂಖ್ಯೆ:24/ನೇಮಕಾತಿ-2/2019-20, ದಿನಾಂಕ:08-07-2022

*****KSFES-FM*****

ಕರ್ನಾಟಕ ರಾಜ್ಯ ಅಗ್ನಿಶಾಮಕ ಮತ್ತು ಪುಸ್ತಕ ಸೇವೆಗಳ ಇಲಾಖೆಯಲ್ಲಿ ಖಾಲಿ ಇರುವ ಅಗ್ನಿಶಾಮಕ ಹುದ್ದೆಗೆ ದಿನಾಂಕ:15-02-2021 ರಿಂದ 15-04-2021 ರವರೆಗೆ ನಡೆದ ದೇಹ ದಾರ್ಶನಿಕ ಮತ್ತು ದೈವಿಕ ಸಾಮರ್ಥ್ಯ ಪರೀಕ್ಷೆಯಲ್ಲಿ ಪಡೆದ ಅಂಕಗಳು ಹಾಗೂ ಎಸ್.ಎಸ್.ಎಲ್.ಸಿ. / ತತ್ಸಮಾನ ಪರೀಕ್ಷೆಯಲ್ಲಿ ಪಡೆದ ಶ್ರೇಯಾಂಕಗಳ ಆಧಾರದ ಮೇಲೆ ಮತ್ತು ಉಲ್ಲೇಖದಲ್ಲಿರುವ ಆದೇಶ ಮತ್ತು ಪತ್ರಗಳಿಗನುಸಾರವಾಗಿ ನೇಮಕಾತಿ ಮೂಲಕ ನೀಡುವ ಅಗ್ನಿಶಾಮಕ ಹುದ್ದೆಗೆ ಅಂತ್ಯಿಯಾಗಿದ್ದು, ರೂ.23500-550-24000-6000-27000-650-29600-750-32600-850-36000-950-39800-1100-46400-1250-47650 ಆ ವೇತನ ಶ್ರೇಣಿಯಲ್ಲಿ ಲಭ್ಯವಾಗುವ ವೇತನ ಹಾಗೂ ಇತರೆ ಫಲಿತಗಳಿಗೆ ಅರ್ಹವಾಗುವಂತೆ ಹಾಗೂ ಇವುಗಳಿಗೆ ಕರ್ನಾಟಕ ಆಡಳಿತ ನ್ಯಾಯ ಮಂಡಳಿ ಮತ್ತು ಇತರೆ ಘನ ನ್ಯಾಯಾಲಯಗಳ ಮುಂದೆ ಉದ್ಘೋಷಿತ ವ್ಯಾಜ್ಯಗಳ ಬಗ್ಗೆ ನೀಡುವ ತೀರ್ಮಾನಗಳು ಮತ್ತು ಅಂತಿಮ ಆಯ್ಕೆಪಟ್ಟಿಗೆ ಒಳಪಟ್ಟಿರುವ ಕಡತಗಳ ಮೇರೆಗೆ ಹಾಗೂ ಯಾವುದೇ ಪ್ರಕರಣದಲ್ಲಿ ಛಾಗಿಯಾಗಿರುವುದು ಕಂಡುಬಂದಲ್ಲಿ ಸೇವೆಯಿಂದ ವಜಾ ಮಾಡುವ




ನಿಭಂದನೆಯ ಮೇರೆಗೆ ನಿಮ್ಮನ್ನು ಅಗ್ನಿಶಾಮಕ ಪುದ್ಗೇ (ಗ್ರೂಪ್-೨) ತಾತ್ಕಾಲಿಕವಾಗಿ ನೇಮಕ ಮಾಡಲಾಗಿರುತ್ತದೆ.

ನೀವು ಕರ್ತವ್ಯಕ್ಕೆ ವರದಿ ಮಾಡಿಕೊಂಡ ದಿನದಿಂದ ಎರಡು ವರ್ಷಗಳ ಕಾಲ ಪ್ರೊಬೇಷನರಿ ಅವಧಿ (PROBATIONARY PERIOD) ಯನ್ನು ಪೂರೈಸಬೇಕಾಗಿರುತ್ತದೆ. ಈ ಪ್ರೊಬೇಷನರಿ ಅವಧಿಯಲ್ಲಿ ಯಾವುದೇ ಉತ್ತಿಯ ಅನರ್ಹತೆ ಕಂಡುಬಂದರೆ ಯಾವುದೇ ಕಾರಣ ನೀಡದೇ ನಿಮ್ಮನ್ನು ಕೆ.ಸಿ.ಎಸ್. ಪ್ರೊಬೇಷನರಿ ನಿಯಮಗಳು 1977ರ ಪ್ರಕಾರ ಕೆಲಸದಿಂದ ತೆಗೆದು ಹಾಕಲಾಗುವುದು.

ಈ ಆದೇಶವನ್ನು ಸ್ವೀಕರಿಸಿದ ನಂತರ ದಿನಾಂಕ:01-08-2022 ರಂದು ಬೆಳಿಗ್ಗೆ 10:00 ಘಂಟೆಗೆ "ಪೊಲೀಸ್ ಮಹಾ ನಿರ್ದೇಶಕರು ಹಾಗೂ ಮಹಾ ನಿರ್ದೇಶಕರು, ಕರ್ನಾಟಕ ರಾಜ್ಯ ಅಗ್ನಿಶಾಮಕ ಮತ್ತು ಪುರ್ವ ಸೇವೆಗಳು, ನಂ.1 ಆಕ್ಟಾಪ್ಲಾಮಿ ಮೊದಲಿಯಾರ್ ರಸ್ತೆ, ಹಲಸೂರು ಕೆರೆ ಹತ್ತಿರ, ಬೆಂಗಳೂರು-560 042 ಇಲ್ಲಿ ವರದಿ ಮಾಡಿಕೊಳ್ಳತಕ್ಕದ್ದು. ನಿಗದಿಪಡಿಸಿದ ದಿನಾಂಕದಂದು ಹಾಜರಾಗದಿದ್ದಲ್ಲಿ ಯಾವುದೇ ಮುನ್ನೂತನೆಯನ್ನು ನೀಡದೆ ನಿಮ್ಮ ನೇಮಕಾತಿ ಆಯ್ಕೆಯನ್ನು ರದ್ದು ಪಡಿಸಲಾಗುವ ಅಂತಿಮ ಅಧಿಕಾರವನ್ನು ನೇಮಕಾತಿ ಪ್ರಾಧೀಕಾರವು ಹೊಂದಿರುತ್ತದೆ.

ನೀವು ಕರ್ತವ್ಯಕ್ಕೆ ಹಾಜರಾಗುವ ಸಮಯದಲ್ಲಿ ಈ ಕೆಳಕಂಡ ಮೂಲ ದಾಖಲೆಗಳನ್ನು ತಪ್ಪದೇ ಹಾಜರು ಪಡಿಸಬೇಕು.

1. ಇತ್ತೀಚಿನ ಪಾಸ್ ಪೋರ್ಟ್ ಮತ್ತು ಸ್ಟಾಂಪ್ ಆಳತೆಯ ತಲಾ ನಾಲ್ಕು ಭಾವಚಿತ್ರಗಳು
2. ಇಬ್ಬರು ಸ್ಥಳೀಯ ಗಣ್ಯ ವ್ಯಕ್ತಿಗಳಿಂದ ಪಡೆದ ನಡತೆ ಪ್ರಮಾಣ ಪತ್ರ
3. ಅಧಾರ್ ಕಾರ್ಡ್
4. ಪಾನ್ ಕಾರ್ಡ್
5. ಅಭ್ಯರ್ಥಿಯ ಹೆಸರಿನಲ್ಲಿರುವ ಯಾವುದಾದರೂ ರಾಷ್ಟ್ರೀಕೃತ ಬ್ಯಾಂಕ್ ಪುಸ್ತಕ
6. ಕರ್ನಾಟಕ ಅಗ್ನಿಶಾಮಕ ಮತ್ತು ತುರ್ತು ಸೇವಾ ಇಲಾಖೆಯಲ್ಲಿ ಕರ್ತವ್ಯಕ್ಕೆ ವರದಿ ಮಾಡಿಕೊಂಡ ನಂತರ ತರಬೇತಿ ಮಧ್ಯೆ ಮತ್ತು ತರಬೇತಿಯ ನಂತರ ಇಲಾಖೆಗೆ ರಾಜೀನಾಮೆ, ಗೈರು ಹಾಜರಿಯಾದಲ್ಲಿ ಕರ್ನಾಟಕ ಸರ್ಕಾರದ ಆದೇಶದಂತೆ ರೂ. 1,00,000-00 (ಒಂದು ಲಕ್ಷ ರೂಪಾಯಿ ಮಾತ್ರ) ಗಳ ವಂಡನಾ ಶುಲ್ಕ ಪಾವತಿಸುವ ಬಗ್ಗೆ ರೂ.500-00 ಗಳ ಭಾಷಾಕಾಗದದಲ್ಲಿ ಮುಚ್ಚಳಕೆ ಪತ್ರವನ್ನು ನೋಟರಿ ರವರಿಂದ ದೃಢೀಕರಿಸಿ ನೀಡುವುದು.

Sl No	Appl No.& DOB	Name	Photo & Signature	Address	Selected category
01	1264040 27-Jul-99	DHEERAJKUMAR DATTATREYA VAJANTRI	 	DHEERAJKUMAR DATTATREYA VAJANTRI SOLAPUR, SOLAPUR, HUKKERI, Belagavi, Karnataka, Pincode - 591313.	SC_RUR



ಈ ನೇಮಕಾತಿ ಆದೇಶವು ಈ ಕೆಳಕಂಡ ನಿಬಂಧನೆಗಳಿಗೆ ಒಳಪಟ್ಟಿರುತ್ತದೆ.

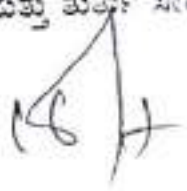
1. ಅಭ್ಯರ್ಥಿಗಳ ಆಯ್ಕೆ ಸಂಬಂಧವಾಗಿ ಮಾನ್ಯ ಕರ್ನಾಟಕ ಆದಳತ ನ್ಯಾಯಮಂಡಳಿಯಲ್ಲಿ ಅಥವಾ ಇತರೆ ಘನ ನ್ಯಾಯಾಲಯಗಳಿಂದ ಹೊರವೀಳುವ ತೀರ್ಮಾನ ಆಧಾರದ ಮೇಲೆ ಕ್ರಮ ತೆಗೆದುಕೊಳ್ಳುವ ಅಧಿಕಾರವನ್ನು ನೇಮಕಾತಿ ಪ್ರಾಧಿಕಾರ ಹೊಂದಿರುತ್ತದೆ.
2. ಅಭ್ಯರ್ಥಿಯು ಕರ್ನಾಟಕ ರಾಜ್ಯ ಅಗ್ನಿಶಾಮಕ ಮತ್ತು ಶುರ್ತು ಸೇವೆಗಳ ಕಾಯ್ದೆ 1964, ಕರ್ನಾಟಕ ಅಗ್ನಿಶಾಮಕ ಮತ್ತು ಶುರ್ತು ಸೇವೆಗಳ ವೃಂದ ಮತ್ತು ನೇಮಕಾತಿ ನಿಯಮ 2013, ಕೆ.ಸಿ.ಎಸ್.ಆರ್. ನಿಯಮ 1958 ಹಾಗೂ ಕರ್ನಾಟಕ ಫೈರ್ ಫೋರ್ಸ್ (ಎಂ.ಡಿ. & ಆರ್.ಎಸ್.) ಕಾಯಿದೆ-1971 ಮತ್ತು ತತ್ಸಂಬಂಧವಾದ ತಿದ್ದುಪಡಿಗಳಿಗೆ ಹಾಗೂ ಕೆ.ಸಿ.ಎಸ್. (ಸಾಮಾನ್ಯ ನೇಮಕಾತಿ) ನಿಯಮಾವಳಿ-1977 ರ ಹಾಗೂ ಕರ್ನಾಟಕ ನಾಗರಿಕ ಸೇವಾ (ಪರಿವೀಕ್ಷಣಾ) ನಿಯಮ-1977 ರ ಪ್ರಕಾರ ಯಾವುದೇ ನ್ಯಾಯಾಲಯವು ನಿಮ್ಮ ನೇಮಕಾತಿಯನ್ನು ಅನುಜ್ಞಿತ ಮತ್ತು ಪರಿಣಾಮ ರೂಪ್ಯ/ ಆನಿಯಮಿತಗೊಳಿಸಿದಲ್ಲಿ, ಯಾವುದೇ ಕಾರಣಗಳಿಂದ ಆಯ್ಕೆಗೊಂಡ ಪುದ್ದಿಗೆ ಅನರ್ಹರಾಗಿ ಕಂಡುಬಂದಲ್ಲಿ, ಯಾವುದೇ ಮುನ್ನೂಚನೆಯನ್ನು ನೀಡದೆ ನಿಮ್ಮನ್ನು ಸೇವೆಯಿಂದ ವಿಮುಕ್ತಿಗೊಳಿಸಲಾಗುವುದು.
3. ಈ ನೇಮಕಾತಿ ಆದೇಶವು ತಾತ್ಕಾಲಿಕವಾಗಿದ್ದು, ನೇಮಕಾತಿ ನಂತರ ಅಭ್ಯರ್ಥಿಯು ಗುಣ ಹಾಗೂ ಜಾರಿತ್ಯದ ಬಗ್ಗೆ ಪ್ರತಿಕೂಲ ವರದಿ ಬಂದರೆ ಅಥವಾ ಅಭ್ಯರ್ಥಿಗಳು ಸಲ್ಲಿಸಿದ ಮೂಲ ದಾಖಲಾತಿಗಳು ನಕಲಿ ಅಥವಾ ಸುಳ್ಳು ಮಾಹಿತಿ ನೀಡಿ ಹಾಜರುಪಡಿಸಿದ ದಾಖಲೆಗಳೆಂಬುವುದು ಯಾವುದೇ ಸಂದರ್ಭದಲ್ಲಿ ಕಂಡುಬಂದಲ್ಲಿ ಯಾವುದೇ ಮುನ್ನೂಚನೆ ನೀಡದೆ ನಿಮ್ಮನ್ನು ಸೇವೆಯಿಂದ ವಜಾ ಮಾಡುವುದರ ಜೊತೆಗೆ ನಿಮ್ಮ ವಿರುದ್ಧ ಕಾನೂನು ಕ್ರಮಜರುಗಿಸಲಾಗುವುದು.
4. ಈ ನೇಮಕಾತಿಯು ಪಿಂಚಣಿಗೆ ಸಂಬಂಧಿಸಿದಂತೆ ಉಲ್ಲೇಖ(3) ರಲ್ಲಿ ಕಾಣಿಸಿರುವ ಸರ್ಕಾರದ ಆದೇಶ ಹಾಗೂ ಮುಂದಿನ ದಿನಗಳಲ್ಲಿ ಆಗಿಂದಾಗ್ಗೆ ಹೊರಡಿಸುವ ಸರ್ಕಾರಿ ಆದೇಶಗಳಿಗೆ ಒಳಪಟ್ಟಿರುತ್ತದೆ.
5. ಈ ಅವಧಿಯಲ್ಲಿ ಇವರು 06 ತಿಂಗಳ ಬುನಾದಿ ತರಬೇತಿ ಹಾಗೂ 03 ತಿಂಗಳ ರಾಜ್ಯ ವಿಪತ್ತು ಸ್ಪಂದನಾ ಪಡೆ ತರಬೇತಿಸೇರಿ ಒಟ್ಟು 09 ತಿಂಗಳ ಬುನಾದಿ ತರಬೇತಿ ಪಡೆಯಬೇಕಾಗಿರುತ್ತದೆ. ಹಾಗೂ ಖಾಯಂ ಪೂರ್ವ ಪರೀಕ್ಷಾ ಅವಧಿಯನ್ನು ಘೋಷಿಸುವ ಮೊದಲು ವೃಂದ ಮತ್ತು ನೇಮಕಾತಿ ನಿಯಮ-2013 ರಲ್ಲಿ ನಿಗದಿಪಡಿಸಿರುವ ಪರೀಕ್ಷೆಗಳನ್ನು ಕಡ್ಡಾಯವಾಗಿ ಉತ್ತೀರ್ಣರಾಗಬೇಕಾಗಿರುತ್ತದೆ.
6. ಅಭ್ಯರ್ಥಿಯು ಕರ್ತವ್ಯಕ್ಕೆ ಹಾಜರಾಗುವ ಸಮಯ ಯಾವುದೇ ಪ್ರಯಾಣ ಭತ್ಯೆಗೆ ಅರ್ಹರವುದಿಲ್ಲ.
7. ಅಭ್ಯರ್ಥಿಗಳ ಆಯ್ಕೆ ಮೀಸಲಾತಿ ವರ್ಗವು ಅಂತಿಮ ಆಯ್ಕೆ ಪಟ್ಟಿಯಲ್ಲಿ ಪ್ರಕಟಗೊಂಡಂತೆ ಪರಿಗಣಿಸಲಾಗುವುದು.



8. ಅಧ್ಯರ್ಥಿಗಳ ಜೇಷ್ಠತೆಯನ್ನು ಕೆ.ಸಿ.ಎಸ್. (ಜೇಷ್ಠತೆ) ನಿಯಮಗಳು 1957 ರ ನಿಯಮ 3(2) ರನ್ವಯ 1222 ಅಗ್ನಿಶಾಮಕ ಪುದ್ಧೆಯ ಅಂತಿಮ ಆಯ್ಕೆ ಪಟ್ಟಿಯ ರೇಖಾಂಕ ಹಾಗೂ ರೋಸ್ಟರ್ ಪದ್ಧತಿಯಂತೆ ಪರಿಗಣಿಸಲಾಗುವುದು.
ಕರ್ತವ್ಯಕ್ಕೆ ವರದಿ ಮಾಡಿದ ದಿನಾಂಕವನ್ನು ಜೇಷ್ಠತೆಗೆ ಪರಿಗಣಿಸಲಾಗುವುದಿಲ್ಲ.
9. ಕರ್ತವ್ಯಕ್ಕೆ ವರದಿ ಮಾಡಿಕೊಂಡ ಮೊದಲ ತಿಂಗಳಲ್ಲಿ ಕರ್ನಾಟಕ ವಿಮಾ ಇಲಾಖೆಯ ಆದೇಶದಂತೆ ಕನಿಷ್ಠ ಮಾಸಿಕ ವಿಮಾಕಂತಿನ ಮೊಬಲಗು ರೂ.2500-00 ಪಾವತಿ, ಕರ್ನಾಟಕ ಸರ್ಕಾರಿ ವಿಮಾಇಲಾಖೆಯಲ್ಲಿ ವಿಮೆ ಮಾಡಿಸಿಕೊಳ್ಳುತ್ತಿದ್ದು.
10. ತರಬೇತಿಯ ಅವಧಿಯಲ್ಲಿ ನೀವು ಕಡ್ಡಾಯವಾಗಿ ತರಬೇತಿ ಕೇಂದ್ರದಲ್ಲಿ ತಂಗಿರತಕ್ಕದ್ದು ಮತ್ತು ಊಟದ ಬಾಬು ಮುಂಗಡ ರೂ.5000-00 ಗಳನ್ನು ನೀವು ಪರದಿ ಮಾಡಿಕೊಂಡ ದಿನದಂದು ನಿರೀಕ್ಷಿತಮೇಸ್ ಅಧಿಕಾರಿಯವರಲ್ಲಿ ಭರಿಸತಕ್ಕದ್ದು.



ಆರಕ್ಷಕ ಉಪ ಮಹಾನಿರೀಕ್ಷಕರು
ಹಾಗೂ ಅಧ್ಯಕ್ಷರು, ಅಗ್ನಿಶಾಮಕ ಸೇವಾಕಾತಿ ಸಮಿತಿ
ಕರ್ನಾಟಕ ರಾಜ್ಯ ಅಗ್ನಿಶಾಮಕ ಮತ್ತು ತುರ್ತು ಸೇವೆಗಳು



ಗೆ,

Application No : 1264040
DHEERAJKUMAR DATTATREYA VAJANTRI
SOLAPUR SOLAPUR HUKKERI
Belagavi 591313
* Mobile Number : 8095174408 (ನೋಂದಣಿ ಅಂಚೆ ಮೂಲಕ)

ಪ್ರತಿಯನ್ನು ಗೌರವಗಳೊಂದಿಗೆ

1. ಮಾನ್ಯ ಮೊಲೀಸ್ ಮಹಾ ನಿರ್ದೇಶಕರು ಹಾಗೂ ಮಹಾ ನಿರ್ದೇಶಕರು, ಕರ್ನಾಟಕ ರಾಜ್ಯ ಅಗ್ನಿಶಾಮಕ ಮತ್ತು ತುರ್ತು ಸೇವೆಗಳು
2. ಹೆಚ್ಚುವರಿ ಮೊಲೀಸ್ ಮಹಾ ನಿರ್ದೇಶಕರು ಹಾಗೂ ಮಹಾ ನಿರ್ದೇಶಕರು, ಕರ್ನಾಟಕ ರಾಜ್ಯ ಅಗ್ನಿಶಾಮಕ ಮತ್ತು ತುರ್ತು ಸೇವೆಗಳು

ಪ್ರತಿಯನ್ನು ಸೂಕ್ತ ಕ್ರಮಕ್ಕಾಗಿ.

1. ನಿರ್ದೇಶಕರು, ಕರ್ನಾಟಕ ರಾಜ್ಯ ಅಗ್ನಿಶಾಮಕ ಮತ್ತು ತುರ್ತು ಸೇವೆಗಳು
2. ಉಪ ನಿರ್ದೇಶಕರು (ಆಡಳಿತ), (ಅಗ್ನಿ ನಿಯಂತ್ರಣ), (ತರಬೇತಿ & ಎಸ್.ಡಿ.ಆರ್.ಎಫ್) (ಶಾಂತಿಕೆ)
3. ಸಮಾಜೇಷ್ವರು, ಆರ್.ಎ.ಮುಂಡ್ಕುರು, ಕರ್ನಾಟಕ ಅಗ್ನಿಶಾಮಕ ಮತ್ತು ತುರ್ತು ಸೇವೆಗಳು ಮಹಾನ್ ಸಿಬ್ಬಂದಿ(4),(6) ಮತ್ತು(8)




ನೀವು ಕರ್ತವ್ಯಕ್ಕೆ ವರದಿ ಮಾಡಿಕೊಂಡ ದಿನದಿಂದ ಎರಡು ವರ್ಷಗಳ ಕಾಲ ಪೂರ್ವಾವಧಿ ಅವಧಿ (PROBATIONARY PERIOD) ಯನ್ನು ಪೂರೈಸಬೇಕಾಗಿರುತ್ತದೆ. ಈ ಪೂರ್ವಾವಧಿ ಅವಧಿಯಲ್ಲಿ ಯಾವುದೇ ರೀತಿಯ ಅನರ್ಹನೆ ಕಂಡುಬಂದರೆ ಯಾವುದೇ ಕಾರಣ ನೀಡದೆ ನಿಮ್ಮನ್ನು ಕೆ.ಸಿ.ಎಸ್. ಪೂರ್ವಾವಧಿ ನಿಯಮಗಳು 1977ರ ಪ್ರಕಾರ ಕೆಲಸದಿಂದ ತೆಗೆದು ಹಾಕಲಾಗುವುದು.

ಈ ಆದೇಶವನ್ನು ಸ್ವೀಕರಿಸಿದ ನಂತರ ದಿನಾಂಕ:01-08-2022 ರಂದು ಬೆಳಿಗ್ಗೆ 10:00 ಘಂಟೆಗೆ "ಮೋಲೀಸ್" ಮಹಾ ನಿರ್ದೇಶಕರು ಹಾಗೂ ಮಹಾ ನಿರ್ದೇಶಕರು, ಕರ್ನಾಟಕ ರಾಜ್ಯ ಅಗ್ನಿಶಾಮಕ ಮತ್ತು ಶುಶ್ರುಕೆ ಸೇವೆಗಳು, ನಂ.1 ಆಸ್ಪತ್ರೆ ಮೊದಲಿಯಾರ್ ರಸ್ತೆ, ಹಲಸೂರು ಕೆರೆ ಪತ್ತಿರ, ಬೆಂಗಳೂರು-560 042 ಇಲ್ಲಿ ವರದಿ ಮಾಡಿಕೊಳ್ಳತಕ್ಕದ್ದು. ನಿಗದಿಪಡಿಸಿದ ದಿನಾಂಕದಂದು ಹಾಜರಾಗಬಿದ್ದಲ್ಲಿ ಯಾವುದೇ ಮನವಿರಿಸಿಯನ್ನು ನೀಡದೆ ನಿಮ್ಮ ಸೇವಾಕಾಲ ಅಂತ್ಯವನ್ನು ರದ್ದುಪಡಿಸಲಾಗುವ ಅಂತಿಮ ಆದೇಶವನ್ನು ಸೇವಾಕಾಲ ಪ್ರದೀಶಕರವು ಹೊಂದಿರುತ್ತದೆ.

ನೀವು ಕರ್ತವ್ಯಕ್ಕೆ ಹಾಜರಾಗುವ ಸಮಯದಲ್ಲಿ ಈ ಕೆಳಕಂಡ ಮೂಲ ದಾಖಲೆಗಳನ್ನು ತಪ್ಪದೇ ಹಾಜರು ಪಡಿಸಬೇಕು:

1. ಇತ್ತೀಚಿನ ಪಾಸ್ ಪೋರ್ಟ್ ಮತ್ತು ಸ್ಟಾಂಪ್ ಅಳತೆಯ ತಲಾ ನಾಲ್ಕು ಭಾವಚಿತ್ರಗಳು
2. ಇಬ್ಬರು ಸ್ವೀಕರಣ ಗಣ್ಯ ವ್ಯಕ್ತಿಗಳಿಂದ ಪಡೆದ ನಡತೆ ಪ್ರಮಾಣ ಪತ್ರ
3. ಆಧಾರ್ ಕಾರ್ಡ್
4. ಪಾನ್ ಕಾರ್ಡ್
5. ಅಭ್ಯರ್ಥಿಯ ಹೆಸರಿನಲ್ಲಿರುವ ಯಾವುದಾದರೂ ರಾಷ್ಟ್ರೀಕೃತ ಬ್ಯಾಂಕ್ ಪುಸ್ತಕ
6. ಕರ್ನಾಟಕ ಅಗ್ನಿಶಾಮಕ ಮತ್ತು ಶುಶ್ರುಕೆ ಸೇವಾ ಇಲಾಖೆಯಲ್ಲಿ ಕರ್ತವ್ಯಕ್ಕೆ ವರದಿ ಮಾಡಿಕೊಂಡ ನಂತರ ತರಬೇತಿ ಮಧ್ಯೆ ಮತ್ತು ತರಬೇತಿಯ ನಂತರ ಇಲಾಖೆಗೆ ರಾಜೀನಾಮೆ, ಗೈರು ಹಾಜರಿಯಾದಲ್ಲಿ ಕರ್ನಾಟಕ ಸರ್ಕಾರದ ಆದೇಶದಂತೆ ರೂ. 1,00,000-00 (ಒಂದು ಲಕ್ಷ ರೂಪಾಯಿ ಮಾತ್ರ) ಗಳ ದಂಡನಾ ಶುಲ್ಕ ಪಾವತಿಸುವ ಬಗ್ಗೆ ರೂ.500-00 ಗಳ ಧಾಪನಾ ಶಾಗದದಲ್ಲಿ ಮುಚ್ಚುಕೆ ಪತ್ರವನ್ನು ನೋಟರಿಯರಿಂದ ದೃಢೀಕರಿಸಿ ನೀಡುವುದು.

Sl No	Appl No. & DOB	Name	Photo & Signature	Address	Selected category
01	1286487 2-Dec-00	RAJU GUDASI	 R. S. Gudasi	RAJU GUDASI AT POST KURANI, KURANI, HUKKERI, Belagavi, Karnataka, Pincode - 591121.	GM_RUR



ನೀವು ಕರ್ತವ್ಯ ವಂದಿ ಮಾಡಿಕೊಂಡ ದಿನದಿಂದ ಎರಡು ವರ್ಷಗಳ ಕಾಲ ಪರೀಕ್ಷಾವಧಿ (PROBATIONARY PERIOD) ಯನ್ನು ಪೂರೈಸಬೇಕಾಗುತ್ತದೆ. ಈ ಪರೀಕ್ಷಾವಧಿ ಅವಧಿಯಲ್ಲಿ ಯಾವುದೇ ರೀತಿಯ ಅನರ್ಹತೆ ಕಂಡುಬಂದರೆ ಯಾವುದೇ ಕಾರಣ ನೀಡದೆ ನಿಮ್ಮನ್ನು ಕೆ.ಎ.ಎ. ಪರೀಕ್ಷಾವಧಿ ನಿಯಮಗಳು 1977ರ ಪ್ರಕಾರ ಕೆಳಸದಿಂಪಡಿಸಿದು ಹಾಕಲಾಗುವುದು.

ಈ ಆದೇಶವನ್ನು ಕೈಕೊಂಡ ನಂತರ ದಿನಾಂಕ:01-08-2022 ರಂದು ಬೆಳಿಗ್ಗೆ 10:00 ಘಂಟೆಗೆ "ಮೋರೇ" ಮತ್ತು ನಿರ್ದೇಶಕರು ಹಾಗೂ ಮಹಾ ನಿರ್ದೇಶಕರು, ಕರ್ನಾಟಕ ರಾಜ್ಯ ಅಗ್ನಿಶಾಮಕ ಮತ್ತು ಕುರ್ಚಿ ಸೇವೆಗಳು, ಸಂ.1 ಅಣ್ಣಾಪ್ಪಾಡಿ ಮೊದಲಯಾರ್ ರಸ್ತೆ, ಹಲಗೂರು ಕೆರೆ ಹತ್ತಿರ, ಬೆಂಗಳೂರು-560 042 ಇಲ್ಲಿ ಐದು ಮಾಡಿಕೊಳ್ಳುತ್ತಿದ್ದು, ನಗದಿಪಡಿಸಿದ ದಿನಾಂಕದಂದು ಹಾಜರಾಗದಿದ್ದಲ್ಲಿ ಯಾವುದೇ ಮುನ್ಸೂಚನೆಯನ್ನು ನೀಡದೆ ನಿಮ್ಮ ನೇಮಕಾತಿ ಆಯ್ಕೆಯನ್ನು ರದ್ದು ಪಡಿಸಲಾಗುವ ಅಂತಿಮ ಆದೇಶವನ್ನು ನೇಮಕಾತಿ ಪ್ರಾಧಿಕಾರದ ಪ್ರಕಟಿಸಿರುತ್ತದೆ.

ನೀವು ಕರ್ತವ್ಯ ಹಾಜರಾಗುವ ಸಮಯದಲ್ಲಿ ಈ ಕೆಳಕಂಡ ಮಾಲ ದಾಖಲೆಗಳನ್ನು ತಪ್ಪದೇ ಹಾಜರು ಪಡಿಸಬೇಕು.

1. ಇತ್ತೀಚಿನ ಪಾಸ್ ಪೋರ್ಟ್ ಮತ್ತು ಸ್ಟಾಂಪ್ ಅಳತೆಯ ತಲಾ ನಾಲ್ಕು ಭಾವಚಿತ್ರಗಳು
2. ದ್ವಾರಾ ಸ್ವೀಕೃತ ಗಣ್ಯ ವ್ಯಕ್ತಿಗಳಿಂದ ಪಡೆದ ನಡತೆ ಪ್ರಮಾಣ ಪತ್ರ
3. ಆರ್.ಎ.ಎ.ಎ.ಎ.
4. ಪಾನ್ ಕಾರ್ಡ್
5. ಅಭ್ಯರ್ಥಿಯ ಹೆಸರಿನಲ್ಲಿರುವ ಯಾವುದಾದರೂ ರಾಷ್ಟ್ರೀಯ ಭೌತಿಕ ಪ್ಯಾಸಪೋರ್ಟ್ ಪುಸ್ತಕ
6. ಕರ್ನಾಟಕ ಅಗ್ನಿಶಾಮಕ ಮತ್ತು ಕುರ್ಚಿ ಸೇವಾ ಇಲಾಖೆಯಲ್ಲಿ ಕರ್ತವ್ಯಕ್ಕೆ ಪದವಿ ಮಾಡಿಕೊಂಡ ನಂತರ ತರಬೇತಿ ಪಡೆದ ಮತ್ತು ತರಬೇತಿಯ ನಂತರ ಪಡೆದಿರುವ ಲಾಜಿಸ್ಟಿಕ್ಸ್, ಗೃಹ ಹಾಜಿರಿಯಾದಲ್ಲಿ ಕರ್ನಾಟಕ ಸರ್ಕಾರದ ಆದೇಶದಂತೆ ರೂ. 100,000-00 (ಒಂದು ಲಕ್ಷ ರೂಪಾಯಿ ಮಾತ್ರ) ಗಳ ವೆಂಚರ್ ಮತ್ತು ಪಾವತಿಸುವ ಬಗ್ಗೆ ರೂ.500-00 ಗಳ ಭಾವಚೀಟಿಯಲ್ಲಿ ಮುಖ್ಯವಾಗಿ ಪತ್ರವನ್ನು ನೋಟು ರವರಿಂದ ದೃಢೀಕರಿಸಿ ನೀಡುವುದು.

Sl No	Appl No. & DOB	Name	Photo & Signature	Address	Selected category
01	1242177 12-Jun-02	OMKAR VIDYARANYA PATIL	 Olatil	OMKAR VIDYARANYA PATIL BELAGAVIROAD, Goudawad, HUKKERI, Belagavi, Karnataka, Pincode - 591309.	GM_OTHERS





ನೀವು ಕರ್ತವ್ಯಕ್ಕೆ ವರದಿ ಮಾಡಿಕೊಂಡ ದಿನದಿಂದ ಎರಡು ವರ್ಷಗಳ ಕಾಲ ಪ್ರೋಬೇಷನರಿ (PROBATIONARY PERIOD) ಯನ್ನು ಪೂರೈಸಬೇಕಾಗಿರುತ್ತದೆ. ಈ ಪ್ರೋಬೇಷನರಿ ಅವಧಿಯಲ್ಲಿ ಯಾವುದೇ ರೀತಿಯ ಅನರ್ಹತೆ ಕಂಡುಬಂದರೆ ಯಾವುದೇ ಕಾರಣ ನೀಡದೆ ನಿಮ್ಮನ್ನು ಕೆ.ಸಿ.ಎಸ್. ಪ್ರೋಬೇಷನರಿ ನಿಯಮಗಳು 1977 ರ ಪ್ರಕಾರ ಕೆಲಸದಿಂದ ತೆಗೆದು ಹಾಕಲಾಗುವುದು.

ಈ ಆದೇಶವನ್ನು ಸ್ವೀಕರಿಸಿದ ನಂತರ ದಿನಾಂಕ:01-08-2022 ರಂದು ಬೆಳಿಗ್ಗೆ 10:00 ಘಂಟೆಗೆ "ಪೊಲೀಸ್ ಮಹಾ ನಿರ್ದೇಶಕರು ಹಾಗೂ ಮಹಾ ನಿರ್ದೇಶಕರು, ಕರ್ನಾಟಕ ರಾಜ್ಯ ಅಗ್ನಿಶಾಮಕ ಮತ್ತು ಕುರ್ಕು ಸೇವೆಗಳು, ನಂ.1 ಅಣ್ಣಾಸ್ವಾಮಿ ಮೊದಲಿಯಾರ್ ರಸ್ತೆ, ಹಲಸೂರು ಕೆರೆ ಹತ್ತಿರ, ಬೆಂಗಳೂರು-560 042 ಇಲ್ಲಿ ವರದಿ ಮಾಡಿಕೊಳ್ಳತಕ್ಕದ್ದು. ನಿಗದಿಪಡಿಸಿದ ದಿನಾಂಕದಂದು ಹಾಜರಾಗದಿದ್ದಲ್ಲಿ ಯಾವುದೇ ಮುನ್ಸೂಚನೆಯನ್ನು ನೀಡದೆ ನಿಮ್ಮ ನೇಮಕಾತಿ ಆಯ್ಕೆಯನ್ನು ರದ್ದು ಪಡಿಸಲಾಗುವ ಆಂತಿಮ ಅಧಿಕಾರವನ್ನು ನೇಮಕಾತಿ ಪ್ರಾಧಿಕಾರವು ಹೊಂದಿರುತ್ತದೆ.

ನೀವು ಕರ್ತವ್ಯಕ್ಕೆ ಹಾಜರಾಗುವ ಸಮಯದಲ್ಲಿ ಈ ಕೆಳಕಂಡ ಮೂಲ ದಾಖಲೆಗಳನ್ನು ತಪ್ಪದೇ ಹಾಜರು ಪಡಿಸಬೇಕು.

1. ಇತ್ತೀಚಿನ ಪಾಸ್ ಪೋರ್ಟ್ ಮತ್ತು ಸ್ಟಾಂಪ್ ಆಳತೆಯ ತಲಾ ನಾಲ್ಕು ಭಾವಚಿತ್ರಗಳು
2. ಇಬ್ಬರು ಸ್ಥಳೀಯ ಗಣ್ಯ ವ್ಯಕ್ತಿಗಳಿಂದ ಪಡೆದ ನಡತೆ ಪ್ರಮಾಣ ಪತ್ರ
3. ಅಧಾರ್ ಕಾರ್ಡ್
4. ಪಾನ್ ಕಾರ್ಡ್
5. ಅಭ್ಯರ್ಥಿಯ ಹೆಸರಿನಲ್ಲಿರುವ ಯಾವುದಾದರೂ ರಾಷ್ಟ್ರೀಕೃತ ಬ್ಯಾಂಕ್ ಪುಸ್ತಕ
6. ಕರ್ನಾಟಕ ಅಗ್ನಿಶಾಮಕ ಮತ್ತು ಕುರ್ಕು ಸೇವಾ ಇಲಾಖೆಯಲ್ಲಿ ಕರ್ತವ್ಯಕ್ಕೆ ವರದಿ ಮಾಡಿಕೊಂಡ ನಂತರ ತರಬೇತಿ ಮಧ್ಯ ಮತ್ತು ತರಬೇತಿಯ ನಂತರ ಇಲಾಖೆಗೆ ರಾಜೀನಾಮೆ, ಗೈರು ಹಾಜರಿಯಾದಲ್ಲಿ ಕರ್ನಾಟಕ ಸರ್ಕಾರದ ಆದೇಶದಂತೆ ರೂ. 1,00,000-00 (ಒಂದು ಲಕ್ಷ ರೂಪಾಯಿ ಮಾತ್ರ) ಗಳ ದಂಡನಾ ಶುಲ್ಕ ಪಾವತಿಸುವ ಬಗ್ಗೆ ರೂ.500-00 ಗಳ ಧಾಪಾ ಕಾಗದದಲ್ಲಿ ಮುಚ್ಚಳಿಕೆ ಪತ್ರವನ್ನು ನೋಟರಿರವರಿಂದ ದೃಢೀಕರಿಸಿ ನೀಡುವುದು.

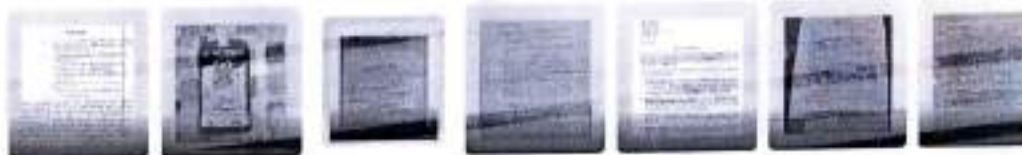
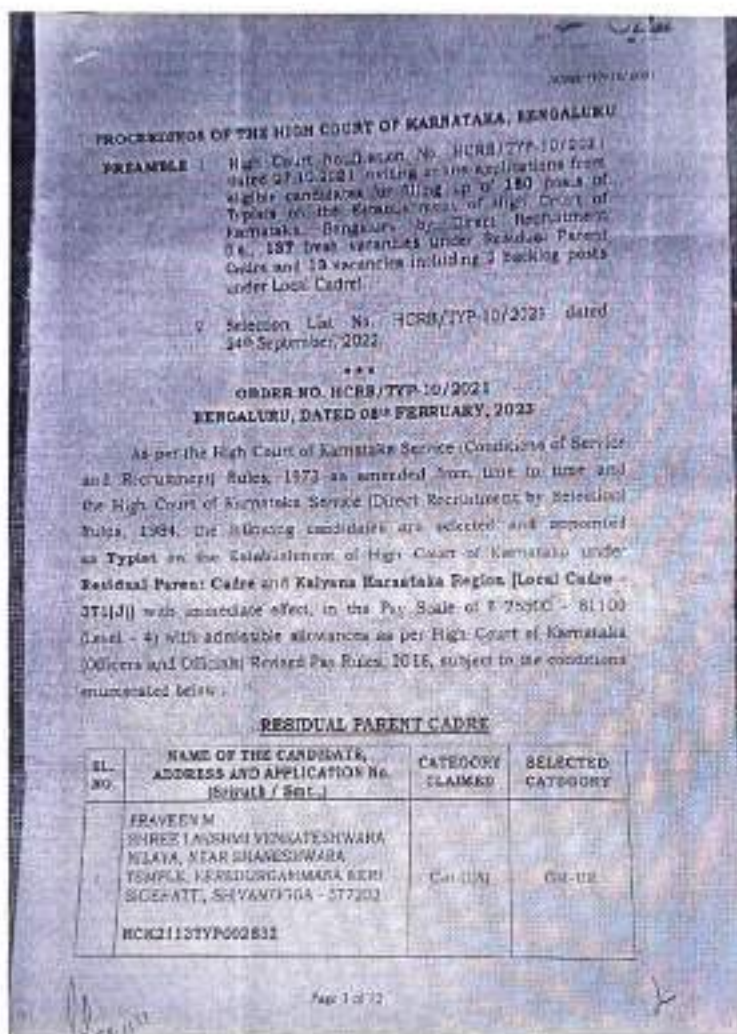
Sl No	Appl No.& DOB	Name	Photo & Signature	Address	Selected category
1	1288421 1-Jul-00	CHETAN NAIK	 	CHETAN NAIK BELAVI, HUKKERI, Belagavi, Karnataka, Pincode - 591309,	3B_OTHERS





You

today at 2:21 PM





You

today at 2:21 PM



26.	FRANCO KISSAR K. NO. 60/002/114, SHANKHA NIAYA, MADHYA SABHARDESHWAR NAGAR, SALADKADI - 431115 HSE221377P000251	CA/125/134	CA/125/134
27.	SHREK CHALAWADI PLOT NO. 42, OASES KADAK, WILDERE TO, BELAGHAT - 431337 HSE221377P000472	SC/04	SC/04
28.	SAVITHRI C DEEPAK'S VILLAGE BANNWALI FCM, BAYLDE WARDHOLI TRUNG, CHAMARJANWAR - 431112 HSE221377P002578	SC/04/108	SC/04
29.	SURESH P A. RESID. CALPAMAGALI ROAD, PURNAL VILAGE AND POST SOLAR - 431101 HSE221377P001174	SC/80	CA/04
30.	VENKATANI A DADIAJ F. NO. 382/1, BANGAR OAD KATDE KOUR JAVAR - 431115 HSE221377P002948	CA/1/04	CA/1/04
31.	SHINDI B 305 CROSS, KALLESWARA EXTENSION, LADDE, NEAR POPULAR SCHOOL, BANSARJARA - 431104 HSE221377P002199	CA/04/1/04	CA/04

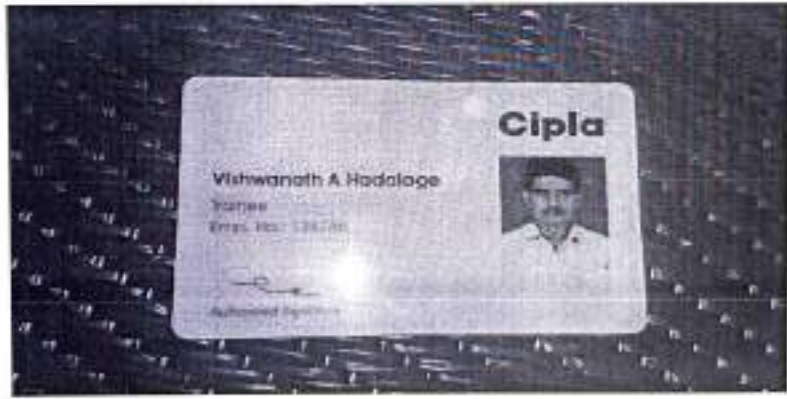
Page 3 of 11





You

Today at 12:15 PM



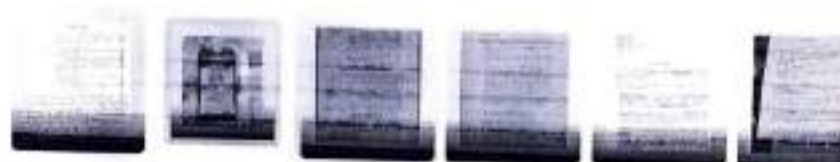


You

Today at 2:21 PM



2 of 13



Mar 16, 2023

Dear Chandrakant Navi

With reference to your application and subsequent interview with us, we are pleased to appoint you as **Trainee** in our organization on the following terms and conditions:



1. Remuneration: Your Annual compensation would be **Rs. 1,80,000/-** (Rupees One Lakh Eighty Thousand Only)
2. In case you choose to avail transport facility for commuting to the Company, **Rs 3000/-** (Rupees One Thousand Nine Hundred Only) per month shall be deducted as conveyance charges
3. All the statutory adjustments will be applicable as per the prevailing laws
4. **Place/Transfer:** You will be posted in the Company located in Aegus SEZ Hattargi, Belgaum. You may be transferred as part of on-the-job training and any further trainings at any time from one place to another, from one establishment to another, from one unit to another, whether owned, operated or managed by the Company or otherwise including the establishments with which Company will have the arrangements (all such places, establishments and units hereinafter referred to as "Establishments") either in India or abroad. On such transfer you will be governed by the terms and conditions of service applicable to your category of trainees in the Establishments where you are placed in as part of your training.
5. **Training:** Training period shall be One Year from **Mar 16, 2023 to Mar 15, 2024** ("Training Period"). Though your training period is for one year, if you are not found suitable for training, your training can be discontinued without assigning any reason thereof with 30 (Thirty) days prior notice. The decision of the Company shall be final and binding upon you.
6. Company does not guarantee employment on completion of your training and any extension thereof and you shall be free to look for employment elsewhere.
7. During the Training period, your Training can be terminated with 90 (Ninety) days' notice by either by you or Company.
8. **Leave:** You will be eligible for leaves as per Company policy.
9. You shall perform as per directions and instructions given to you whether given by the Company or by such officers who are placed in authority over you during your on-the-job training or further training.
10. During the period of your training with the Company, you will devote full time to the Company. Further, during the training period, you will not take up any other employment or assignment or any office, honorary or for any consideration, in cash or in kind or otherwise, without the prior written permission of the Company.

Assemble Process India Private Limited

Corporate Identity Number: U35303KA2007PTC045313

Corporate Office: Aegus SEZ, No. 437/A, Hattargi Village, Hukkeri Taluk,

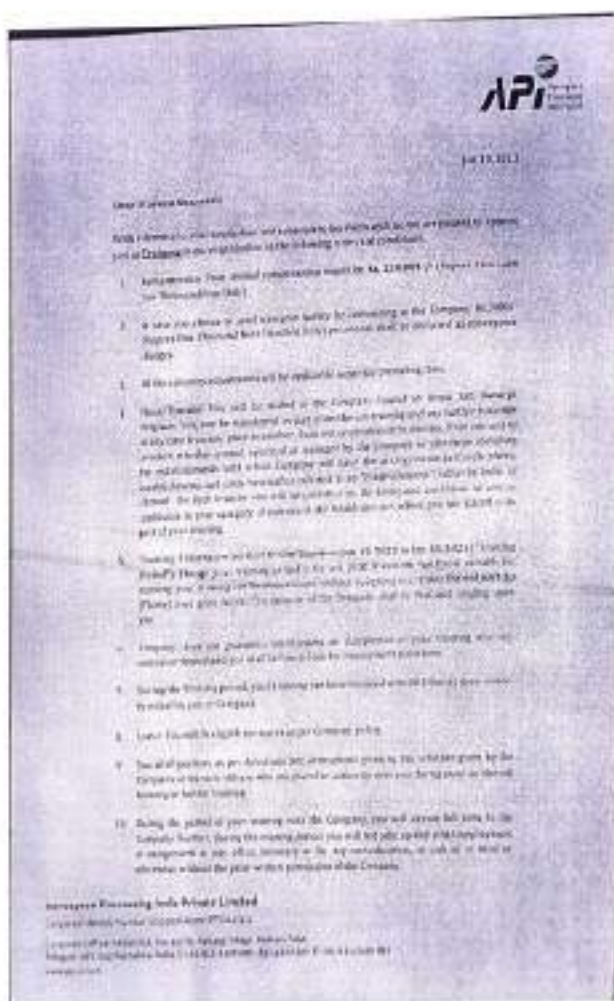
Belgaum - 591 243, Karnataka, India. T: +91 831 2499 000, 831 4222 500 F: +91 831 2499 001

api.com



You

today at 2:21 PM





You

Today at 2:21 PM



← 3403 veena Ap...   

 **AGASTYA**
S.S. Agastya College & Research Centre

AGASTYA
S.S. Agastya College & Research Centre
Bangalore, Karnataka, India
560016

Ref: AP/HR/APP/2023/600

Date: 30 Nov 2023

Ms. Veena Pall
14/03/1990
Bangalore, India
Bangalore, Karnataka, 560016
Emp ID: 1401

Dear Veena,

Letter of Appointment

With reference to your application and subsequent interview, we have pleasure in informing you that you are appointed as **Instructor (Health Edu)** at **Balakeri College** effective from the date of joining which should not be later than 30th April 2024 on the following terms and conditions set out here below:

Your appointment is being made on contractual basis for a fixed period unless you wish to provide with renewed appointment.

- Salary:** You would be paid a consolidated salary of **Rs.5200/- (Rupees Five Thousand Two Hundred Fifty Only)** per month, which may include basic salary & DA, HRA, and other allowances etc. **Additional HRA of Rs.750/- (Seven Hundred and Fifty Rupees)** will be added to it for reimbursement for stay provided by the Foundation and your third provident fund be vested of **Rs.10000/-** after completion of probation.
- Program/Tenure:** You are being appointed for post of **AGASTYA'S MAJASRATU WISNUSIA FUTURE SKILL** for a period of **12 months** from the date of your joining. Your tenure is commensurate with the program. It may be renewed on mutual agreement and a subject to continuation of the said program.
- Probation:** You will have to undergo 60 days probation and on successful completion of the probation period, you would be eligible to continue the contractual employment beyond the period.
- Provisional Charge:** As per the existing policy of the Foundation, you will be placed under **Provisional Charge** (D.C. Quarter Scheme) during probationary period and Medical Allowance is applicable.
- Leave and Holidays:** You are entitled to Leave as per the existing Leave Policy of Foundation. You are also entitled to holidays as fixed by Foundation as per National & Festival holidays etc.
- Transfer:** You are liable to be transferred / posted to one of the Foundation's location within the limits of India and you are also liable to accept / posted / transfer to one Department. Decision is assigned such other duties is deemed to be in the discretion of the management in any of the post or other Office of the Foundation.

Signature / Transmission





Provisional Offer : BUSINESS PROCESS SERVICES

Ref: TCSL/DT20234226948/Bangalore/BPS/BTN

Date:22/08/2023

Dear Ms. Veena Suresh Muchandi,

Sub: Letter of Provisional Offer and Terms of Employment.

Thank you for exploring opportunities with **Tata Consultancy Services Limited(TCSL)**. You have successfully completed our initial selection process and we are pleased to make you a provisional offer of Traineeship.

You have been selected for a twelve month traineeship program at grade BPOS. You will receive a fixed monthly stipend during your internship. Your stipend amount will be decided on the basis of joining location and the process in which you will get allocation. The same will be communicated to you along with the detailed offer letter.

Kindly confirm your acceptance on the traineeship offered by signing Annexure 1. If not accepted within 30 days of receipt, this offer of traineeship is liable to lapse at the discretion of the Company.

This is a provisional offer of traineeship and should not be construed as an Offer of Employment from TCSL. A detailed offer of traineeship will follow within 7 days from completion of all documentation formalities and your aforesaid acceptance on this provisional offer. The Offer of traineeship will be made to you provided this - opportunity continues to be available with TCSL.

Your traineeship with TCS is subject to your being declared medically fit and retaining that fitness during the tenure in the company and your Background / Reference check being favourable and acceptable to the Company.

On joining and successful completion of all Joining formalities including the back ground verification, you will be issued a Letter of Appointment by TCSL.

Your appointment will be governed by the policies, rules, regulations, practices, processes and procedures of TCSL as applicable to you and the changes therein from time to time.

Private and Confidential

TCSL/DT20234226948

TATA CONSULTANCY SERVICES

Tata Consultancy Services Limited

No 42, Think Campus, Electronic City phase II, Bangalore - 560 100, Karnataka India

Ph: +91 80 6724 2000 Fax:91 80 2252 1310 E-mail: corporate.offic@tcs.com Website: http://www.tcs.com

Registered Office: 39th Floor, Nxtma Building, Nariman Point, Mumbai- 400 021

Corporate Identification No. (CIN): L22210MH1995PLC054791



Please also note, TCS BPS provides company transport facility within a pre-defined radius for each location as defined in the company transport policy. Those living beyond these boundaries would be required to make their own arrangements to reach the nearest location convenient to them from where they can be picked up or dropped.

Yours Sincerely,

For Tata Consultancy Services Limited.

Girish V. Nandimath
Global Head Talent Acquisition & AIP



[Click Here](#) or use a QR code scanner from your mobile to validate the offer letter

ANNEXURE 1

For the candidate to complete:

This is to confirm that I have received & hereby accept the Provisional Letter of Traineeship Ref No TCSL/DT20234226948/Bangalore/BPS/BTN on _____(DD/MMM/YYYY).

Signature:

Name:

Date:



CENTRAL INDUSTRIAL SECURITY FORCE
(Ministry of Home Affairs)

CISF UNIT SZ-I HQRS CHENNAI
CISF SZ-I HQrs Chennai
D Block, Rajaji Bhawan
Basant Nagar, Chennai
Tamil Nadu-600090

Dated: 11-11-2022

E-32017/Rectt/SSC CT(GD)-2021/SZ-I (RRC)/2022- 1009

To,

No. 9001026706
SACHIN S DESAI

at post AMMANAGI TAL HUKKERI Dist-
BELAGAVI, State- KARNATAKA, PIN- 591236.

**Subject: RECRUITMENT OF CONSTABLE/GD IN CENTRAL INDUSTRIAL SECURITY FORCE :
OFFER OF APPOINTMENT**

Reference your selection to the post of Constable/GD in Central Industrial Security Force.

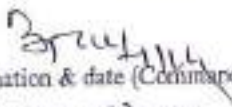
2. You have been provisionally selected for appointment as Constable/GD in CISF on the following terms and conditions:-

- i. You will draw the pay in the Pay Matrix Level-3, Rs.21700-69100.
- ii. Your appointment will be subject to the conditions given in the Agreement Form, which will be required to be filled at the time of reporting at

RTC RTC DEOLI
CISF RTC DEOLI, PO- DEOLI, TONK, RAJASTHAN
Nearest Airport:- JAIPUR
Nearest railway station:- KOTA JN
Nearest bus Depot:- DEOLI

- iii. You will be on probation for a period of two years.
- iv. The Appointing Authority may discharge you from service at any time during the period of probation, if in their opinion, your work or conduct during this period is considered unsatisfactory, or shows that you are not fit for permanent appointment.
- v. You will be considered for confirmation in service on your successful completion of probation and if you are found fit in every respect for confirmation.
- vi. It should be understood that your appointment is subject to any change in the Recruitment Rules framed from time to time and that you will have no claim for compensation in consequence of any such change. Further you will be subjected to the provisions of Central Industrial Security Force Act, 1968 (50 of 1968) and Central Industrial Security Force Rules, 2001 as amended from time to time.
- vii. You are liable for transfer to any station in the Union of India.
- viii. You are liable to be employed at any place within or outside India.
- ix. You are liable to serve in NSG, SPG or any other Force of the Country in the broader interest of National security.
- x. In case you belong to SC/ST category your appointment will be subject to the Caste/Tribe certificates being verified through the proper channels and if the verification reveals that your claim to belong to Scheduled Caste or Scheduled Tribe, as the case may be, is false, the services will be terminated forthwith without assigning any further reasons and without prejudice to such further action as may be taken under the provisions of the Indian Penal Code for production of false certificates.
- xi. In case you belong to OBC category, you are required to submit the original OBC Certificate. In addition to this, you are also required to submit a declaration about your creamy layer status. Your appointment is

7. You must open a simple saving bank account in your name in State Bank of India repeat State Bank of India before joining at the Training Center. You should bring passbook, chequebook and ATM card for drawal of payment. If feasible, you should also bring PAN Card and Aadhar Card (as proof of Identity) for easy and quick opening of your account for New Pension Scheme.
8. You should be in possession of sufficient money in your account, at least Rs.8000/- for your own mess deposit which will be deposited to the Training Centre at the time of reporting. The mess deposit will be done by cheque.
9. You should also carry your personal belongings including proper clothing and bedding and other items of daily use which may be required by you.
10. You are advised not to be in possession of jewellery or expensive ornaments.
11. You will not be allowed to carry mobile phones during the training activities.
12. You are also advised not to bring any expensive gadget or any expensive item.
13. No TA/DA will be admissible to you for this journey.
14. The "NEW RE-STRUCTURED DEFINED CONTRIBUTION PENSION SYSTEM" applicable for the new entrants to the Central Government Services w.e.f. 1st January, 2004 will also be applicable to you.


Signature of appointing authority with designation & date (Commandant only)

Encls(If not supplied earlier):

- i. Two Attestation Forms
- ii. Annexure-IV
- iii. Form of SHO certificate.

आजय कुमार खंडेलवाल
AJAY KUMAR KHANDELWAL
समूह कमाण्डेंट
GROUP COMMANDANT

मुख्यालय चेन्नई-90
CHENNAI - 90